

Interfacial structure and dynamics

**Thesis submitted for the degree of
Doctor of Philosophy
at the University of Leicester**

By

Samantha Jayne Daisley BSc (Coventry)

Department of Chemistry

University of Leicester

September 2008

ABSTRACT

Interfacial structure and dynamics

By Samantha Daisley

Thin nanoporous metallic films have been prepared by electrochemical deposition around spherical polystyrene particles deposited on gold substrates. The characterisation of both the polystyrene templates and the films were carried out by in situ electrochemical quartz crystal microbalance (EQCM) and atomic force microscopy. The formation of the polystyrene template significantly depends on the deposition conditions (sedimentation time and rate of solvent evaporation). The resultant metallic films mirror the morphology of the polystyrene arrays. The frequency shifts for films in air and in water indicate only partial fluid filling of the hemispherical voids left by the dissolved polystyrene templates.

EQCM measurements were made during the p-, n- and sequential p-and n-doping of PEDOT films exposed to a range of electrolytes in two different solvents. The films were acoustically thin, so the EQCM response was simply gravimetric. Dopant ion and solvent fluxes were determined by the use of time differentials obtained from the current and mass response. Normalisation of the flux data as a function of potential or charge lead to mechanistic information.

For the case of p-doping of PEDOT films exposed to $\text{LiClO}_4/\text{CH}_3\text{CN}$, during both the doping and un-doping half cycles, all fluxes normalised with respect to scan rate. However, the responses in the two directions are not mirror images suggesting the two processes have different mechanistic paths. Comparison of data obtained for a PEDOT film cycled in two different solvents showed distinct differences. The normalisation procedure works well for both sets of data, but illustrates that they have different mechanisms. Both sets of data showed a mechanistic switch occurring during both the doping and un-doping half cycles.

There was significant solvent transfer for PEDOT films cycled in the n-doping region, but the direction was cation dependent. The fluxes normalised with respect to scan rate, indicating no kinetic or transport limitations. Considerable hysteresis between the responses suggested that polymer reconfiguration occurs. Extension of the potential range to include both p- and n-doping regimes, showed additional features appear on the edge of the two doping peaks, signalling the release of trapped charge.

STATEMENT OF ORIGINALITY

The work within this thesis is original except where a reference or acknowledgement has been made. It is based on work carried out in the Department of Chemistry, University of Leicester during the period between July 2004 and September 2007.

Samantha Daisley

Acknowledgements

I would like to thank my supervisor, Professor A.R. Hillman for making this study possible and providing the support, guidance, enthusiasm and encouragement throughout my Ph.D. A special thank you goes to Professor Stanley Bruckenstein for his collaboration and help.

I would also like to thank Dr K. Ryder for his encouragement and support. Thank you to Graham Clarke for all the work carried out on the scanning electron microscope.

Finally I would like to say thank you to Magda Skopek, and Igor Efimov for being good friends during my time at Leicester. Finally a really big thank you to my family, especially my children Thomas and Jaymee, for their understanding, support and encouragement.

Table of Contents

	Page
Chapter 1 Introduction	1
1.1 Introduction	1
1.2 Wetting	3
1.2.1 Contact angle measurements	4
1.3 Modified Electrodes	5
1.3.1 Template modified electrodes	5
1.3.2 Polymer modified electrodes	7
1.3.2.1 Conducting polymers	8
1.3.2.2 Redox polymers	10
1.4 Survey of techniques	11
1.4.1 Electrochemical techniques	12
1.4.1.1 Cyclic voltammetry	12
1.4.1.2 Chronoamperometry/chronocoulometry	12
1.4.2 Surface imaging techniques	13
1.4.2.1 Scanning electron microscopy (SEM)	13
1.4.4.2 Atomic force microscope (AFM)	14
1.4.3 Acoustic wave techniques	16
1.5 Objective	18
References	19
Chapter 2 Theory	23
2.1 Introduction	23
2.2 Voltammetry	24
2.2.1 Fundamentals	24
2.2.2 Mass transport	24
2.2.3 Cyclic voltammetry	26

2.2.4	Cyclic voltammetry for modified electrodes	28
2.3	Quartz crystal microbalance (QCM)	29
2.3.1	Background	29
2.3.2	The piezoelectric effect	30
2.3.3	Quartz crystal's orientation of cut	31
2.3.4	Sauerbrey equation	32
2.3.5	Harmonics	35
2.3.6	Quartz crystal microbalance in liquid media	36
2.4	Undesirable contributions to QCM	37
2.4.1	Excess mass	37
2.4.2	Surface roughness	38
2.4.3	Non-uniform mass	38
2.4.4	Temperature	38
2.4.5	Interfacial slippage	39
2.5	The electrochemical quartz crystal microbalance	39
2.6	Equivalent circuit models of QCM	40
2.6.1	Transmission line model	42
2.6.2	Butterworth Van Dyke (BVD) model	43
2.6.3	Modification of the BVD model	44
2.7	Physical models for mass loading of QCM	47
2.7.1	Ideal mass layer	47
2.7.2	Semi-infinite Newtonian fluid	48
2.7.3	Viscoelastic layers	50
2.7.4	Multi-layer physical models	52
2.7.5	QCM response for complete/incomplete wetting	53
	References	56

Chapter 3 Experimental	58
3.1 Introduction	58
3.2 Quartz crystal resonator	58
3.2.1 Surface finish of quartz crystal	59
3.3 Electrochemical instrumentation	59
3.4 Nanoporous metal film preparation	60
3.4.1 Overview	60
3.4.2 Instrumentation and materials	61
3.4.3 Procedure	62
3.5 Wetting at textured surfaces	63
3.5.1 Overview	63
3.5.2 Instrumentation and materials	63
3.5.3 Procedure	63
3.6 Pedot p-doping	64
3.6.1 Overview	64
3.6.2 Instrumentation and materials	64
3.6.3 Procedure	64
3.7 Pedot n-doping	65
3.7.1 Overview	65
3.7.2 Instrumentation and materials	65
3.7.3 Procedure	66
References	67
Chapter 4 Interfacial wetting at nanoporous surfaces	68
4.1 Introduction	68
4.2 Aims and objectives	71

4.3 Procedure	71
4.4 Results	73
4.4.1 Investigation of quartz crystal surface features	73
4.4.1.1 AFM and SEM investigation of quartz crystal surface features	73
4.4.1.2 Investigation of surface features using fluid entrainment measurements	76
4.4.2 Template formation	79
4.4.2.1 QCM response for settling period	82
4.4.3 Copper nanoporous film preparation	83
4.4.3.1 Surface roughness of copper deposition	83
4.4.3.2 Nanoporous film preparation	87
4.4.3.3 Confirmation of pore size using fluid entrainment measurements	91
4.4.3.4 The effect of surface roughness on wetting	93
4.4.4 Platinum nanoporous films	95
4.5 Conclusions	102
References	105
Chapter 5 P-doping of PEDOT films	107
5.1 Introduction	107
5.2 Aims and objectives	109
5.3 Procedure	110

5.4 Data analysis	111
5.5 Results	113
5.5.1 Kinetic and mechanism of electrochemical p-doping of PEDOT	113
5.5.1.1 Film preparation	113
5.5.1.2 Overview of population changes and fluxes	114
5.5.1.3 Potential dependance of fluxes	116
5.5.1.4 Normalisation of fluxes as a function of charge state	121
5.5.1.5 Mechanistic possibilities	124
5.5.2 Effect of electrolyte concentration of permselectivity	128
5.5.3 Solvent effects on the electrochemical p-doping	132
5.5.3.1 Overview of population changes	132
5.5.3.2 Potential dependence of fluxes	135
5.5.3.3 Flux normalisation with respect to timescale and film charge state	141
5.5.3.4 Mechanistic possibilities	148
5.5.3.4.1 PEDOT film cycled using acetonitrile as the solvent	148
5.5.3.4.2 PEDOT film cycled using dichloromethane as the solvent	150
5.6 Conclusions	152
References	154
Chapter 6 n-doping of PEDOT films	156
6.1 Introduction	156
6.2 Aims and objectives	157

6.3	Procedure	158
6.4	Data analysis	159
6.5	Results	161
6.5.1	Overview of n-doping	161
6.5.2	Fluxes of mobile species during n-doping	164
6.5.3	Effect of consecutive p- and n-doping	169
6.6	Conclusions	182
	References	184
	Chapter 7 Conclusions and future work	186
7.1	Conclusions	186
7.2	Future work	190

CHAPTER 1

INTRODUCTION

1.1 Introduction

The research presented within this thesis has two main objectives. The first part involves the investigation of interfacial wetting using nano-porous metallic films. The second part of the study aims to characterize ion and solvent dynamics for the electroactive polymer film poly(3,4-ethylenedioxythiophene) (PEDOT).

Interfacial wetting is an important phenomenon for electrochemical devices, since only the part of the interface that is wet by the solution may take part in the required (electro)chemical process. Although the wetting of an interface is mainly dominated by the lyophobic nature of the surface, the geometric microstructure will also affect the wettability of the surface¹⁻⁵. Surface roughness or surfaces with well-ordered microstructures can alter the lyophobic nature of a surface¹⁻⁹.

Nano-porous material with pore sizes of a few hundred nanometers may be prepared using colloidal crystal template techniques¹⁰⁻¹⁵. These techniques involve the formation of a sacrificial template followed by the permeation of a chemical precursor of the target material into the spaces within the template. The latter is converted into a porous material by a suitable reaction. The comparison of nano-porous films prepared by this method to those that are prepared by traditional lithography highlights the templating method as having the advantage of being more cost effective but at the possible price of being a more time consuming method. As well as unique physical properties these films may also offer interesting chemical properties with particular relevance to electrocatalysis. In this area of application, one would anticipate that the critical issue would be the extent of fluid penetration into the porous film.

Nanoporous films were prepared on the surface of a quartz crystal resonator, to investigate the effect of surface roughness on interfacial wetting. It has been shown that the quartz crystal microbalance operates in liquid media¹⁶⁻¹⁸. Surface features of

a quartz crystal resonator can have a drastic effect on the resonant frequency when the resonator is immersed in liquid^{16, 19}. It is believed that fluid may become trapped within the surface features and act like a rigid mass layer²⁰. Comparison of a smooth quartz crystal microbalance immersed in liquid and a quartz crystal microbalance with nano-porous film exposed to liquid allows analysis of the properties of the rigid mass layer. The properties of the rigid mass layer gives the amount of fluid penetration into the pores of the film.

The latter half of this thesis examines the dynamics of acoustically thin electro-active polymer films of poly(3,4-ethylenedioxythiophene) (PEDOT). Conducting polymers based on polyheterocycles such as thiophenes have distinct optical, electrochemical and electronic properties. The interesting nature of such materials and the ability to exploit their physical and chemical properties has lead to this being one of the largest areas of electrochemical research^{21, 22}. The ability of these polymer films to store charge implies potential applications in rechargeable batteries²²⁻²⁴ and supercapacitors²⁵⁻²⁷. However a comprehensive understanding of their properties is required for future development and realisation of possible applications.

The ability to modify electrodes with electroactive films²⁸ has called upon the deployment of a number of characterisation techniques, including electrochemical²⁹⁻³¹, spectroscopic³⁰⁻³³ and physical methods. The main methods utilized in the later chapters of this thesis are the quartz crystal microbalance (QCM)³⁴ and cyclic voltammetry. The QCM has been used in both sensing and characterization applications.

The in situ electrochemical quartz crystal microbalance (EQCM)^{16-18, 35} can be used to study acoustically thin films (see section 2.7). Ion and solvent transfers that occur during the redox switching of the electro-active polymer film can be investigated by analysis of the differential mass and charge data obtained from the EQCM.

1.2 Wetting

Wetting is an important phenomenon in a number of electrochemical devices notably within membranes used for (electro)catalysis, fuel cells and sensors, since only the part of the interface that is wet by the solution may take part in the required (electro) chemical processes. Surface wetting of a solid interface is an important property controlled by the surface energy and the geometric microstructure of the surface¹⁻⁵. Therefore one of the important characteristics of a liquid is its ability to wet the surface of a solid interface.

The definition of wetting can therefore be described as the contact between a liquid and a surface, when they are brought into contact with each other. Wetting is dominated by the lyophobic nature of the surface. If a liquid has a high surface tension, the cohesive forces are stronger than the adhesive forces. Then the liquid will form beads on the surface i.e. wetting will not occur. However if the molecules within the liquid have a stronger attraction to the surface than to each other (strong adhesive forces, low surface tension) the solution will spread out over a greater area, bonding to the surface molecules.

It is well known that de-wetting occurs at textured surfaces. Wetting of a solid surface is an important property that is not only controlled by the chemical properties of the materials but also the geometric microstructure of the surface^{3, 36}. There are two possible scenarios for textured surfaces^{6, 7}: the liquid will either follow the solid surface or it will trap air inside the surface features (figure 1.1). Therefore wetting may be viewed as the level of fluid penetration into surface features. The extent to which fluid penetration occurs will be dependent upon the balance of forces associated with the compression of the trapped gas and surface tension.

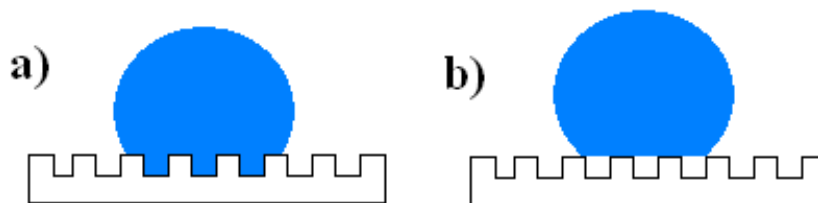


Figure 1.1 Wetting of textured surfaces a) liquid follows the surface features and b) liquid compresses and traps gas within the surface features

1.2.1 Contact angle measurements

Wettability depends on the properties of the fluid and the solid surface⁸. The wettability of a solid surface by a liquid is characterised by the contact angle a liquid drop makes on the surface (figure 1.2)⁸. The wetting angle θ is given by the angle between the interface of the droplet and the surface. The condition $\theta < 90^\circ$ indicates that the solid is wet by the liquid (figure 1.2b) and $\theta > 90^\circ$ indicates a non-wetting scenario (figure 1.2a). The limits $\theta = 0^\circ$ and $\theta = 180^\circ$ define complete wetting and complete non-wetting respectively. The wetting angle θ is a thermodynamic variable that depends on the interfacial tension of the surfaces. The contact angle θ and the surface energies of the materials involved are related by the Young-Dupré equation (1.1). In thermodynamic equilibrium the wetting angle is given by:

$$\gamma_{s,g} = \gamma_{s,l} + \gamma_{l,g} \cos \theta \quad (1.1)$$

where $\gamma_{s,g}$ denotes the interfacial tension due to the solid/gas interface, $\gamma_{s,l}$ denotes the interfacial tension due to the solid/liquid interface and $\gamma_{l,g}$ denotes the interfacial tension due to the liquid/gas interface.

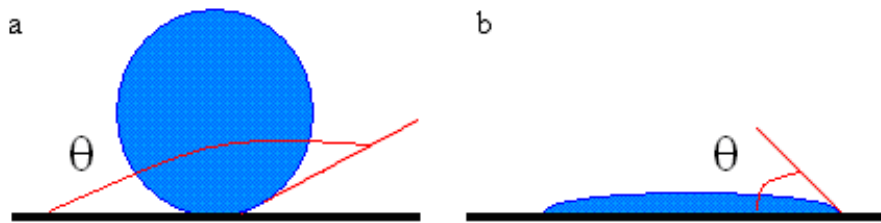


Figure 1.2 A liquid droplet in equilibrium with a horizontal surface surrounded by gas. (a) $\theta > 90^\circ$, a non-wetting scenario and (b) $\theta < 90^\circ$, surface wetting

1.3 Modified Electrodes

The first modified electrode was reported over thirty years ago^{37, 38}. Since then it has been an expanding research field. When the electrode surface is coated with a chemical species it is no longer in direct contact with the bathing solution; this limits the charge transfer reactions to ones that take place through the surface immobilized species. Hence, the electrochemical response will be dictated by the properties of the additional layer on the modified electrode³⁹.

There are many different ways to modify an electrode and each method yields unique and specific chemical effects, leading to a variety of different applications. Electrodes are commonly modified with inorganic materials, such as metal oxides, or organic conducting polymers²⁸. Electrodes are often modified with thin films of these materials as they are generally porous in nature. Therefore they offer a reactive surface area that is much larger than the unmodified electrode. As a consequence they can give a current response that is much larger than one that is normally possible without the modification.

Another, rather recent, modification of electrodes is the application of nano-porous films. Nano-porous films have unique optical properties due to pore diameters being similar to the wavelength of visible light¹³. The development and functionality of materials with spatially ordered features offer possible applications within data storage devices^{40, 41}, biosensors¹⁰, microchip reactors⁴² and photonics⁴³.

1.3.1 Template modified electrodes

The nano-structured films are often produced through templates of spherical colloidal particles (usually polystyrene latex microspheres)^{44, 45}. Many different methods to produce colloidal crystalline templates that are free from defects have been proposed. However one of the most popular techniques used is gravity sedimentation of a dispersion of the polystyrene latex microspheres^{44, 45} or silica particles^{10, 46} in a suitable solvent. As the volume fraction of these spherical particles in solution increases, the particles crystallize into hexagonal close packed arrays, driven by maximization of the vibrational entropy of the system.

Templates of three dimensional close-packed arrays of uniform colloidal spherical particles, produced using this and other techniques, are known as artificial opals due to their diffractive properties¹³.

The most popular method for fabrication of a porous metallic film is the formation of the template followed by permeation into the spaces within the template of a solution of a chemical precursor of the target material. The chemical precursor is then converted into the porous material by a suitable reaction; subsequent removal of the template, commonly by dissolution, leaves the required nanoporous film. Variants of this approach include deposition of colloidal gold particles into colloidal crystals⁴⁶, lithography⁴⁷, electroless deposition⁴⁸⁻⁵⁰ and hydrogen reduction of pre-formed oxides⁵¹. However these techniques often produce films that have performance limitation, arising as a consequence of structure shrinkage during their formation, incomplete filling, and chemical or mechanical instability due to contamination by residues from the chemical reagents used.

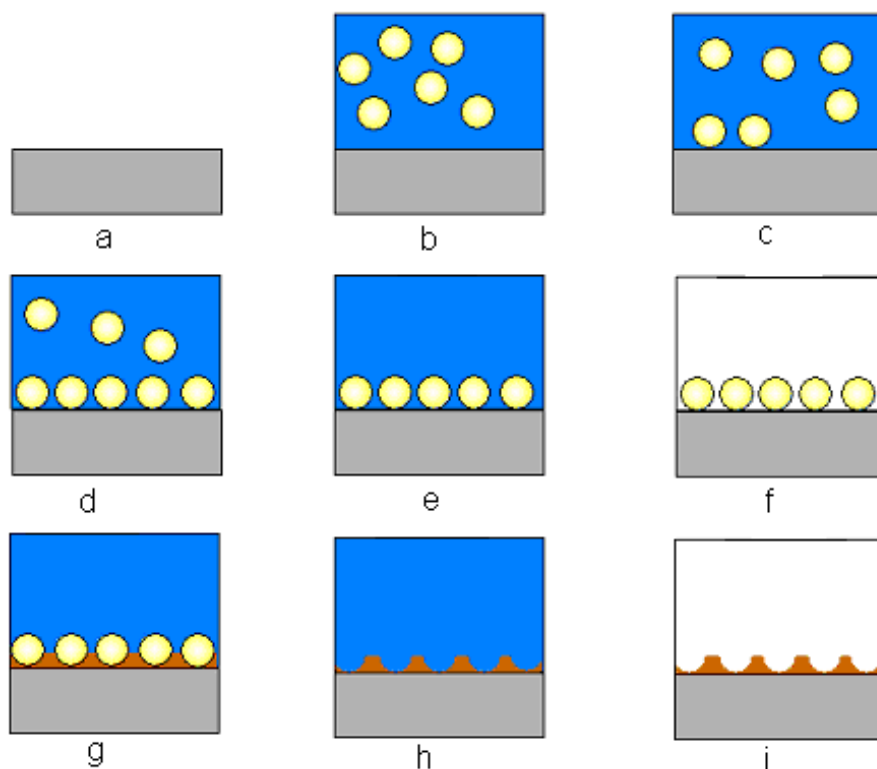


Figure 1.3 Schematic illustration of the formation of nanoporous film: a is the bare crystal; b – d denote the settling of the latex sphere; e shows the drying process of the

template; f represents the dried templated; g illustrates the deposition of metallic species into the spaces; h is the dissolution of the template and i is the final product. One approach that overcomes these problems utilises electrochemical deposition^{45, 52-54}. This study uses this very successful approach, in which a close-packed array of monodisperse polystyrene spheres is used to form a template on the quartz crystal (using gravity sedimentation). The required metal is then electrochemically deposited within the interstices in the close-packed array of spheres. Dissolution of the template leaves a highly ordered porous film. The pore diameter and thickness of the film can be controlled via the template sphere size and the electrodeposition charge passed, respectively. A schematic illustration of this procedure is given in figure 1.3. These quartz crystals with modified surfaces are then used to investigate fluid penetration into the surface features.

1.3.2 Polymer modified electrodes

Up until the 1970's organic polymers were regarded as insulators and the thought that they may indeed conduct electricity was simply believed impossible. In fact some carbon based polymers are used by the electronics industry as inactive packaging and insulating materials. During the 1970's a new class of polymers known as intrinsically conductive polymers was discovered and this is now a very rapidly growing research area.

The reactivity of a metal electrode can often be slow and non-specific towards solution species. However the addition of an electroactive polymer can lead to a modified electrode that has a greater degree of chemical specificity⁵⁵. When an electrode is modified using a polymer, the reactivity towards the species in solution is determined by the nature of the film and no longer by the electrode itself, as the solution is now in contact with the polymer film. The reactivity towards the solution species will be determined by the redox state of the polymer, which is controlled by the potential applied to the underlying electrode.

Applying a potential to the electrode causes electron transfer to take place at the interface between the film and the electrode. In order to maintain electroneutrality there is a movement of ions from the solution into the film or vice versa. Therefore the current response is a measure of the reduction/oxidation of the film. If the

polymer is permeable then the electrode may no longer be classed as a 2D interface, but now a 3D matrix. Solution species may enter inside and react with the reduced/oxidised sites, within the polymer film and not just with the surface sites giving a much greater flux in comparison to the unmodified electrode.

The ability to use a wide variety of functional groups, in order to generate polymers with specialised properties for a specific performance requirement, has led to many potential applications of modified electrodes. These include electronic devices⁵⁶⁻⁵⁸, electrochromic displays⁵⁹⁻⁶¹, electrocatalysts⁶², sensors²², corrosion protection²² and charge storage/rechargeable batteries²³.

Electroactive polymer films may be categorised into two main groups, according to the backbone of the polymer structure, these are known as redox and conducting polymers.

1.3.2.1 Conducting Polymers

The first class of electroactive films was discovered by accident in the mid 1970's by Shirakawa^{63, 64}. While attempting to oxidatively couple aromatic compounds they made polyphenylene and polythiophene and noticed that these polymers had electrical conductivities of up to 0.1 S cm^{-1} . Soon after the discovery by Shirakawa, Heeger and MacDiarmid⁶⁵ reported an increase in conductivity of 12 orders of magnitude by simply doping polyacetylene. Since then there has been a vast amount of research dedicated to conducting polymers.

The main characteristic of all conducting polymers is a conjugated backbone that has a large degree of delocalisation of π electrons²². Table 1.1 highlights the main classes of conducting polymers. The simplest possible conducting polymer is polyacetylene $(\text{CH})_x$ (shown in table 1.1). However due to the polymer's unstable nature it is of limited value. Polymers with delocalised π electrons are insulating since there is a filled valency band and an empty conduction band, conductivity increases dramatically when the film is oxidised or reduced.

The oxidation and/or reduction of the polymer may occur by a process called doping. This terminology is borrowed from the literature of semi-conductors, although the

process is somewhat different. The p-doping (oxidation) process may be summarized in the following way: An electron is removed from the polymer backbone, producing a positive charge. Counter-ions from the bathing electrolyte enter the film to balance the charge. The counter-ions do not react with the polymer (i.e. substitution for any atoms in the polymer does not occur), they simply associate with the redox sites along the polymer chain. Because the counter-ion simply associates itself with the redox site, the polymer may be doped and undoped reversibly and relatively easily.

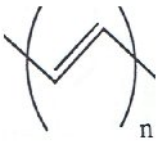
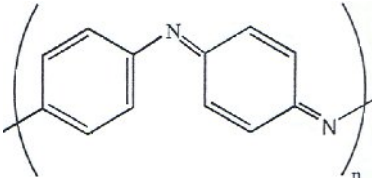
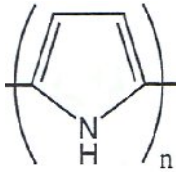
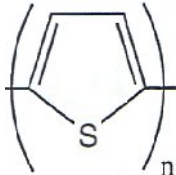
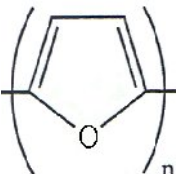
Name	Structure
Polyacetylene ^{23, 66}	
Polyaniline ⁶⁷⁻⁶⁹	
Polypyrrole ^{23, 67}	
Polythiophene ^{23, 70, 71}	
Polyfuran ^{23, 72}	

Table 1.1 Examples of conducting polymer structures

1.3.2.2 Redox polymers

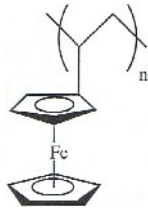
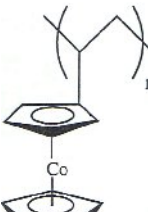
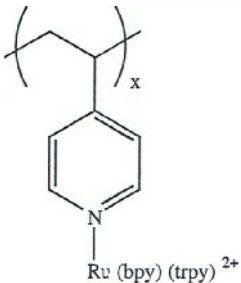
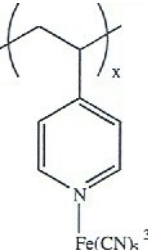
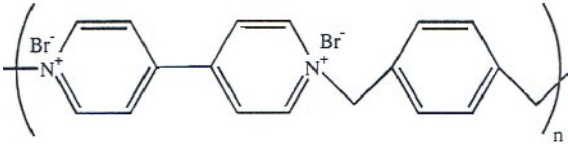
Name	Structure
Poly(vinylferrocene) ⁷³⁻⁷⁵	
Poly(vinylcobaltocene)	
Poly(pyridyl) ruthenium(II) complex	
Poly(pyridyl) iron(II) complex	
Poly(xylyviologen dibromide)	

Table 1.2 examples of redox polymer structures

In contrast to conducting polymers, redox polymers do not have a conjugated backbone. Table 1.2 shows examples of typical structures of redox polymers. Redox polymers consist of an insulating backbone with specific redox sites. Unlike the electrochemical process in conducting polymers, where the electrochemical process leads to reorganisation of the polymer bonds, the process associated with the redox polymer is highly localised. Another distinct difference within the conductivity of the two types of polymers is the potential range of conductivity: redox polymers have conductivity over a very narrow potential range.

It has been proposed that redox polymers conduct by a process known as the ‘electron hopping’ mechanism^{76, 77}. Here the polymers conduct by electrons hopping from one redox site to another as depicted in figure 1.4.

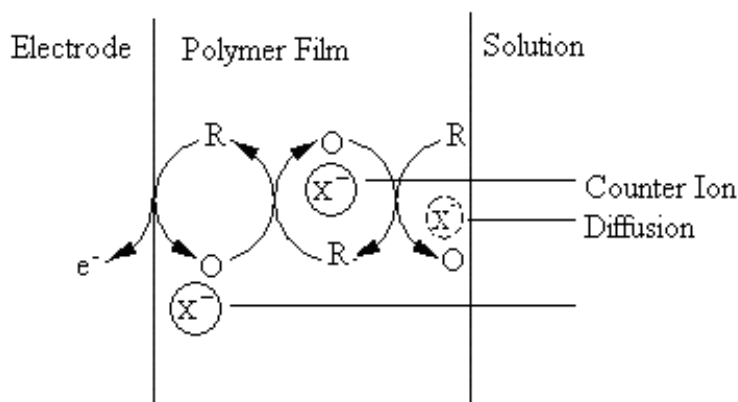


Figure 1.4 Schematic representation of coupled electron/ion diffusion mechanism for electrodes modified with a redox polymer

1.4 Survey of Techniques

Over the last two decades there has been a vast amount of research dedicated to modified electrodes and their potential applications. It is therefore necessary to be able to give as much insight into the film’s physical and chemical character, in order to improve both the design and performance of the resulting films. The majority of questions resulting from the production of modified electrodes centre round the

thickness and uniformity of the film. Other important issues are the mechanism of charge transport, redox composition and extent of solvation; chapters 5 and 6 address these issues.

The deciding factor as to which analytical technique is most appropriate will depend upon whether a qualitative or quantitative analysis is required. Electrochemical techniques generally give a good quantitative indication of the film thickness or available redox sites and are often supported by spectroscopic or microscopic technique that give a more qualitative analysis of composition /structure.

1.4.1 Electrochemical techniques

1.4.1.1 Cyclic voltammetry

Cyclic voltammetry is a very popular method used for the analysis of electroactive polymers as it is easily implemented and can lead to a wealth of data relating to surface species and their electrochemical properties.

This technique requires a standard three-electrode (working electrode (WE), counter electrode (CE), and reference electrode (RE)) electrochemical cell containing an electrolyte solution. The technique involves sweeping the potential of the working electrode between pre-set limits at a constant scan rate. A potentiostat is used to control the applied potential at the WE. The resulting current versus potential plots give information on the electroactive species present. Charge may then be obtained by simple integration of the current with respect to time obtained via the potential sweep.

1.4.1.2 Chronoamperometry/chronocoulometry

In contrast to voltammetric methods, in which the potential is scanned between two values at a fixed scan rate, potential step methods involve instantaneous change of the potential of the working electrode between two selected values. For potential step experiments either a current – time or charge - time curve is recorded. This

information is often used in the study of adsorption phenomena associated with electroactive species^{22, 78, 79}.

1.4.2 Surface imaging techniques

1.4.2.1 Scanning electron microscopy

The SEM uses electrons rather than light to form an image. It has the advantage of a large depth of field, which allows a large amount of the sample to be in focus at one time. It also has the ability of producing images of high resolution even at high magnification. Preparation of the samples is relatively easy since the only prerequisite is that the sample should be conductive. It is the combination of the high magnification, large depth of field, greater resolution, and ease of sample observation that makes the SEM an attractive instrument for surface imaging for modified electrodes⁸⁰⁻⁸⁸.

SEM provides a direct image of a topographical nature by scanning a primary beam of high-energy electrons (typically 10 - 50 keV in energy) across the surface. Figure 1.8 shows a schematic representation of a SEM. A beam of electrons is fired from the electron gun and accelerated by the anode through a series of magnetic lenses that are designed to focus the electrons to a very fine spot. Near the bottom, a set of scanning coils moves the focused beam back and forth across the sample, row by row. As the electron beam hits each spot on the sample, secondary electrons are loosened from the sample surface. The emitted electrons are then collected by a detector, which sends the signal to the amplifier. The final image is built up from the number of electrons emitted from each spot on the sample.

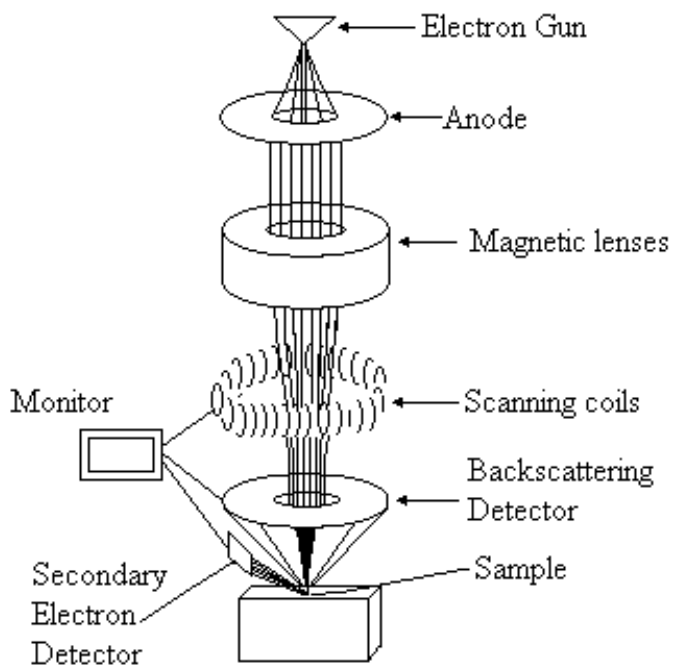


Figure 1.8 Schematic representation of scanning electron microscope

1.4.2.2 Atomic force microscopy

Atomic force microscopy (AFM) uses an atomically sharp probe to obtain an atomic map of the surface. The AFM probe detects inter-atomic forces, such as ionic repulsion/attraction and Van der Waal forces, between the atoms on the surface of the sample and the atomic tip.

The AFM works by the atomically sharp tip being rastered over a sample surface. The atomically sharp tip is typically made of Si or Si_3N_4 and is attached to the underside of a cantilever. A diode laser is focused onto the back of the reflective cantilever. As the tip scans the surface it moves up and down with the surface features causing the laser beam to be reflected off the cantilever into photo-detectors. The photo-detectors measure the difference in light intensities and convert it into a voltage. The information feeds back to the computer that controls the piezoelectric scanner in order to maintain the tip at either a constant height (to obtain force information) or constant force (to obtain height information). Three dimensional

topographical maps of the surface are then constructed by plotting the local sample height versus horizontal probe tip position. AFM gives information about surface features^{89, 90}. A schematic representation of the AFM is given in figure 1.9. In principle there are three modes that can be used with the AFM, the contact mode, the non-contact mode and the tapping mode, all of which will image liquid or solid samples.

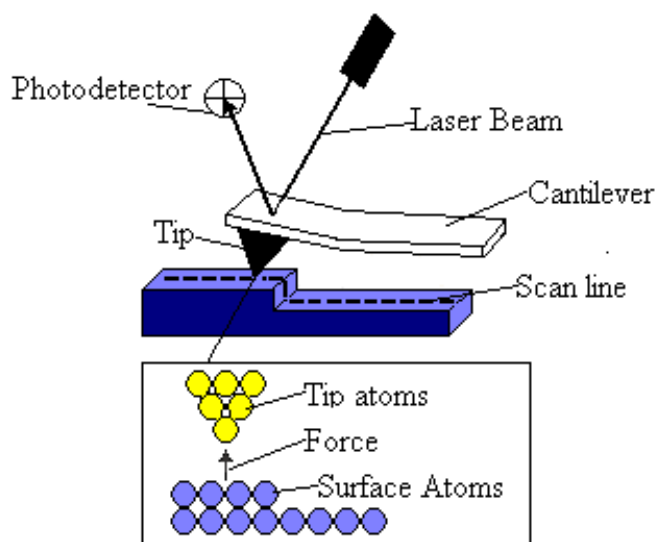


Figure 1.9 Schematic representation of atomic force microscope

The contact mode is most commonly used in atomic force microscopy; it involves the tip being in very close contact with the sample as it moves across the surface. A repulsive force on the tip has a mean value of 10^{-9} N, which is set by pushing the cantilever against the sample with a piezoelectric positioning element. The deflection of the cantilever is monitored and compared in a DC feedback amplifier to the desired value of deflection. When the measured deflection is different from the desired deflection the DC feedback amplifier applies a voltage in order to maintain the desired deflection. The voltage that the feedback amplifier applies is a measure of the height of features on the sample surface and is displayed as a function of the lateral position of the sample.

The non-contact mode is used in situations where tip contact might alter the sample in subtle ways. This mode involves the tip hovering between 500 – 1500 nm above the sample surface. Topographic images are constructed by scanning the tip above the surface, then observing the attractive Van der Waals forces acting between the tip and the sample. However the attractive forces from the sample are a lot weaker than the repulsive forces seen in contact mode. Therefore the tip is given a small oscillation. This small oscillation allows AC detection methods to be used to detect the small forces between the tip and the sample, by measuring the change in amplitude or frequency of the oscillating cantilever in response to force gradients from the sample.

Tapping mode AFM allows high resolution topographic imaging of sample surfaces that are easily damaged, loosely held to their substrate, or difficult to image by other AFM techniques. Alternately placing the tip in contact with the surface to provide high resolution, then lifting the tip off the surface to avoid dragging the tip along the surface overcomes problems such as friction, adhesion and electrostatic forces. Tapping mode imaging is obtained by oscillating the cantilever at or near the cantilever's resonant frequency using a piezoelectric crystal. When the tip is not in contact with the surface the cantilever oscillates with high amplitude. The oscillating tip is then moved towards the sample until it begins to lightly tap the surface. As the oscillating cantilever intermittently contact the surface the cantilever oscillation is reduced due to energy loss. The reduction in oscillation amplitude is used to identify and measure surface features. During scanning, the vertically oscillating tip alternately contacts the surface and lifts off, generally at a frequency of 50 to 500 KHz.

1.4.3 Acoustic wave techniques

The quartz crystal microbalance (QCM) is a small device that is often used as an ultra-sensitive mass sensor. It consists of a thin piece of AT cut quartz with vacuum deposited metal, most commonly gold, on either side (figure 1.10). The quartz crystal resonator utilises the converse piezoelectric effect (see chapter 2.3.2) in which a potential of a certain polarity is applied; this causes a shear motion in one direction. The reverse polarity results in a shear motion of equal strain but in the opposite direction. Applying a continuous alternating potential causes the quartz crystal to

oscillate at a resonant frequency. Addition or removal of mass to the surface of the quartz crystal causes the resonant frequency to decrease or increase respectively. The addition or removal of mass is directly proportional to the frequency shift of the quartz crystal. The frequency response is gravimetric and quantitatively described by the Sauerbrey equation⁹¹ as discussed in chapter 2.

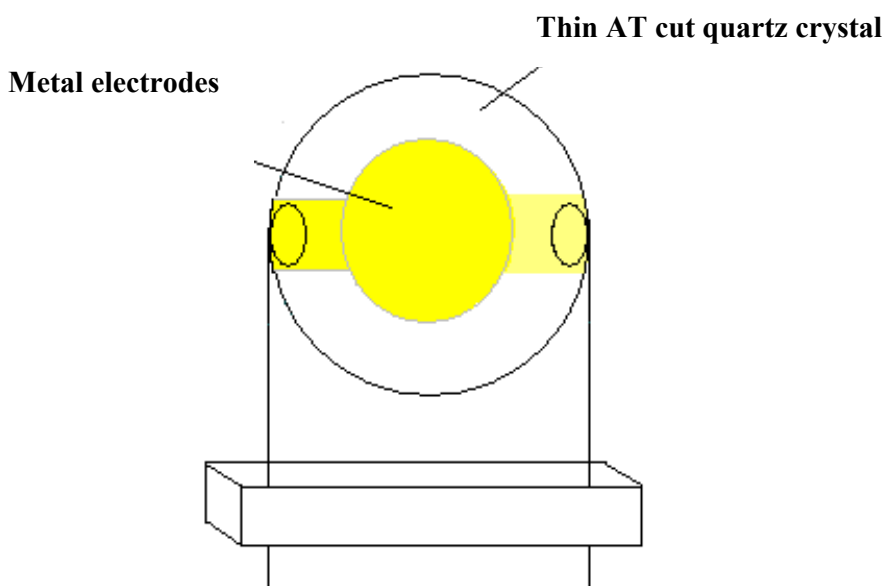


Figure 1.10 schematic representation of a quartz crystal microbalance

Around 1980 it was reported that the quartz crystal microbalance could oscillate when in contact with a liquid medium⁹². In 1985 the link between the frequency shift and the liquid properties was quantified. The resonant frequency shift of a QCM when immersed in a liquid medium is proportional to the square root of the product of the liquid density and viscosity.

When the QCM is used in liquid media, the solution can become trapped within the surface features. The trapped fluid acts as a rigidly deposited mass and therefore shows the same decrease in frequency as if the trapped media were not a liquid. This means the QCM is a sensitive tool to investigate surface wetting / de-wetting²⁰. Here we explore experimentally the amount of fluid entrapped within surface features through the frequency response of the quartz crystal microbalance.

Developments made by Kanazawa¹⁶⁻¹⁸ and Bruckenstein³⁵ have led to the quartz crystal resonator being a valuable tool for several research areas. The short data

acquisition time and high sensitivity of the QCM have made it an invaluable tool for electrochemistry, leading to information for both thermodynamic and kinetic responses^{93, 94}. In the EQCM one face of the quartz is exposed to air while the other side is in direct contact with the electrolyte solution. The electrode that is in direct contact to the solution is then used as the working electrode. The EQCM enables the mass (frequency) changes to be monitored whilst simultaneously controlling the potential and measuring the current (or vice versa). One particular area that has found use for the EQCM is the analysis of electro-active polymers. Here the EQCM enables the determination of mobile species between the polymer film and its bathing electrolyte^{69, 95}. Further mathematical analysis can lead to flux data for both the solvent and ion species present^{27, 61, 72, 96-98}.

1.5 Objectives

The aims of this thesis are to investigate aspects of interfacial processes, namely wetting of metallic films and ion/solvent transfers of electro-active films. Processes that occur at the interface, such as ion/solvent transfer and wetting are important phenomena for both electrodes and modified electrodes. Analyses of these interfacial processes are a necessity if improvements in both performance and design are to occur.

Only the part of the interface that is wet by the solution may take part in the required electrochemical process. Therefore an understanding of interfacial wetting is important for the development of electrochemical devices. The first part of the thesis deals with the interfacial wetting at contoured surfaces. Here surfaces with controllable wetting characteristics are prepared by electrodeposition through a template of hexagonal packed polystyrene latex microspheres. Liquid penetration into the contoured surfaces was analyzed gravimetrically using QCM.

The movement of both ions and solvent in and out of a polymer film are important concepts. The second part of this thesis develops a dynamic method (based on ion and solvent fluxes) to monitor interfacial ion and solvent transfer. The effects of solvent characteristics on conducting polymers during redox switching, is also explored using PEDOT. Finally a comparison of p- and n-doping dynamics of PEDOT films is carried out.

References

- (1) Chen, W.; Fadeev, A. Y.; Hsieh, M. C.; Oner, D.; Youngblood, J.; McCarthy, T. J. *Langmuir* **1999**, *15*, 3395-3399.
- (2) de Ruijter, M. J.; De Coninck, J.; Blake, T. D.; Clarke, A.; Rankin, A. *Langmuir* **1997**, *13*, 7293-7298.
- (3) Oner, D.; McCarthy, T. J. *Langmuir* **2000**, *16*, 7777-7782.
- (4) Semal, S.; Blake, T. D.; Geskin, V.; de Ruijter, M. J.; Castelein, G.; De Coninck, J. *Langmuir* **1999**, *15*, 8765-8770.
- (5) Voue, M.; De Coninck, J. *Acta Mater.* **2000**, *48*, 4405-4417.
- (6) Callies, M.; Chen, Y.; Marty, F.; Pepin, A.; Quere, D. *Microelect. Eng.* **2005**, *78-79*, 100-105.
- (7) Callies, M.; Quere, D. *Soft Matter* **2005**, *1*, 55-61.
- (8) Hazlett, R. D. *J. Coll. Interface Sci.* **1990**, *137*, 527-533.
- (9) Yoshimitsu, Z.; Nakajima, A.; Watanabe, T.; Hashimoto, K. *Langmuir* **2002**, *18*, 5818-5822.
- (10) Velev, O. D.; Kaler, E. W. *Langmuir* **1999**, *15*, 3693-3698.
- (11) Bartlett, P. N.; Baumberg, J. J.; Birkin, P. R.; Ghanem, M. A.; Netti, M. C. *Chem. Mater.* **2002**, *14*, 2199-2208.
- (12) Bartlett, P. N.; Dunford, T.; Ghanem, M. A. *J. Mater. Chem.* **2002**, *12*, 3130-3135.
- (13) Galisteo, J. F.; Garcia-Santamaria, F.; Golmayo, D.; Juarez, B. H.; Lopez, C.; Palacios, E. *J. Optics. A-Pure Appl. Optics.* **2005**, *7*, S244-S254.
- (14) Zhukov, A. A.; Filby, E. T.; Goncharov, A. V.; Ghanem, M. A.; Bartlett, P. N.; Boardman, R.; Fangohr, H.; Metlushko, V. V.; Novosad, V.; Karapetrov, G.; de Groot, P. A. J. *J. Low Temp. Phys.* **2005**, *139*, 339-349.
- (15) Zhukov, A. A.; Goncharov, A. V.; de Groot, P. A. J.; Bartlett, P. N.; Ghanem, M. A.; Kupfer, H.; Pugh, R. J.; Tomka, G. J. *IEE Proceedings-Science Measurement and Technology* **2003**, *150*, 257-259.
- (16) Kanazawa, K. K. *J. Electrochem. Soc.* **1985**, *132*, C368-C368.
- (17) Kanazawa, K. K.; Gordon, J. G. *Anal. Chim. Acta* **1985**, *175*, 99-105.
- (18) Kanazawa, K. K.; Gordon, J. G. *Anal. Chem.* **1985**, *57*, 1770-1771.
- (19) Stockel, W.; Schumacher, R. *Berichte Der Bunsen-Gesellschaft-Phys. Chem. Chem. Phys.* **1987**, *91*, 345-349.
- (20) Theisen, L. A.; Martin, S. J.; Hillman, A. R. *Anal. Chem.* **2004**, *76*, 796-804.
- (21) *Handbook of Conducting Polymers*, 2nd ed.; Marcel Dekker, New York, 1998.
- (22) Chandrasekhar, P. *Conducting Polymers, Fundamentals and Applications. A practical Approach*; Kluwer Academic Publishers, Boston, 1999.
- (23) Nishio, K.; Fujimoto, M.; Yoshinaga, N.; Furukawa, N.; Ando, O.; Ono, H.; Suzuki, T. *J. Power Sources* **1991**, *34*, 153-160.
- (24) MacDiarmid, A. G.; Kaner, R. B. *Handbook of Conducting Polymers*, 2nd ed.; Marcel Dekker, New York, 1998.
- (25) Fusalba, F.; El Mehdi, N.; Breau, L.; Belanger, D. *Chem. Mater.* **1999**, *11*, 2743-2753.
- (26) Loveday, D. C.; Hmyene, M.; Ferraris, J. P. *Synth. Metals* **1997**, *84*, 245-246.
- (27) Rudge, A.; Raistrick, I.; Gottesfeld, S.; Ferraris, J. P. *Electrochim. Acta* **1994**, *39*, 273-287.
- (28) Hillman, A. R.; Bandey, H. L.; Saville, P. M.; Wilson, R. W.; Bruckenstein, S.; Vos, J. G. *Polymer Surfaces and Interfaces III*; John Wiley and Sons Ltd, 1999.

- (29) Ahonen, H. J.; Lukkari, J.; Kankare, J. *Macromolecules* **2000**, *33*, 6787-6793.
- (30) Damlin, P.; Kvarnstrom, C.; Nyback, A.; Kaldstrom, M.; Ivaska, A. *Electrochim. Acta* **2006**, *51*, 6060-6068.
- (31) Dietrich, M.; Heinze, J.; Heywang, G.; Jonas, F. *J. Electroanal. Chem.* **1994**, *369*, 87-92.
- (32) Neugebauer, H. *J. Electroanal. Chem.* **2004**, *563*, 153-159.
- (33) Neugebauer, H.; Cravino, A.; Luzzati, S.; Catellani, M.; Petr, A.; Dunsch, L.; Sariciftci, N. S. *Synth. Metals* **2003**, *139*, 747-750.
- (34) Ballantine, D. S.; White, R. M.; Martin, S. J.; Ricco, A. J.; Frye, G. C.; Zellers, E. T. *Acoustic Wave Sensors*; Academic Press: New York, 1997.
- (35) Bruckenstein, S.; Shay, M. *Electrochim. Acta* **1985**, *30*, 1295-1300.
- (36) Fadeev, A. Y.; McCarthy, T. J. *Langmuir* **1999**, *15*, 3759-3766.
- (37) Moses, P. R.; Murray, R. W. *J. Am. Chem. Soc.* **1976**, *98*, 7435-7436.
- (38) Moses, P. R.; Wier, L.; Murray, R. W. *Anal. Chem.* **1975**, *47*, 1882-1886.
- (39) Hillman, A. R. *Electrochemical Science and Technology of Polymers*; Elsevier Applied Science London, 1987.
- (40) Haginoya, C.; Ishibashi, M.; Koike, K. *App. Phys. Lett.* **1997**, *71*, 2934-2936.
- (41) Haginoya, C.; Koike, K.; Hirayama, Y.; Yamamoto, J.; Ishibashi, M.; Kitakami, O.; Shimada, Y. *App. Phys. Lett.* **1999**, *75*, 3159-3161.
- (42) Gau, H.; Herminghaus, S.; Lenz, P.; Lipowsky, R. *Science* **1999**, *283*, 46-49.
- (43) Painter, O.; Lee, R. K.; Scherer, A.; Yariv, A.; O'Brien, J. D.; Dapkus, P. D.; Kim, I. *Science* **1999**, *284*, 1819-1821.
- (44) Bartlett, M. A.; Yan, M. D. *Adv. Mater.* **2001**, *13*, 1449-+.
- (45) Bartlett, P. N.; Birkin, P. R.; Ghanem, M. A. *Chem. Comm.* **2000**, 1671-1672.
- (46) Velev, O. D.; Jede, T. A.; Lobo, R. F.; Lenhoff, A. M. *Nature* **1997**, *389*, 447-448.
- (47) Li, J. R.; Henry, G. C.; Garno, J. C. *Analyst* **2006**, *131*, 244-250.
- (48) Cong, H. L.; Cao, W. X. *J. Coll. Interface Sci.* **2004**, *278*, 423-427.
- (49) Jiang, P.; Cizeron, J.; Bertone, J. F.; Colvin, V. L. *J. Am. Chem. Soc.* **1999**, *121*, 7957-7958.
- (50) Yamauchi, Y.; Yokoshima, T.; Mukaibo, H.; Tezuka, M.; Shigeno, T.; Momma, T.; Osaka, T.; Kuroda, K. *Chem. Lett.* **2004**, *33*, 542-543.
- (51) Yan, H. W.; Blanford, C. F.; Holland, B. T.; Parent, M.; Smyrl, W. H.; Stein, A. *Adv. Mater.* **1999**, *11*, 1003-1006.
- (52) Bartlett, P. N.; Baumberg, J. J.; Coyle, S.; Abdelsalam, M. E. *Faraday Disc.* **2004**, *125*, 117-132.
- (53) Bartlett, P. N.; Ghanem, M. A.; El Hallag, I. S.; de Groot, P.; Zhukov, A. *J. Mater. Chem.* **2003**, *13*, 2596-2602.
- (54) Bartlett, P. N.; Marwan, J. *Phys. Chem. Chem. Phys.* **2004**, *6*, 2895-2898.
- (55) King, W. H. *Anal. Chem.* **1964**, *36*, 1735.
- (56) Demanze, F.; Cornil, J.; Garnier, F.; Horowitz, G.; Valat, P.; Yassar, A.; Lazzaroni, R.; Bredas, J. L. *J. Phys. Chem. B* **1997**, *101*, 4553-4558.
- (57) Dkhissi, A.; Beljonne, D.; Lazzaroni, R.; Louwet, F.; Groenendaal, L.; Bredas, J. L. *Inter. J. Quantum Chem.* **2003**, *91*, 517-523.
- (58) Harrison, M. G.; Fichou, D.; Garnier, F.; Yassar, A. *Optical Mater.* **1998**, *9*, 53-58.
- (59) Mortimer, R. J. *Electrochim. Acta* **1999**, *44*, 2971-2981.
- (60) Cutler, C. A.; Bouguettaya, M.; Kang, T. S.; Reynolds, J. R. *Macromolecules* **2005**, *38*, 3068-3074.
- (61) Groenendaal, L.; Zotti, G.; Aubert, P. H.; Waybright, S. M.; Reynolds, J. R. *Adv. Mater.* **2003**, *15*, 855-879.

- (62) Rodriguez, M.; Romero, I.; Sens, C.; Llobet, A.; Deronzier, A. *Electrochimica Acta* **2003**, *48*, 1047-1054.
- (63) Ito, T.; Shirakawa, H.; Ikeda, S. *J. Polymer Sci. Part A-Polymer Chem.* **1974**, *12*, 11-20.
- (64) Shirakawa, H.; Louis, E. J.; Macdiarmid, A. G.; Chiang, C. K.; Heeger, A. J. *J. Chem. Soc.-Chem. Comm.* **1977**, 578-580.
- (65) Macdiarmid, A. G.; Akhtar, M.; Chiang, C. K.; Cohen, M. J.; Kleppinger, J.; Heeger, A. J.; Louis, E. J.; Milliken, J.; Moran, M. J.; Peebles, D. L.; Shirakawa, H. *J. Electrochem. Soc.* **1977**, *124*, C304-C304.
- (66) Liu, G. K.; Ren, B.; Wu, D. Y.; Lin, T. M.; Gu, R. A.; Tian, Z. Q. *J. Electroanal. Chem.* **2006**, *594*, 73-79.
- (67) Blinova, N. V.; Stejskal, J.; Trchova, M.; Prokes, J.; Omastova, M. *Euro. Polymer J.* **2007**, *43*, 2331-2341.
- (68) Mohamoud, M. A.; Hillman, A. R. *J. Solid State Electrochem.* **2007**, *11*, 1043-1050.
- (69) Hillman, A. R.; Mohamoud, M. A. *Electrochim. Acta* **2006**, *51*, 6018-6024.
- (70) Ding, H.; Pan, Z.; Pigani, L.; Seeber, R.; Zanardi, C. *Electrochim. Acta* **2001**, *46*, 2721-2732.
- (71) Roncali, J. *Chem. Rev.* **1992**, *92*, 711-738.
- (72) Tirkes, S.; Onal, A. M. *J. Appl. Polymer Sci.* **2007**, *103*, 871-876.
- (73) Pater, E.; Bruckenstein, S.; Hillman, A. R. *J. Phys. Chem. B* **2006**, *110*, 14761-14769.
- (74) Jureviciute, I.; Bruckenstein, S.; Hillman, A. R. *Electrochim. Acta* **2006**, *51*, 2351-2357.
- (75) Yu, L.; Sathe, M.; Zeng, X. Q. *J. Electrochem. Soc.* **2005**, *152*, E357-E363.
- (76) Kaufman, F. B.; Schroeder, A. H.; Engler, E. M.; Kramer, S. R.; Chambers, J. Q. *J. Am. Chem. Soc.* **1980**, *102*, 483-488.
- (77) Kaufman, F. B.; Engler, E. M. *J. Am. Chem. Soc.* **1979**, *101*, 547-549.
- (78) Lee, B.; Seshadri, V.; Sotzing, G. A. *Langmuir* **2005**, *21*, 10797-10802.
- (79) Seshadri, V.; Wu, L.; Sotzing, G. A. *Langmuir* **2003**, *19*, 9479-9485.
- (80) Li, N. Y.; Shan, D.; Xue, H. G. *Euro. Polymer J.* **2007**, *43*, 2532-2539.
- (81) Pawar, P.; Gaikwad, A. B.; Patil, P. P. *Electrochim. Acta* **2007**, *52*, 5958-5967.
- (82) El Mir, L.; Kraiem, S.; Bengagi, M.; Elaloui, E.; Ouederni, A.; Alaya, S. *Phys. B-Condensed Matter* **2007**, *395*, 104-110.
- (83) Patil, D.; Gaikwad, A. B.; Patil, P. *J. Phys. D-Appl. Phys.* **2007**, *40*, 2555-2562.
- (84) Zhou, H.; Jin, L.; Xu, W. *Chinese Chem. Lett.* **2007**, *18*, 365-368.
- (85) Dixon, M. C.; Daniel, T. A.; Hieda, M.; Smilgies, D. M.; Chan, M. H. W.; Allara, D. L. *Langmuir* **2007**, *23*, 2414-2422.
- (86) Dalmolin, C.; Biaggio, S. R.; Rocha, R. C.; Bocchi, N. *J. Solid State Electrochem.* **2007**, *11*, 609-618.
- (87) Yildiz, H. B.; Kiralp, S.; Toppare, L.; Yagci, Y.; Ito, K. *Mater. Chem. Phys.* **2006**, *100*, 124-127.
- (88) Kim, J.; Dohnalek, Z.; Kay, B. D. *Surf. Sci.* **2005**, *586*, 137-145.
- (89) Pozo-Gonzalo, C.; Pomposo, J. A.; Alduncin, J. A.; Salsamendi, M.; Mikhaleva, A. I.; Krivdin, L. B.; Trofimov, B. A. *Electrochim. Acta* **2007**, *52*, 4784-4791.
- (90) Tamm, J.; Raudsepp, T.; Marandi, M.; Tamm, T. *Synth. Metals* **2007**, *157*, 66-73.
- (91) Sauerbrey, G. *Z. Phys.* **1959**, *155*, 206.

- (92) Nomura, T.; Minemura, A. *Nippon Kagaku Kaishi* **1980**, 1621-1625.
- (93) Bruckenstein, S.; Hillman, A. R. *J. Phys. Chem. B* **1988**, *92*, 4837-4839.
- (94) Hillman, A. R.; Loveday, D. C.; Bruckenstein, S. *J. Electroanal. Chem.* **1989**, *274*, 157-166.
- (95) Hillman, A. R.; Glidle, A. *J. Electroanal. Chem.* **1994**, *379*, 365-372.
- (96) Bund, A.; Neudeck, S. *J. Phys. Chem. B* **2004**, *108*, 17845-17850.
- (97) Chazalviel, J. N.; Etman, M.; Ozanam, F. *J. Electroanal. Chem.* **1991**, *297*, 533-540.
- (98) Tittes, K.; Bund, A.; Plieth, W.; Bontien, A.; Paschen, S.; Plotner, M.; Grafe, H.; Fischer, W. *J. Solid State Electrochem.* **2003**, *7*, 714-723.

CHAPTER 2

THEORY

2.1 Introduction

Interfacial wetting is important in a number of chemical and electrochemical devices. Wetting is dominated by the lyophobic nature of the surface. However changes in the geometric microstructure of the surface can have drastic a effect on the lyophobic nature of the interface¹⁻⁴. It is evident^{5, 6} that de-wetting can occur at textured surfaces, where the solution can either completely fill the features or it can skate over the top, trapping gas within them.

The QCM is very sensitive to small mass changes. When a uniform rigid mass is added to the quartz crystal the response is that of a gravimetric sensor. Several reports⁷⁻¹⁰ have illustrated that quartz crystal resonators can operate in liquid media. The response is then a route to analysis of the liquid's viscosity and density. Other studies^{11, 12} have suggested that surface features of the quartz crystal resonator have a drastic effect on the response when immersed in liquid. It is believed that the liquid may become trapped within the corrugations. This trapped liquid is thought to cause a response that is usually associated with a rigid layer (commonly referred to as an ideal mass layer). Here we are interested in using the quartz crystal microbalance technique to investigate this trapped ideal mass layer as an indication of interfacial wetting.

The electrochemical quartz crystal microbalance is a powerful analytical tool for modified electrodes. Several studies have used the EQCM to explore the properties and composition of electroactive films¹³⁻¹⁶. When the film is acoustically thin (films that are less than 1% of the mass of the quartz crystal¹⁷) the QCM acts a gravimetric probe of the transfer of mobile species between the film and solution.

This chapter presents the basic theory and principles of the quartz crystal micro balance/electrochemical quartz crystal microbalance techniques. More specific

developments of these basic concepts are given in chapters 4, 5 and 6, where they are applied to particular situations.

2.2 Voltammetry

2.2.1 Fundamentals

The work presented in chapters 5 and 6 uses the electrochemical quartz crystal microbalance to investigate the redox switching process of an electroactive polymer. The fundamental principles of cyclic voltammetry are used as the basic foundations for this work.

The electrochemical reaction of a surface confined redox species, such as a conducting polymer, can be expressed as¹⁸;



where OX and RED represent the oxidized and reduced redox sites, respectively. The application of a potential to a modified electrode leads to a current response that is determined by the kinetics of reaction (2.1) and/or diffusion of charge balancing counter ions. Modification of electrodes with conducting polymers has been an expanding research field within electrochemistry over the last few decades. The most commonly used electrochemical method used for the analysis of conducting polymer films is cyclic voltammetry^{13, 15, 16, 19-22}, which will be discussed in section 2.2.3.

2.2.2 Mass transport

One of the fundamental laws of electrochemistry is Faraday's Law.

$$Q = nFN \quad (2.2)$$

It relates the number of moles of analyte electrolysed (N) to the total charge passed (Q). The differential form of this law is:

$$\frac{dQ}{dt} = i = nF \frac{dN}{dt} \quad (2.3)$$

This shows that the current is directly proportional to the rate of electrolysis. It is the relative values of the applied potential and the standard redox potential for the OX/RED couple that determines the direction of transfer of electrons between the electrode and the interfacial region. When the molecules within the interfacial region have been electrolysed they must be replaced by molecules from within the bulk solution in order for the electrolysis to continue. Therefore it is obvious that the current will also depend on the rate of mass transport between the interfacial region and the bulk solution. Depending on the potential, the rate determining process may be mass transport or electron transfer. The transport of mobile species to the electrode surface can occur by either convection, migration or diffusion²³. Three types of mass transport are possible in an electrochemical experiment:

- a) Diffusion – molecular or ion motion down a concentration gradient
- b) Convection - molecular or ion motion imposed by mechanical motion of the solution, for example stirring or vibration.
- c) Migration – ion motion imposed by an electrical potential gradient.

Diffusion is the movement of chemical species, ions or molecules, under the influence of a concentration gradient. The species will move from a high concentration region to a region with a low concentration until the concentration is uniform in the whole phase. In electrochemical systems the mass transport is generally limited to the diffusion rate because of the presence of an inert electrolyte to suppress potential gradients.

In contrast to diffusion, which is concerned with molecular motion, convection involves the motion of the bulk solution. There are two types of convection, “natural” and “forced”. An example of “forced” convection is mechanical stirring. Natural convection is the tendency for bulk and surface concentrations to match.

Migration is the movement of ions under the influence of an electrical potential gradient. This is generally limited by the addition of excess background electrolyte.

2.2.3 Cyclic voltammetry

There are a number of methods available for the study of modified electrode processes. One of the most important and most commonly used methods is cyclic voltammetry. The data obtained from cyclic voltammetry can lead to information on reaction mechanism, reaction rates and adsorption processes^{23,24}. Cyclic voltammetry involves sweeping the potential linearly across a potential range and recording the resulting current. The potential is measured between the working electrode and the reference electrode and is controlled by a potentiostat. The current is measured between the working electrode and the counter electrode.

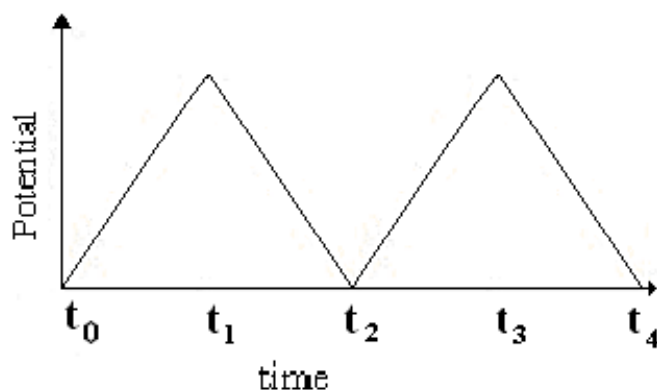


Figure 2.1 cyclic voltammetry waveform²⁴

Figure 2.1 shows the waveform for cyclic voltammetry. It illustrates that the potential is swept in the forward direction until reaching a pre-programmed potential, at time (t_1) the sweep is reversed.

Figure 2.2 shows a cyclic voltammogram for the reversible process given by equation (2.1). The shape of the voltammogram will depend on the reversibility of the redox couple. Reversible systems have distinct characteristics given as follows:

- a) The voltage separation between the current peaks is

$$\Delta E = E_p^a - E_p^c = \frac{59}{n} mV$$

- b) The peak potential is independent of voltage scan rate
- c) The ratio of the peak currents is equal to one (for equal diffusion coefficients)
- d) Peak currents are proportional to the square root of the scan rate

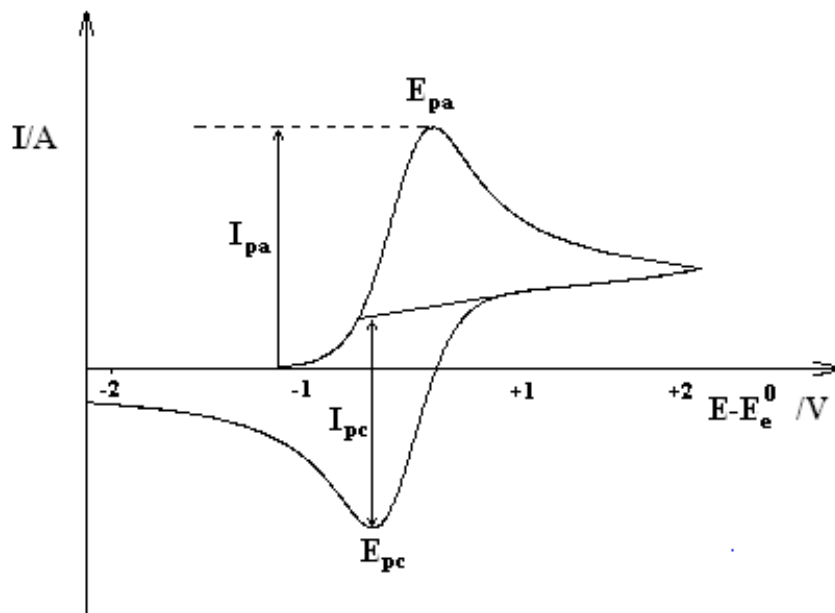


Figure 2.2 cyclic voltammogram for a reversible process²⁵

In a reversible system, the electron transfer rates at all potentials are faster than the mass transport rate and so the concentration of the reduced and oxidised species at the electrode surface can be described by the Nernst equation (2.4):

$$E = E^0 + \frac{RT}{nF} \ln \frac{C_O}{C_R} \quad (2.4)$$

where C_O and C_R represent the surface concentrations of oxidised and reduced species. When the electron transfer rate is not sufficient to maintain this surface equilibrium then the shape of the voltammogram changes to that of an electrochemically irreversible one. The total charge passed, which is often required

for surface film analysis, may be calculated by integrating of the area under the cyclic voltammogram.

2.2.3.1 Cyclic voltammetry for modified electrodes

Ideally, for surface modified electrodes there is no voltage separation between the current peaks (see figure 2.3). This means that the voltammograms for surface immobilised species shows identical peak potentials for the cathodic and anodic scans, i.e. $\Delta E = 0$. This is because diffusion has no part to play in the process²⁵.

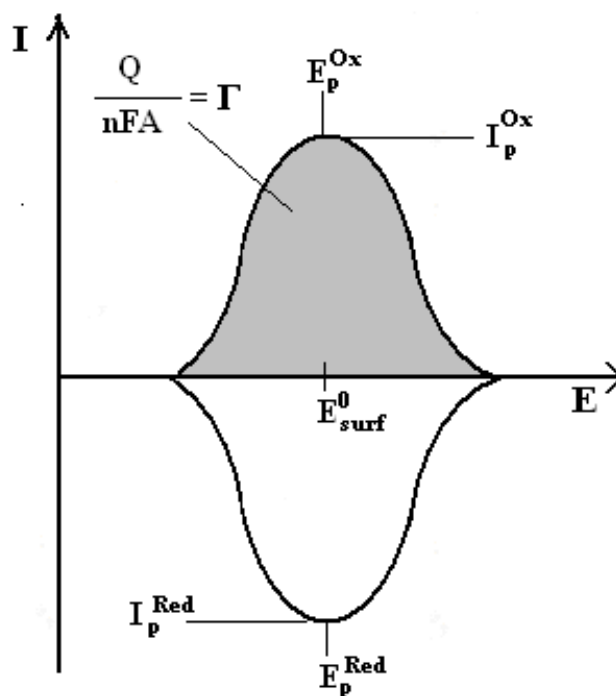


Figure 2.3 cyclic voltammogram of an immobilised redox species²⁵

The properties of the voltammogram arise from the amount of reaction which is determined by the number of available redox sites on the film. For modified electrodes, such as conducting polymers, the coverage Γ_p can be calculated using equation (2.5).

$$\Gamma_p = \frac{Q}{nFA} \quad (2.5)$$

where n is the dopant level, Q is the total charge passed and A is the area. The symmetrical shape shown in figure 2.3 is rarely seen, suggesting that the assumptions of the Langmuir isotherm (on which it is based) are not adhered to; the most likely assumption isolated is that of no interactions between sites.

2.3 The Quartz Crystal Microbalance

2.3.1 Background

Over the past fifty years, advances in technology have led to the use of high frequency resonators as a tool for precise measurement of mass. The quartz crystal microbalance (figure 2.4) may be used as an ultra-sensitive mass sensor. The first quartz crystal oscillator was described in 1921, based on a X-cut (refers to the cutting angle, see figure 2.7) quartz crystal. The use of X-cut quartz crystals was limited due to their temperature sensitivity (the main use of X-cut quartz crystals is in transducers used in space sonar, where the large temperature coefficient is not important). The AT-cut quartz crystal (see figure 2.7), with a near zero temperature dependence at room temperature, was introduced in 1934 and soon became the principal component for almost all frequency controlled applications. The quartz resonator is a thin piece of quartz that is placed between two electrodes, which provide a way of connecting it to a circuit. If an alternating voltage is applied to these electrodes then the quartz will oscillate at a well defined frequency, determined by the crystal dimensions and the properties of quartz.

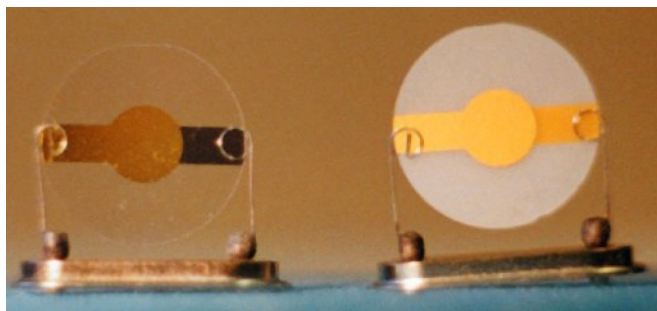


Figure 2.4. Polished (left) and rough (right) quartz crystals (surface features 40nm and 200nm respectively)

2.3.2 The Piezoelectric Effect

The pioneering work by the Curies^{26, 27} in 1880 demonstrated the connection between the piezoelectric effect and crystal structure. Their initial work demonstrated that applying a stress to the surface of certain crystals produces an electrical potential between the surfaces, which is proportional to the applied stress (figure 2.5): this is known as the direct piezoelectric effect. Shortly after the discovery of the direct piezoelectric effect, Lippman illustrated mathematically by thermodynamic principles the converse piezoelectric effect, in which a potential difference across the crystal faces causes a distortion in the crystal lattice; this results in mechanical strain at the surface. The converse piezoelectric effect was confirmed experimentally in 1881 by the Curies²⁷. However, due to lack of interest, no serious work on piezoelectric devices was carried out until the development of the ultrasonic submarine detector in 1917. Since the first ultrasonic detector, interest in piezoelectric devices has grown.

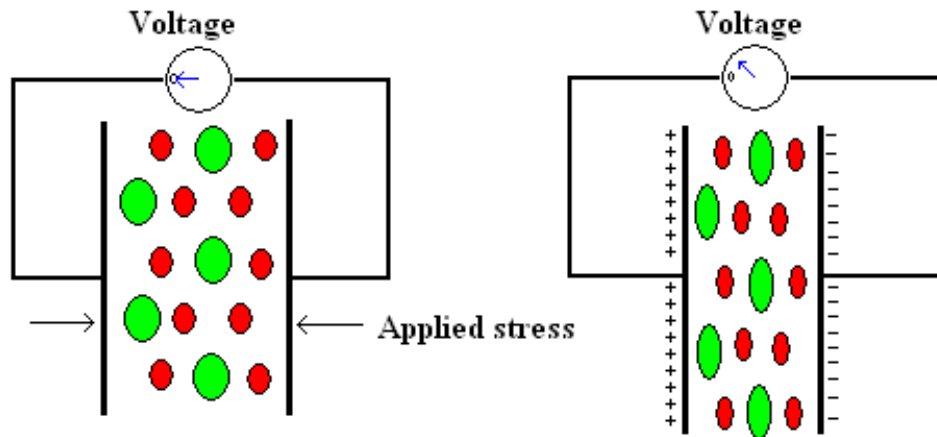


Figure 2.5. Schematic representation of the direct piezoelectric effect

Piezoelectric effects are only seen in ionic crystal structures that do not have a center of symmetry, for example quartz, Rochelle salts, barium/lead titanate, lead zirconate and tourmaline. Although a solid may be electrically neutral, it may consist of electrically charged particles, such as ions. Also the polar bonds between atoms of different electronegativities lead to dipole moments. The majority of materials do not have a net dipole moment because the arrangements of the ions cause a cancellation of individual dipole moments. Quartz is piezoelectric because it will develop a net dipole moment if it is mechanically/potentially deformed.

Quartz crystal resonators, occasionally referred to as thickness shear mode (TSM) resonators, utilize the converse piezoelectric effect in which a potential of a certain polarity is applied; this causes a shear motion in one direction. The reverse polarity results in shear motion of equal strain but in the opposite direction. The quartz crystal will oscillate at the required frequency when a continuous alternating potential is applied.

2.3.3 Quartz Crystal Orientation of Cut

It is the thermal, chemical and mechanical stability of a quartz crystal that makes it an excellent inexpensive material for use in a wide range of frequency-controlled devices. However piezoelectric quartz in its natural form has many different modes of vibration²⁸. The major modes of vibration (figure 2.6) are longitudinal (extensional), lateral (flexural and shear) and torsional (twist); overtones for each these modes can also occur.

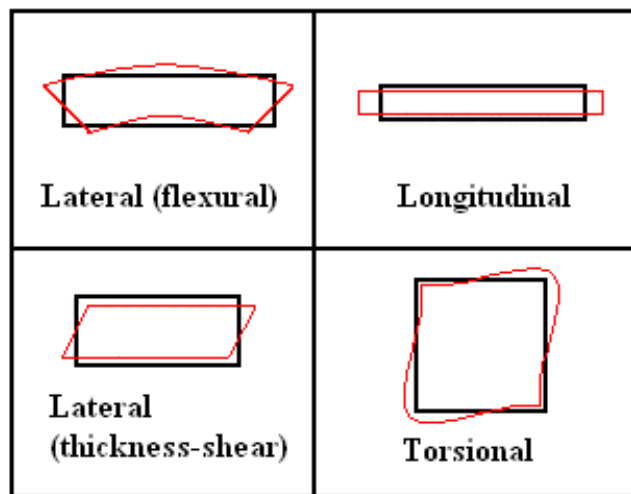


Figure 2.6. The four major modes of vibration²⁸

In order to avoid all other modes of vibration than the required one, the quartz crystal is cut at a specific orientation and shape. When a quartz crystal is cut at either the AT or BT angle (figure 2.7) then vibrations in the thickness-shear mode are obtained. This vibrational mode is the most sensitive to added mass. The thickness-shear mode has motions that are fundamentally in a lateral dimension, (figure 2.6)²⁹.

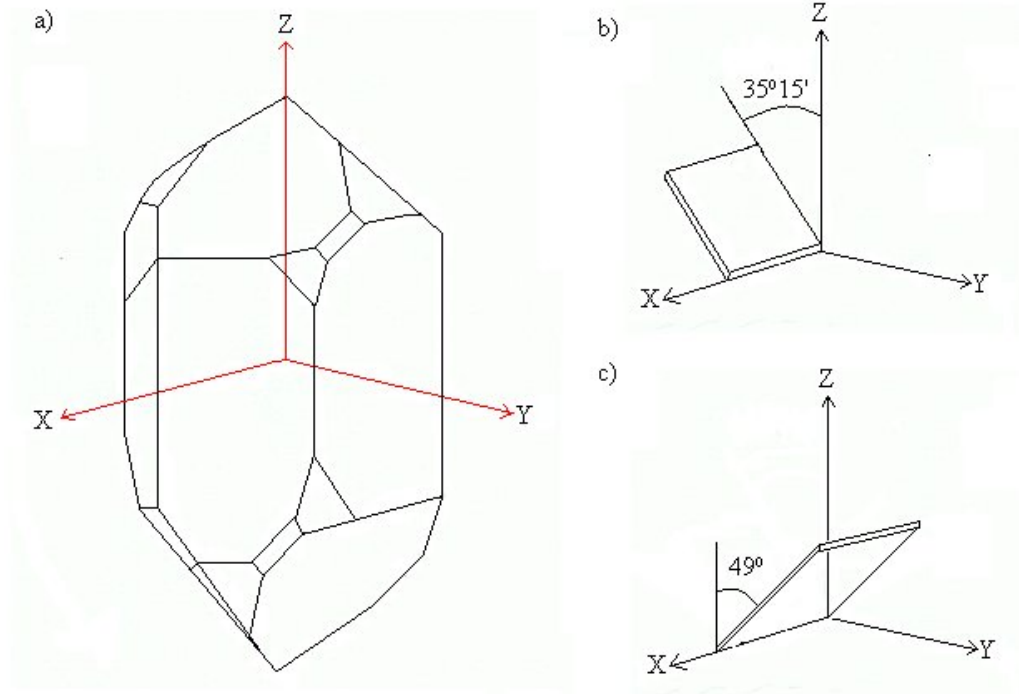


Figure 2.7.schematic diagram showing a) the assignment of axis to a quartz crystal block, b) the cutting angle of AT cut quartz and c) the cutting angle of BT cut quartz crystal²⁸.

The cut of the quartz crystal not only has a direct effect on the mode of vibration but it also determines the frequency – temperature stability. Small changes in the crystal orientation will have a drastic effect on the resonant frequency when stress or temperature deviates²⁸. To ensure that the maximum stability is achieved an AT-cut quartz crystal is required to be cut at an angle of 35°15' with respect to the crystallographic axis. X-ray diffraction techniques are usually used to ensure that the precise angle is obtained.

2.3.4 Sauerbrey Equation

It was common practice when using a quartz crystal resonator as a frequency control device, to decrease / increase the resonant frequency by the addition or removal of a pencil mark (addition/subtraction of mass). This mass induced frequency shift was

originally thought to be only a qualitative effect. The frequency – mass relationship was first studied by Lord Rayleigh^{30, 31} in which he hypothesised that the resonant frequency of the vibrating body was connected to its mass and that for any mass added to the surface, the resonant frequency must change in order to rebalance the kinetic and potential energies. However it was not until 1959 that a true link between frequency shift and mass added to the quartz crystal oscillator was made. It was shown by Sauerbrey³² that the added mass was directly proportional to the frequency shift of the quartz crystal.

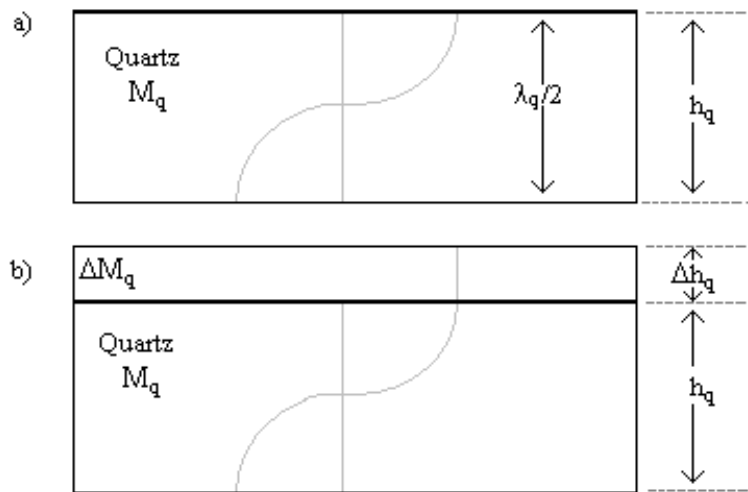


Figure 2.9. Schematic representation of quartz crystal microbalance (a). Thickness h_q is related to acoustic wavelength λ_q (b) a rigid mass results in an increase in h_q and therefore an increase in λ

It follows that the thickness of the quartz crystal is related to shear velocity by equation (2.6),

$$h_q = \frac{\lambda_q}{2} \quad (2.6)$$

where h_q is the quartz thickness and λ_q is the acoustic wavelength.

For the quartz crystal to oscillate at its resonant frequency it must satisfy equation (2.7), in which v_q is the shear velocity.

$$f_q = \frac{v_q}{\lambda_q} \quad (2.7)$$

Any change in thickness of the quartz crystal produced by the addition of a mass will lead to an increase in wavelength (decrease in resonant frequency) (see figure 2.9). This leads to:

$$\frac{\Delta f_q}{f_q} = \frac{-M_q}{M_q} \quad (2.8)$$

Assuming that the mass is added uniformly across the quartz crystal equation 2.8 may be written in the approximate form using mass per unit area (referred to as “areal mass density”):

$$\frac{\Delta f_q}{f_q} = \frac{m_f}{m_q} \quad (2.9)$$

where m_f and m_q are the mass per unit area of the uniformly distributed added mass and the quartz crystal respectively. The mass per unit area is equivalent to the thickness and density of the quartz crystal/added mass:

$$m_q = h_q \rho_q \quad (2.10)$$

Combining equations (2.6) and (2.7) and substituting into equation (2.10) leads to (2.11).

$$m_q = \frac{v_q \rho_q}{2f_q} \quad (2.11)$$

Equation (2.9) may now be written as:

$$m_f = -\Delta f_q \frac{v_q \rho_q}{2f_q^2} \quad (2.12)$$

Sauerbrey assumed that any small, rigid, uniformly distributed mass added to the surface of a quartz crystal may be treated as an change in the crystal mass itself, so equation 2.12 may be written in a more general form:

$$\Delta m = -\Delta f_q \frac{v_q \rho_q}{2f_q^2} \quad (2.13)$$

For a quartz crystal v_q and ρ_q are $3.34 \times 10^5 \text{ cm s}^{-1}$ and 2.650 g cm^{-3} respectively^{28, 33}. Therefore 4.4 ng cm^{-2} of material will lead to a frequency shift of 1 Hz for a 10 MHz crystal. It is worth noting that this assumption may fail for very thick films.

2.3.5 Harmonics

The use of quartz crystal resonators at a higher oscillating frequency increases the sensitivity. However in order to obtain a crystal with a higher resonant frequency, one requires an inversely proportional decrease in thickness of the crystal (see equation 2.6). Therefore, crystals with high resonant frequencies become increasingly thin and so more fragile.

One solution would be to apply a high frequency driving potential across the crystal surface in order to excite higher harmonics.

$$f_N = \frac{Nv_q}{2h_q} \quad (2.14)$$

Here the resonant frequency is denoted by f_N , N (an integer) and is the harmonic number. A key point to consider when deciding whether to use higher harmonics or crystals with high oscillating frequency is the sensitivity. The sensitivity increases linearly with higher harmonics but is squared for the fundamental frequency.

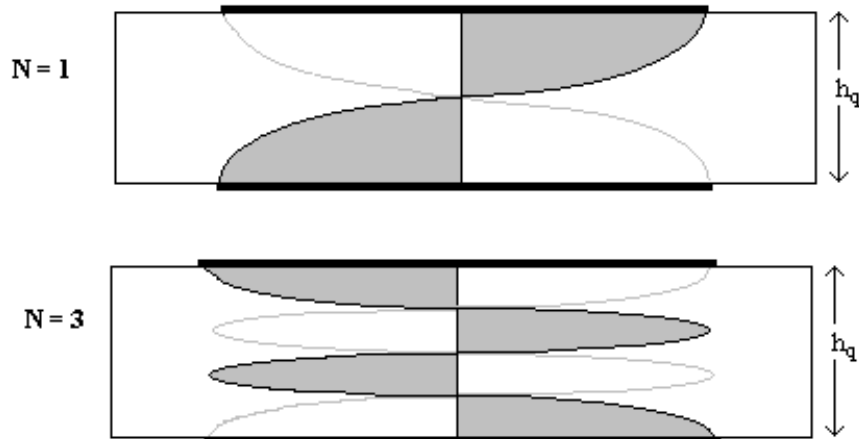


Figure 2.10 Displacement profiles across quartz thickness for 1st and 3rd harmonics

More detailed considerations of the boundary conditions indicate the electrodes on the surface can only excite odd harmonics (figure 2.10) because of location of anti-nodes at exterior faces of the crystal and so N can only be an odd number.

2.3.6 Quartz Crystal Microbalance and Liquid Media

The work of Sauerbrey laid the groundwork for the quartz crystal microbalance as a new quantitative tool to measure the masses of thin films. The use of the QCM was restricted to use in vacuum or gaseous environments. In the early 1980's a few reviews illustrated the quartz crystal microbalance as a possible tool to be used for other types of analysis, including liquid samples. These include mass detectors in liquid chromatography³⁴ and analysis of organic liquids^{35, 36}.

$$\Delta f = -2.26 \times 10^{-6} f^2 \Delta m \quad (2.15)$$

Although the use of a quartz oscillator in liquids had become a plausible technique, it was not until 1985 that the link between the frequency shift and liquid properties was quantified. In 1985 the Sauerbrey equation (2.15) was modified⁷⁻¹⁰. It was clearly demonstrated that the quartz crystal microbalance could be used as a sensitive mass detector with a liquid sample.

$$\Delta f = -f_0^{3/2} \left(\frac{\eta \rho}{\pi \mu_q \rho_q} \right)^{1/2} \quad (2.16)$$

Equation 2.16 is the modified Sauerbrey equation in which the factors of fluid properties are included. Here η and ρ are the viscosity and density of the fluid respectively, μ_q and ρ_q are the shear modulus and density of quartz with values of $2.947 \times 10^{11} \text{ g cm}^{-1} \text{ s}^{-2}$ and 2.65 g cm^{-3} , respectively.

2.4 Undesirable Contributions to QCM response

A thin film deposited on a quartz crystal will move synchronously with the quartz when the crystal is excited, if the acoustic properties of the added mass are identical to the quartz itself. In this case the Sauerbrey equation is valid and any frequency change is related directly to the mass of the film. This approximation is good for low loading (small added masses). However, some physical parameters can cause deviations from these assumptions, producing results that are inadequately described by the Sauerbrey theory.

2.4.1 Excess Mass

It is proven that a small mass loading (where m_f is much less than m_q equation 2.9) will cause a change in resonant frequency that is proportional to the added mass. However, a high mass loading (where m_f is greater than m_q) will result in a failure in the validity of the Sauerbrey equation. It has been shown that the Sauerbrey equation is only valid for a film mass that is up to 10 % increase of the mass of the quartz crystal³⁷. The shear modulus and density of the film must be known if the mass to be added is more than 2% of the mass of the quartz crystal, as above 2% the added mass no longer behaves as a simple addition to the quartz, so there will be a properties issue.

2.4.2 Surface Roughness

In 1985 Schumacher et al³⁸ suggested that surface roughness of a quartz crystal oscillator will have a significant effect on the resonant frequency of an oscillator when immersed in solution. For perfectly smooth surfaces, the resonant frequency shift is proportional to the square root of the viscosity-density product of the solution. However, for rough surfaces the response is somewhat different. The surface features may become partially or completely filled with liquid. The fluid is constrained within the surface features and as a result behaves as a rigidly coupled mass¹¹. Quartz crystal oscillators consist of a thin piece of AT-cut quartz with vacuum deposited metal (usually gold) electrodes on either side, deposition of films occurs only on the electrode surface. The smoothness of the electrodes depends on the surface features of the quartz crystal itself. Minimisation of surface roughness effects can be achieved by the use of highly polished quartz crystals.

2.4.3 Non – uniform mass distribution

Martin and Hager³⁹ demonstrated that the sensitivity of the quartz crystal oscillator varies across the electrodes, with the maximum amplitude of oscillations being at the centre of the electrodes. Therefore it may be assumed that the mass sensitivity will not be uniform across the surface of the oscillator. The Sauerbrey equation uses a laterally averaged sensitivity, which is acceptable if the deposition of mass is uniform. This of course is a possibility but far from a guaranteed scenario, and must be proven for each case studied, using a surface imaging technique such as scanning electron microscopy or atomic force microscopy (see section 1.4.4). However, if there is not an excessive departure from a uniform deposit the Sauerbrey equation will give an average value for mass per unit area.

2.4.4 Temperature

It has already been discussed in section 2.1.3 that there are variations of the resonant frequency of a quartz crystal oscillator with temperature. This is minimised by the use of AT-cut quartz. The density and viscosity of the contacting medium are also affected by temperature, since the fluid properties have a significant effect on a quartz

resonator response. In practice, this is a bigger temperature effect than the intrinsic crystals sensitivity to temperature (figure 2.8). It is therefore essential to record the temperature at which the frequency measurements are made.

2.4.5 Interfacial slip

Although not an issue with the work presented in this thesis, interfacial slip is sometimes a undesirable contribution to the QCM response. A requirement of the Sauerbrey equation is that there is a “no-slip” boundary between the crystal surface and the contacting medium i.e. the displacement of the quartz and the first layer of the contacting medium is the same. This situation occurs when the interfacial forces of attraction between the quartz oscillator and the contacting medium are large enough to ensure that continuity of displacement is retained across the interface⁴⁰⁻⁴².

2.5 The Electrochemical Quartz Crystal Microbalance (EQCM)

Since the developments made by Kanazawa⁸⁻¹⁰ and Bruckenstein⁷, the quartz crystal resonator has been used in several research areas, including electrochemistry⁴³. The QCM consists of a piece of quartz with a vacuum deposited electrode (typically gold) on either side (figure 1.10). One face of the quartz is exposed to air while the other side is in direct contact with the electrolyte solution. The electrode that is in direct contact to the solution is then used as the working electrode. The EQCM enables the mass (frequency) changes to be monitored whilst simultaneously controlling the potential and measuring current (or vice versa).

The short data acquisition time (typically < 1s) and high sensitivity of the QCM has made it an invaluable tool in electrochemistry, leading to information for both thermodynamic and kinetic responses^{44, 45}.

2.6 Equivalent Circuit Models of the QCM electrical response

The quartz crystal microbalance is now a technique that is regularly used to probe interfacial properties in both gas and liquid environments. As previously suggested, the quartz crystal microbalance works extremely well as an accurate gravimetric device for rigidly deposited films. However, for liquids (section 2.1.6) or layers that are thick/soft and non-rigidly coupled to the underlying resonator the situation is different. The response of the quartz crystal microbalance for non-rigidly coupled mass depends on the viscoelastic properties of the film.

Crystal impedance analysis is a technique that is used to investigate viscoelastic films⁴⁶. It involves determination of the impedance response by measuring the admittance as a function of frequency (admittance spectra). This contrast with the simple QCM method, in which only the resonant frequency is recorded. Figure 2.11 shows a typical admittance spectrum. The three peaks shown are for the original (unloaded) quartz crystal, rigidly coupled loaded crystal and a non-rigidly coupled mass.

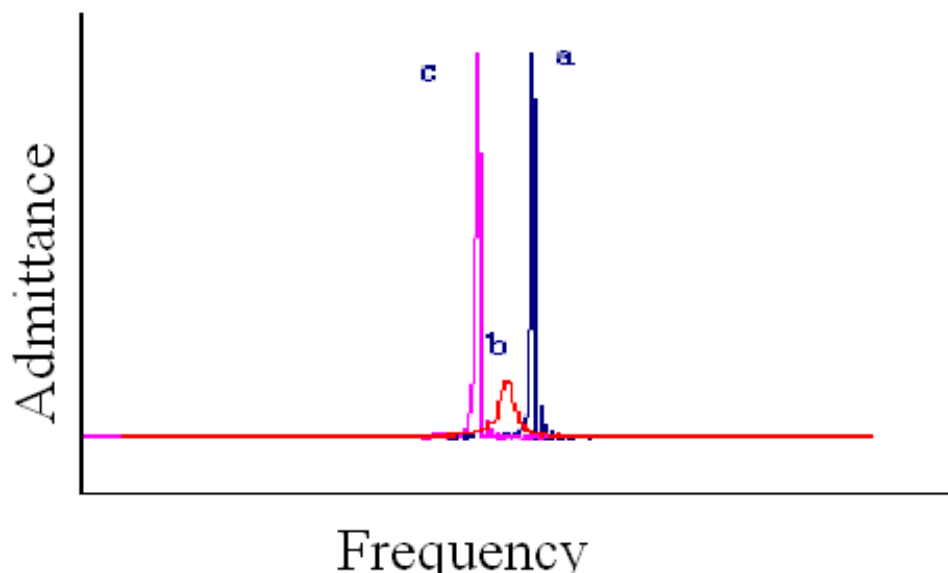


Figure 2.11. Schematic admittance spectrum showing the frequency change from (a) unloaded crystal to (b) viscoelastic mass loaded crystal and (c) rigidly coupled film.

For rigid films, the analysis is a simply evaluation using the Sauerbrey equation and is a direct frequency shift with no reduction in admittance (compare peaks a and c in figure 2.11). Viscoelastic films show a broadening of the peak and a large decrease in admittance, representing energy dissipation (compare peaks a and b in figure 2.11).

Crystal impedance analysis is a diagnostic tool for rigid vs. non-rigid films. For a quantitative analysis it is necessary to employ an equivalent circuit model. The equivalent circuit model enables the mechanical properties of a loaded quartz resonator to be modelled on electrical circuit components (resistive, capacitive and inductive components). The oscillation of a quartz crystal is analogous to the motion of a pendulum or a mass on a spring¹⁵. The mechanical model of a mass on a spring can be shown to correspond to an electrical circuit as illustrated in figure 2.12. For these models C' and C_m represent energy storage during oscillation, while energy dissipation is represented by R and r . The inductor L , in figure 2.12 panel b, affects the electrical response similar to the displaced mass (M panel a figure 2.12) of an oscillating crystal. C_0 represents the static capacitance associated with the attached gold electrodes.

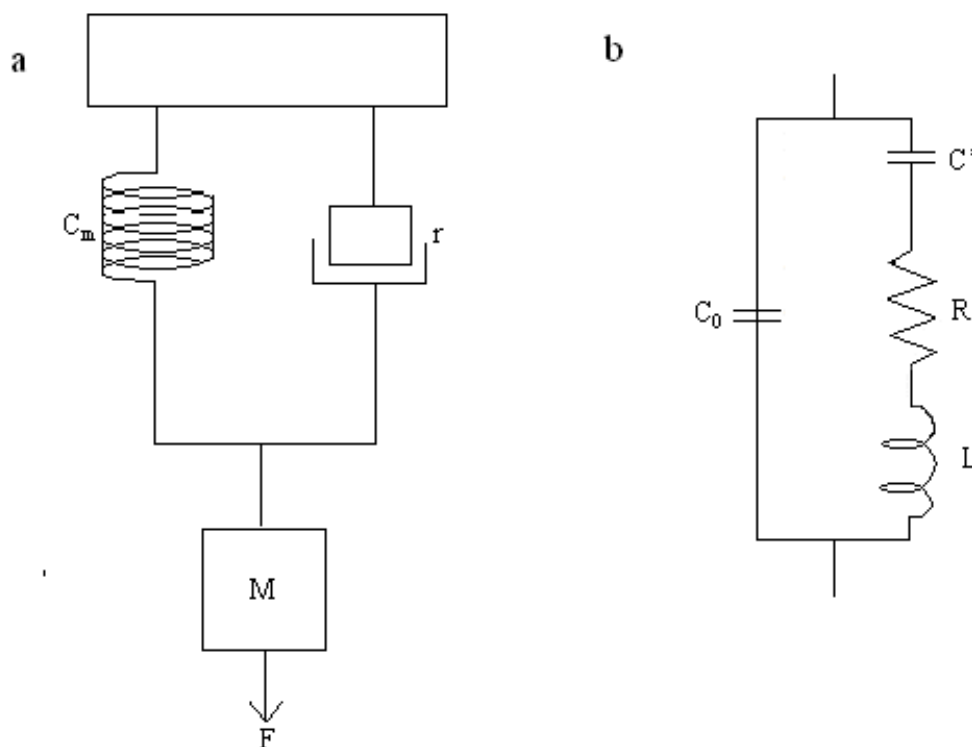


Figure 2.12. Schematic representations of (a) mechanical model of a loaded quartz crystal oscillator with (b) the corresponding electrical equivalent circuit¹⁵.

2.6.1 Transmission Line Model

In the transmission line model the electrical energy supplied to the quartz crystal is converted into acoustic variables, using a transformer. Stress, τ , and velocity, v , (acoustic variables) are analogous to the electrical variables voltage and current. Acoustic impedance caused by perturbations at the crystal surface change the progression of the acoustic energy within the transmission line. The transformer then converts the acoustic energy back to electrical energy.

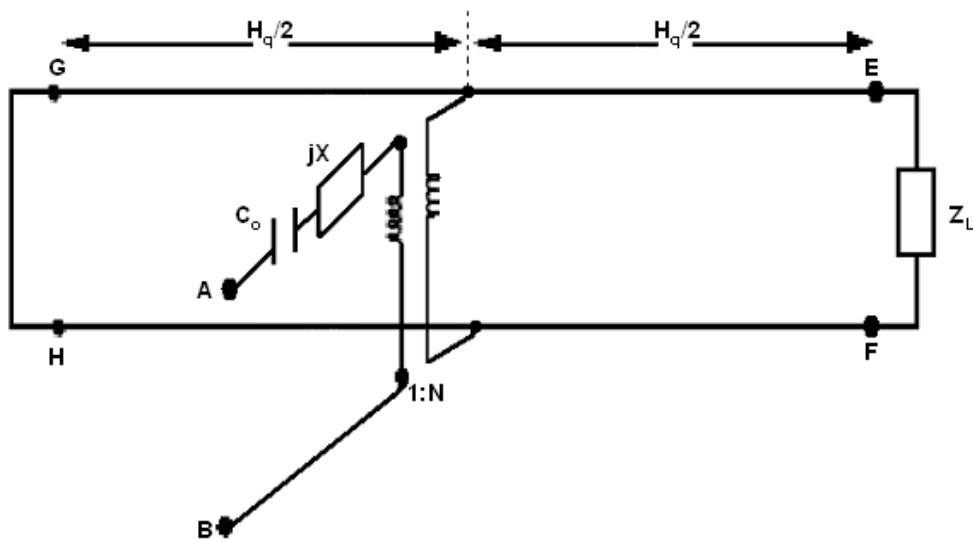


Figure 2.13. Schematic representation of the Transmission Line Model⁴⁷.

Figure 2.13 shows a schematic diagram of the transmission model. It has an electrical input and two acoustic parts. The acoustic part labelled G-H is in direct contact with air and therefore is stress free, thus acts as a short circuit. The other acoustic part E-F, is loaded by the acoustic input impedance Z_L . The piezoelectric components are described by the transformer of turn ratio (1:N) and the reactance of element jX , both N and X are define in more detail elsewhere⁴⁸ and $j = (-1)^{1/2}$. C_o is the static capacitance and $H_q/2$ is the thickness of the quartz.

2.6.2 Butterworth Van Dyke (BVD) Model

The lumped element circuit model, known as the Butterworth-Van Dyke (BVD) equivalent circuit model, is a simplified version of the transmission line model³³, it is a limiting case of the TLM for low loadings. The transmission line model is more accurate than the BVD model. However, due to the ease of visualisation and extraction of parameters, the BVD model is more commonly used. It is also worth noting that the BVD and TLM are experimentally indistinguishable for mass loadings that are less than 10% of the quartz mass.

The BVD equivalent circuit shown in figure 2.14 may be used as a model for the unperturbed quartz crystal resonator. The BVD equivalent circuit consists of a series branch, often referred to as the motional arm (containing an inductor, resistor and capacitor), in parallel with a static arm (a capacitor). The three components of the motional arm (L_1 , R_1 and C_1) represent the electromechanical characteristics of the quartz resonator. The inductor represents inertial mass, while the capacitive component corresponds to the energy storage (mechanical elasticity of the system) and the resistor represents energy loss (viscous effects and internal friction)⁴⁹. The static arm consists of a capacitor C_0^* and is given by:

$$C_0^* = C_0 + C_p \quad (2.17)$$

where C_p is the parasitic capacitance that arises due to stray capacitance from the geometry of the gold electrode and C_0 is the capacitance from the gold electrodes attached to the two faces of the quartz crystal.

The elements of Butterworth-Van Dyke circuit are given by⁵⁰:

$$R_1 = \eta_q / \mu_q C_1' \quad (2.18a)$$

$$L_1 = 1 / \omega_s^2 C_1' \quad (2.18b)$$

$$C_1 = 8K^2 C_0 / (N\pi)^2 \quad (2.18c)$$

$$C_0 = \epsilon_{22} A / h_s \quad (2.18d)$$

where ϵ_{22} is the dielectric permittivity; A is the electrode area; h_s the substrate thickness; K^2 is the electromechanical coupling coefficient of quartz; N is the harmonic number; η_q and μ_q are the viscosity and shear stiffness of quartz respectively. $\omega = 2\pi f_s$ where f_s is the resonant frequency for the unperturbed quartz resonator.

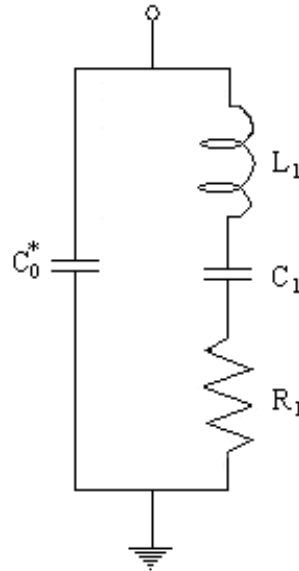


Figure 2.14 Butterworth – Van Dyke equivalent circuit⁵⁰

The total QCM admittance, Y , for the circuit in figure 2.15 is:

$$Y(\omega) = j\omega C_0^* + (1/Z_m) \quad (2.19)$$

The motional impedance for the circuit is given by:

$$Z_m^0 = R_1 + j\omega L_1 + (1/j\omega C_1) \quad (2.20)$$

2.6.3 Modification of the Butterworth Van Dyke (BVD) Model

The Butterworth Van Dyke model is for unperturbed crystals for which the resonator's electrical response is approximated using a series of lumped elements. Perturbation of the surface, such as added mass, causes an increase in the motional impedance, which may be coupled to the change in electrical impedance of the

device, by the use of a continuum model⁵¹. A modified BVD electrical equivalent circuit for the perturbed crystal may be obtained by solving the continuum model.

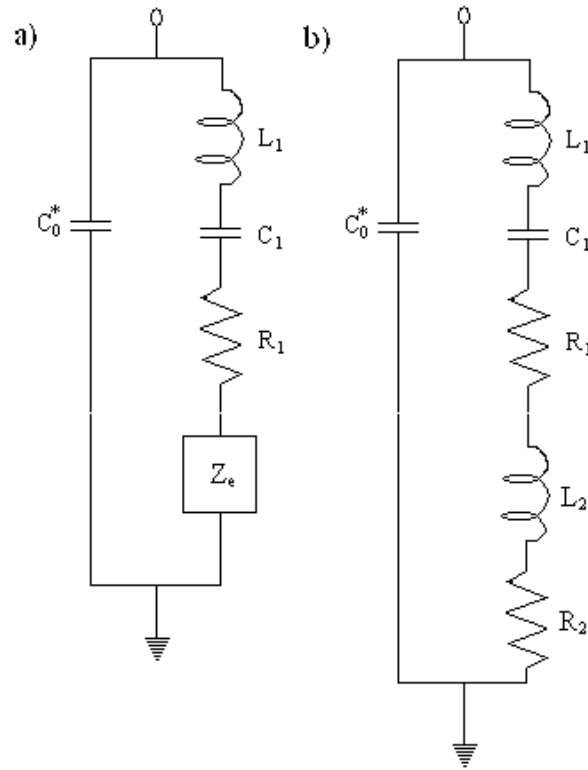


Figure 2.15 Modified Butterworth-Van Dyke equivalent circuit of a perturbed quartz crystal resonator (a) with complex impedance element (b) with motional inductance L_2 and resistance R_2 ⁵²

The modified Butterworth-Van Dyke equivalent circuit (figure 2.15a) has an additional component Z_e (electrical impedance). This represents the addition of mass on the quartz crystal surface. Z_e is given by:

$$Z_e = \left(\frac{N\pi}{4K^2 \varpi_s C_0} \right) \left(\frac{Z_s}{Z_q} \right) \quad (2.21)$$

where N is the harmonic number, C_0 is the static capacitance, ϖ_s the angular frequency and K is the coupling constant. Z_q and Z_s are the quartz and the surface mechanical impedance respectively; they are defined as:

$$Z_q = (\rho_q \mu_q)^{1/2} \quad (2.22)$$

$$Z_s = \frac{T_{xy}}{v_x} \Big|_{y=0} \quad (2.23)$$

where T_{xy} is the sinusoidal steady state shear stress occurring in the contacting medium and is caused by the force exerted by the oscillating quartz and v_x is the resulting x-directed surface particle velocity. Z_s is a complex quantity and so has both real and imaginary parts.

Letting $Z_e = R_2 + j\omega L_2$ allows the complex electrical impedance Z_e to be separated into real and imaginary components (see Figure 2.15), for which R_2 represents the real part and L_2 represents the imaginary part of Z_e . Equation 2.21 can be written:

$$R_2 = \left(\frac{N\pi}{4K^2 \omega_s C_0} \right) \left(\operatorname{Re} \frac{Z_s}{Z_q} \right) \quad (2.24a)$$

$$L_2 = \left(\frac{N\pi}{4K^2 \omega_s C_0} \right) \left(\operatorname{Im} \frac{Z_s}{Z_q} \right) \quad (2.24b)$$

When surface perturbations occur at the quartz crystal surface the motional impedance is given by:

$$Z_m = (R_1 + R_2) + j\omega(L_1 + L_2) + (1/j\omega C_1) \quad (2.25)$$

The total QCM admittance, Y , for the circuit in figure 2.12 is:

$$Y(\omega) = j\omega C_0^* + (1/Z_m) \quad (2.26)$$

However there are several different types of surface perturbations that the quartz crystal may be exposed to; section 2.7 deals with some of the more common cases.

2.7 Physical Models for Mass Loading of QCM

The admittance or impedance of the quartz crystal resonator will depend upon the conditions at the surface. There are three main types of loading to which the quartz crystal surface may be subjected: an ideal mass layer, a viscoelastic layer (which may be finite or semi-finite; section 2.6.4) and a fluid (which may be finite or semi-infinite, and Newtonian or non-Newtonian; section 2.6.2). From the four possibilities, the fluid case that is relevant to electrochemical studies is a semi-infinite Newtonian fluid.

2.7.1 Ideal Mass Layer

The addition of a thin rigid mass to the quartz crystal surface has the effect of increasing the inertial mass and therefore the acoustic property of the mass may be assumed to be identical to that of the quartz resonator itself.

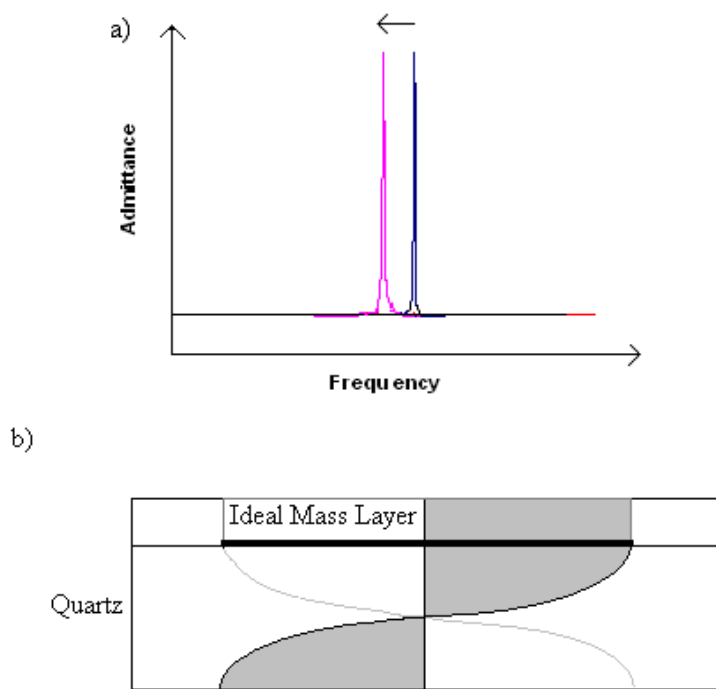


Figure 2.16. (a) Admittance vs. frequency plot illustrating shift of frequency for ideal mass and (b) cross sectional view of quartz crystal oscillator showing wave propagation through the quartz crystal and the ideal mass

The electrical response may be calculated using the Butterworth – Van Dyke equivalent circuit after the addition of an inductor L_2 . The electrical response of the quartz crystal to the ideal mass is illustrated in figure 2.16a. A cross sectional view of the quartz crystal oscillator with an ideal mass is shown in figure 2.17b, it illustrates how the wave propagates in the crystal and through the mass layer without any damping or phase shift of the wave.

The surface mechanical impedance of the oscillator containing the ideal mass layer is given by:

$$Z_s = j\omega m_s \quad (2.27)$$

where m_s is defined as the areal density (the mass per unit area) of the ideal mass layer and is given by:

$$m_s = h_s \rho_{iml} \quad (2.28)$$

where ρ_{iml} and h_s are the density and thickness of the ideal mass layer.

2.7.2 Semi-infinite Newtonian Fluid

A Newtonian fluid may be defined as a fluid for which the shear stress and the gradient in fluid velocity are related by a constant, independent of amplitude or frequency⁵³ (simple solvents used in many electrochemical experiments conform to this definition). The liquid at the crystal / liquid interface moves synchronously with the quartz crystal oscillator due to viscous coupling. The fluid is entrained by the transverse wave that is radiated into the medium as illustrated in figure 2.17.

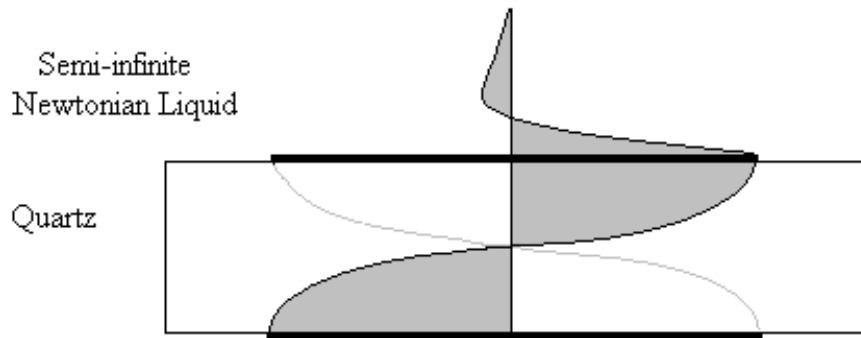


Figure 2.17. Schematic diagram of the quartz resonator in contact with a semi-infinite Newtonian liquid

Addition of the inertial mass from the entrained fluid causes the kinetic energy of the resonating system to increase and a decrease in resonant frequency. However, frictional forces that are proportional to the fluid's density and viscosity cause the transverse wave to be dampened. The wave damps rapidly as a function of distance from the surface. Figure 2.18 shows the severe damping of the resonance peak caused by the quartz oscillator in contact with the Newtonian fluid.

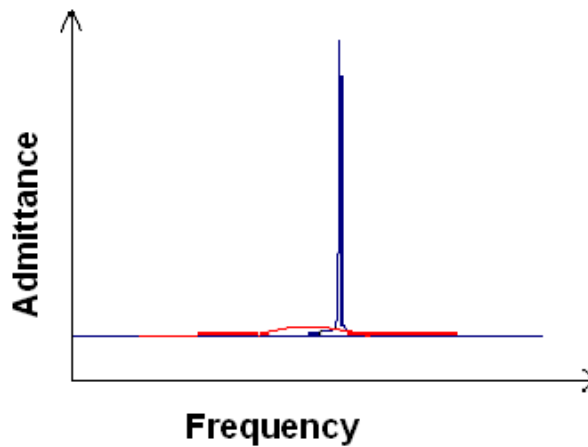


Figure 2.18 Schematic admittance vs. frequency plot illustrating shift of frequency for Newtonian liquid

A semi-infinite Newtonian liquid occurs when the thickness of the fluid layer exposed to the oscillator is larger than the decay length of the transverse wave (given by equation 2.29). The decay length of the acoustic wave in the Newtonian liquid is given by⁵⁴:

$$\delta = (2\eta_1/\omega\rho_1)^{1/2} \quad (2.29)$$

Equation 2.28 gives the surface mechanical impedance due to a Newtonian fluid⁵⁴.

$$Z_s = (\eta_1\omega\rho_1/2)^{1/2} (1+j) \quad (2.30)$$

where η_1 and ρ_1 are the fluid viscosity and density, respectively and j reflects complex impedance, with in/out of phase components ($j = \sqrt{-1}$).

The decay length of a transverse wave when immersed in a semi-infinite Newtonian fluid may be calculated using equation 2.29. A 10 MHz quartz crystal resonator has typical decay length of 0.18 μm when immersed in water. For most cases the thickness of the fluid layer is more than the calculated decay length; therefore they are known as semi-infinite Newtonian fluids.

$$\delta = \left(\frac{n_L}{\rho_L \omega} \right)^{1/2} \quad (2.31)$$

where n_L and ρ_L are the viscosity and density of the liquid

2.7.3 Viscoelastic Layers

A viscoelastic material may be explained in terms of its reaction to a force exerted upon it. A rigid material subjected to a force will be accelerated; however when a viscoelastic material has a force exerted upon it, some of the force will be used to accelerate the material, while some will cause deformations within the body. These deformations will either be elastic (in response to which the energy is stored within the material) and/or viscous (where the material is deformed by the force causing loss of energy due to friction). The properties of a viscoelastic material may be explained using the shear modulus, which is represented by³³:

$$G = G' + jG'' \quad (2.32)$$

where G' is the storage modulus and G'' is the loss modulus.

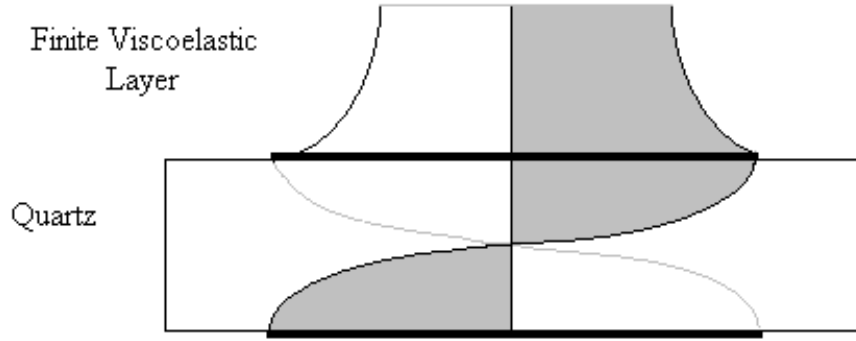


Figure 2.19. Schematic diagram of the quartz resonator in contact with a finite viscoelastic film

A finite viscoelastic layer is one for which the decay length of the propagating wave is larger than the film thickness and is defined as⁵⁵:

$$\delta = \frac{(2G/\rho_f)^{1/2}}{4} \quad (2.33)$$

where ρ_f is the film density.

Due to the finite thickness of the film, the acoustic wave reaches the outer limits of the film and is reflected back to the resonator / film interface. The reflected wave may interfere with the wave from the oscillating crystal in either a destructive or constructive manner. Figure 2.19 illustrates the quartz crystal oscillator with a finite viscoelastic film deposited on the surface. The base of the film moves synchronously with the resonator and the upper part lags behind. The impedance for the quartz crystal oscillator with a finite viscoelastic film is given by⁵⁶:

$$Z_s = Z_0 \tanh(\gamma h_f) \quad (2.34)$$

where γ is the complex wave propagation constant:

$$\gamma = j\omega \left(\frac{\rho_f}{G} \right)^{1/2} \quad (2.35)$$

and Z_0 is $(G\rho_f)^{1/2}$, G is the shear modulus; ρ_f and h_f are the film density and thickness respectively.

When the acoustic wave decay length is smaller than the film thickness the viscoelastic film is classed as semi-infinite and the film is classed as acoustically thick. The impedance for these thick films is given by equation 2.35. This equation shows that film thickness has no relevance for semi-infinite viscoelastic layers, for which it is assumed that the quartz resonator does not see the film boundary (i.e. the wave does not propagate as far as the outer boundary so there is no reflected wave).

2.7.4 Multi-Layer Physical Models

Real systems studied using a quartz crystal oscillator often consist of more than one layer. It is possible to derive equations that approximate the surface mechanical impedance for systems with a combination of different layers.

Loading	Example of loading	Surface mechanical impedance	Typical $Z_s / \text{g cm}^{-2}$
Unperturbed	Air	0	0
Ideal mass layer	Thin rigid film such (10 – 100 nm Cu)	$Z_s = j\omega m_s$	563 - 5630
Semi-infinite Newtonian liquid	Water	$Z_s = (\eta_1 \omega \rho_1 / 2)^{1/2} (1+j)$	1121
Finite viscoelastic layer	Thin polymer film	$Z_s = Z_0 \tanh(\gamma h_f)$	630-3050
Ideal mass + semi-infinite Newtonian liquid	Copper film and water layer	$Z_s = j\omega m_s + (\eta_1 \omega \rho_1 / 2)^{1/2} (1+j)$	1684 - 6751

Table 2.1 Summary of physical models.

Table 2.1 shows the relative values for surface mechanical impedance. It illustrates that when the film added (either ideal mass or finite viscoelastic) is around 10 nm the surface mechanical impedance is less than that of the semi infinite Newtonian liquid, therefore there is a need (sometimes) for a precise fluid correction.

It is important when compiling multi-layer models to note whether there is a phase shift of the acoustic wave. For the simple case, where no phase shift occurs or the phase shift is in the outer layer the surface mechanical impedance is simply an addition of the components (see table 2.1). However, if there is a phase shift within the lower layers then the situation is more complicated.

2.7.5 QCM Response for Complete/Incomplete Wetting

It has already been discussed in section 2.1.6 that the quartz crystal microbalance can be used as a sensitive mass detector with a liquid sample. Via a modification of the Sauerbrey equation; information about the fluid properties may be obtained. However, this model assumes that the quartz resonator is completely wet at the quartz/liquid interface. It is well documented that de-wetting may occur at rough surfaces and as already outlined in section 2.1.6, the QCM is sensitive to fluid trapped within the surface features. This means the QCM is a sensitive tool to investigate surface wetting / de-wetting.

The extent to which wetting / de-wetting occurs is dependent upon the balance of forces associated with the compression of the trapped gas and surface tension. Wetting / de-wetting may be viewed as the level of fluid penetration into surface features. Figure 2.20 illustrates the four possible scenarios; wetting may be complete or incomplete (for which there is trapped gas within the surface features).

The first case (figure 2.20a) illustrates a “smooth” surface, for which the decay length of the propagating acoustic wave is larger than the fluid depth. The frequency shift for a “smooth” surface is given by equation 2.10^{10, 38, 51} and illustrates that for perfectly smooth surfaces, viscous entrainment of fluid results in a resonant frequency

shift proportional to the square root of the liquid viscosity-density product. This case is discussed in more detail in section 2.1.6.

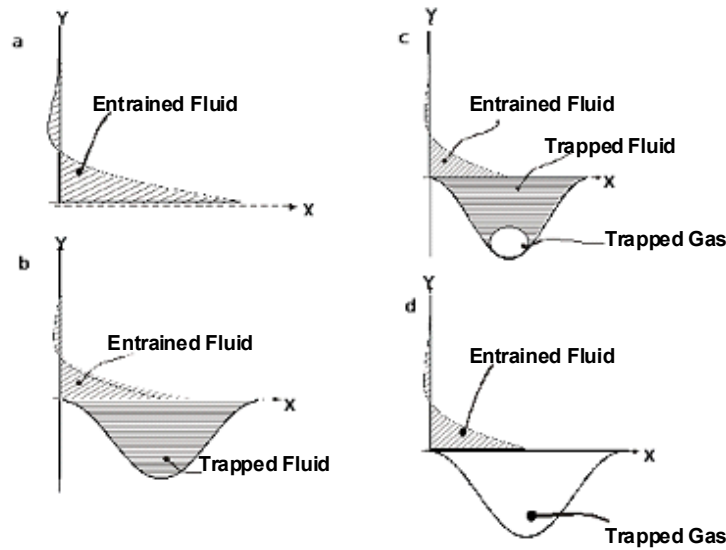


Figure 2.20. Schematic representations of viscously entrained fluid and fluid trapped at the surface (a) smooth, (b) rough and completely wetted, (c) rough and partially wetted and (d) rough and completely de-wetted¹²

Figure 2.20b represents the complete wetting of corrugated surfaces for which the surface is completely wet i.e. corrugations are completely filled with solution. The motion of the trapped liquid within these pores is constrained. The constraint of the trapped fluid means the liquid within the pores move synchronously with the oscillating crystal surface. The response is similar to that of a rigidly coupled mass. The QCM response is then given by the sum of the Kanazawa expression (equation 2.16) and applying the Sauerbrey equation (equation 2.13) to the areal mass density of the trapped fluid. The total frequency shift for the quartz resonator with a completely wet surface is given by¹²:

$$-\frac{\Delta f}{\rho} = \frac{f_0^{3/2}}{N(\pi\mu_q\rho_q)^{1/2}} \left(\frac{\eta}{\rho}\right)^{1/2} + \frac{\pi h f_s^2}{N(\mu_q\rho_q)^{1/2}} \quad (2.36)$$

where h is defined as the average deflection about the mean (corresponding to how roughness will be quantified, one can show that $h = (2/\pi)A$)⁵².

A more complex situation arises when the surface features are only partially filled by the fluid (figure 2.20c). A few reports have indicated this partial filling occurs when gas becomes trapped within the surface features^{12, 57}. The extent to which wetting takes place is dependent upon the balance of forces associated with the compression of the trapped gas and surface tension. It has been suggested that partially filling of the surface features occurs because the fluid sheets over the surface only contacting the tops of the corrugations, the liquid then enters the pores compressing the gas into microbubbles at the bottom of the pits⁵⁸. How deep the liquid penetrates into the pores will depend on surface roughness⁵⁰ and the liquid contact angle⁵⁹. In a model by Theisen et al³⁴ it is suggested that the QCM may be used to investigate the wetting / de-wetting, contact angle and surface roughness using equation 2.36, with the prediction that at a contact angle of 120° the sharpness of the wetted to de-wetted increases as the surface feature size decreases. At high contact angles the surface remains un-wetted regardless of the surface feature size.

References

- (1) Chen, W.; Fadeev, A. Y.; Hsieh, M. C.; Oner, D.; Youngblood, J.; McCarthy, T. J. *Langmuir* **1999**, *15*, 3395-3399.
- (2) Oner, D.; McCarthy, T. J. *Langmuir* **2000**, *16*, 7777-7782.
- (3) Semal, S.; Blake, T. D.; Geskin, V.; de Ruijter, M. J.; Castelein, G.; De Coninck, J. *Langmuir* **1999**, *15*, 8765-8770.
- (4) Voue, M.; De Coninck, J. *Acta Mater.* **2000**, *48*, 4405-4417.
- (5) Hazlett, R. D. *J. Coll. Interface Sci.* **1990**, *137*, 527-533.
- (6) Yoshimitsu, Z.; Nakajima, A.; Watanabe, T.; Hashimoto, K. *Langmuir* **2002**, *18*, 5818-5822.
- (7) Bruckenstein, S.; Shay, M. *Electrochim. Acta* **1985**, *30*, 1295-1300.
- (8) Kanazawa, K. K. *J. Electrochem. Soc.* **1985**, *132*, C368-C368.
- (9) Kanazawa, K. K.; Gordon, J. G. *Anal. Chim. Acta* **1985**, *175*, 99-105.
- (10) Kanazawa, K. K.; Gordon, J. G. *Anal. Chem.* **1985**, *57*, 1770-1771.
- (11) Stockel, W.; Schumacher, R. *Berichte Der Bunsen-Gesellschaft-Phys. Chem. Chem. Phys.* **1987**, *91*, 345-349.
- (12) Theisen, L. A.; Martin, S. J.; Hillman, A. R. *Anal. Chem.* **2004**, *76*, 796-804.
- (13) Bund, A. *J. Solid State Electrochem.* **2004**, *8*, 182-186.
- (14) Bund, A.; Neudeck, S. *J. Phys. Chem. B* **2004**, *108*, 17845-17850.
- (15) Buttry, D. A.; Ward, M. D. *Chem. Rev.* **1992**, *92*, 1355-1379.
- (16) Hillman, A. R.; Efimov, I.; Ryder, K. S. *J. Am. Chem. Soc.* **2005**, *127*, 16611-16620.
- (17) Hillman, A. R. "The electrochemical quartz crystal microbalance", in *Encyclopaedia of Electrochemistry*; Wiley, New York, 2003.
- (18) Sawyer, D. T.; Sobkowiak, A.; Roberts, J. L. *Electrochemistry for Chemists*, 2nd ed.; John Wiley & Sons, Inc., 1995.
- (19) Loveday, D. C.; Hmyene, M.; Ferraris, J. P. *Synth. Metals* **1997**, *84*, 245-246.
- (20) Plieth, W.; Bund, A.; Rammelt, U.; Neudeck, S.; Duc, L. M. *Electrochim. Acta* **2006**, *51*, 2366-2372.
- (21) Rudge, A.; Raistrick, I.; Gottesfeld, S.; Ferraris, J. P. *Electrochim. Acta* **1994**, *39*, 273-287.
- (22) Visy, C.; Lukkari, J.; Kankare, J. *J. Electroanal. Chem.* **1991**, *319*, 85-100.
- (23) Rieger, P. H. *Electrochemistry*, 2nd edition ed.; Chapman and Hall, 1993.
- (24) Hamann, C. A.; Hamnett, A.; Vielstich, W. *Electrochemistry*; Wiley-VCH, Weinheim, 1998.
- (25) Pletcher, D. *A First Course in Electrode Processes*; Romsey, Hants, UK, 1991.
- (26) Curie, P.; Curie, J. *C. R. Acad. Sci.* **1880**, *91*, 294.
- (27) Curie, P.; Curie, J. *C. R. Acad. Sci.* **1881**, *93*, 1137.
- (28) Lu, C.; Czanderna, A. W. *Applications of Piezoelectric Quartz Crystal Microbalances*; Elsevier, 1984.
- (29) Deakin, M. R.; Buttry, D. A. *Anal. Chem.* **1989**, *61*, A1147-&.
- (30) Rayleigh, L. *London Math. Soc.* **1885**, *17*, 4-11.
- (31) Strutt, J. W. L. R. *The Theory of Sound*, Revised edition ed.; Dover: New York, 1945.
- (32) Sauerbrey, G. *Z. Phys.* **1959**, *155*, 206.
- (33) Ballantine, D. S.; White, R. M.; Martin, S. J.; Ricco, A. J.; Frye, G. C.; Zellers, E. T. *Acoustic Wave Sensors*; Academic Press: New York, 1997.
- (34) Konash, P. L.; Bastiaans, G. J. *Anal. Chem.* **1980**, *52*, 1929-1931.
- (35) Nomura, T.; Minemura, A. *Nippon Kagaku Kaishi* **1980**, 1621-1625.

- (36) Nomura, T.; Okuhara, M. *Anal. Chim. Acta* **1982**, *142*, 281-284.
- (37) Lu, C. S.; Lewis, O. *J. Appl. Phys.* **1972**, *43*, 4385-&.
- (38) Schumacher, R.; Borges, G.; Kanazawa, K. K. *Surf. Sci.* **1985**, *163*, L621-L626.
- (39) Martin, B. A.; Hager, H. E. *J. Appl. Phys.* **1989**, *65*, 2627-2629.
- (40) Lu, F.; Lee, H. P.; Lim, S. P. *Smart Mater. Struct.* **2003**, *12*, 881-888.
- (41) Lu, F.; Lee, H. P.; Lim, S. P. *J. Phys. D-Appl. Phys.* **2004**, *37*, 898-906.
- (42) McHale, G.; Newton, M. I. *J. Appl. Phys.* **2004**, *95*, 373-380.
- (43) Oyama, N.; Ohsaka, T. *Progress In Polymer Science* **1995**, *20*, 761-818.
- (44) Bruckenstein, S.; Hillman, A. R. *J. Phys. Chem. B* **1988**, *92*, 4837-4839.
- (45) Hillman, A. R.; Loveday, D. C.; Bruckenstein, S. *J. Electroanal. Chem.* **1989**, *274*, 157-166.
- (46) Bandey, H. L.; Hillman, A. R.; Glidle, A.; Gonsalves, M.; Bruckenstein, S. *J. Electroanal. Chem.* **1996**, *410*, 219.
- (47) Filiatre, C.; Bardeche, G.; Valentin, M. *Sensors Actuators A-Phys.* **1994**, *44*, 137-144.
- (48) Krimholt, R.; Leedom, D. A.; Matthaei, G. L. *Electron.Lett.* **1970**, *6*, 398-&.
- (49) Bandey, H. L.; Martin, S. J.; Cernosek, R. W.; Hillman, A. R. *Anal. Chem.* **1999**, *71*, 2205-2214.
- (50) Martin, S. J.; Granstaff, V. E.; Frye, G. C. *Anal. Chem.* **1991**, *63*, 2272-2281.
- (51) Reed, C. E.; Kanazawa, K. K.; Kaufman, J. H. *J. Appl. Phys.* **1990**, *68*, 1993-2001.
- (52) Martin, S. J.; Frye, G. C.; Ricco, A. J.; Senturia, S. D. *Anal. Chem.* **1993**, *65*, 2910-2922.
- (53) White, F. M. *Viscous Fluid Flow*; McGraw-Hill, New York, 1974.
- (54) Glassford, A. P. M. *J. Vacuum Sci.Tech.* **1978**, *15*, 1836-1843.
- (55) Skompska, M.; Jackson, A.; Hillman, A. R. *Phys. Chem. Chem. Phys.* **2000**, *2*, 4748-4757.
- (56) Martin, S. J.; Frye, G. C., New York 1991; IEEE; 393-398.
- (57) Lubetkin, S. *Langmuir* **2003**, *19*, 10774-10778.
- (58) Jones, S. F.; Evans, G. M.; Galvin, K. P. *Adv. Coll. Interface Sci.* **1999**, *80*, 27-50.
- (59) Bankoff, S. G. *AICHE J.* **1958**, *4*, 24 - 26.

CHAPTER 3

EXPERIMENTAL

3.1 Introduction

This chapter describes the methodologies employed to record and interpret data for both the interfacial wetting at nanoscale surfaces and the electrochemical analysis of PEDOT, for which the experimental results are given in chapters 4,5 and 6.

3.2 Quartz crystal resonator

10 MHz AT – cut quartz crystals were prepared and supplied by International Crystal Manufacturing Co. Ltd., Oklahoma City, OK. They consist of a thin piece (ca. 0.16mm) of AT cut quartz with vacuum deposited gold electrodes on either side. The piezoelectric and electrochemical areas associated with the gold electrode are 0.21 and 0.23 cm² respectively. The small difference of 0.02 cm² corresponds to the connecting tab to the one side of the electrode (figure 3.1)

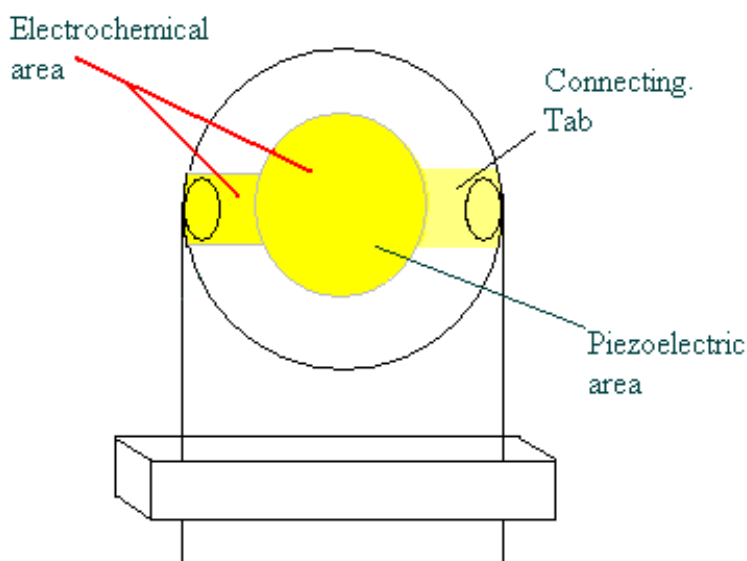


Figure 3.1 Schematic diagram of quartz crystal.

3.2.1 Surface finish of quartz crystal

There are two types of surface used during this study. The first type is classed as etched or un-polished and has finish that is less than a 0.3 μm . For etched crystals the gold electrode is deposited directly onto the quartz, as the unpolished surface makes the quartz/gold bonding better. The etched surface finish increases the effective surface area of the electrode making it ideal for electrochemical applications.

The other type of quartz surface is classed as a polished crystal: it has less than a 0.1 μm finish. These types of crystals have chromium under layer that helps the gold to adhere to the highly polished surface. The surface features of an un-polished quartz crystal are larger than the acoustic decay length of a transverse wave when immersed in a semi-infinite Newtonian fluid. A 10 MHz resonator has a typical decay length of 0.18 μm (section 2.7.2), therefore using polished crystals helps to keep the effects of surface roughness, as discussed in section 2.4.2, to a minimum¹.

3.3 Electrochemical instrumentation

All electrochemical experiments were carried out in a standard three-electrode cell (figure 3.2). The working electrode was one of gold electrode of the quartz crystal, the counter electrode was a platinum foil disk and the reference electrode was either silver wire or SCE. The working electrode/quartz crystal was glued to the base of the glass electrochemical cell, using silicon adhesive (Dow-Corning). The counter electrode was positioned parallel with the working electrode (figure 3.2) to ensure that there would be a uniform electric field. Thus, in the case of PEDOT studies particularly, enabling the growth of a uniform film across the surface of the QCM. This is essential when using the Sauerbrey equation, for which the distribution of the mass must be uniform² (see section 2.4.3).

Due to the nature of the experiment outlined in chapter 5, nitrogen gas was bubbled through the electrolyte for 15 minutes before the start of the experiment and then gently over the top of the solution during all electrochemical analysis of the films.

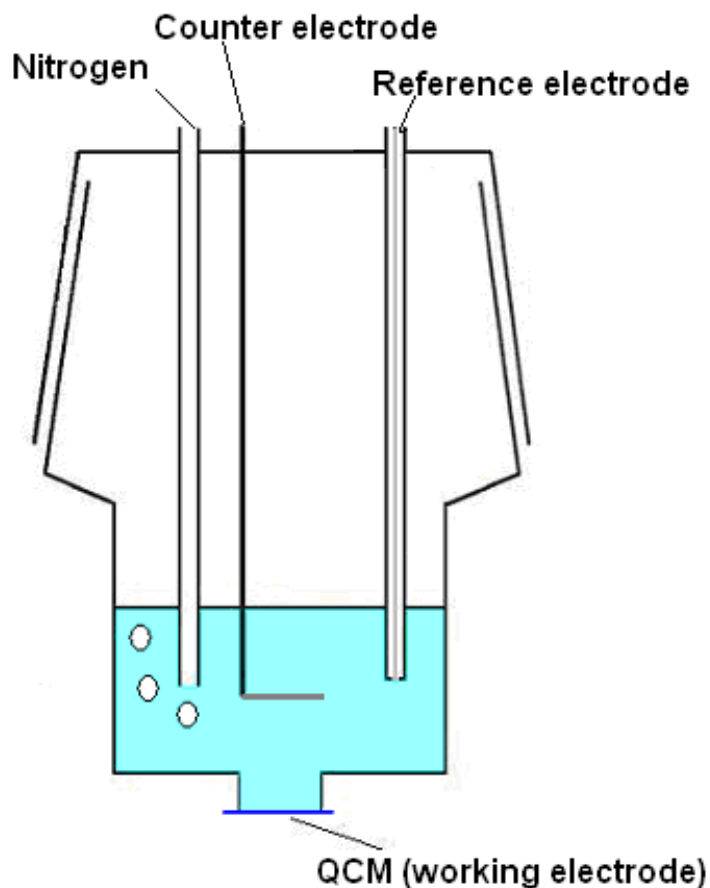


Figure 3.2 Schematic representation of the three-electrode electrochemical cell used for EQCM experiments

The potential was supplied by a PGSTAT 20 autolab and controlled using GPESW 4.2 computer software. The potentiostat was combined with an oscillator circuit as described by Bruckenstein and Shay³.

Nanoporous metal film preparation

3.4.1 Overview

Here nanoporous metallic films were electrochemically deposited onto a quartz crystal through a hexagonal close packed polystyrene latex microsphere template. Hexagonal close packed polystyrene latex microsphere templates were prepared on the gold electrodes of quartz crystals. Polystyrene latex microspheres are readily available with diameters on the order of a few hundred nanometres. Their use as

templates has been well documented⁴⁻⁷, with various methods of template formation ranging from meniscus techniques to simple gravity sedimentation. Here we form templates by gravity sedimentation of a colloidal dispersion of polystyrene latex microspheres (100, 200, 500 or 1000 nm).

Nanoporous metallic films were prepared using electrochemical deposition of metallic copper and platinum through the previously prepared hexagonal close packed polystyrene latex microsphere template. Galvanostatic deposition into the interstices between the close packed spheres was followed by subsequent removal of the template to reveal metallic films with pores of size corresponding to the diameter of the spheres within the template. The thickness of the film was controlled by the charge passed during deposition.

3.4.2 Instrumentation and Materials

Monodisperse polystyrene latex microspheres (stabilized by sulphonate groups) were supplied by Alfa Aesar as a 2.5% wt aqueous solution. Separate experiments used 1000 nm, 500 nm 200 nm and 100 nm diameter spheres to prepare the highly ordered hexagonal close packed templates. Hexachloroplatinic acid H_2PtCl_6 (purity 99.99 %), copper sulphate, sulphuric acid, toluene and propanol were obtained from Aldrich (used as received). The quartz resonators used during these experiments were 10 MHz polished quartz crystals coated with a Cr under-layer and a Au top layer. The gold electrode of the QCM was used as the substrate for the preparation of the nanoporous films. The electrode was cleaned prior to use using propan-1-ol followed by distilled water.

The electrochemical deposition of platinum through the polystyrene template was performed in a three-electrode EQCM cell (as described above). The working electrode was one of the Au electrodes of the 10 MHz polished AT- cut quartz crystals with platinum and SCE as the counter and reference electrodes respectively. Platinum was deposited under potentiostatic conditions. The potential was supplied by a PGSTAT 20 autolab and controlled using GPESW 4.2 computer software.

Copper deposition was carried out in the EQCM cell described above. In this case, a two-electrode configuration was used, in which the working electrode was one of the Au electrodes of a 10 MHz AT-cut quartz crystal. The counter electrode was platinum foil (area 1 cm²). The Cu deposition was carried out at constant current density (see procedure below for optimization) maintained by an Autolab potentiostat/galvanostat. All frequency data and admittance spectra were recorded using an Agilent E5061A network analyser. Film structure was confirmed using AFM/SEM.

3.4.3 Procedure

Quartz crystals were cleaned using propan-1-ol prior to use. The preparation of polystyrene latex microsphere templates were carried out by attaching an O-ring (10mm diameter) to the crystal using silicone adhesive; the O-ring was then glued to the base of the glass cell. The polystyrene latex spheres were diluted to 0.5 wt% using distilled water. 0.08 ml of solution was carefully applied to each of the working gold electrode of the quartz crystal. The templates were then formed by the sedimentation of the spheres, achieved by sealing the cells (with parafilm) and allowing the sedimentation of the spheres to occur. Sedimentation occurred over a period of 3 – 21 days depending on the sphere size. It is assumed that sedimentation and attractive capillary forces encourage the spheres to pack into hexagonal close packed arrays. Once the settling process had finished, a layer of clear water was visible. Evaporation of the water layer leads to a well-formed template.

The deposition of copper was carried out using a 0.1 mol dm⁻³ CuSO₄ / 0.1 M H₂SO₄ (Aldrich) deposition bath; chemicals were AnalaR reagent and used as received. Optimisation of copper deposition was carried out by galvanostatically depositing copper onto smooth AT-cut quartz crystals at range of current densities. The smoothness of the deposited copper was investigated using an SEM. Galvanostatic deposition of copper in the interstices between the close packed spheres was carried out at a current density of 4.52 mA cm⁻² (found empirically to give smooth deposits on bare Au / polished quartz crystals).

Platinum was electrochemically deposited into the interstices of the template, at a fixed potential of 0.1 V vs. SCE using a plating bath of 25 mmol dm⁻³ H₂PtCl₆. The charge passed was monitored using the Autolab.

The polystyrene template was removed by dissolution in toluene over a 24-hour period, to leave the nanoporous films. Film structure was confirmed using AFM/SEM.

3.5 Wetting

3.5.1 Overview

If the surface is smooth, the frequency shift of QCM in liquid is proportional to the square root of the liquid's viscosity – density product^{3, 8}. However, for corrugated surfaces the situation is more complex. The fluid becomes trapped within the surface features and acts as a rigidly coupled mass. Here we deliberately develop a quartz crystal that has surface features, which are uniformly distributed across the surface and are of a known size. The frequency shift in solution for these crystal will be different from that of a smooth crystal (with very small surface features) in solution, this frequency difference will lead to information on the fluid penetration into the pores.

3.5.2 Instrumentation and Materials

Nanoporous films were deposited onto AT-cut quartz crystals as outlined in chapter 3.4.1. These crystals were then glued to the base of a cell. Frequency data and admittance spectra were recorded for 0% (water), 5, 10, 20, 40, 60 and 80% glycerol - water, solutions using an Agilent E5061A network analyser.

3.5.3 Procedure

Frequency data for a range of glycerol/water solutions was recorded for bare quartz crystals. These crystals were then used to prepare nano-porous films as outlined in

section 3.4.2.1. Frequency data was then recorded for the nanoporous films, using a range of glycerol solutions (0 – 80% glycerol/water).

3.6 PEDOT p-doping

3.6.1 Overview

Thin films of the conducting polymer poly(3,4-ethylenedioxythiophene), PEDOT, were electrochemically prepared. EQCM experiments were then carried out on these films while exposed to a variety of different electrolytes and solvents, using a potential range that corresponds to the p-doping region of the polymer. Current and frequency data were then used to obtain time resolved flux data as a function of potential and charge. A more detailed outline of the analysis is given in chapter 5.

3.6.2 Instrumentation and materials

PEDOT films were potentiodynamically deposited using a solution of 50 mmol dm⁻³ monomeric EDOT (Bayer) / 0.1 M LiClO₄ in dry acetonitrile (Aldrich, anhydrous 99.8%; stored over 4Å molecular sieves). The cell and electrochemical equipment are described in chapter 3.3. Crystal admittance data were recorded using an Agilent E5061 network analyzer, to ensure films were acoustically thin. The quartz resonators used during these experiments were 10 MHz unpolished crystals with Au coating (ICM, Oklahoma City, OK) as described in section 3.2. The working electrode was one of the gold faces of the crystal, with the counter and reference electrodes being platinum foil and silver wire respectively. All data were acquired at room temperature (20 ± 2 °C).

EQCM experiments were performed on PEDOT films exposed to solutions of lithium perchlorate in acetonitrile (LiClO₄/CH₃CN), tetraethylammonium tetrafluoroborate in acetonitrile (TEABF₄/CH₃CN), tetraethylammonium tetrafluoroborate in dichloromethane (TEABF₄/CH₂Cl₂). All chemicals were supplied by Aldrich and used as received.

3.6.3 Procedure

PEDOT films were electrochemically deposited using cyclic voltammetry (-0.2 – 1.2V, 100 mV s⁻¹). The thickness of the film was controlled by the number of cycles used: 4 cycles gave films with a thickness between 1 – 2 μm, the actual volume of which was determined gravimetrically. Frequency and current responses were recorded and compared to those previously reported⁹. Crystal admittance data were recorded using an Agilent E5061A network analyser, to ensure the films were acoustically thin and free from any viscoelastic effects¹⁰.

Different PEDOT films but with similar thickness were prepared for characterization in each of the electrolyte solutions (see 3.6.2). Following deposition, films were rinsed in acetonitrile before being transferred to the monomer free electrolyte solution (see 3.6.2) for voltammetric characterization. Before characterization commenced, the films were cycled 3-4 times in the electrolyte solution, to ensure complete exchange of electrolyte from that of the deposition solution. Films were characterized by cycling the potential (-0.8 – 1.2 V) at various scan rates (20, 50, 100, 150, 200 and 250 mV s⁻¹). The frequency and current responses were recorded using EQCM equipment as outlined in section 3. 3.

3.7 PEDOT n-doping

3.7.1 Overview

Thin films of the PEDOT (see section 3.6.1) were electrochemically prepared. EQCM experiments were then carried out on these films while exposed to a range of electrolytes tetrapropylammonium tetrafluoroborate (TPABF₄), tetraethylammonium tetrafluoroborate (TEABF₄) and tetraethylammonium tosylate (TEAToS) in acetonitrile (CH₃CN), using a potential range that corresponds to the both n and p-doping regions of the polymer. Current and frequency data were then used to obtain time resolved flux data as a function of potential and charge. A more detailed outline of the analysis is given in chapter 6

3.7.2 Instrumentation and materials

The instrumentation and materials for these experiments were exactly the same as those outlined in section 3.6.2. The EQCM characterisation was limited to only one solvent (acetonitrile) and three different electrolytes TPABF₄, TEABF₄ and TEAToS (see section 3.6.2).

3.7.3 Procedure

PEDOT films were electrochemically deposited as described in section 3.6.3. Different PEDOT films but with similar thickness were prepared for characterization in each of the electrolyte solutions (see section 3.6.3). Following deposition, films were rinsed in acetonitrile before being transferred to the monomer free electrolyte solution (see section 3.5.2) for voltammetric characterization. Before characterization commenced, the films were cycled 3-4 times in the electrolyte solution, to ensure complete exchange of electrolyte from that of the deposition solution. Films were characterized first in the p-doping region by cycling the potential (-0.8 – 1.2 V) at various scan rates (20, 50, 100, 150, 200 and 250 mV s⁻¹). The same films were then cycled in the n-doping region (-0.8 - -2.0 V) using the same scan rates and finally cycled sequentially through n and p regions (using both potential ranges as above). The frequency and current responses were recorded using EQCM equipment as outlined in section 3.3.

References

- (1) Schumacher, R.; Borges, G.; Kanazawa, K. K. *Surface Science* **1985**, *163*, L621-L626.
- (2) Martin, B. A.; Hager, H. E. *J. App. Phys.* **1989**, *65*, 2627-2629.
- (3) Bruckenstein, S.; Shay, M. *Electrochim. Acta* **1985**, *30*, 1295-1300.
- (4) Bartlett, M.; Jiang, H. B. *Phys. Rev. E* **2002**, *65*, art. no.-031906.
- (5) Bartlett, P. N.; Baumberg, J. J.; Coyle, S.; Abdelsalam, M. E. *Faraday Discuss.* **2004**, *125*, 117-132.
- (6) Bartlett, P. N.; Dunford, T.; Ghanem, M. A. *J. Mater. Chem.* **2002**, *12*, 3130-3135.
- (7) Bartlett, P. N.; Marwan, J. *Phys. Chem. Chem. Phys.* **2004**, *6*, 2895-2898.
- (8) Kanazawa, K. K. *J. Electrochem. Soc.* **1985**, *132*, C368-C368.
- (9) Seshadri, V.; Wu, L.; Sotzing, G. A. *Langmuir* **2003**, *19*, 9479-9485.
- (10) Hillman, A. R.; Efimov, I.; Ryder, K. S. *J. Am. Chem. Soc.* **2005**, *127*, 16611-16620.

CHAPTER 4

INTERFACIAL WETTING AT NANOSCALE CONTOURED SURFACES

4.1 Introduction

Interfacial wetting is important in a number of electrochemical devices, notably within membranes used for (electro)catalysis, fuel cells and sensors, since only the part of the interface which is wet by the solution may take part in the required (electro)chemical processes. Wetting is dominated by the lyophobic nature of the surface. One of the many ways to quantify surface wetting is to measure the contact angle¹, that is the angle between the interface of the water/liquid droplet and the surface. However wetting is not only controlled by the chemical properties of the materials but also by the geometric microstructure of the surface²⁻⁶. There are two possible scenarios for textured surfaces: the liquid will either follow the solid surface or it will trap gas inside the surface features^{7, 8}. Therefore de-wetting can occur at textured surfaces (see section 1.2). Wetting for textured surfaces may be viewed as the level of fluid penetration into the surface features. The extent to which this takes place is dependent upon the balance of forces associated with the compression of the trapped gas and surface tension. Thus, changing the surface roughness or producing surfaces with well-ordered microstructures can alter the lyophobic nature of a surface^{1,9}.

The development of materials with spatially ordered features and functionality is significant for a range of applications including (bio)sensors¹⁰, data-storage^{11, 12}, microchip reactors¹³ and photonics¹⁴. The fabrication of materials with nano/meso-scale architecture often involves the use of expensive techniques such as electron beam lithography or nanoscale lithography. Recent developments have illustrated a simple cost efficient route for the preparation of mesoporous surfaces with pore sizes of a few hundred nanometers, using colloidal liquid crystal template techniques¹⁵. These techniques involve the formation of 3D close packed arrays of uniform colloidal spherical particles (by sedimentation, electrophoresis or vertical deposition) as sacrificial templates.

One of the most popular templating techniques involves permeation of a solution of a chemical precursor of the target material into the spaces within the template. The latter is then converted into the porous materials by a suitable reaction followed by removal of the template, commonly by dissolution. Variations of this approach include deposition of colloidal gold particles into the colloidal crystal¹⁵, lithography¹⁶, electroless deposition¹⁷⁻¹⁹ and hydrogen reduction of preformed oxides²⁰. However, limitations on the performance of the resulting films can arise as a consequence of shrinkage of the structure during its formation, incomplete filling and chemical or mechanical instability arising from contamination by residues from the chemical reagents.

One approach that overcomes any limitations on the performance involves the electrochemical deposition of the required metal/semiconductor into the interstices of a close packed array of spheres. The template is finally removed to leave the highly ordered porous film^{21, 22}. This method has the attraction that film thickness may be controlled via the diameter and number of layers of the templating spheres and the electrochemical charge used to deposit the metal.

As well as the unique physical properties of nanoporous films it is anticipated that these structure may also offer interesting chemical properties, with particular relevance to electrocatalysis. In this area of application, one would anticipate that critical issues would be the extent of penetration of solution (both the solvent and reactant components) into the porous film and the very large surface area potentially available for adsorption.

Here nanoporous metallic films are used to investigate the effect of surface roughness on interfacial wetting using the electrochemical quartz crystal microbalance (EQCM). The EQCM oscillates at a resonant frequency and when a thin film is deposited onto the gold electrode of the EQCM a decrease in the resonant frequency is observed. The addition of small, rigid uniformly deposited masses on the quartz crystal surface can be treated as an extension of the quartz crystal itself. Under these circumstances the EQCM acts as a gravimetric sensor of the mass added. The change in resonant frequency is related to the deposited mass according to the Sauerbrey equation²³.

$$\Delta f = -k \Delta m \quad (4.1)$$

$$\text{where } k = -2f_o^2 / ([\rho_q \mu_q]^{1/2})$$

Several reports have illustrated the use of quartz crystal resonators with liquid media²⁴⁻²⁶. It was outlined that quartz crystals with a face in contact with a liquid will have a resonant frequency shift proportional to the square root of the product of the liquid's viscosity and density. Other studies have suggested that surface features of a quartz crystal resonator can have a drastic effect upon the resonant frequency when the resonator is immersed in liquids²⁷. It is believed that surface features may cause liquid to become trapped within the corrugations. When the surface feature size is less than the decay length of the acoustic wave, it is believed that the trapped liquid causes a frequency decrease that is usually associated with a rigid mass layer. The mass of the trapped liquid is often treated as a rigid mass layer as it is assumed that there is no movement of this liquid. It is the competition between the compression of trapped gas and the surface tension that dictates the level of fluid penetration into the surface features. If the fluid is trapped below the surface peaks but above the gas/liquid meniscus then it will behave like a rigid mass layer. This rigid mass layer is often referred to as an "ideal mass layer" and will contribute to any frequency shift observed. This ideal mass layer offers a means of establishing the wetting/de-wetting of rough surfaces.

A recent model²⁸ suggested that surface roughness of a quartz crystal can be represented as a sinusoidal corrugation. A more detailed explanation can be found in section 2.7.5. This model predicts that the solution "sheets" across the surface trapping gas within the surface corrugations. The shape and area of the interface, between the bulk liquid and the gas trapped within the surface corrugations, may be determined by the internal pressure and the surface tension forces. Therefore, the effects of surface roughness on the wetting behaviour of a quartz crystal microbalance can be viewed as a function of liquid properties and contact angle. The model postulates that at low contact angle and small surface features, the surface is nearly or completely wet, suggesting that the surface tension forces cause a crushing of the trapped gas.

Here nanoporous films are prepared onto the surface of the gold electrode of the quartz crystal to explore experimentally the amount of fluid entrapped within surface features through the frequency response of the quartz crystal microbalance. The effects of pore size and fluid properties on film wetting will be examined and compared to the recent theoretical model for the wetting of idealized corrugated surfaces²⁸.

4.2 Aims and Objectives

Recent studies^{21, 22, 29-31} have illustrated that the electrochemical deposition of metals through a 3D close packed array of polystyrene latex microspheres leads to a cost effective route to nanoporous metallic films. As well as the unique physical properties of nanoporous films these films may also offer interesting chemical properties, with particular relevance to electrocatalysis. In this area of application, one would anticipate that critical issues would be the extent of penetration of solution into the porous film. Therefore these films also offer a route to the analysis of interfacial wetting at contoured surfaces.

There has been a theoretical study carried out²⁸ on the QCM response to wetting of corrugated surfaces. Here we aim to compliment this study by:

- Producing 3D close-packed array of polystyrene latex microsphere templates on the surface of quartz crystals.
- Producing nanoporous metallic films by electrochemical deposition through the templates.
- Quantify interfacial wetting of the nanoporous contoured surfaces produced.

4.3 Procedure

Quartz crystals consist of a thin piece of AT-cut quartz with vacuum deposited gold electrodes on either side. The smoothness of the gold electrodes will depend on whether the quartz is polished or unpolished. The surface feature size is ca. 200 nm

for an unpolished crystal while polished crystals will have at least an order of magnitude smaller.

Here two types of 10 MHz AT-cut quartz crystals (ICM, Oklahoma City, OK) were investigated, in which the Au was deposited on either (i) an unpolished (“rough”) AT-cut crystal or (ii) a polished AT-cut crystal. Frequency changes for a range of glycerol/water solutions was carried out by attaching a quartz crystal (separate experiments used polished and un-polished crystals) to the bottom of a cell, then applying 5 ml of each solution (0 – 80% glycerol/water) directly onto the gold electrode. Frequency data and admittance spectra were recorded using an Agilent E5061A network analyser.

Hexagonal close packed polystyrene latex microsphere templates were prepared on the gold electrodes of quartz crystals. Polystyrene latex microspheres are readily available with diameters on the order of a few hundred nanometres. Their use as templates has been well documented^{22, 30, 32, 33}, with various method of template formation ranging from meniscus techniques to simple gravity sedimentation. Here we form templates by gravity sedimentation of colloidal dispersion of polystyrene latex microspheres (Alfa Aesar; 2-wt% aqueous solution, stabilised by sulphonate groups); separate experiments used 200, 500, 750 and 1000 nm spheres. Quartz crystals were cleaned using propan-1-ol prior to use. Preparation of the polystyrene latex microsphere templates were carried out by attaching an O-ring (10mm diameter) to the crystal using silicon adhesive; the O-ring was then glued to the base of the glass cell. The polystyrene latex spheres were diluted to 0.5 wt% using distilled water. Volumes of 0.1 ml were carefully applied to the working gold electrode of the quartz crystals. The templates were then formed by the sedimentation of the spheres, achieved by sealing the cells (with parafilm) and allowing the spheres to settle. After the settling process had finished, the visible water layer was allowed to evaporate, leaving the dry template. The admittance spectrum of the blank crystal was taken at the start of each experiment in both air and water, using an Agilent E5061A network analyser. The structures of the templates were confirmed using tapping mode AFM (Veeco Dimension).

10 MHz (polished and unpolished) AT-cut quartz crystals (ICM, Oklahoma City, OK) that had been previously prepared with a polystyrene template (section 3.2) were used for the preparation of platinum and copper nanoporous films. Copper deposition was carried out at a constant current density of 4.52 mA cm^{-2} (obtained from the optimisation procedure as described in section 3.4.3) maintained by a PGSTAT 20 Autolab and controlled using GPESW 4.2 computer software. The counter electrode was a piece of platinum foil, area 1 cm^2 . The required nanoporous film was obtained by dissolution of the template using toluene.

Platinum was electrochemically deposited, into the interstices of the template, at fixed potential of 0.1 V vs. SCE using a plating bath of $25 \text{ mmol dm}^{-3} \text{ H}_2\text{PtCl}_6 / 25 \text{ mmol dm}^{-3} \text{ KCl}$. The charged passed was monitored using the Autolab. The working electrode was a quartz crystal (containing the previously prepared template) mounted on an O-ring, which was then attached to the bottom of the cell using silicone glue. The reference and counter electrodes were a silver wire and a piece of platinum foil (1 cm^2) respectively. Removal of the template was by dissolution in toluene. Frequency and admittance data for the nanoporous films in both water and air were recorded. All frequency data and admittance spectra were recorded using an Agilent E5061A network analyser. Surface structure of all films and templates were confirmed using AFM (Veeco dimension).

4.4 Results and Discussion

4.4.1 Investigations of quartz crystal surface features

4.4.1.1 AFM / SEM investigations of quartz crystal surface features

Two types of working electrodes were investigated, in which the Au was deposited on either (i) an unpolished (“rough”) AT-cut crystal or (ii) a polished AT-cut crystal. SEM images (Figure 4.1) indicate that the surface feature size is ca. 200 nm for the unpolished crystal. The surface features of the polished quartz crystal cannot be clearly measured from the SEM image (figure 4.1 b) but are at least an order of magnitude smaller.

AFM images (figure 4.2) confirm the magnitude of the surface roughness for the unpolished AT-cut quartz crystal. During AFM analysis a laser is focused onto the back of a reflective cantilever, as the tip moves up and down with the surface features the laser is deflected off the cantilever into photo-detectors. The reflective nature of the polished gold surface limits the resolution of the AFM's response, therefore a clear image of the surface was not possible.

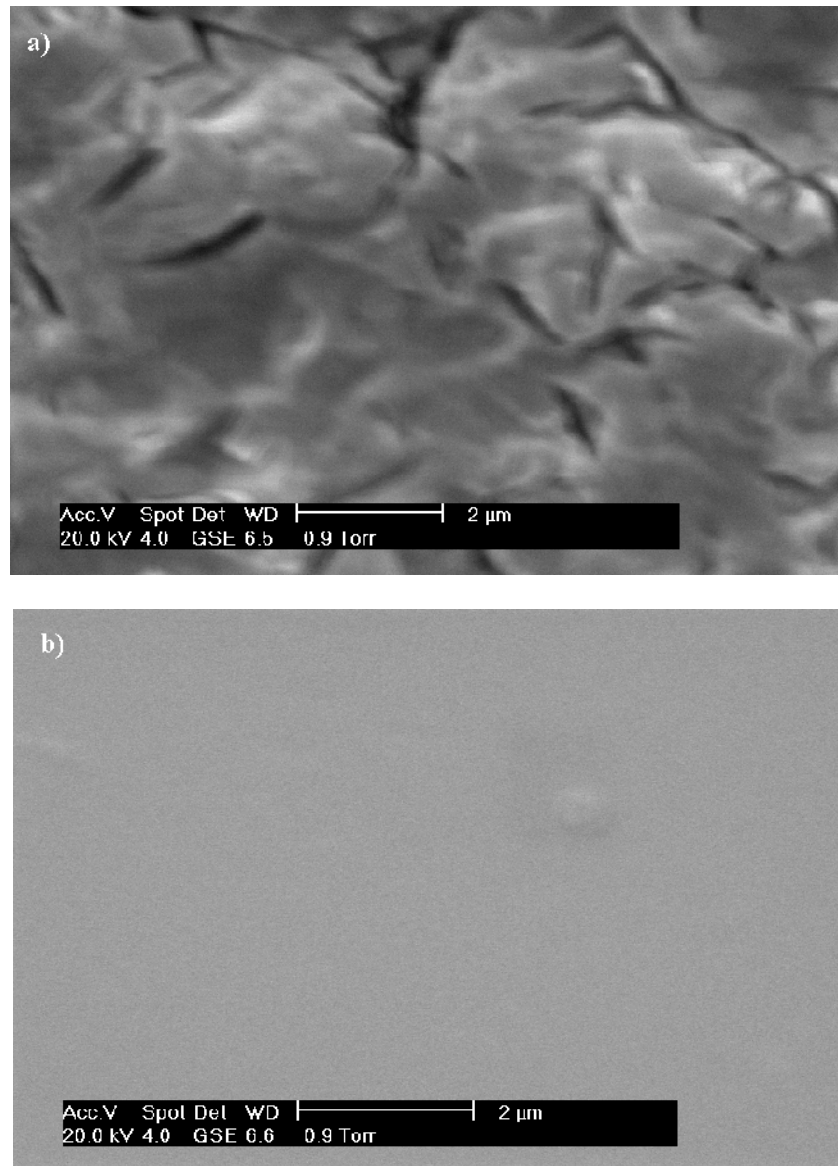


Figure 4.1 SEM images of Au electrodes deposited on (a) rough quartz crystal, (b) polished quartz crystal

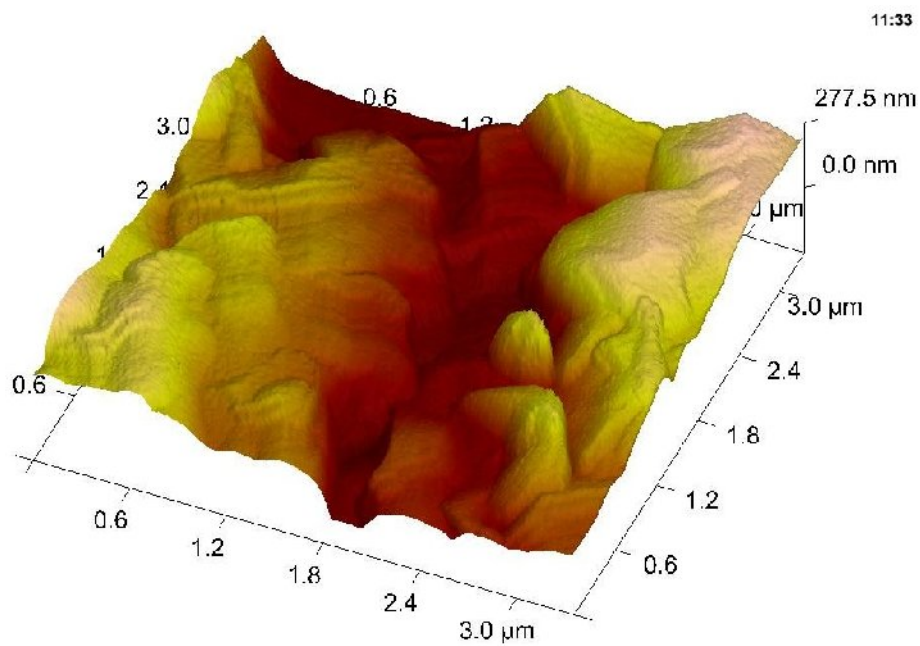
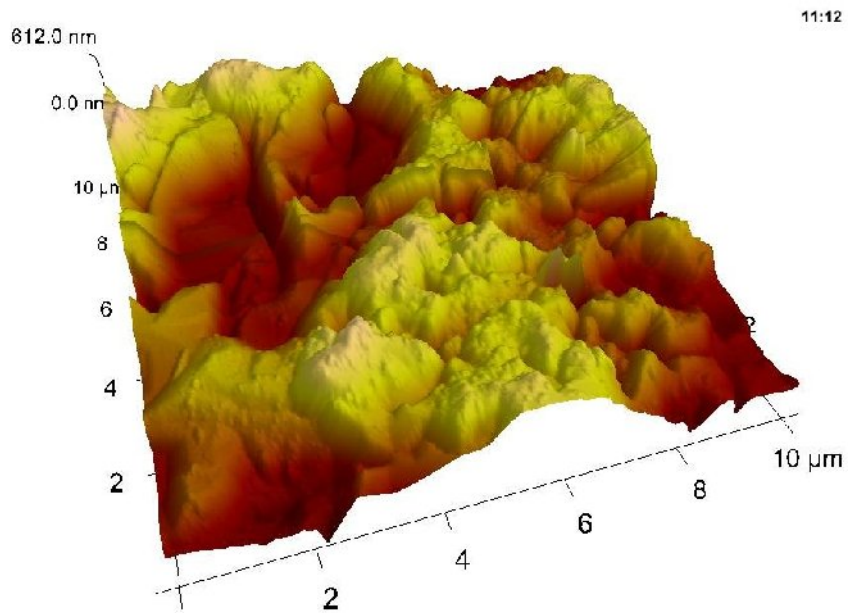


Figure 4.2 AFM images of gold electrode (the two images are the same sample, but different areas of the electrode) deposited on unpolished AT-cut quartz crystal

4.4.1.2 Investigation of surface features using fluid entrainment

The QCM is a sensitive tool for probing liquid properties. When the surface is smooth the frequency shift is given by equation (2.16) for which, the viscous entrainment of fluid results in a resonant frequency shift proportional to the square root of the product of liquid density and viscosity. However, for surfaces that are corrugated the situation is more complex. The fluid becomes trapped within the surface features and acts as a rigidly coupled mass (as discussed in section 2.7.5).

As outlined in section 2.7.5 there are three possibilities for the trapped fluid: the pores may be completely filled with liquid or gas or by a combination of the two. When the corrugations are completely filled with liquid, the total frequency shift is given by equation (2.36).

$$-\frac{\Delta f}{\rho} = \frac{f_0^{3/2}}{N(\pi\mu_q\rho_q)^{1/2}} \left(\frac{\eta}{\rho}\right)^{1/2} + \frac{\pi h f_s^2}{N(\mu_q\rho_q)^{1/2}} \quad (2.36)$$

The relationship outlined in equation (2.36) provides a means for extracting the surface feature size (h), by fitting the frequency response ($\Delta f/\rho$) for a series of different fluid properties ($(\eta/\rho)^{1/2}$). Therefore a plot of ($\Delta f/\rho$) against $(\eta/\rho)^{1/2}$ should yield a straight line with a gradient of $f_s^{3/2}/n(\rho_q\mu_q\pi)^{1/2}$ and an intercept of $f_s^2\pi h/n(\rho_q\mu_q)^{1/2}$. The QCM response for a range of glycerol/water solutions is shown in figure 4.3. The results obtained (figure 4.3) are plotted using equation (2.36), a straight line is achieved (figure 4.4).

The gradient is calculated as follows:

$$Grad. = \frac{f_s^{3/2}}{N(\rho_q\mu_q\pi)^{1/2}} \quad (4.2)$$

where ρ_q and μ_q are the density and shear modulus of quartz, f_s is the initial frequency of the quartz and N is the harmonic number. Thus the calculated gradient is $\approx 20100 \text{ cm}^2 \text{ s}^{-1/2} \text{ g}^{-1}$.

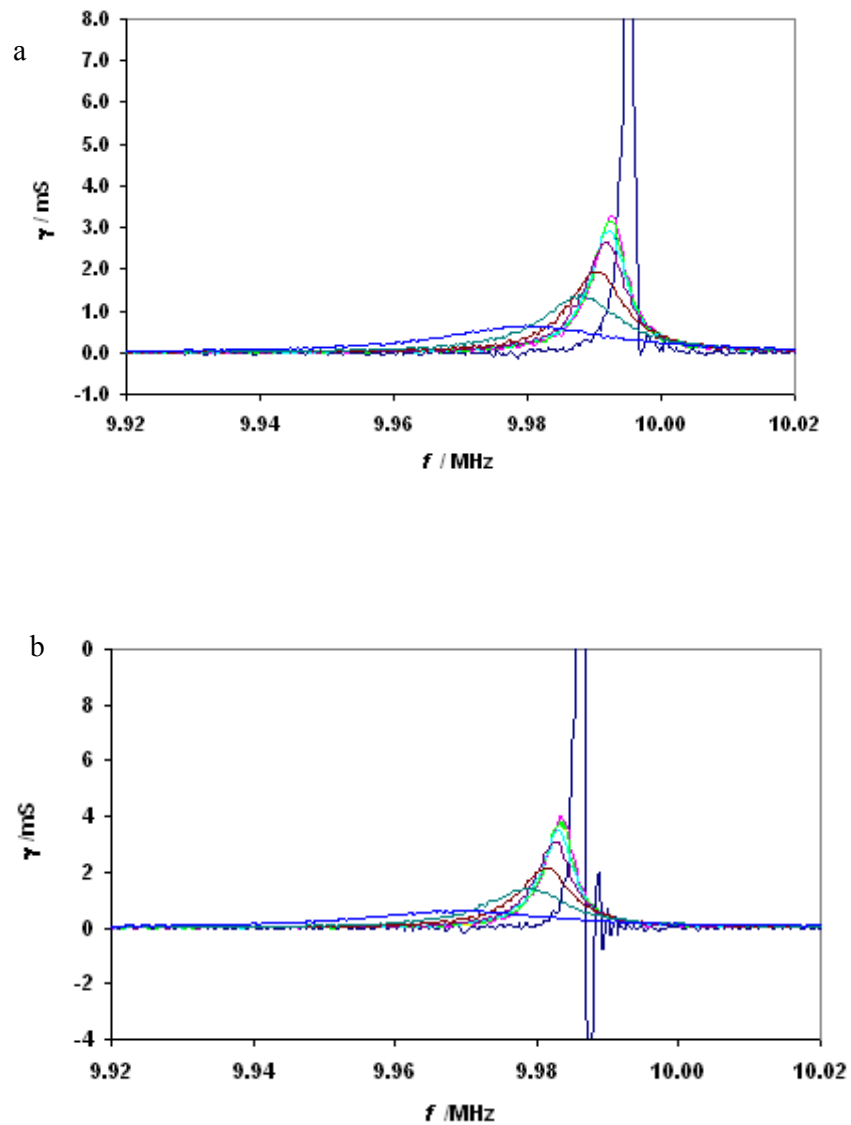


Figure 4.3 QCM admittance spectra for different concentrations of glycerol illustrating how the increase in viscosity (higher glycerol concentrations) leads to both a frequency shift and dampening of the admittance. (a) un-polished crystal; (b) polished AT-cut quartz crystal. Blank: —; 0%: —; 5%: —; 10%: —; 20%: —; 40%: —; 60%: —; 80%: — glycerol.

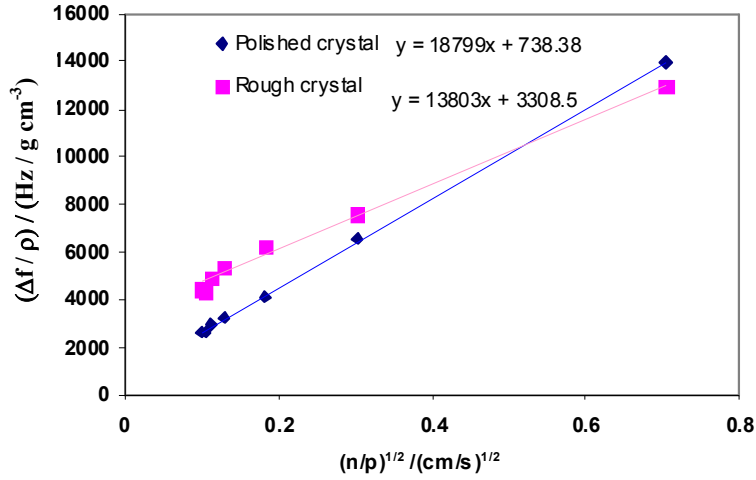


Figure 4.4 Frequency responses for unpolished and polished AT-cut quartz crystals for a series of different fluid properties (water/glycerol mixtures)

The calculated gradient is very close to that obtained for the experimental data for the polished crystal. The experimental gradient and intercept leads to the surface feature size by:

$$\frac{I}{G} = \pi^2 f_s^2 h \quad (4.3)$$

where I is the experimental intercept and G is the experimental gradient. Using equation (4.3) and the experimental values (figure 4.4) for the polished ($G = 18800$ and $I = 738$) and the rough ($G = 13800$ and $I = 3300$) crystals, the surface feature sizes are calculated as ca. $0.02 \mu\text{m}$ and $0.14 \mu\text{m}$ for polished and rough crystals respectively.

The calculations indicate that the average surface features sizes are 140 nm for the unpolished crystal, this is very similar to the fluid decay, whereas the 20 nm surface feature size of the polished crystal is well below that of the fluid decay length. The calculated value for the surface feature size of the unpolished crystal is confirmed by the observed pore size seen on the SEM/AFM images (figure 4.1/4.2). A comparison of the calculated and the measured value for the surface feature size of the polished

crystal is not available due to the unclear surface images obtained using both the AFM and SEM.

During this chapter polystyrene latex microspheres that are 200 nm in diameter and above will be used. As the surface features of the rough crystal are large enough for the smallest spheres to sit in, it obvious that the 200 nm particles will not form a neat hexagonal closed packed array on the rough surface.

4.4.2 Template Formation

The formation of a hexagonal close packed template is dependent on the settling and evaporation period along with the humidity and temperature of the cell^{33, 34}. A diverse range of sedimentation / solvent evaporation times showed the optimum preparation conditions to be a long settling period (between 2 - 5 days for 1000 nm, 4 - 8 days for 750 nm template, 7 - 10 days for 500 nm and 10 – 21 days for 200 nm template) followed by a slow evaporation period of 3 days. The settling periods vary slightly; the cause of this variation is believed to the change in the temperature and humidity of the cell. The end of the settling period is signified by the development a clear liquid layer (the water from the initial polystyrene latex sphere solution).

The AFM images shown in figure 4.5/4.6 illustrate that with adequate time to settle and slow evaporation of the solvent layer, leads to well formed hexagonal close packed arrays of polystyrene spheres. The images in figure 4.5 for the 200 nm template show that the packing has very few deformities over a large area (panels a, b, c and e), while panels d and f confirm the sphere size.

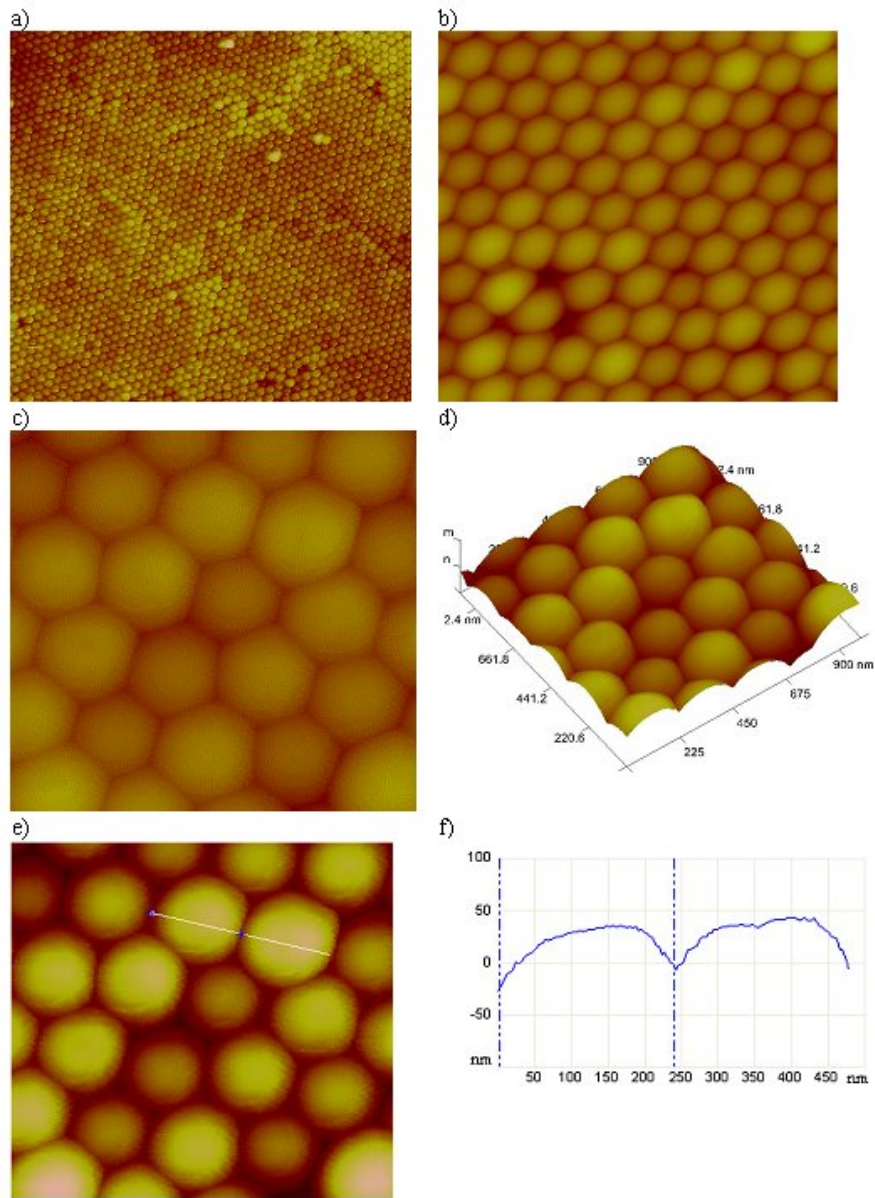


Figure 4.5 AFM images of 200 nm polystyrene latex microsphere template a) 10 μm scan size, b) 5 μm scan size, c - e) 2 μm scan size. The graph (f) shows the measurement for the line in image e.

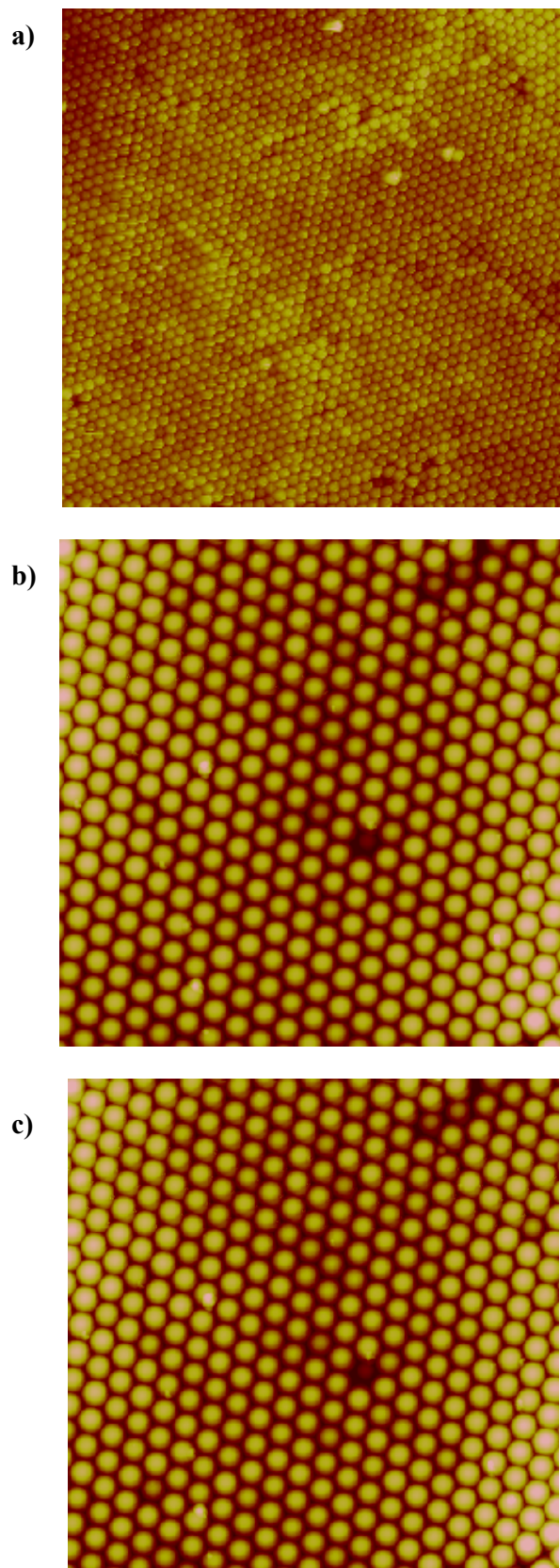


Figure 4.6 AFM images of polystyrene latex microsphere templates (all $10\ \mu\text{m} \times 10\ \mu\text{m}$ scan size): a) 200 nm spheres; b) 500 nm spheres; and c) 1000 nm spheres.

4.4.2.1 QCM response for settling period

The settling process was monitored using the quartz crystal microbalance. As the polystyrene latex microspheres settle there is a change in frequency and admittance. Figure 4.7 and 4.8 illustrate that there is a significant change in admittance as the settling time elapses. This change in admittance is believed to be caused by the changes in the viscoelastic effects of the solution / polystyrene microspheres.

When comparing the two spectra there is a significant difference in the response of the QCM exposed to 200 nm particles and that of the QCM exposed to the 500 nm particles. The difference between the two responses is not fully understood but is believed to be due to the speed of the settling and packing of the 500 nm particles. Analysis of admittance data for both, may lead to information on the shear modulus³⁵. Very little is understood about the shear modulus for the polystyrene latex microspheres and is beyond this present study. However, this leads to opportunities for future investigation within this area.

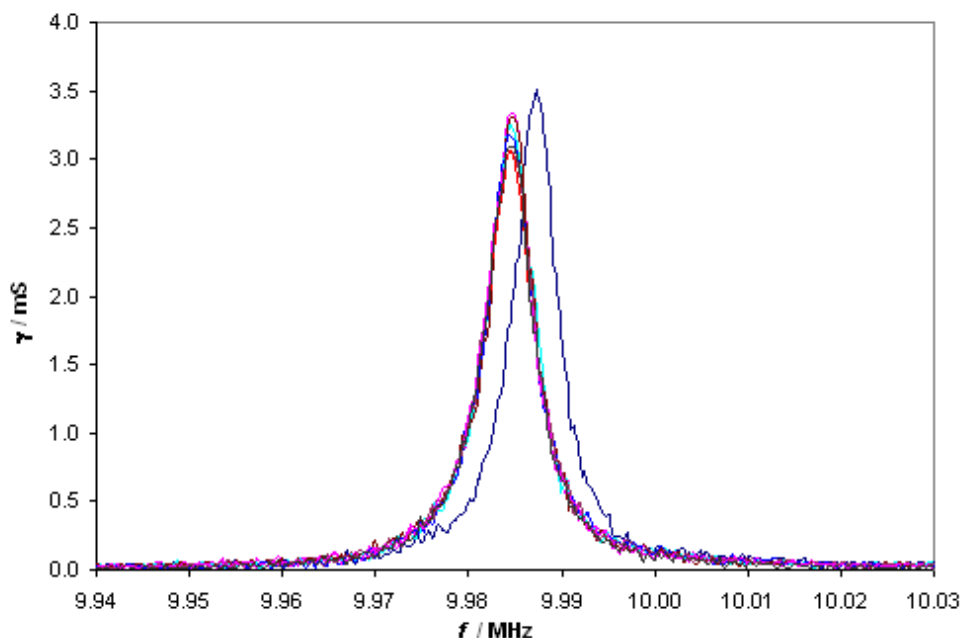


Figure 4.7 QCM responses during the settling process of 200 nm diameter polystyrene latex microspheres. Settling times 0: —; 44: —; 96: —; 168: —; 240: —; 288: —; 360: — hours.

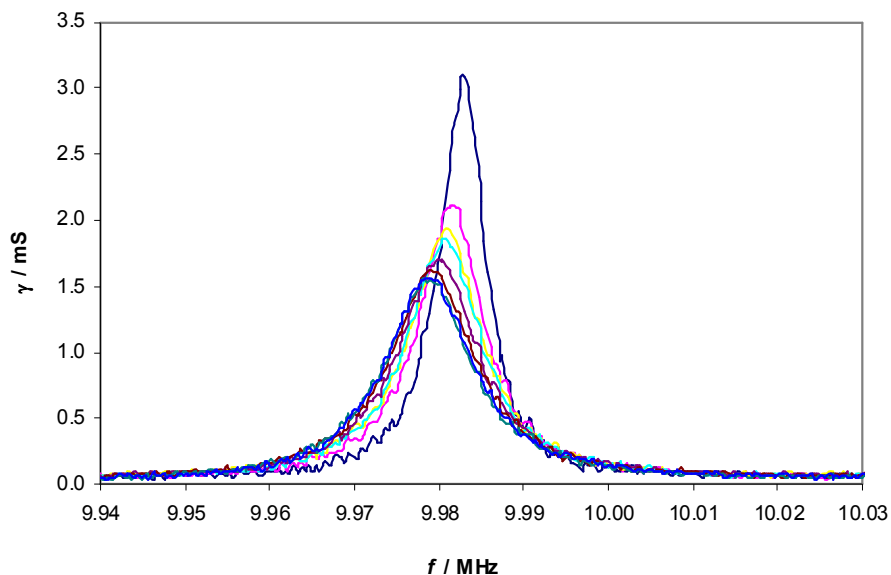


Figure 4.8 QCM responses during the settling process of 500 nm diameter polystyrene latex microspheres. Settling times 0: —; 44: —; 96: —; 168: —; 240: —; 288: —; 360: —; 432: — hours.

4.4.3 Copper nanoporous film

4.4.3.1 Surface roughness of copper deposition

It has been shown that surface roughness of copper films strongly influences the signal of an EQCM³⁶. The smoothness of the copper deposition is dependent on the current density used. This study requires the development of nanoporous copper films on quartz crystals. These films will be used for wetting analysis; it is therefore essential that all surface features other than the required pores be kept to a minimum. In order to find the optimum conditions for a smooth film, various different current densities were used in the deposition of copper onto a polished AT-cut quartz crystal. The mass of the copper film was calculated using the frequency shift of the quartz crystal (equation (2.13)) and the surface roughness of the copper film was investigated using SEM.

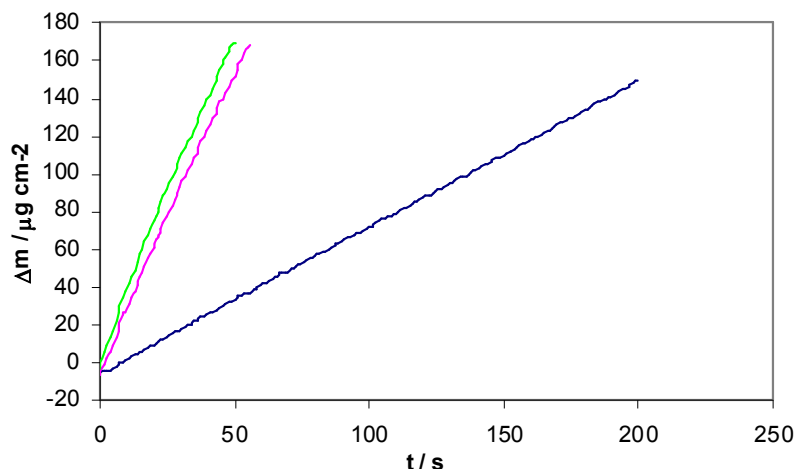


Figure 4.9 QCM data for copper deposition at various current densities. 0.226 mA cm^{-2} : —; 2.26 mA cm^{-2} : —; 4.52 mA cm^{-2} : —.

Figure 4.9 illustrates the mass change during the galvanostatic deposition of copper at different current densities. Figures 4.10 panels a – c show the admittance spectra for the same crystals before and after deposition of copper. The mass of the film was calculated from both EQCM data and the frequency changes recorded with the network analyser.

Table 4.10 shows the mass changes calculated from the data obtained from the EQCM and the network analyser. There is a difference in the calculated mass obtained by the EQCM and that of the network analyser. The cause of the difference is thought to be the contacting media in which the analysis was performed. The results obtained by the network analyser were for the dry film, while the EQCM data are for the film immersed in electrolyte solution.

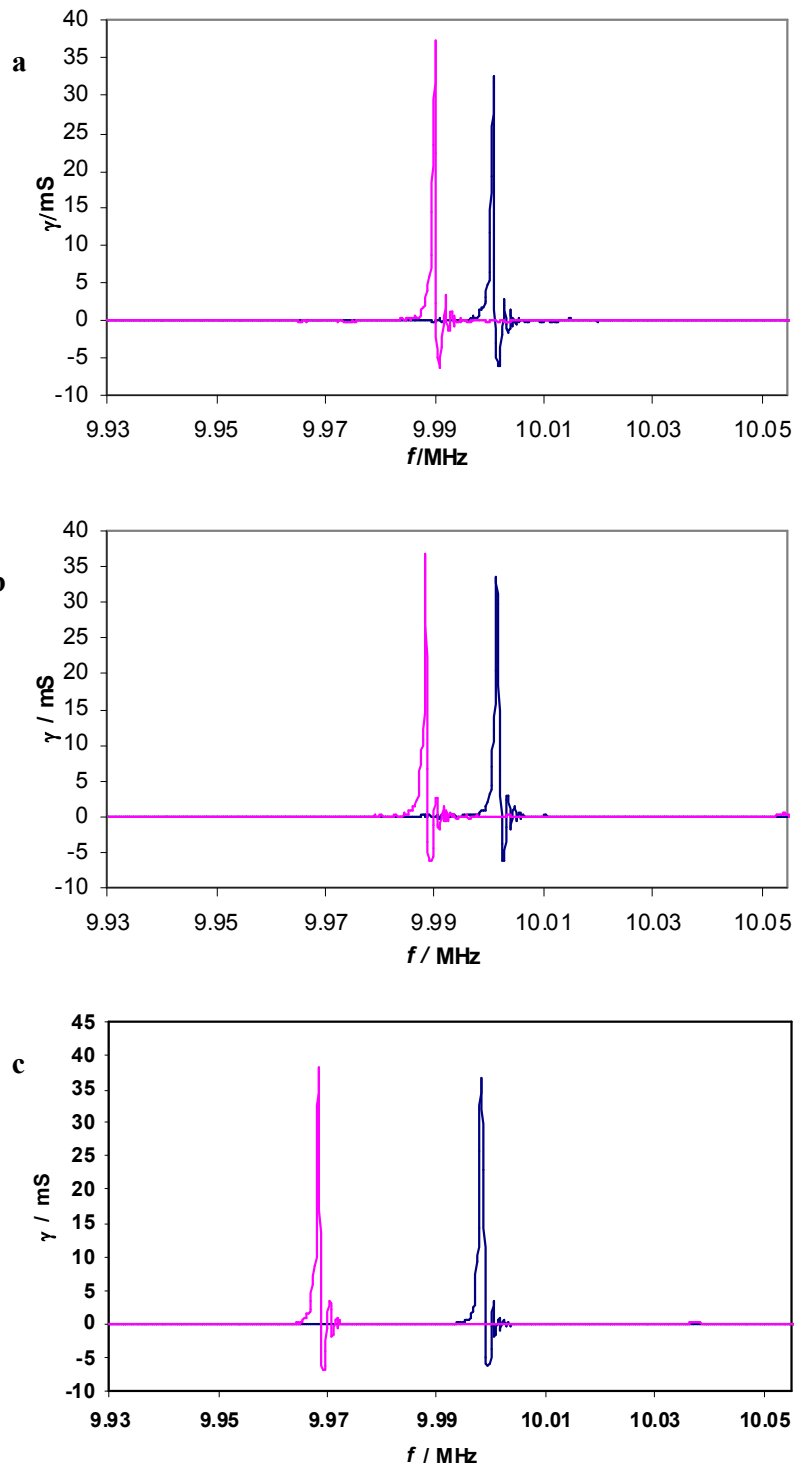


Figure 4.10 Admittance spectra for copper deposition at current densities (a) 0.226 mA cm^{-2} ; (b) 2.26 mA cm^{-2} and (c) 4.52 mA cm^{-2} for 50 s, on polished AT-cut quartz crystal. Blank crystal (in air): —; copper plated crystal (in air): —.

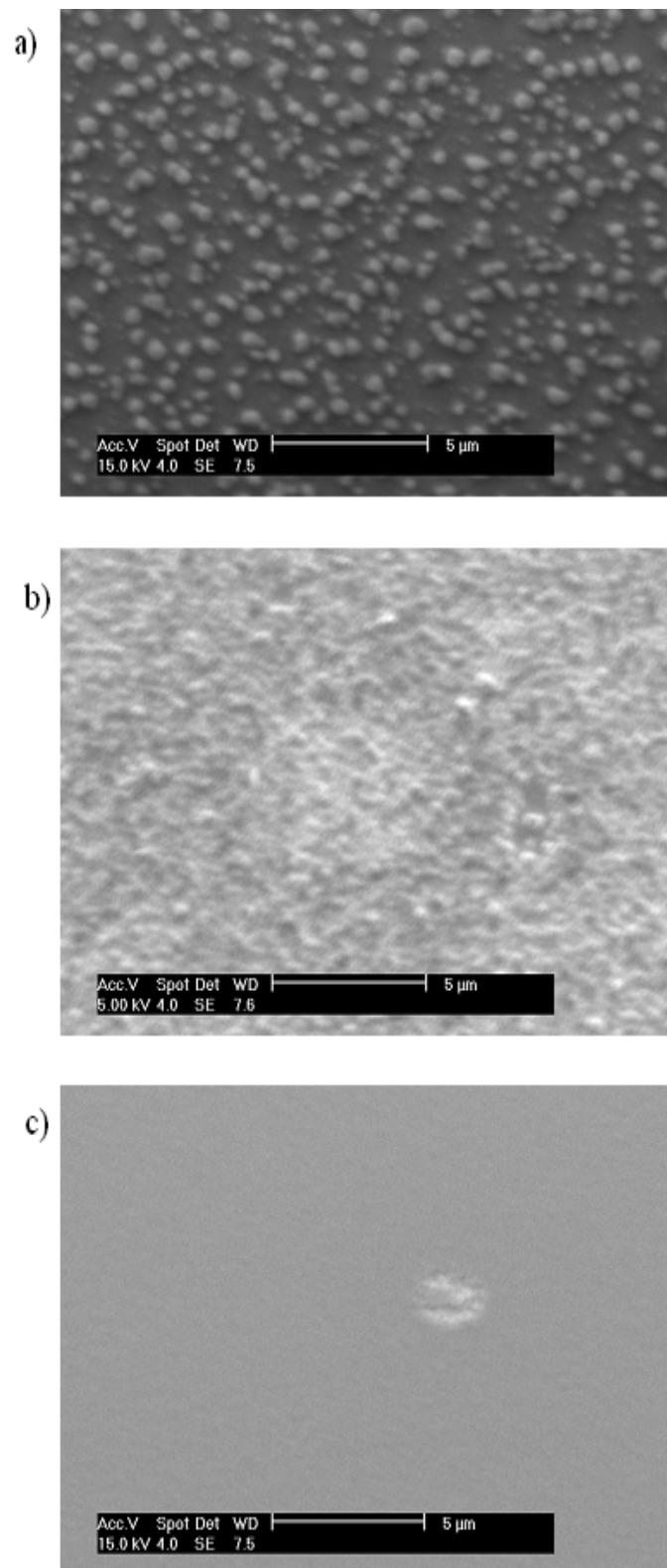


Figure 4.11 SEM images of copper deposits deposited using current densities (a) 0.226 mA cm^{-2} ($Q=10\text{mC}$); (b) 2.26 mA cm^{-2} ($Q=26\text{mC}$); (c) 4.52 mA cm^{-2} ($Q=52\text{mC}$).

Current Density / mA cm ⁻²	Deposition time / s	Mass added / μg cm ⁻²	
		EQCM	Network analyser
0.226	200	149.4	48.68
2.26	50	168.2	57.53
4.52	50	169.2	132

Table 4.1 Total copper added to quartz crystal, calculated from EQCM (measurements take while crystal immersed in electrolyte) and network analyser (measurement take in air) responses. Results limited to the maximum mass measured by EQCM, after the time periods above no more mass addition was recorded by EQCM.

The SEM images show that the surface roughness decreases with increasing current density (figure 4.11). Small deposition currents and long deposition time, give very few but large grains of copper. However, for large currents densities and shorter deposition periods, many grains are formed which, due to competitive growth, do not become large³⁷.

It has already been suggested that rough surfaces will trap fluid within their corrugations; therefore films produced at lower current densities will have undesirable surface features. Fluid trapped within these features will add to the QCM response. The optimum current density for copper deposition on bare Au / polished quartz crystals was experimentally found to be 4.52 mA cm⁻²; this gave the smoothest deposits. Based on the associated observed rate of frequency change, $\delta f/\delta t$, this corresponds to a gravimetric deposition rate of ca. 3 μg cm⁻² s⁻¹.

4.4.3.2 Nanoporous film preparation

Section 4.4.3.1 illustrates that the optimum current density for smooth copper deposition on bare Au / polished quartz crystals is 4.52 mA cm⁻², with a gravimetric deposition rate of 3 μg cm⁻² s⁻¹. For the preparation of nanoporous films the amount of metal required to fill the interstices within a single layer of templating particles, of radius r needs to be estimated. For a close-packed array of spherical particles, the fractional free volume, $\phi = 0.26$. The volume of metal required on an electrode of area

A is $2\phi Ar$. For a metal of density ρ , the associated areal mass density change, $\Delta m/A = 2\phi(\rho-1)r$.

Nanoporous copper films were prepared by deposition of metal within the interstices of the close packed array of spheres to a depth of approximately half the height of the spheres. $\Delta m/A$ was estimated for spheres of 500 and 200 nm diameter to be $57.98 \mu\text{g cm}^{-2}$ and $23.19 \mu\text{g cm}^{-2}$ respectively. At the optimum current density as outlined in section 4.3.1 ($4.52 \mu\text{A cm}^{-2}$) the estimated times to plate to half the sphere diameters are 16.9 s and 6.8 s. The deposition of copper through polystyrene latex microsphere template required 55 s and 30 s for 500 nm and 200 nm diameter spheres respectively. This shows that experimentally the deposition of copper through the template is less efficient than for the bare Au surface. Although there is no evidence, this inefficiency may be caused by either partial wetting, deposition of loose (mechanically detachable or gravimetrically undetected) copper on the external surface or ohmic loss. The dissolution of the template using toluene leaves the nanoporous copper film with pore diameters that corresponds to the sphere size.

As described in section 2.3.4, small, rigid, uniformly deposited masses on a quartz crystal resonator surface may be treated as an extension of the quartz crystal itself. The decrease in resonant frequency of the quartz crystal (Δf) is proportional to the mass change (Δm) as indicated by the Sauerbrey equation (2.13). Typical experimental frequency changes are shown in figure 4.12.

The results obtained for the copper film produce through the 500 nm template are shown in figure 4.12 (a). The frequency change Δf is ca. -14.5 kHz . Using equation (2.8) gives the areal mass density deposited onto the crystal as $61 \mu\text{g cm}^{-2}$. This corresponds to a layer of copper ca. 275 nm thick, which is comparable to the template radius of 250 nm.

The AFM images (figure 4.13) illustrate that the deposited film has pores that correspond to the diameter of the spheres used in the template. The majority of the surface of the quartz crystal appears to be covered in pores. However they are not uniform across the surface and there are some areas that have large voids.

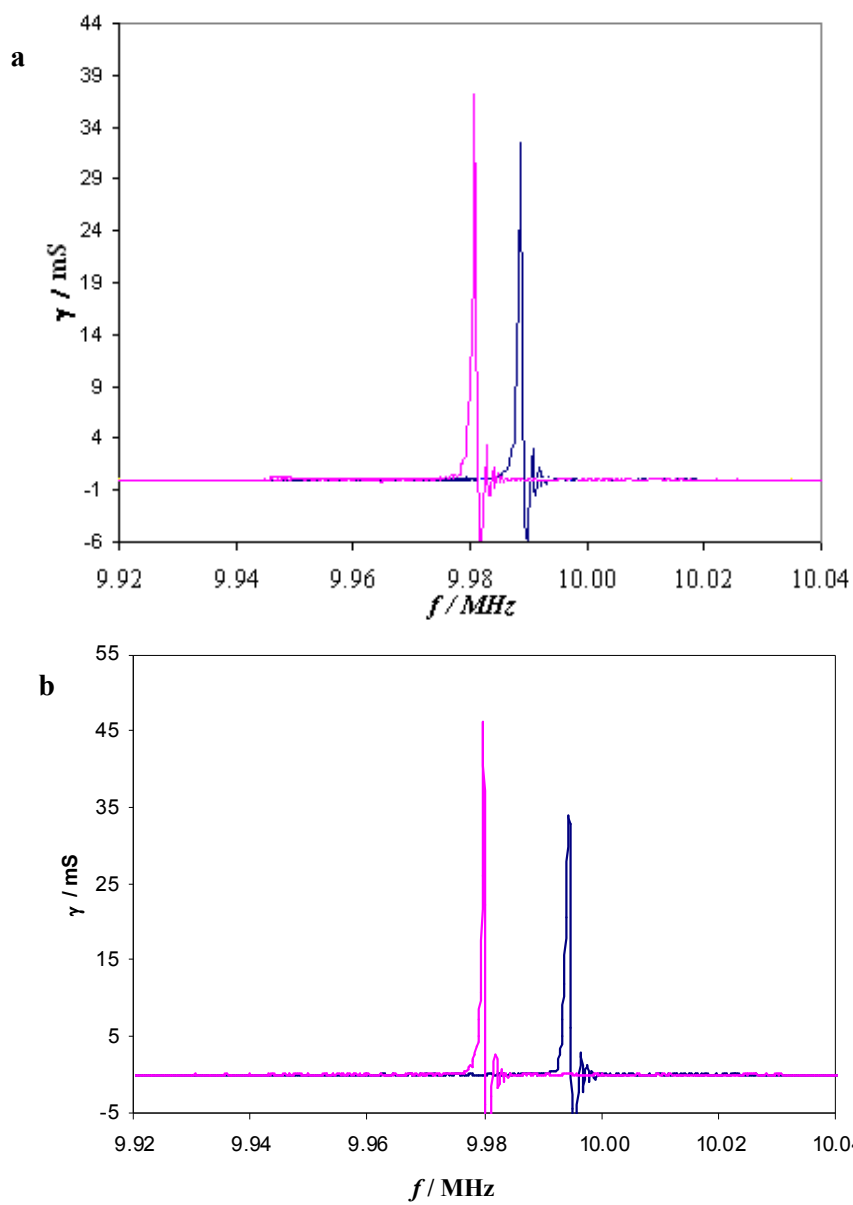


Figure 4.12 QCM admittance spectra for Cu electrochemically deposited through two different templates, (a) 500 nm template, deposition time 55 s and (b) 200 nm template, deposition time 30 s. Blank crystal (in air): —; copper plated crystal (in air): —

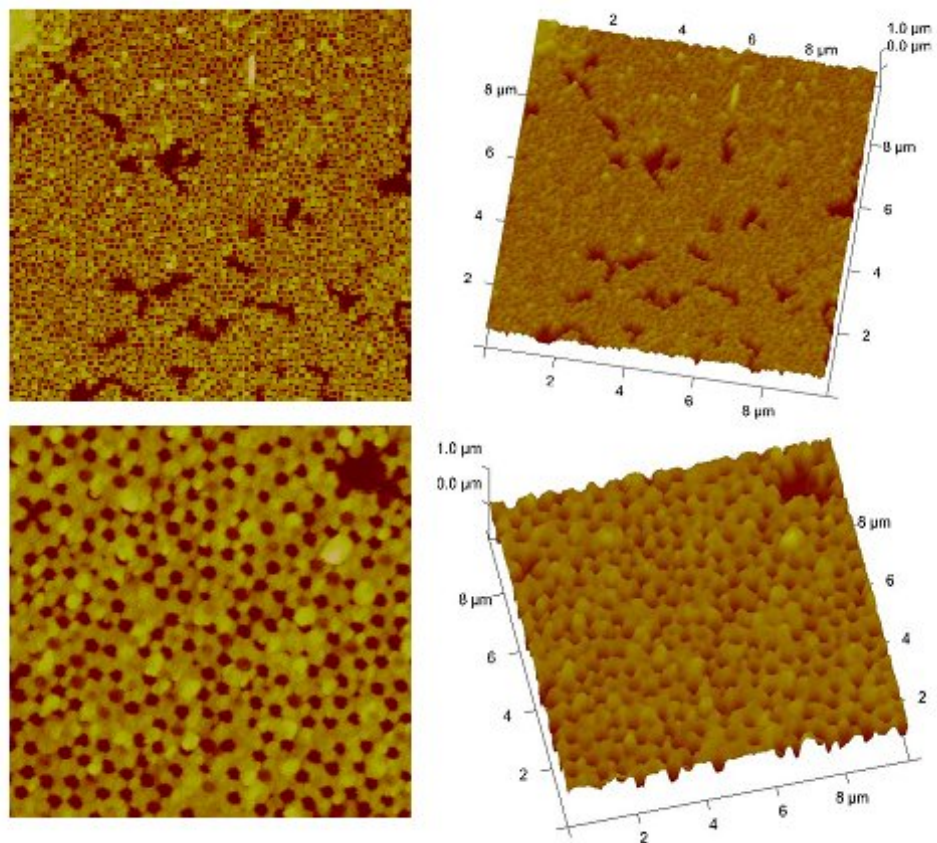


Figure 4.13 AFM images nanoporous copper film deposited through 500 nm template.

The results obtained for the copper film with 200 nm pores (figure 4.15 b), gave a frequency change Δf is ≈ -8 kHz. This corresponds to an areal mass density deposited onto the crystal of $35 \mu\text{g cm}^{-2}$ and a film thickness of ≈ 150 nm. The SEM images (figure 4.17) illustrate that the deposited film has pores that correspond to the diameter of the spheres used in the template. The majority of the surface of the quartz crystal is covered in pores that appear to be arranged in a hexagonal closed packed array that corresponds to the original template.

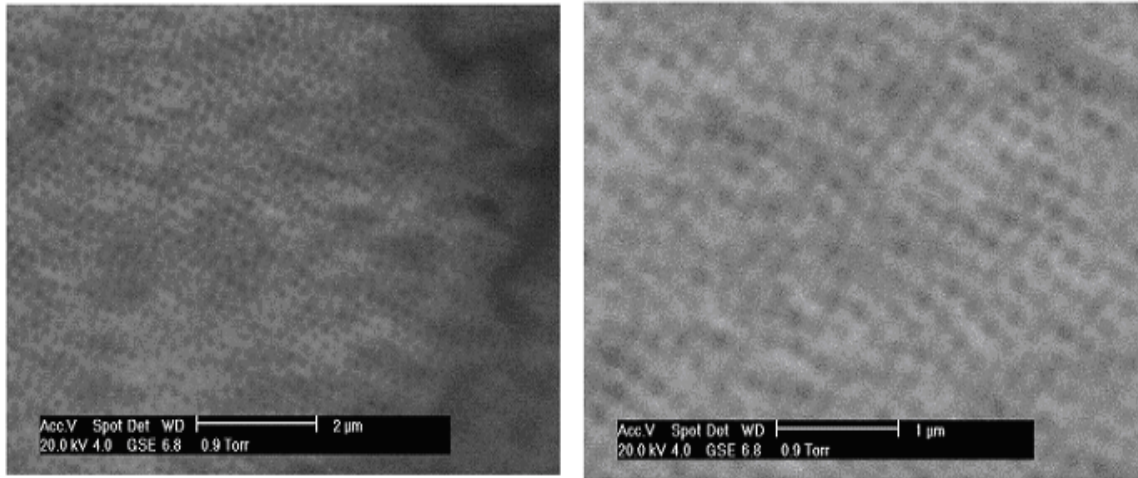


Figure 4.14 SEM images of a nanoporous copper film deposited through 200 nm template at different resolutions.

4.4.3.3 Confirmation of pore size using fluid entrainment

As described in section 4.4.1.2, fluid properties may be used to investigate surface features. The relationship in equation (2.21) provides a means for extracting the surface feature size (h), by fitting the frequency response ($\Delta f/\rho$) for a series of different fluid properties ($(\eta/\rho)^{1/2}$). Therefore a plot of ($\Delta f/\rho$) against $(\eta/\rho)^{1/2}$ should yield a straight line with a gradient of $f_s^{3/2}/n(\rho_q\mu_q\pi)^{1/2}$ and an intercept of $f_s^2\pi h/n(\rho_q\mu_q)^{1/2}$.

Figure 4.15 illustrates the frequency change recorded for a range of glycerol / water solutions. For a copper film prepared through a polystyrene template with sphere size of 500 nm, the expected pore size would have a radius of 500 nm and a depth of around 250 nm. The depth of these pores may be extracted using the frequency response for a series of different fluid properties.

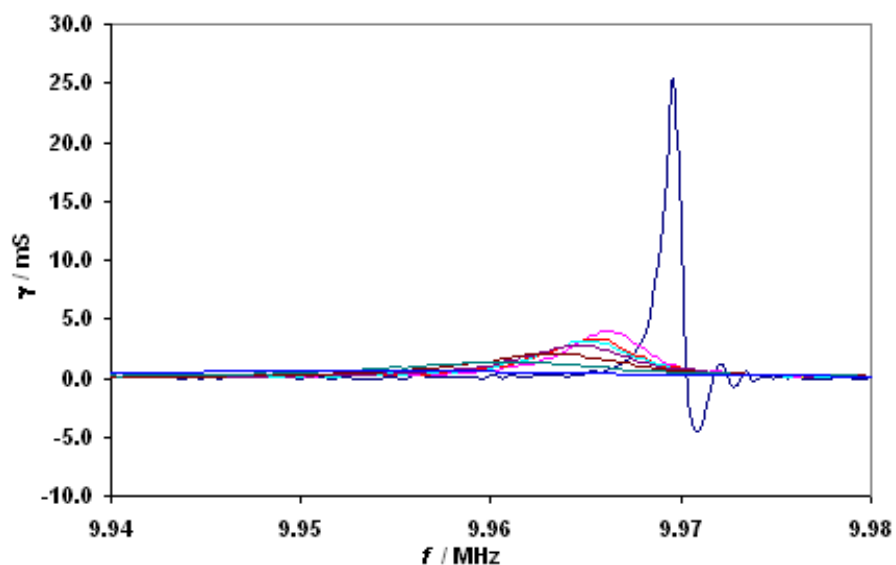


Figure 4.15 QCM admittance spectra for different concentrations of glycerol for a quartz crystal containing a nanoporous copper film (copper deposited galvanostatically using a current density of 4.52 mA cm^{-2} for 55 s) with pore sizes of ca. 500 nm blank crystal (nanoporous film in air): —; 0%: —; 5%: —; 10%: —; 20%: —; 40%: —; 60%: —; 80%: — glycerol.

Using the information gained in figure 4.16 and equation (4.3) the depth of the pores within the copper film was calculated to be 80 nm. The expected depth, which should be half the sphere diameter used in the template, was 250 nm. Some surface features being smaller than others may cause the difference in the two results. The deposition of copper through a template left a nanoporous film of around 275 nm thick (calculated from the admittance data). The film was not uniformly deposited with some areas being thicker than others. As the thickness of the film changes, so will the pore sizes within the film. The areas where the nanoporous film is thicker than 250 nm will have pores with openings smaller than the expected diameter (250 nm). The smaller pore openings may stop the viscous fluids entering the pores, giving a frequency response of a smoother surface. The result of 80 nm is therefore average depth of surface features.

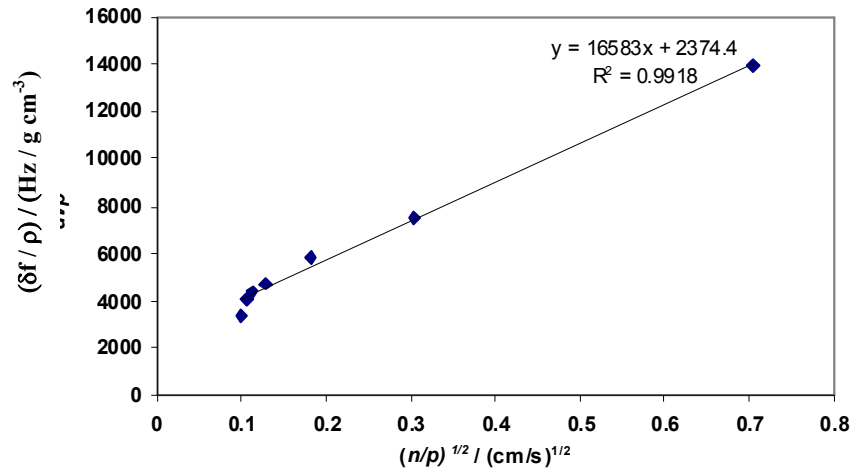


Figure 4.16 Frequency response for a quartz crystal, containing a nanoporous copper film with pore sizes of ca. 500 nm, for a series of different concentrations of water/glycerol solutions (0 – 80%)

4.4.3.4 The Effect of Surface Roughness on Wetting

The results presented in this section are for the nanoporous film made by galvanostatically depositing copper through a 500 nm polystyrene latex microsphere template only.

The interaction of quartz crystal resonators with liquid media has been discussed in detail in section 2.3.6 and 2.7.5. As previously described for textured (“rough”) surfaces, there is a component of the liquid response arising from fluid trapped in the surface features. The motion of the fluid trapped within the surface features is constrained; as a result of this constraint, the fluid behaves as a rigidly coupled mass. A more complex situation arises when the surface features are only partially filled (wetted) by the fluid, due to the competition between forces associated with the compression of trapped gas and surface tension. Here, we have deliberately started with a surface that is smooth and created one that is textured in a controlled manner to allow evaluation of the wetting phenomena.

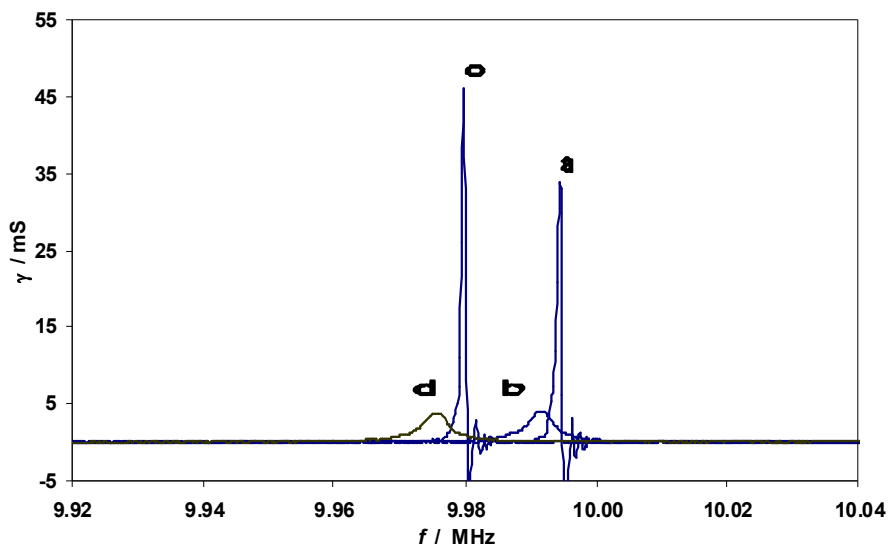


Figure 4.17 QCM admittance spectra at different stages during template deposition procedure. Cu electrochemically deposited for 55 s through 500 nm diameter polystyrene latex sphere template. (a) bare Au in air; (b) bare Au immersed in water; (c) Au/Cu (thickness equal to sphere radius ca. 250 nm) in air; and (d) Au/Cu (as in (c)) immersed in water.

Figure 4.17 shows the full frequency responses for bare (polished) quartz crystal and nanoporous film in both air and liquid media. Table 4.2 compares these responses in which vertical comparisons relate to a change in medium (air vs. water) and horizontal comparisons relate to the deposition of copper. The frequency shift (air – liquid) for the blank crystal was of 2.500 kHz, while the templated copper film showed a frequency shift of 4.250 kHz. The former is very close to what one would expect for viscous entrainment of fluid at a smooth surface. The increase in frequency difference for the templated film, 1.750 kHz, is associated with trapped fluid within the newly created nanoporous surface.

The extent of fluid filling in the surface features can be calculated analogously to the amount of copper deposited. If the deposited copper occupies a fraction ϕ of the film then the fluid can occupy a fraction from zero to $(1-\phi)$ of the film. The frequency change for complete fluid filling is given by:

$$\Delta f^{\text{wet}} = -k (0.74A\phi) \quad (4.2)$$

where ρ_1 is the fluid density and the other symbols have their previous significance. For $r = 250$ nm (500 nm template), $\Delta f^{\text{wet}} = -4.273$ kHz. The experimental frequency shift was 1.750 kHz, this compared with the calculated frequency shift for completely wet surface gives an estimate of fluid penetration to be around 41%.

Polished quartz/Au surface			
Medium	f(Au) / MHz	f(Au/Cu) / MHz	$\Delta f(\text{Cu})$ / kHz
Air	9.994,250	9.979,750	14.500
Water	9.971750	9.975,500	16.250
$\Delta f(w)$ /kHz	2.500	4.250	

Table 4.2. Frequency shifts for rough and polished AT-cut crystals coated with Au and Au/Cu (deposited through 500nm polystyrene template) and exposed to air and to water.

The contact angle values for water on copper surfaces have been reported to be between $96^\circ - 115^\circ$ ^{38, 39}. The theoretical calculations carried out by Theisen et al²⁸ suggest that between the angles of $90^\circ - 120^\circ$ the surface is in the transition of being fully wet to completely de-wet. The sharpness of the transition depends on surface feature size. The contact angle value and QCM observations place the results obtained here within this region.

4.4.4 Platinum Nanoporous Films

Platinum was electrochemically deposited onto a polished gold substrate that did not contain a template, using a potential of 0.1 V vs. SCE and a plating bath of 25 mmol dm^{-3} H_2PtCl_6 / 25 mmol dm^{-3} KCl. The total amount of charge passed during the deposition was -0.21 C cm^{-2} (figure 4.18 a) and the total mass added to the electrode surface (calculated by the EQCM data figure 4.18 b) was $75 \mu\text{g cm}^{-2}$. The current efficiency here is 70%.

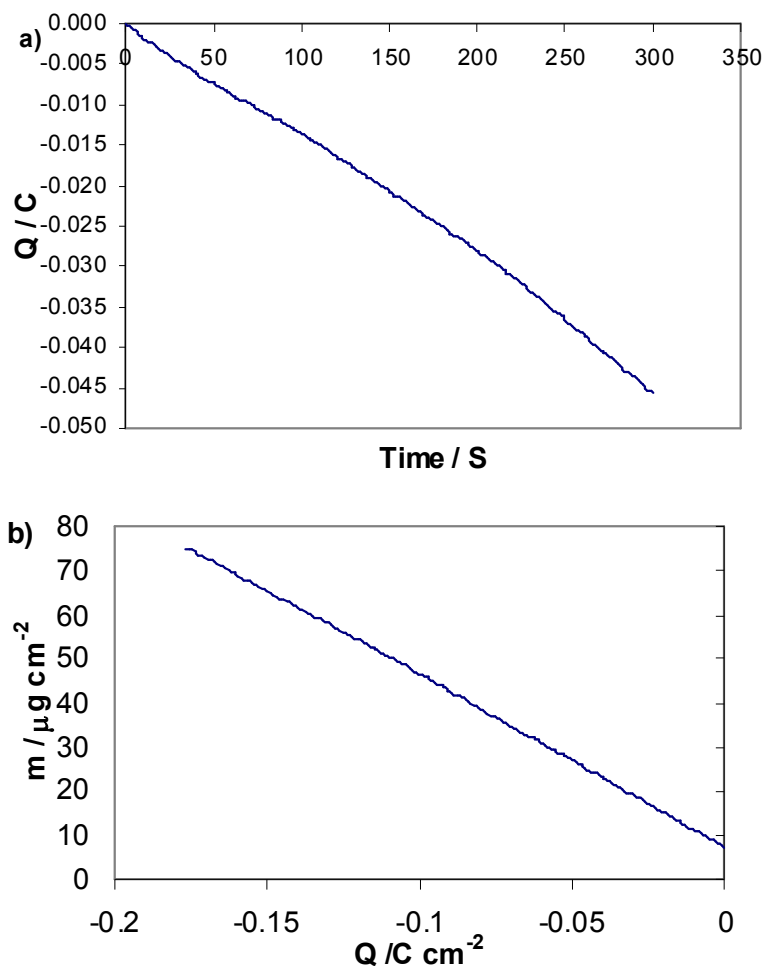


Figure 4.18. EQCM experimental data a) charge versus time; b) Δm versus current density; for the deposition of platinum onto polished Au substrate (no template), using a fixed potential of 0.1 V vs. SCE using a plating bath of 25 mmol dm⁻³ H₂PtCl₆ / 25 mmol dm⁻³ KCl.

On the template-covered electrodes, illustrated in Figure 4.6, the situation was somewhat different. We first estimate the amount of metal required to fill the interstices within a single layer of templating particles, of radius r . For a close-packed array of spherical particles, the fractional free volume, $\phi = 0.26$. The volume of metal required to fill the spaces within the template, to half the sphere diameter, for an electrode of area A is $2\phi Ar$. For a metal of density ρ , the associated areal mass density change, $\Delta m/A = 2\phi(\rho-1)r$ if the particle raft is fully wetted and $2\phi\rho r$ if the particle raft is completely de-wetted. In general for most metals $\rho \gg 1$ (for platinum, $\rho = 21.45 \text{ g cm}^{-3}$) so this distinction will make relatively little practical difference.

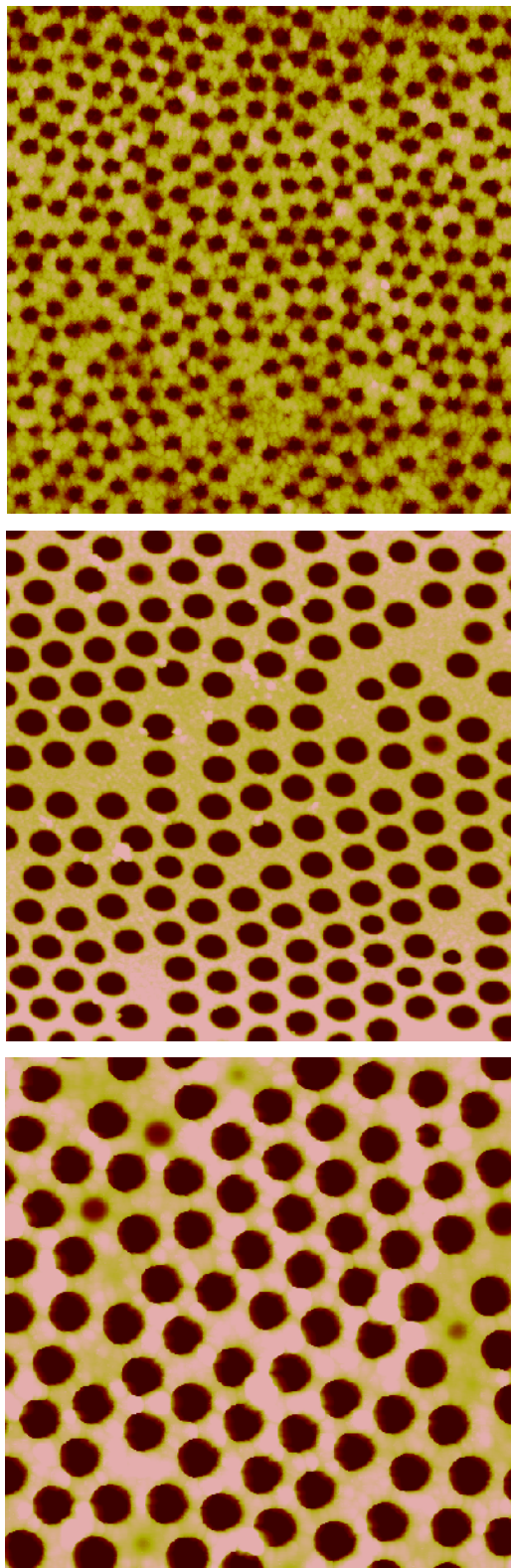


Figure 4.19 AFM images (all $10\ \mu\text{m} \times 10\ \mu\text{m}$ scan size) of nanoporous platinum films, obtained by electrochemical deposition through polystyrene templates. (a) 500 nm; (b) 750 nm; (c) 1000 nm spheres.

Nanoporous metallic films were prepared by deposition of metal within the interstices of the close packed array of spheres. Deposition to approximately half the height of the sphere allowed the production of a film with pore sizes that correspond to the original diameter of the spheres within the template. It therefore follows that the calculated charge required to deposit to half the sphere height would be 0.338, 0.514 and 0.691 C cm⁻² for templates prepared from 0.5, 0.75 and 1.0 μm sphere diameters. The experimental deposition charge was 0.714, 0.755 and 1.238 C cm⁻² for 0.5, 0.75 and 1.0 μm templates respectively. Clearly, deposition efficiency is rather less in the templating case. Although we have no direct evidence for the cause(s) of this, possible reasons might be partial wetting, deposition of loose (mechanically detachable or gravimetrically undetected) platinum on the external surface or ohmic losses.

The polystyrene template was removed by dissolution in toluene over a 24-hour period. The removal of the template leaves a well order nanoporous metallic film as illustrated in figure 4.19.

Deposition of small rigid masses onto the quartz crystal shows a decrease in the resonant frequency of the crystal ²³, which is proportional to the mass added according to the Sauerbrey equation (2.13). According to the Sauerbrey equation, when small amounts of platinum are deposited onto the surface of a quartz crystal microbalance a decrease in resonant frequency should be recorded (figure 2.20). This frequency shift is proportional to the mass added to the surface.

Electrochemical deposition of platinum onto templated crystals, followed by the subsequent removal of the templates leads to a decrease in the resonant frequency as listed in table 4.3. Using equation (2.13) the mass of the deposited layer can be calculated, which in turn leads to the thickness of the platinum film. The average pore diameter recorded using the AFM was 0.41, 0.62 and 0.8 μm for films produced using 0.5, 0.75 and 1.0 μm sphere diameter, respectively.

Template sphere diameter / μm	Frequency shift / kHz	Mass added / $\mu\text{g cm}^{-2}$	Thickness obtained (calculated from Δf) / μm
0.5	37	164	0.3
0.75	48	210	0.37
1.0	91	403	0.7

Table 4.3. Frequency shifts and corresponding mass changes observed from the production of nanoporous films

Figure 4.20 illustrates the frequency changes of a blank polished (Au) quartz crystal in air and water as well as the same measurements for the crystals after the deposition of nanoporous films. The frequency results obtained from these measurements are recorded in table 4.4 where vertical comparisons relate to a change in medium (air vs. water) and horizontal comparisons relate to the deposition of platinum. For the smooth substrate (no nanoporous film), the frequency shift (air – liquid) was around 3.0 kHz this is very close to what one would expect for viscous entrainment of fluid at a smooth surface. There is an increase in the frequency difference for the platinum films (air – liquid), this is associated with trapped fluid within the newly created nanoporous surfaces.

The extent of fluid filling in the surface features can be calculated analogously to the amount of platinum deposited: the platinum occupies a fraction ϕ of the film and the fluid can occupy a fraction from zero to $(1-\phi)$ of the film. Using equation (4.2) we can calculate the frequency change associated with complete fluid filling of the pores.

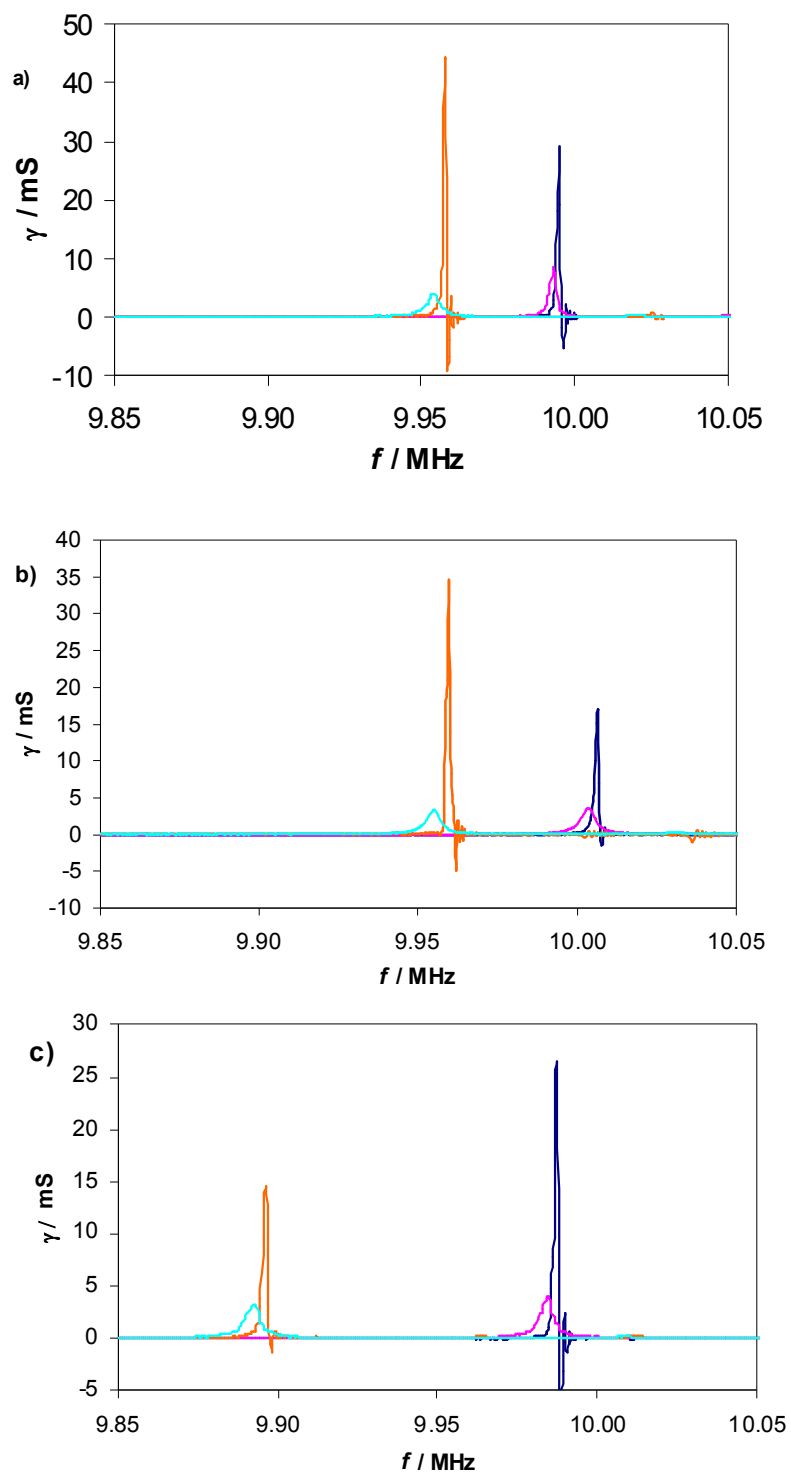


Figure 4.20 QCM admittance spectra at different stages during wetting analysis, Au in air: —; Au in water: —; Au/Pt film in air: —; Au/Pt film in water: —. Platinum films deposition through (a) 0.5 μm (b) 0.75 μm and c) 1.0 μm sphere diameter templates.

Pore size		f^{Au} / (MHz)	$F^{\text{Au/Pt}}$ / (MHz)	Δf^{Pt} / (KHz)
0.5 μm	f^{air} / (MHz)	9.99475	9.957625	37.125
	f^{water} / (MHz)	9.99225	9.953250	39.00
	Δf^{water} / (KHz)	-2.500	-4.375	(-1.875)
0.75 μm	f^{air} / (MHz)	10.006375	9.959500	47.625
	f^{water} / (MHz)	10.003375	9.955000	48.375
	Δf^{water} / (KHz)	-3.000	-4.500	(-1.500)
1.0 μm	f^{air} / (MHz)	9.987625	9.896500	91.125
	f^{water} / (MHz)	9.984625	9.892375	92.250
	Δf^{water} / (KHz)	-3.000	-4.125	(-1.125)

Table 4.4. Frequency shifts for polished AT-cut crystals coated with Au and Au/Pt (deposited through polystyrene templates) and exposed to air and to water

For the platinum films obtained here, the calculations suggest that for complete filling of the pores for the given film thickness (outlined in table 4.3) the observed frequency shift would be $\Delta f^{\text{water}} = -5.006$ kHz, -6.174 kHz, -11.682 for, $h = 0.7$ μm , 0.37 μm and 0.3 μm respectively. The experimental frequency shifts for wetting of both the plain crystal (Au) and the platinum nanoporous film (Au/Pt) is given in table 4.4 Comparison with the experimental frequency shift and mass change, (table 4.3) the fluid penetration was 37%, 24% and 10%. It is worth noting that the “%” figures are relative, while the “ Δf ” figures are absolute, i.e. 10% filling between the large particles is actually more liquid than 37% between the smaller particles. Table 4.5 compares the experimental results with the calculated results for wetting at nanoporous films.

Contact angle values for water on platinum surfaces have been reported to be between $40^\circ - 80^\circ$ ⁴⁰. Theoretical calculations²⁸ suggest that the transition between full wetting and de-wetting takes place in the range $80^\circ - 120^\circ$, the sharpness of the transition depending on surface feature size. Both the contact angle value and our QCM observations for experimental place us within this region.

Pore diameter / μm	Film thickness / μm (calculated from Δf)	Complete filling Calculated mass / μg	Frequency change / kHz	Experimental mass change / μg	% filling
0.35	0.3	4.653	1.875	1.743	37
0.65	0.37	5.738	1.500	1.934	24
0.80	0.7	10.856	1.125	1.046	10

Table 4.5 level of fluid penetration for different nanoporous films

4.5 Conclusions

Wetting is an important phenomenon in a number of electrochemical devices. Only the part of the interface that is wet by the solution may take part in the required (electro) chemical processes. It is well documented that de-wetting occurs at rough surfaces. During this study thin nanoporous films were used to investigate wetting of surface features.

During this study two types of electrodes were investigated, Au deposited on an unpolished or polished AT-cut quartz crystal. The surface features of each substrate were investigated using atomic force microscopy (AFM), scanning electron microscopy and viscosity measurements using the quartz crystal microbalance. The surface feature size for the rough (unpolished) AT-cut quartz crystal was found to be around 200 nm using both SEM and AFM. Neither SEM or AFM could give a clear indication of the surface features on the polished crystal, due to the limitations of the resolution caused by the polished surface. Analysis of the surfaces using QCM response for a variety of glycerol/water concentrations lead to calculations that outlined the surface features to be 140 nm and 20 nm for unpolished and polished quartz crystals respectively. Analysis of surface features confirmed that the unpolished crystal had surface feature that were too large for the templates to be prepared on.

It has been shown that sedimentation of (2 - 5 days for 1000 nm, 4 - 8 days for 750 nm, 7 - 10 days for 500 nm and 10 – 21 days for 200 nm sphere diameter templates) polystyrene latex microspheres leads to hexagonal close packed templates. There is a slight variation in the settling period which is, although not proved, believed to be caused by changes in the temperature and humidity during the preparation period. SEM and AFM images confirmed the structure and ordering of the templates.

This study has clearly shown that it is possible to produce nanoporous copper films by simple galvanostatic deposition through a polystyrene latex microsphere template. SEM and AFM are excellent technique for confirmation of the structure for both the template and copper film. Analysis of fluid penetration shows that only partial wetting occurs, when surface features are around 500 nm.

The optimum current density for the deposition of copper was found to be $4.52 \mu\text{A cm}^{-2}$. The production of a thin copper nanoporous film with a thickness that corresponds to half the sphere diameter of the template, requires a deposition time of (at the optimum current density) 55 s and 30 s for 500 nm and 200 nm diameter spheres, respectively. The dissolution of the template using toluene leaves the nanoporous copper film. SEM and AFM confirm deposition of copper within the interstices of the template. Subsequent dissolution of the template leaves a copper film that mirrors the morphology of the polystyrene arrays.

Copper films were then used to investigate the wetting of the nanoporous surface. For the most highly ordered deposits the frequency shifts for films in air and in water indicate partial (ca. 41%) fluid filling of the spherical voids left by the dissolved polystyrene templates. The theoretical calculations carried out by Theisen et al²⁸ suggest that between the angles of 90° - 120° the surface is in the transition of being fully wet to completely de-wet. The sharpness of the transition depends on surface feature size. The contact angle (water on copper surfaces are between 96° - 115° ^{38, 39}) value and QCM observations place the results obtained here within this region.

Platinum nanoporous films were prepared through polystyrene latex sphere templates; separate experiments used spheres with 500 nm, 750 nm and 1000nm diameters. The deposition of the platinum gave a smoother film than those acquired using copper.

Wetting of the resulting films illustrated that the smaller the pore size the more percentage filling occurred, as suggested by Theisen and Hillman²⁸.

Although this study shows that the preparation of both platinum and copper nanoporous films by deposition through a polystyrene latex microsphere template is possible, the results are not complete. It is clear from the result that both the template and film preparations requires a more detailed study to obtain the optimum conditions. Further investigation on settling time and solvent evaporation time should include more information on both temperature and humidity within the cell. It is believed that the large range of settling period may be a result of a constant change in both humidity and temperature. It was also outlined in section 4.4.2.1 that monitoring the admittance during the settling process may lead to information on the shear modulus, future studies should investigate the possibility of gaining this valuable information.

References

- (1) Hazlett, R. D. *J. Coll. Interface Sci.* **1990**, *137*, 527-533.
- (2) Voue, M.; De Coninck, J. *Acta Materialia* **2000**, *48*, 4405-4417.
- (3) Oner, D.; McCarthy, T. J. *Langmuir* **2000**, *16*, 7777-7782.
- (4) Semal, S.; Blake, T. D.; Geskin, V.; de Ruijter, M. J.; Castelein, G.; De Coninck, J. *Langmuir* **1999**, *15*, 8765-8770.
- (5) Chen, W.; Fadeev, A. Y.; Hsieh, M. C.; Oner, D.; Youngblood, J.; McCarthy, T. J. *Langmuir* **1999**, *15*, 3395-3399.
- (6) de Ruijter, M. J.; De Coninck, J.; Blake, T. D.; Clarke, A.; Rankin, A. *Langmuir* **1997**, *13*, 7293-7298.
- (7) Callies, M.; Chen, Y.; Marty, F.; Pepin, A.; Quere, D. *Microelect. Eng.* **2005**, *78-79*, 100-105.
- (8) Callies, M.; Quere, D. *Soft Matter* **2005**, *1*, 55-61.
- (9) Yoshimitsu, Z.; Nakajima, A.; Watanabe, T.; Hashimoto, K. *Langmuir* **2002**, *18*, 5818-5822.
- (10) Velev, O. D.; Kaler, E. W. *Langmuir* **1999**, *15*, 3693-3698.
- (11) Haginoya, C.; Koike, K.; Hirayama, Y.; Yamamoto, J.; Ishibashi, M.; Kitakami, O.; Shimada, Y. *App. Phys. Lett.* **1999**, *75*, 3159-3161.
- (12) Haginoya, C.; Ishibashi, M.; Koike, K. *App. Phys. Lett.* **1997**, *71*, 2934-2936.
- (13) Gau, H.; Herminghaus, S.; Lenz, P.; Lipowsky, R. *Science* **1999**, *283*, 46-49.
- (14) Painter, O.; Lee, R. K.; Scherer, A.; Yariv, A.; O'Brien, J. D.; Dapkus, P. D.; Kim, I. *Science* **1999**, *284*, 1819-1821.
- (15) Velev, O. D.; Jede, T. A.; Lobo, R. F.; Lenhoff, A. M. *Nature* **1997**, *389*, 447-448.
- (16) Li, J. R.; Henry, G. C.; Garno, J. C. *Analyst* **2006**, *131*, 244-250.
- (17) Cong, H. L.; Cao, W. X. *Journal Of Colloid And Interface Science* **2004**, *278*, 423-427.
- (18) Yamauchi, Y.; Yokoshima, T.; Mukaibo, H.; Tezuka, M.; Shigeno, T.; Momma, T.; Osaka, T.; Kuroda, K. *Chemistry Letters* **2004**, *33*, 542-543.
- (19) Jiang, P.; Cizeron, J.; Bertone, J. F.; Colvin, V. L. *J. Am. Chem. Soc.* **1999**, *121*, 7957-7958.
- (20) Yan, H. W.; Blanford, C. F.; Holland, B. T.; Parent, M.; Smyrl, W. H.; Stein, A. *Adv. Mater.* **1999**, *11*, 1003-1006.
- (21) Bartlett, M. A.; Yan, M. D. *Adv. Mater.* **2001**, *13*, 1449-+.
- (22) Bartlett, P. N.; Birkin, P. R.; Ghanem, M. A. *Chem. Comm.* **2000**, 1671-1672.
- (23) Sauerbrey, G. *Z. Phys.* **1959**, *155*, 206.
- (24) Bruckenstein, S.; Shay, M. *Electrochim. Acta* **1985**, *30*, 1295-1300.
- (25) Kanazawa, K. K.; Gordon, J. G. *Anal. Chim. Acta* **1985**, *175*, 99-105.
- (26) Kanazawa, K. K.; Gordon, J. G. *Anal. Chem.* **1985**, *57*, 1770-1771.
- (27) Stockel, W.; Schumacher, R. *Ber. Bunsenges. Phys. Chem.* **1987**, *91*, 345.
- (28) Theisen, L. A.; Martin, S. J.; Hillman, A. R. *Anal. Chem.* **2004**, *76*, 796-804.
- (29) Bartlett, P. N.; Dunford, T.; Ghanem, M. A. *J. Mater. Chem.* **2002**, *12*, 3130-3135.
- (30) Bartlett, P. N.; Ghanem, M. A.; El Hallag, I. S.; de Groot, P.; Zhukov, A. *J. Mater. Chem.* **2003**, *13*, 2596-2602.
- (31) Bartlett, P. N.; Marwan, J. *Phys. Chem. Chem. Phys.* **2004**, *6*, 2895-2898.
- (32) Bartlett, P. N.; Baumberg, J. J.; Coyle, S.; Abdelsalam, M. E. *Faraday Discussions* **2004**, *125*, 117-132.

- (33) Zhukov, A. A.; Ghanem, M. A.; Goncharov, A.; de Groot, P. A. J.; El-Hallag, I. S.; Bartlett, P. N.; Boardman, R.; Fangohr, H. *J. Magn. Magn. Mater.* **2004**, 272-76, 1621-1622.
- (34) Abdelsalam, M. E.; Bartlett, P. N.; Baumberg, J. J.; Coyle, S. *Adv. Mater.* **2004**, 16, 90-+.
- (35) Lagier, C. M.; Efimov, O.; Hillman, A. R. *Anal. Chem.* **2005**, 77, 335-343.
- (36) Bund, A.; Schneider, O.; Dehnke, V. *Phys. Chem. Chem. Phys.* **2002**, 4, 3552-3554.
- (37) Plieth, W. J. *Journal Of Physical Chemistry* **1982**, 86, 3166-3170.
- (38) Shirtcliffe, N. J.; McHale, G.; Newton, M. I.; Perry, C. C. *Langmuir* **2005**, 21, 937 - 943.
- (39) Tonosaki, M.; Kato, E.; Yajima, M.; Takei, Y. *Vacuum* **2004**, 74, 693 - 698.
- (40) Adamson, A. W. *Physical Chemistry of Surfaces*; Wiley, 1990.

CHAPTER 5

P-DOPING OF PEDOT

5.1 Introduction

A carbon atom has 6 electrons, two are held close to the nucleus in the 1s orbital and 4 valence electrons are in the 2s and 2p orbitals. Four electrons fill the 1s and 2s orbitals and the 2p orbitals contain the remaining two. In theory this means that carbon has only 2 available electrons for bonding. However, the energy gap between 2s and 2p orbitals is small, thus only taking a small amount of energy to promote an electron from the 2s orbital to a 2 p orbital, leading to 4 electrons available for bonding. When bonds are formed energy is released and the system becomes more stable, so promoting the 2 electrons gives carbon more stability. The process of promoting and organising these electrons is known as “hybridisation”. In order to lower the total energy carbon can form two primary hybrid structures, sp^3 (for which the s and all 3 of the p orbitals take part) and sp^2 (for which only 2 p orbitals take part) hybridised forms as in diamond and graphite respectively.

Polymers such as polyethylene (used in electrical wire insulation) have all of the valence electrons bound in the sp^3 hybridised orbitals, giving no free electrons, making them excellent insulators. Conjugated, conducting polymers (such as polythiophene) are formed from sp^2 hybridized carbons. This gives them a backbone created from the, in plane, σ orbitals of the sp^2 carbons (two of them bonded to neighbouring carbons and the third to a hydrogen atom). The fourth electron is in the pz orbital, it is this electron and its ability to form π bonds that enable these polymers to conduct.

Conjugated polymers are insulating until either oxidised or reduced, since there is a filled valence band and an empty conduction band. Oxidation or reduction of the polymer causes a dramatic increase in the conductivity separated by a large energy gap. The oxidation/reduction of these polymers may occur by a process called doping. The p-doping (oxidation) process involves the removal of an electron from

the polymer backbone leaving it positively charged. Counter-ions from the bathing electrolyte enter the film to balance the charge. As these counter-ions only associate with the redox sites along the polymer chain, the polymer may be doped and undoped relatively easily.

The relative ease of the doping process and the stability of conducting polymers based on pyrrole, thiophene and aniline monomers^{1, 2} has led them to be widely studied, with a view to their application in electronic or optical devices³⁻⁵, electrocatalysis⁶, ion complexation⁷ or “wiring” of redox^{2, 7, 8} groups.

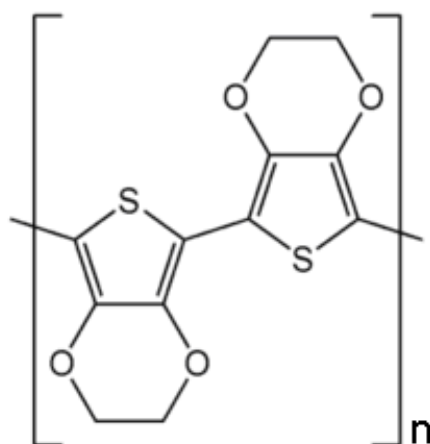


Figure 5.1 Structure of PEDOT

PEDOT (poly(3,4-ethylenedioxythiophene)) is an insoluble polymer, that may be doped either chemically or electrochemically. In the un-doped state PEDOT is an opaque insulator, which when chemically or electrochemically doped gives a material that is quasi-transparent with a high electrical conductivity. The problems normally associated with cross-linking and regio-isomerism have been removed by the ether groups at positions 3- and 4- of the thiophene (see figure 5.1)⁹. The addition of the ether groups has also lowered the oxidation potential allowing for a wider choice of solvent/electrolyte medium. As a consequence, the properties of the resulting polymer, PEDOT, have been widely studied¹⁰⁻¹⁷ and exploited in electroluminescent¹⁸ and electrochromic displays¹⁹⁻²¹, artificial muscles and actuators^{22, 23} and other applications^{14, 24}.

Many studies have illustrated the possible use of electroactive films in charge storage, sensors, electrocatalysis and electronic / optical devices, for which the film may be in a partially converted redox state. Moving across these partially converted redox states results in the changes in the properties and composition of the film. These part-converted states have been very successfully explored using the electrochemical quartz crystal microbalance (EQCM)²⁵. If the film is acoustically thin (rigid) then the EQCM may be used as a quantitative gravimetric probe of the mobile species, such as the movement of ion and solvent between the film and its bathing electrolyte. Here we use the quantitative gravimetric data obtained from the EQCM to determine the properties and composition of the film in partially converted redox states.

5.2 Aims and Objectives

Many studies have shown that the doping / un-doping of the film along with the solvent exchange and polymer reconfiguration control the performance of the film²⁶. However, although these contributions are recognised, very few studies identify their individual contributions or attempt to assemble them into a mechanism.

The EQCM has been used to study the acoustic impedance measurements of the deposition²⁷ and the redox cycling²⁸ of thick PEDOT films, for which the response is not simply a gravimetric one but is viscoelastically controlled. This thesis aims to complement these previous studies, focusing on films that are acoustically thin, thus giving a result that is gravimetrically controlled and therefore yielding information on ion and solvent transfers. There have been previous gravimetric studies on redox driven ion and solvent exchange processes^{11, 29} but these reports mainly focus on *complete* film redox conversion. Here the aim is to go beyond these studies in five respects:

- Explore the effects of partial film redox conversion
- Consider the fluxes (time differentials of populations) of both dopant and solvent
- Explore the effect of experimental timescale on these fluxes
- Directly compare the fluxes for solvents with different characteristics

- Use the flux data to identify shifts in mechanism involving different elementary processes.

Here we aim not only to give specific insights for PEDOT, but also pave the way for the interpretational methodology developed to be used on EQCM data obtained for other electroactive films.

5.3 Experimental

PEDOT films were deposited potentiodynamically (-0.2–1.2 V; 100 mV s⁻¹) from 50 mmol dm⁻³ monomeric EDOT (Bayer) / 0.1 M LiClO₄ (Aldrich) in dry acetonitrile (Aldrich, anhydrous 99.8%; stored over 4 Å molecular sieves). The cell and electrochemical equipment are described in chapter 3.3. The quartz resonators (ICM, Oklahoma City, OK) used during these experiments were 10 MHz unpolished crystals with piezoelectric and electrochemically active areas 0.23 and 0.25 cm², respectively; the difference relates to the small tab that connects to one side of the working electrode. The quartz resonator was glued to the base of the electrochemical cell in a way that one of the crystal faces was exposed to solution, this formed the working electrode in a three-electrode cell, with the counter and reference electrodes being platinum foil and silver wire respectively. All data were acquired at room temperature (20 ± 2 °C).

Crystal admittance data were acquired using an Agilent E5061 network analyzer, at the end of the film deposition to ensure that the deposit was acoustically thin (rigid); this ensured that the response obtained here contrasts with the viscoelastic responses of thicker films studied previously^{12, 14, 27, 28}.

EQCM experiments were performed on PEDOT films exposed to solutions of lithium perchlorate in acetonitrile (LiClO₄/CH₃CN), tetraethylammonium tetrafluoroborate in acetonitrile (TEABF₄/CH₃CN) and tetraethylammonium tetrafluoroborate in dichloromethane (TEABF₄/CH₂Cl₂). All chemicals were supplied by Aldrich and used as received. The EQCM instrumentation (as described in chapter 3.3) has been previously described in detail³⁰. The potentiostat used was a PGSTAT 20 Autolab, and was controlled by GPESW 4.2 computer software. The EQCM circuit converted

the mass change to a voltage output change within 0.01 seconds. The digital ramp was set to generate voltage steps of 0.048 V at a frequency to ensure the desired voltage scan rate was achieved. This ensured that the mass change and current data were produced with identical applied voltages regardless of the scan rate.

Following deposition, films were rinsed with CH₃CN and transferred to monomer-free electrolyte solution for voltammetric characterization. Before characterisation was carried out the polymer films were cycled 3 – 4 times (until the response was reproducible) after the solution exchange. This ensured that there was complete exchange of electrolyte from that of the deposition solution to that of the solution being used for characterisation. This procedure was also used for the change of solvent. Reliability of the results was confirmed by the repetition of the first scan rate used at the end of a set of measurements, at different scan rates.

5.4 Data analysis

The current and charge data for each experiment were corrected for residual background currents; these were typically no more than 5 μ A. Charge data (Q) for each cycle were also normalised (Q*) to help avoid the cumulative effects of small errors that may occur. Normalisation of charge was carried out by dividing the charge data (Q) for each cycle, by the total charge injected (Q_T) for that experiment. We can therefore define Q* as Q/Q_T. A five point moving average smoothing process was applied to flux data. The frequency responses recorded were then interpreted gravimetrically according to the Sauerbrey equation³¹. For 10 MHz quartz crystals:

$$\Delta f/\text{Hz} = -0.227 \times 10^8 (\Delta m/A) \quad (5.1)$$

where Δm (g) is the mass change and A (cm²) is the electrode area.

Due to the low concentration of electrolyte used in the experiments, described within this thesis, the film can be assumed to be permselective¹¹. This means it can be assumed that the total mass change (Δm_T / g) recorded by the EQCM, at any stage of the redox process, is simply just the contributions of the solvent (Δm_S), and the anion

(Δm_A) transfers. At high concentrations of electrolyte the film is no longer permselective and there is co-ion participation (quantifying co-ion transfer would require an additional population monitor, such as probe beam deflection³².) Here we are going to focus on dynamics so we will only consider time differentials of the mass contributions, related by:

$$m'_T = m'_A + m'_S \quad (5.2)$$

where the prime indicates a time derivative and the subscript letter indicates the species. As we want the stoichiometry of the processes, it is more helpful to express the contribution of each species in terms of their fluxes $j / \text{mol s}^{-1}$. Application of the electroneutrality condition and the Faraday to the current data yields the ion flux, j_A .

$$j_A = \frac{m'_A}{M_A} = \frac{i}{z_A F} \quad (5.3)$$

where M_A and z_A , are the molar mass and charge number of the anion respectively. It is clear from equation 2.2 that there is no single molar mass that will normalize m'_T note there are two species contributing to it, so for diagnostic convenience we choose to define a total mass flux:

$$j_T = \frac{m'_T}{M_A} \quad (5.4)$$

Comparing j_T with j_A gives an immediate appraisal of whether or not solvent transfer has occurred. Thus any difference between j_T and j_A indicates the extent of solvent transfer and equality of j_T with j_A signals solvent transfer does not occur. The solvent flux is defined by:

$$j_S = \frac{m'_S}{M_S} \quad (5.5)$$

The combining equations (5.2)-(5.5) gives the solvent flux:

$$j_S = \left(m'_T - \frac{i}{z_A F} \right) / M_S \quad (5.6)$$

5.5 Results and Discussion

5.5.1 Kinetics and mechanism of electrochemical p-doping of PEDOT

5.5.1.1 Film preparation

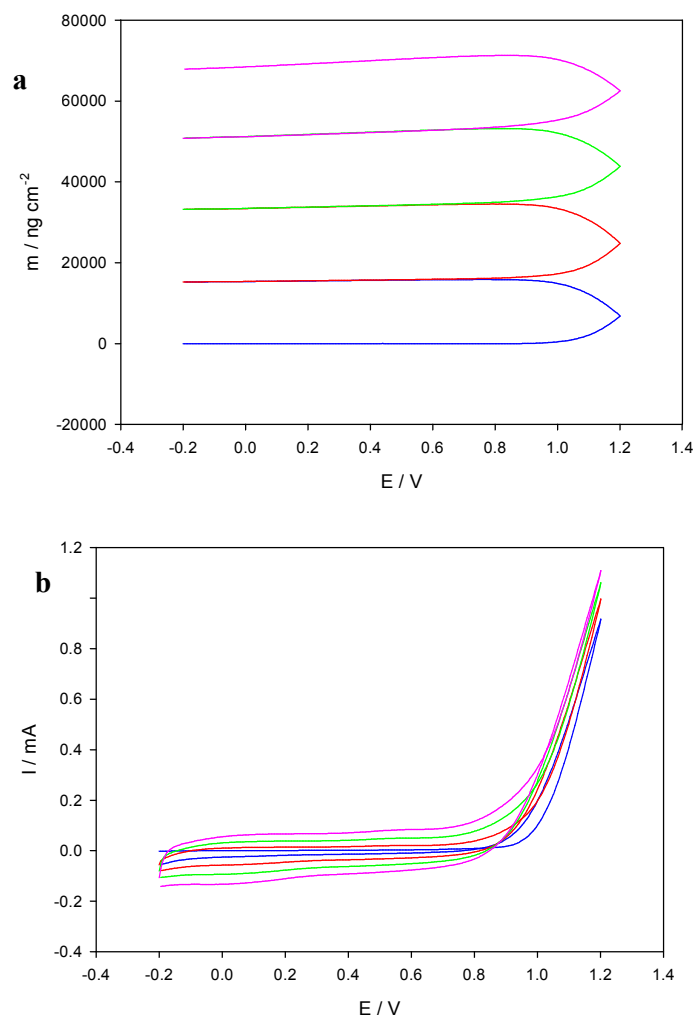


Figure 5.2 EQCM data for the preparation of a PEDOT film deposited potentiodynamically (-0.2 – 1.2 V; 100 mV s⁻¹) from 50 mmol dm⁻³ monomeric EDOT / 0.1 M LiClO₄ (Aldrich) in dry acetonitrile. a) EQCM, mass vs potential plot; b) C.V. current vs. potential plot; First cycle: —; second cycle —; third cycle: — and fourth cycle —.

PEDOT can be produced by electrochemical polymerisation on a conduction substrate from a solution of the monomer and a supporting electrolyte. Figure 5.2 shows the experimental data obtained (both the mass and the current traces) from the EQCM for the electrochemical deposition of PEDOT, from a monomeric solution of EDOT/LiClO₄. The polymerisation was carried out by cycling the voltage between -0.2 V and 1.2 V, 4 times at 100 mV s⁻¹. These four cycles lead to a deposition of around 16.5 μg cm⁻² which gives a film that is around 0.12 μm thick (calculated from frequency change in air). Figure 5.3 shows the admittance spectrum for the quartz crystal resonator before and after the film deposition. The frequency of the unloaded quartz resonator was 9.977,875 MHz and after the deposition it was 9.974,125, this means that the mass added caused the frequency to shift by 3750 Hz. This corresponds to 16.5 μg cm⁻² of PEDOT being added to the quartz crystal resonator. From figure 5.3 it is clear to see that there has been a small frequency shift but no decrease in admittance, this verifies that the film is still acoustically thin.

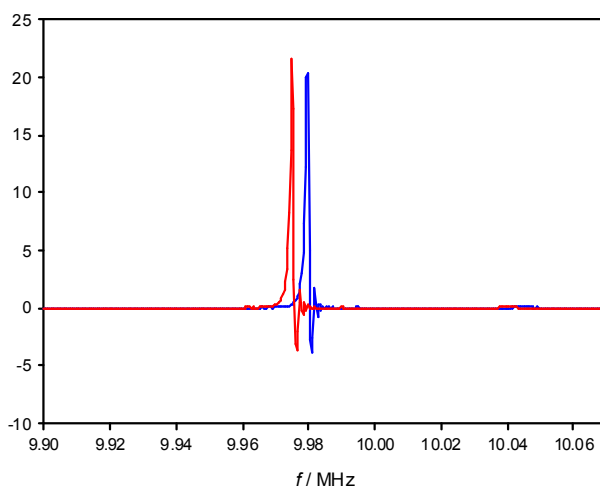


Figure 5.3 Admittance vs, frequency plot showing the frequency of the quartz crystal resonator before deposition in air (—) and the polymer loaded resonator in air (—).

5.5.1.2 Overview of population changes and fluxes

Figure 5.4 shows currents responses (i-E curves; panel a) and mass change responses (Δm-E; panel b) for the PEDOT film (produced in figure 5.2) exposed to 0.1 mol dm⁻³

$\text{LiClO}_4 / \text{CH}_3\text{CN}$ and undergoing redox switching at a selection of scan rates between 10 mV s^{-1} and 250 mV s^{-1} .

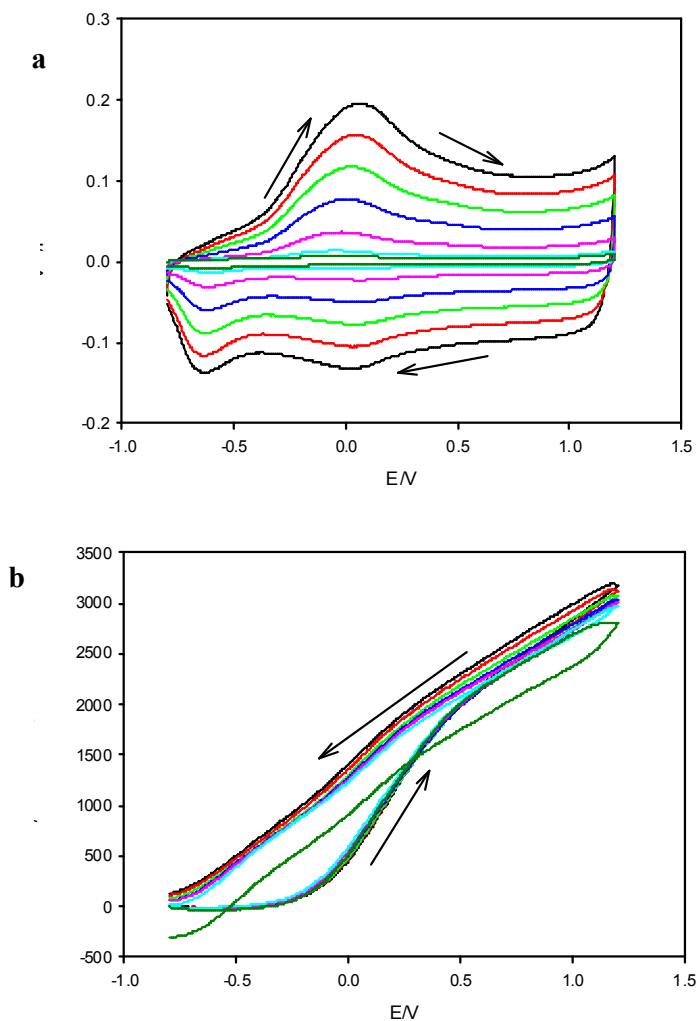


Figure 5.4 Experimental data for a cyclic voltammetric experiment on a representative PEDOT film ($\Gamma = 131 \text{ mol cm}^{-2}$) exposed to $0.1 \text{ mol dm}^{-3} \text{ LiClO}_4 / \text{CH}_3\text{CN}$. (a): I vs E ; panel (b): Δm vs E . Film mass changes calculated using Sauerbrey equation³¹. Scan rate, $v / \text{mV s}^{-1} = 10$: —; 20: —; 50: —; 100: —; 150: —; 200: —; 250: —.

The potential responses are typical of those reported in the literature: the current responses show one significant feature (at all scan rates), is the doping (forward scan) and un-doping (reverse scan) processes are not mirror images. This to some degree

this is the same for the $\Delta m - E$ curve. The $i-E$ curve shows a feature peak during doping (oxidation) and two broad peaks during un-doping. The $\Delta m - E$ curve also gives some basic but essential facts, during the doping process there is an initial decrease. As the $\Delta m - E$ curve shows an initial drop in mass this clearly indicates a solvent loss that is gravimetrically more than the dopant entry. Acetonitrile has a mass of 41 g / mol^{-1} and the anion (ClO_4^-) has a mass of 99 g / mol^{-1} suggesting that the solvent loss is much faster than the dopant entry.

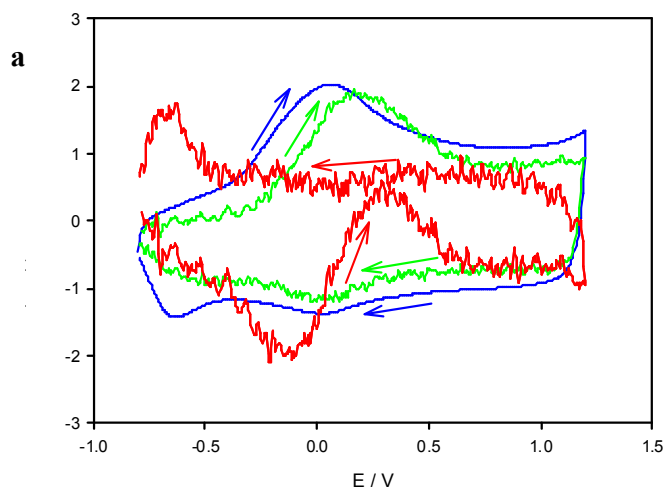
5.5.1.3 Potential dependence of fluxes

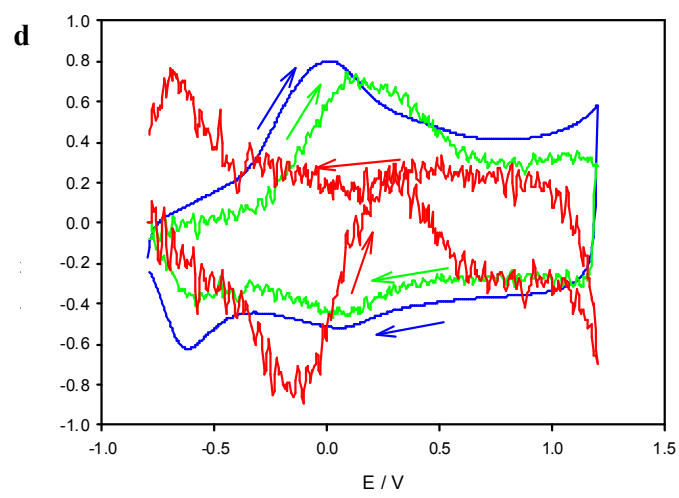
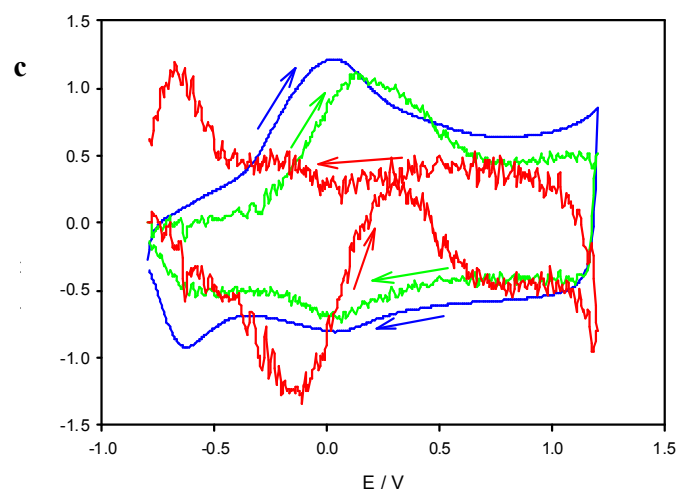
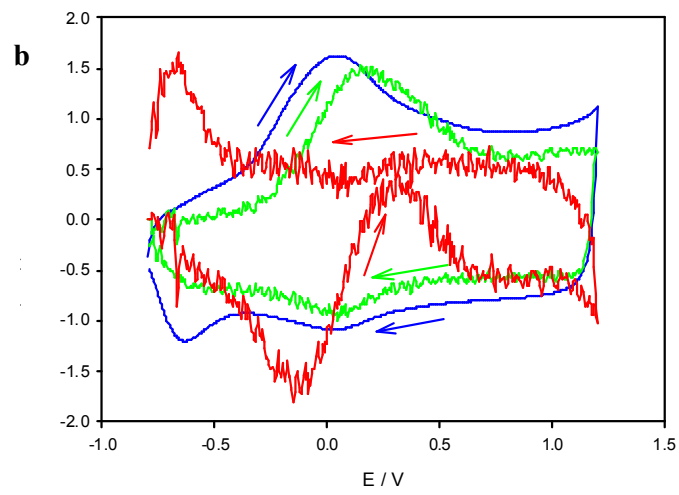
The individual solvent, total and ion fluxes were calculated from the data obtained in figure 5.4 using equations 5.2-5.6; the resulting j (flux) – E plots are given in figure 5.5 panels a - g. On all of the traces in figure 5.5 it is clear that during the p-doping the solvent flux is non-monotonic; as expected (and predicted from $\Delta m - E$ curve) there is a large initial loss of solvent from the film. This is then followed by a small amount of re-solvation, which is then followed by further loss of solvent. This implies that the most solvated state is when the film is totally reduced. From the traces in figure 5.5 it is also clear that the solvent and anion fluxes are not coupled. On the reverse scan the anion and solvent fluxes are monotonic and relatively featureless until the very negative end of the cycle, for which they remain monotonic but show some small features. The trace behaviour remains the same for all the scan rates (figure 5.5 panels a-g).

The aim here is to identify the kinetic and diffusional processes that underlie the above responses. In order to interpret this data we first need to take into account the differing timescales of the experiments. For surface-immobilized (“diffusionless”) species that do not have any kinetic or diffusional complications the response pattern should be one in which the total population change is independent of timescale and the flux is linear with scan rate and independent of scan direction. A test for this is to see if the current response normalises with respect to voltage scan rate. Normalisation of the flux data may be carried out by a simple dividing the flux data by its corresponding scan rate, the outcomes of this procedure for each of the fluxes as a function of potential are shown in figure 5.6.

The experimental data illustrated (although just a few μA) a correction for background currents was required. It was noted that these background currents lay within 1 – 4 μA , further analysis lead to a 3 μA background current correction being applied to the anion flux. Although it is only small its effect is cumulative. Consequently, though negligible for current responses at scan rates 50 mV s^{-1} and above (ranging from <10% down to 1% correction), its effect on slow scan rate responses was significant (typically a 30-40% correction). The normalization procedure is excellent for all but the slowest scan rate experiment where, given the above, it is satisfactory.

The normalization procedure shows that there is no question of timescale dependent dispersion for the total mass flux. Using equation 5.6 along with the combination of the total mass flux (figure 5.5b) with the anion flux (figure 5.5a) yields the solvent flux (figure 5.5c). Again the fluxes normalise with respect to scan rate. At first this is somewhat surprising considering that the result is that of a subtraction of two measured quantities. However, it is obvious that the solvent should normalise, as it is the algebraic outcome of equation 5.6, which uses the flux data from anion and the total mass, both of which normalise by the same timescale function. The solvent flux normalisation is again excellent except for the lowest scan rate, where background current correction is most problematical.





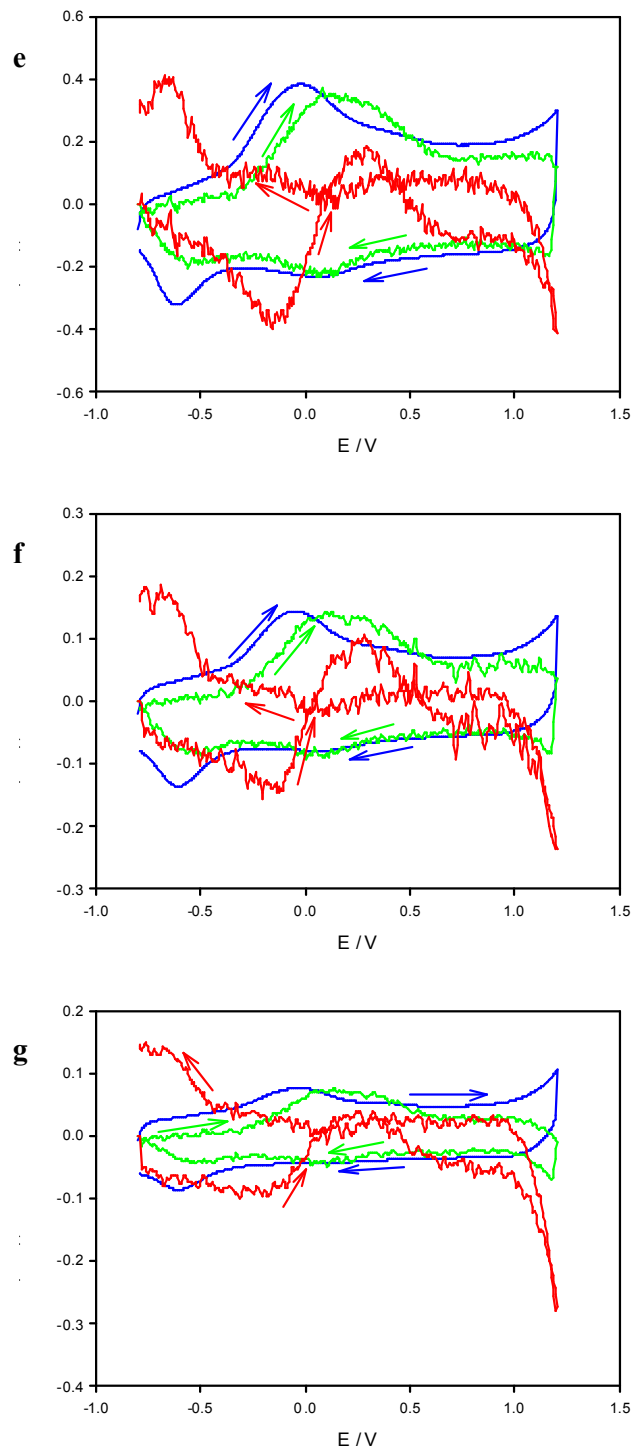


Figure 5.5 Flux representation, as a function of potential (E), of data from Figure 5.4 for (a) $v = 250 \text{ mV s}^{-1}$; (b) $v = 200 \text{ mV s}^{-1}$; (c) $v = 150 \text{ mV s}^{-1}$; (d) $v = 100 \text{ mV s}^{-1}$; (e) $v = 50 \text{ mV s}^{-1}$; (f) $v = 20 \text{ mV s}^{-1}$; (g) $v = 20 \text{ mV s}^{-1}$. (—) represents coupled electron/anion flux (j_A). (—) represents combined fluxes of anion and solvent (j_T). Solvent flux (j_S) is represented by (—).

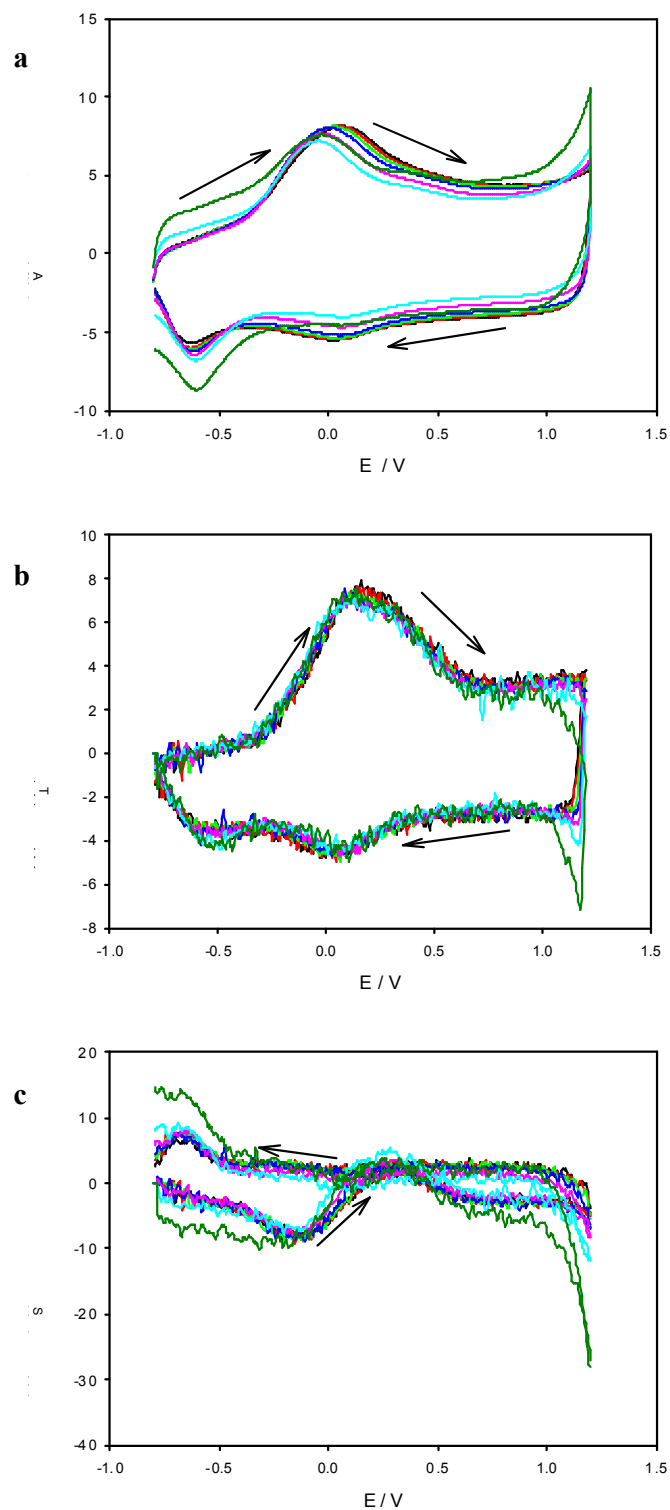


Figure 5.6 Normalized fluxes as functions of applied potential, E , of (a) coupled electron/anion flux (j_A); (b) combined fluxes of anion and solvent (j_T); (c) Solvent flux (j_S) scan rate, v , where $v / \text{mV s}^{-1} = 10$: —; 20: —; 50: —; 100: —; 150: —; 200: —; 250: —.

Figure 5.6 shows that the electron/anion and solvent fluxes normalize with respect to scan rate. This is true for both the oxidation and reduction half-cycles, however these two normalised branches are not the same. This difference may be signifying that the film has two pseudo-equilibrium states. This suggests that the doping process, on all the timescales used, takes the same mechanistic pathway. The pathway taken by the un-doping process is again the same across all timescales, but is different to that taken by the doping process. It is important to note that EQCM data cannot give any direct information on the polymer structure during the redox processes. However, the oxidised forms of PEDOT have a different configuration as a consequence of their requirement for planarity of the aromatic rings. It is the energetics of these different forms that cause them to have different redox potentials²⁶, such that the same applied potential corresponds to a different overpotential in the two scan directions.

5.5.1.4 Normalisation of fluxes as a function of charge state

An approach often used to investigate film population is to analyse EQCM data via plots of mass change vs. charge, rather than mass change vs. potential. The advantage of this format is that one correlates overall population changes of mobile species with the redox state changes (represented directly by charge) that drive them. Here we use the same concept, but for the flux data (rather than the integral quantities) obtained in the previous section. Plotting fluxes rather than populations has the advantage of focusing on the film compositional regions where redox processes occur. Differential figures are more sensitive and it is more natural to consider rates rather than concentration when considering kinetics. Figure 5.7 shows plots for each of the fluxes as functions of charge for three of the scan rates (250, 100 and 10 mV cm⁻¹) used. The appearance is very similar to that of their corresponding $j - E$ (figure 5.5) plots, this may be due to the fact that initial $i - E$ (figure 5.4 panel a) are relatively featureless.

Figure 5.6 a – c gives an indication to the sensitivity and dynamic range of the method. The largest solvent flux (expulsion during the oxidation half-cycle) involved is on the order of 2 nmol s⁻¹ and the smallest is less than 0.1 nmol s⁻¹, measured with a signal:noise ratio of ca. 10. These figures show that this method has exceptional sensitivity and the performance, it is also worth noting that the limiting factor is not the QCM gravimetric response but the accuracy of estimating the background current.

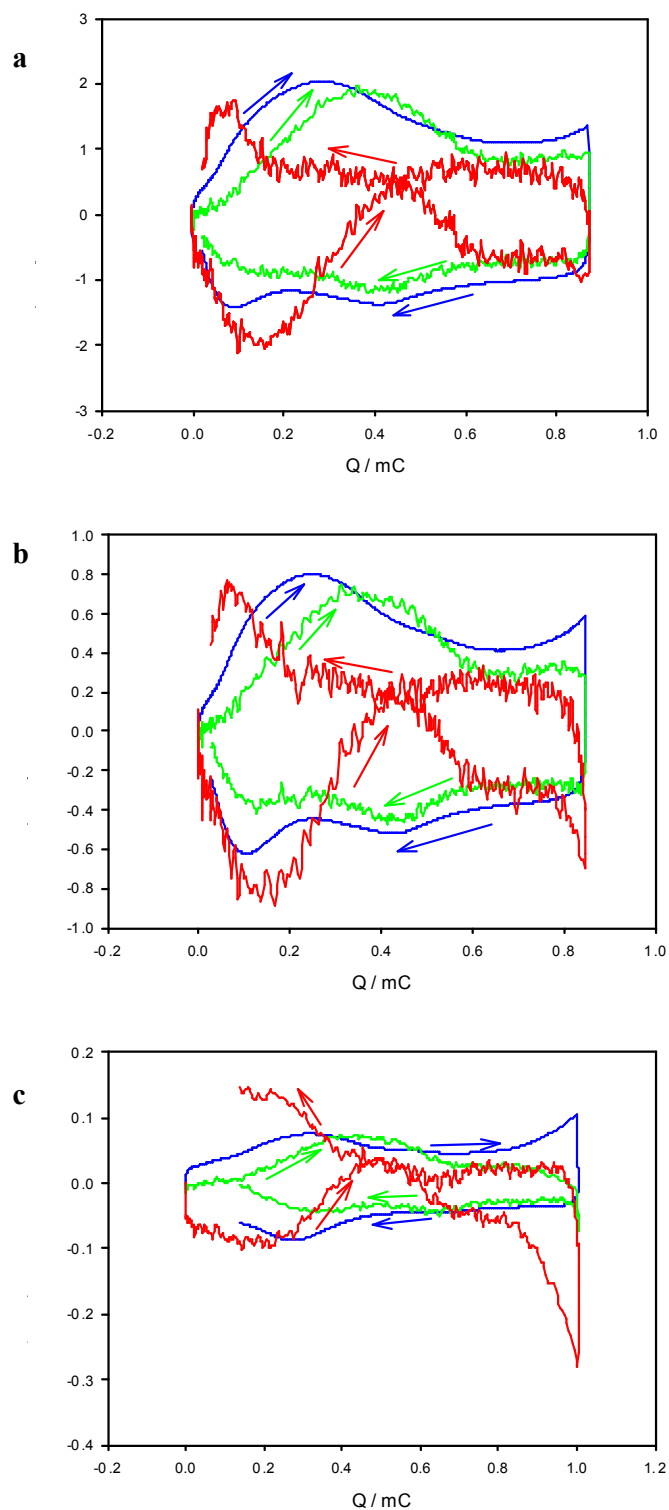


Figure 5.6 Flux representation, as a function of charge (Q), of data from Figure 5.4 for (a) $v = 250 \text{ mV s}^{-1}$; (b) $v = 100 \text{ mV s}^{-1}$; (c) $v = 10 \text{ mV s}^{-1}$. (—) represents coupled electron/anion flux (j_A). (—) represents total flux (j_T). Solvent flux (j_S) is represented by (—).

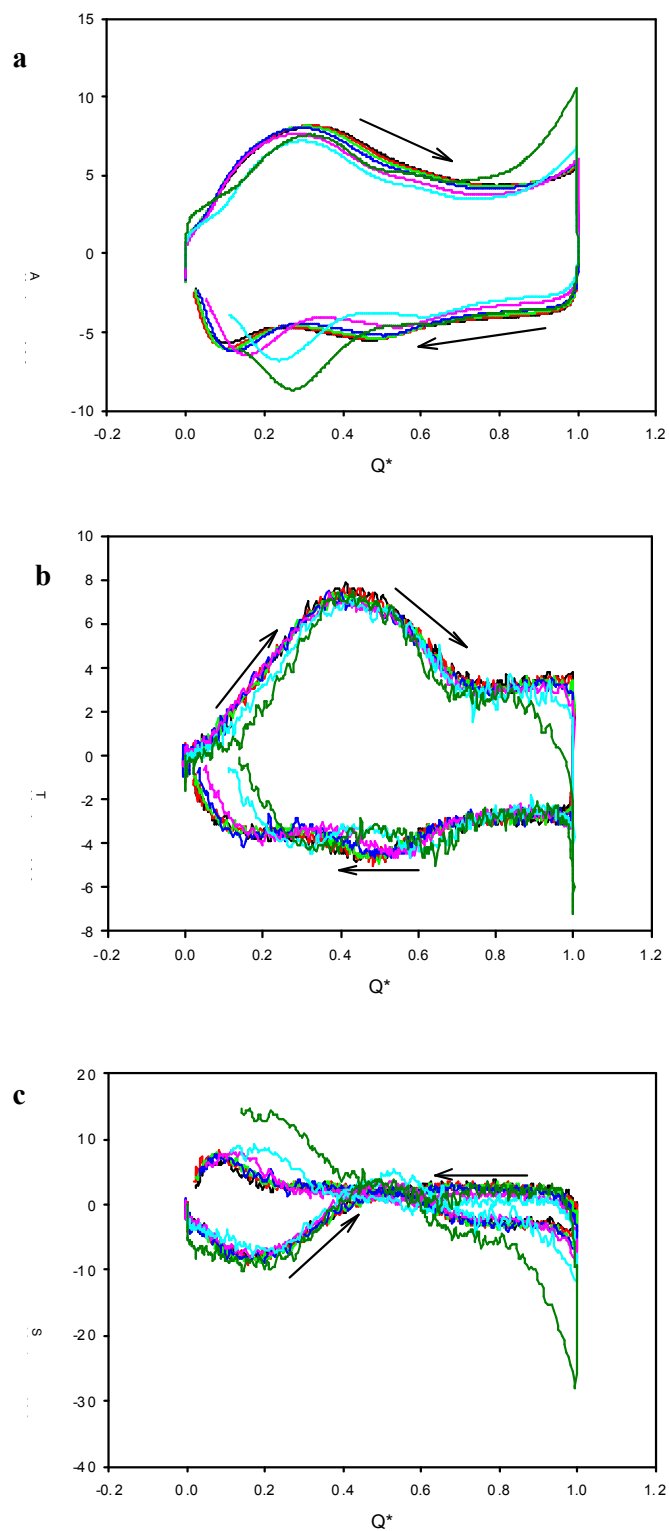


Figure 5.7 Normalized fluxes as functions of normalised charge Q^* , of (a) coupled anion flux (j_A); (b) total fluxes (j_T); (c) Solvent flux (j_S) scan rate, $v / \text{mV s}^{-1} = 10$: —; 20: —; 50: —; 100: —; 150: —; 200: —; 250: —.

However, plotting the fluxes against normalised charge Q^* (defining normalized charge as $Q^* = Q/Q_T$, where Q_T is the charge for total redox conversion) gives more mechanistic insights. Figure 5.7 shows flux vs. Q^* plots corresponding to figure 5.6. Once again due to the background current correction not being perfect (especially for the slowest scan rate), the flux data is plotted as a function of normalised charge, for which zero corresponds to the fully reduced film and unity to the fully oxidized film thus avoiding over-interpretation of minor peak shifts. As with the normalised flux vs. potential, the normalization shown for the Q^* is once again remarkable across the 25-fold timescale variation. Figure 5.7 c shows that there is significant solvent expulsion for the first 40% of the oxidation cycle. This is followed by solvent entry for the next 25% of the process, with a small amount of solvent expulsion for the remaining 35% of the half cycle. During reduction there is constant rate of solvent entry, firstly at low levels but then at a more significant rate during the later parts of the reduction process.

5.5.1.5 Mechanistic possibilities

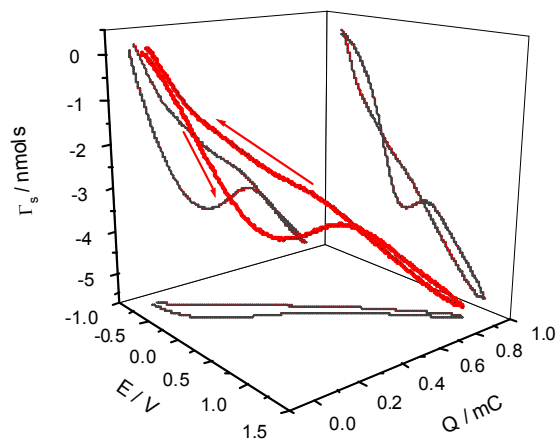


Figure 5.8 Trajectory through (E, Q, Γ_s) compositional space for PEDOT redox switching. Data from the experiment of figure 5.4a using a scan rate of 250 mV s^{-1} .

Figure 5.8 illustrates how films mobile species populations can be shown in a 3D figure in (E, Q, Γ_S) -space (where Γ_S / mol is the change in solvent population, i.e. $\Delta m_S / M_S$) that trace out the trajectory through compositional space. These 3D plots complement the differential (flux) plots shown in the previous section. There is obviously hysteresis in the solvent populations, whether viewed through the (E, Γ_S) - or (Q, Γ_S) -projections, but because this hysteresis is independent of the scan rate then the source is not just a simple kinetic one.

This type of system has previously been represented using a “scheme-of-cube(s)”²⁶, which is a representation in terms of chemical species (the corners) and electrochemical processes (the edges) that are involved in their interconversion. For the switching process of a thin polymer film, there are three types of elementary steps, thus a $1 \times 1 \times 1$ cube will be sufficient. For the experimental timescales used here, the electrons and counterions may be considered as coupled and so are represented by a single coordinate (here, selected as the x-coordinate). Polymer reconfiguration and redox driven solvent transfer are considered as the z and y coordinates, respectively. The cube (figure 5.9) has eight species, four for each redox state. The O (right hand face) and R (left hand face) symbolise the oxidised and reduced forms of the polymer. There are two solvation states on the rear and front faces (subscript s or the absence thereof indicates the more or less solvated polymer state) and two polymer reconfigurations on the upper and lower faces. The superscript letters a and b represent the two limiting polymer configuration states (the labels are arbitrary). Different energy barriers result in individual steps occurring on different timescales, thus movement through the cube generally proceeds along its edges. Movement through a diagonal is possible, but is energetically disfavoured. The model is descriptive and qualitative: it cannot predict or represent stoichiometry and cannot give any a priori indication of the mechanism or rate constants. However, it is a good visualisation tool for complex and competing mechanistic pathways.

The starting state of the polymer represented here is given by R_s^a , the product at the end of the oxidation half cycle is O^b , and there are 6 possible mechanistic pathways (at the start there are 3 different routes available, each of the three routes has a possibility of going down two subsequent mechanistic paths and for each of the two paths there is just one path left, therefore $3 \times 2 \times 1 = 6$) connecting them in each switching direction²⁶.

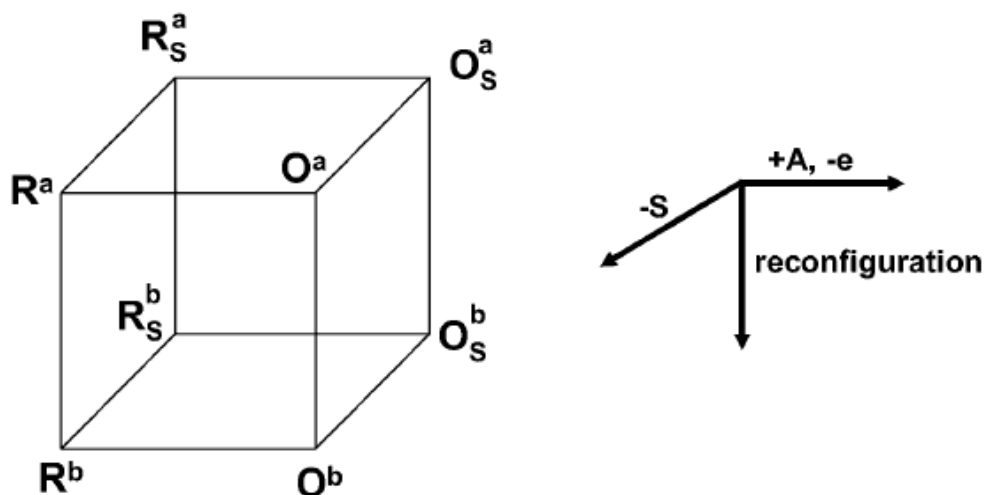


Figure 5.9 Generic 1x1x1 cube scheme, for an electroactive polymer, where O and R symbolise the oxidised and reduced forms of the polymer. Subscript s (or lack of) indicates the solvation state and the superscript letters a and b represent the polymer configurations.

The scan rates used in the PEDOT in LiClO₄ / CH₃CN experiments do not enable the electron/anion nor the solvent fluxes to be separated with respect to timescale. Therefore the resolution of these steps will not be reported here. However, it is known that the electrochemical step (coupled electron/ion transfer) is the trigger for the chemical steps, thus we can say that the first step must be R_s^a to O_s^a. On the range of timescales, used for the PEDOT p-doping experiments above, it is not possible to say what order the solvent transfer and polymer reconfiguration steps occur; in fact it is not possible to even confirm if these two steps are coupled or if there is an intermediate state (O_s^b or O^a). If the two steps (solvent transfer and polymer reconfiguration) are coupled then there is no intermediate state, this step then has a single energy minimum across the diagonal face of the cube. The universally accepted concept is that the solvent transfer and the polymer reconfiguration are coupled, but either way the complete oxidation cycle is represented by sequence 5.7 and is illustrated in figure 5.10 a, the chemical steps are represented by a diagonal between the cube corners O_s^a and O^b.



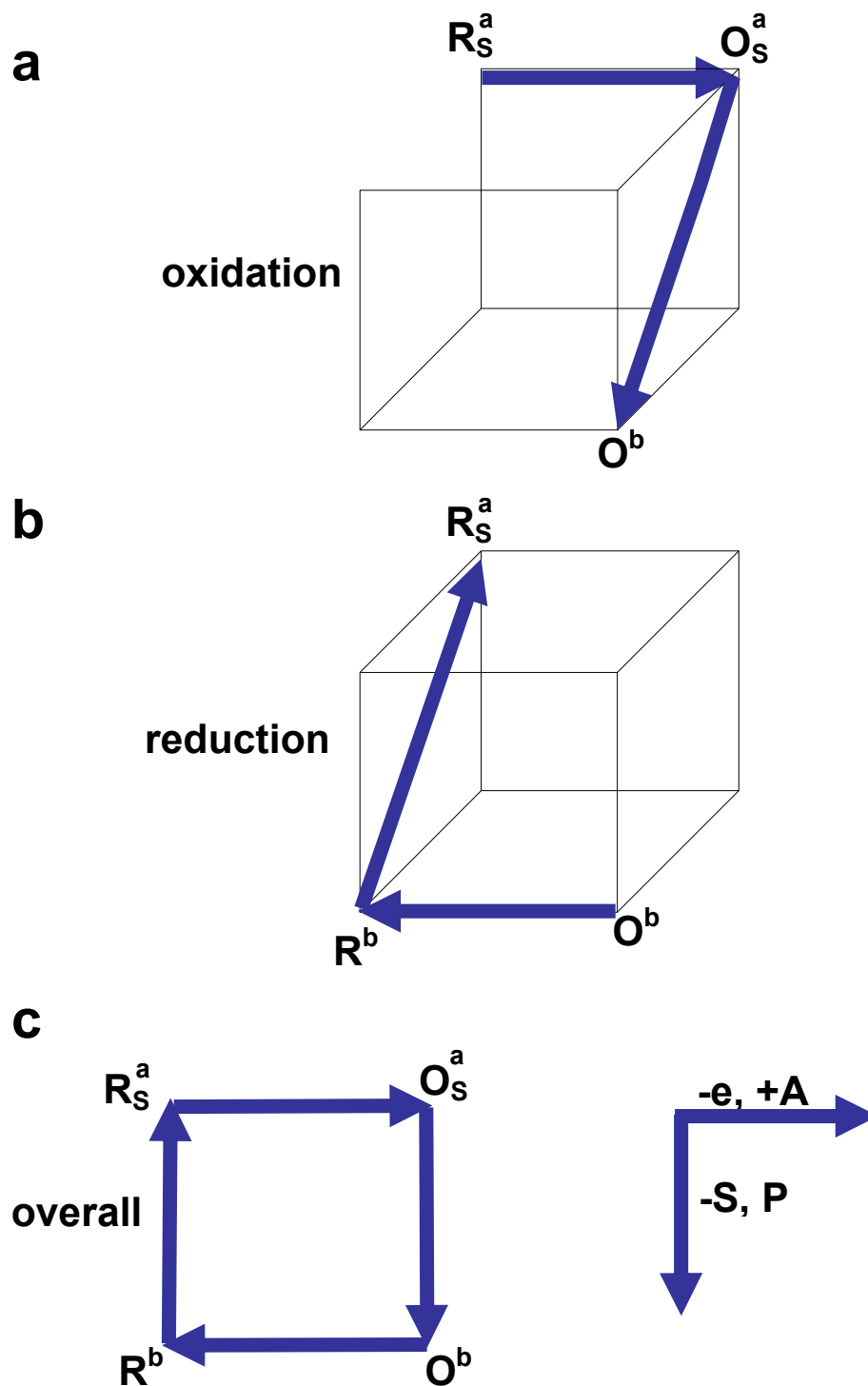


Figure 5.10 Cube scheme showing species and mechanistic pathways for PEDOT redox switching. (a) represents the doping (oxidation) of the film; (b) represents the un-doping of the film; (c) gives the overall redox process.

Similarly, in the reduction (de-doping) half cycle the trigger is again the electrochemical step, but now species O^b is the starting point. Once again the first step can be represented by $O^b \rightarrow R^b$. For the reasons stated above, the solvent and polymer processes are represented by a diagonal across the left side of the cube, which gives R_S^a from R^b . The complete process, is illustrated in figure 5.10 b and is given by;



The complete redox cycle can be illustrated in figure 5.10 c, it shows how the whole cycle can be represented by a “square” of four species, indicated by the heavy lines.

5.5.2 Effect of electrolyte concentration on the permselectivity of PEDOT films

The procedure used in section 5.5.1 to analyse the p-doping process for PEDOT in $LiClO_4/CH_3CN$, were based on the assumption that the film was under permselective conditions. This means that during the redox process there was both anion and solvent transfer but not salt transfer. Here it is demonstrated that the (acoustically) thin films produced for analysis in this and the next chapter are indeed permselective. Any film at a sufficiently low electrolyte concentration will be permselective; the failure of permselectivity will escalate as the concentration is increased. The point at which permselectivity failure becomes significant is when the concentration of the electrolyte is around the same concentration of fixed charge sites in the polymer. The concentration of fixed sites used here is around 2 mol dm^{-3} (with some variation according to the level of solvent swelling), thus well above the concentration of electrolyte (0.1 mol dm^{-3}) being used. At such low electrolyte concentrations there should not be any dramatic permselectivity failure, but as a more practical test, here measurements have been made using other concentrations of electrolyte (0.01 and 0.25 mol dm^{-3}). The test is whether the outcomes are independent of concentration: if they are, then the films are permselective.

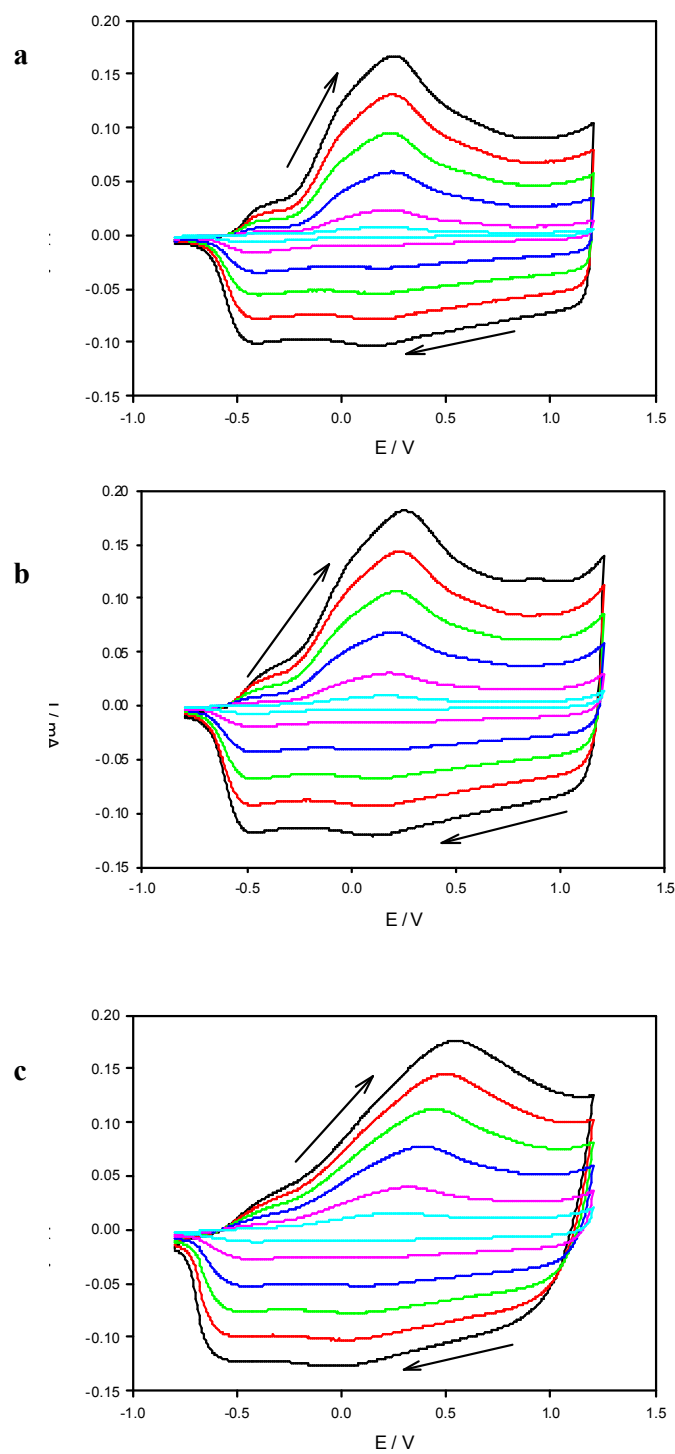


Figure 5.11 Experimental i - E data for a cyclic voltammetric experiment on a PEDOT film ($\Gamma = 131 \text{ nmol cm}^{-2}$). Solution: (a) 0.25 mol dm^{-3} (b): 0.1 mol dm^{-3} (c): 0.01 mol dm^{-3} TEABF₄ /CH₃CN. Scan rate, $\nu / \text{mV s}^{-1} = 10$: —; 20: —; 50: —; 100: —; 150: —; 200: —; 250: —.

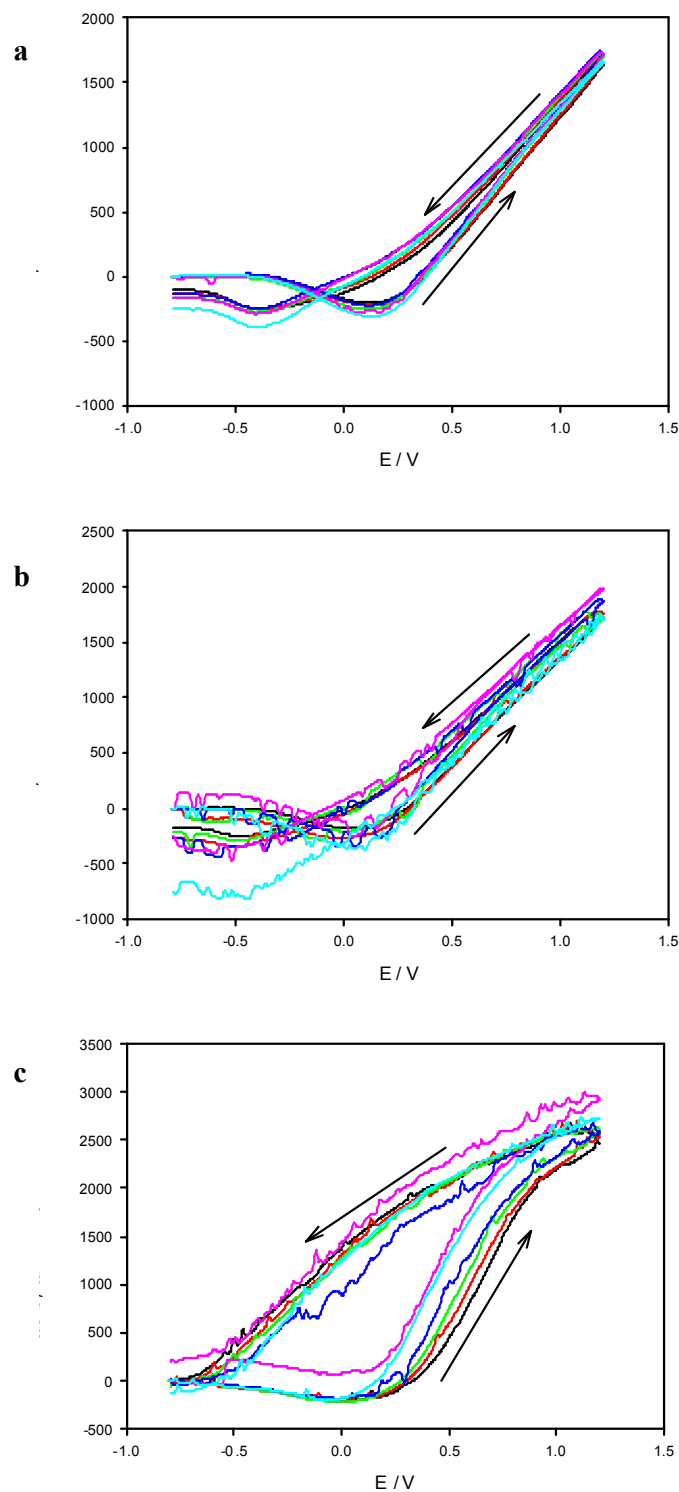


Figure 5.12 Experimental Δm -E data for a cyclic voltammetric experiment on the PEDOT film of figure (5.11). Solution: (a) 0.25 mol dm^{-3} (b) 0.1 mol dm^{-3} (c) 0.01 mol dm^{-3} TEABF₄/CH₃CN. Scan rate, $\nu / \text{mV s}^{-1} = 10$: —; 20: —; 50: —; 100: —; 150: —; 200: —; 250: —.

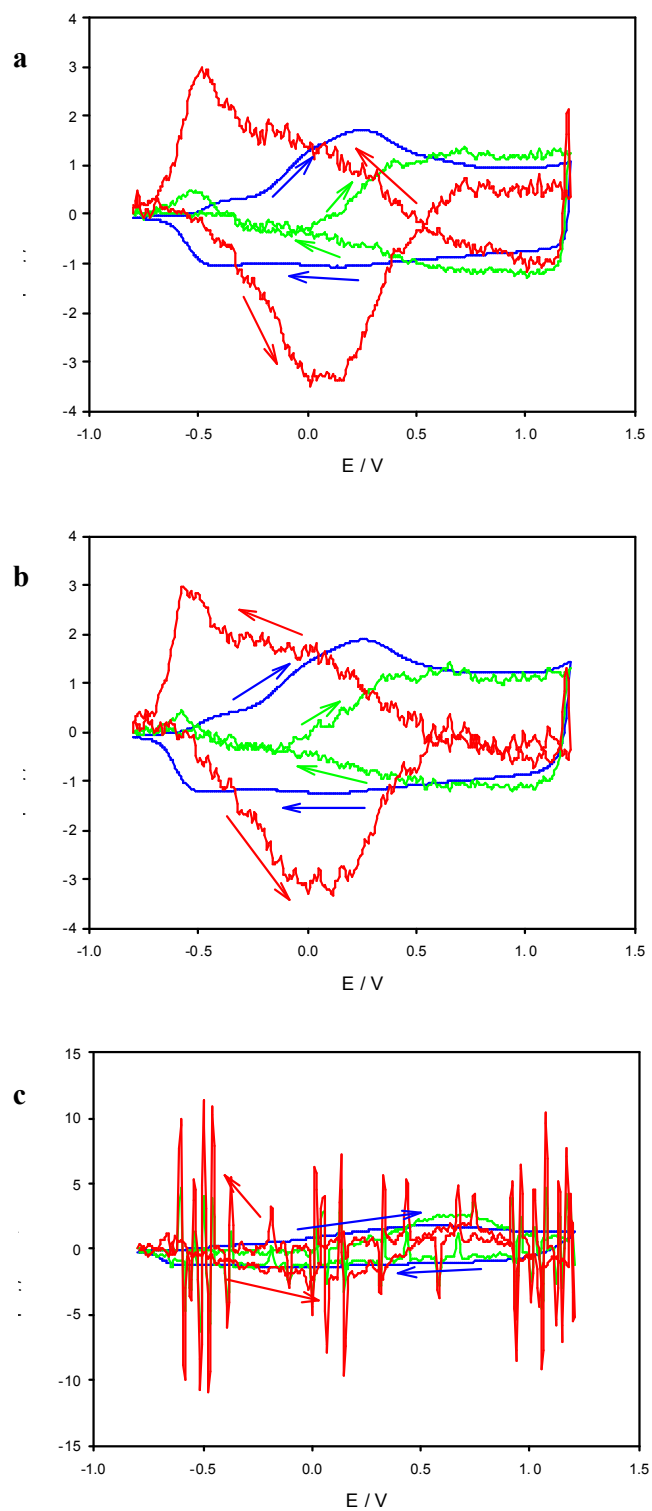


Figure 5.13 Fluxes of mobile species as functions of potential (E) for the experiment of figure 5.12/5.13 Panels a -c for (a) 0.25; (b) 0.1; (c) 0.01 j_A (—) represents j_A anion flux, (—) represents j_T combined fluxes of anion and solvent flux, j_S trace (—).

Figures 5.11, and 5.12 show the experimental data for the p-doping of a PEDOT film using different concentrations of electrolyte. Figure 5.13 illustrates flux results, for the data obtained in figures 5.11 and 5.12, using a scan rate 250 mV s^{-1} . In all three figures the data are comparable across the different electrolyte concentrations. However, the data for the lower concentration (0.01 mol dm^{-3}) can offer only qualitative support (see figure 5.13) to the permselectivity assumption. Quantitative support is not possible, since detailed evaluation is compromised by electrolyte conductivity. This is because at slow scan rates the background currents accumulate, then at high scan rate the ohmic drop in solution distorts the responses. The problems associated with the ohmic drop in solution do not occur at the higher levels of electrolyte concentration, thus allowing a more quantitative analysis to be carried out on the data. Figure 5.13 panels a and b show the flux analysis carried out on the two higher concentrations of electrolyte. The similarity of the fluxes in the two cases confirms that the salt population change within the film is (within experimental uncertainty) zero. If the films were not permselective then one would see a difference in the fluxes of the neutral species (solvent + salt).

5.5.3 Solvent effects on the electrochemical p-doping of PEDOT

5.5.3.1 Overview of population changes

A similar PEDOT film to that outlined in section 5.5.1.1 was produced by electrochemical deposition.

Figures 5.14 and 5.15 show initial experimental data (current responses (i-E) and mass change responses) for a PEDOT film undergoing redox switching while exposed firstly to a solution of 0.1 mol dm^{-3} TEABF₄/CH₃CN (figure 5.14) and then a 0.1 mol dm^{-3} TEABF₄/CH₂Cl₂ solution (figure 5.15). Figure 5.16 groups together both sets of data, for ease of comparison between the two solvents. It is clear in figure 5.16 that, although there are a number of common features, between the responses in two solvents there are several differences. One significant feature that is present between the two solvents (also reported in section 5.5.1 for LiClO₄) is the lack of a mirror-image symmetry for the forward and reverse half cycles on the i-E curves. The i-E curves, for both solvents, show a peak-shaped response for the oxidation (doping) half cycles, but the reduction (un-doping) half cycle appears relatively featureless. Secondly, the Δm -E

curves for both solvents do not have traces that are mirror images for the oxidation and reduction cycle. For both solvents, the mass traces show that the film's mass during the oxidation half cycle does not undergo a monotonic change: there is an initial decrease in mass. This initial decrease signifies a loss of solvent, which gravimetrically outweighs the anion (dopant) entry. It is clear that the mechanisms for the doping and un-doping is different, irrespective of whether they are viewed via the current response or the film's mass response.

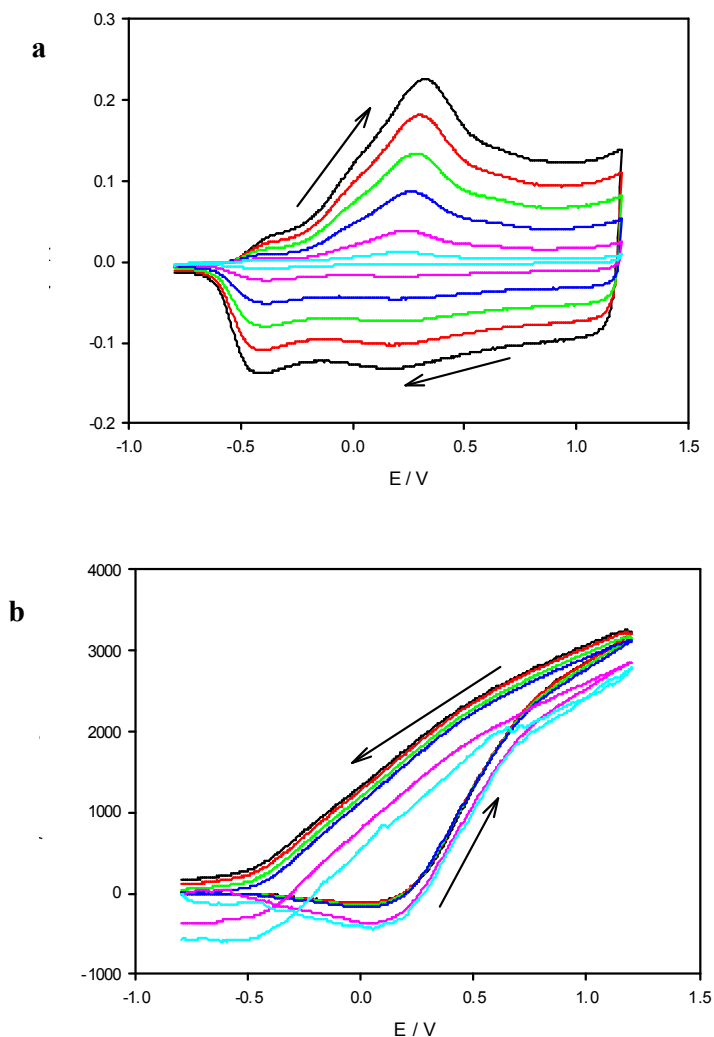


Figure 5.14 Experimental data for a cyclic voltammetric experiment on a representative PEDOT film ($\Gamma = 128 \text{ nmol cm}^{-2}$; where mol refers to monomer units, coulometrically determined from the 250 mV s^{-1} i - E curve with the maximum doping level taken as 0.3) exposed to 0.1 mol dm^{-3} TEABF₄/CH₃CN. Panel (a): i vs E ; panel (b): Δm vs E . Film mass changes calculated using Sauerbrey equation³¹. Scan rate, $v / \text{mV s}^{-1} = 20$: —; 50: —; 100: —; 150: —; 200: —; 250: —. . Arrows show the direction of the scan.

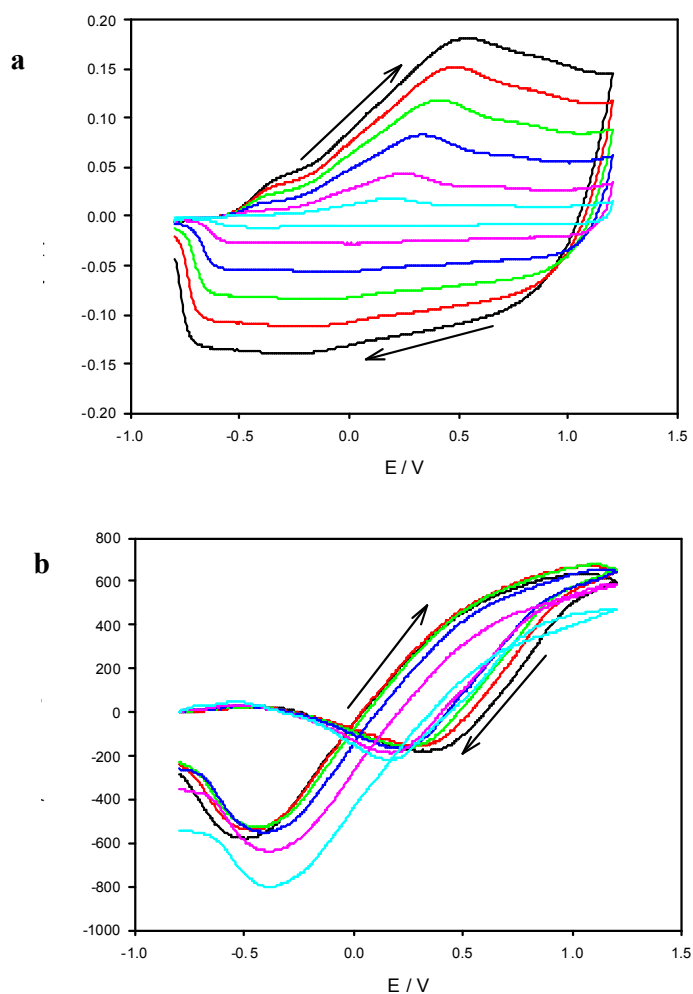


Figure 5.15 Experimental data for a cyclic voltammetric experiment on the film of figure 5.14 exposed to $0.1 \text{ mol dm}^{-3} \text{ TEABF}_4 / \text{CH}_2\text{Cl}_2$. Panel (a): i vs E ; panel (b): Δm vs E . Film mass changes calculated using Sauerbrey equation³¹. Scan rate, $v / \text{mV s}^{-1} = 20$: —; 50: —; 100: —; 150: —; 200: —; 250: —. . Arrows show the direction of the scan.

There are several differences that can be seen when comparing the $i - E$ and $\Delta m - E$ response for the films in two solvents. In figure 5.16a, it is clear that the peak for the doping half cycle for the film cycled in $\text{TEABF}_4/\text{CH}_3\text{CN}$ is much sharper and more symmetrical than that of the corresponding peak for the film cycled in $\text{TEABF}_4/\text{CH}_2\text{Cl}_2$. The current response for the film cycled in $\text{TEABF}_4/\text{CH}_2\text{Cl}_2$ shifts significantly towards more positive potentials with increasing scan rate. In contrast there is very little peak movement for the film cycled in $\text{TEABF}_4/\text{CH}_3\text{CN}$. The $\Delta m - E$ in figure 5.16b illustrates how the overall mass change for doping in dichloromethane is

much smaller than that in acetonitrile, despite the fact that the dopant in both is BF_4^- . For the film cycled in $\text{TEABF}_4/\text{CH}_2\text{Cl}_2$ the mass trace shows a mass decrease then an increase for the un-doping part of the scan, while in acetonitrile the same process is simply monotonic.

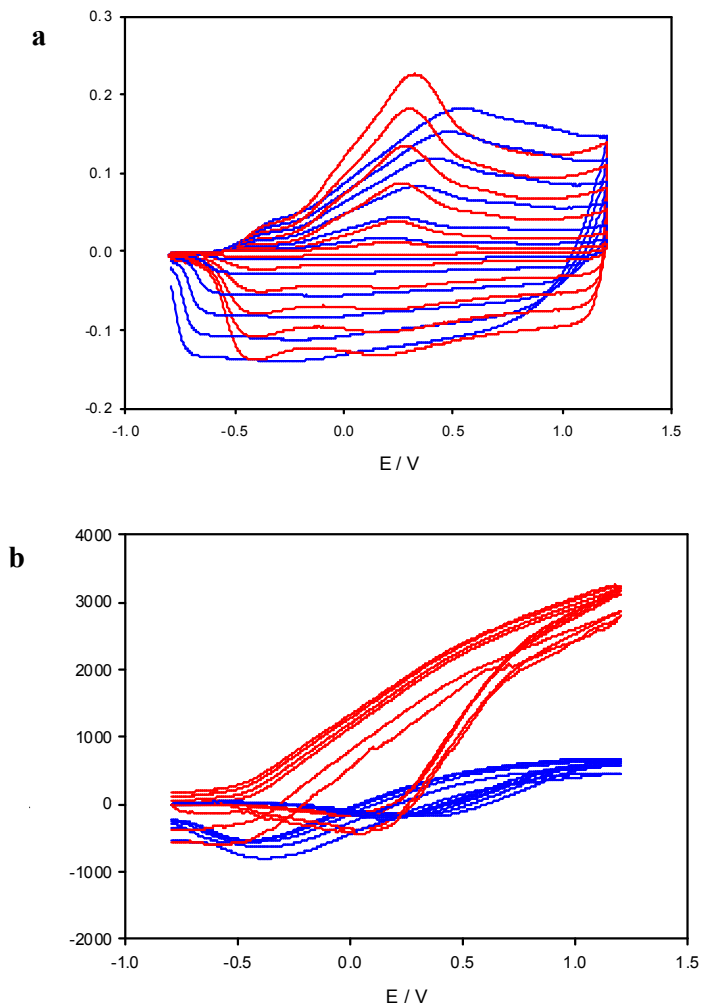


Figure 5.16 Comparison of experimental data from figures 5.11 and 5.12 $\text{TEABF}_4/\text{CH}_3\text{CN}$: — and $\text{TEABF}_4/\text{CH}_2\text{Cl}_2$: —. Panel (a): i vs E ; panel (b): Δm vs E . Film mass changes calculated using Sauerbrey equation³¹.

5.5.3.2 Potential dependence of fluxes

It was confirmed in section 5.5.2 that the films for which data are reported in this and the following chapter are permselective. Here anion and solvent transfers (fluxes) are calculated from the data in figures 5.14 and 5.15, using equations (5.2)–(5.6). Figures

5.17 and 5.18 for the films cycled in $\text{TEABF}_4/\text{CH}_3\text{CN}$ and $\text{TEABF}_4/\text{CH}_2\text{Cl}_2$ respectively, show the individual fluxes as functions of potential for two different scan rates (250 and 50 mV s^{-1}). The $\Delta m - E$ (figure 5.16b) curves illustrate that there are definitely differences between the film responses in the two solvents during both the doping and un-doping half cycles. However, the total fluxes (j_T) for the two films in different solvents reveal even more than the mass traces. At first glance, the j_T traces in both solvents look similar, but the magnitudes of the flux excursions are rather different. Analysis of the j_S traces gives the reasons for such a large difference in the size of the flux excursions.

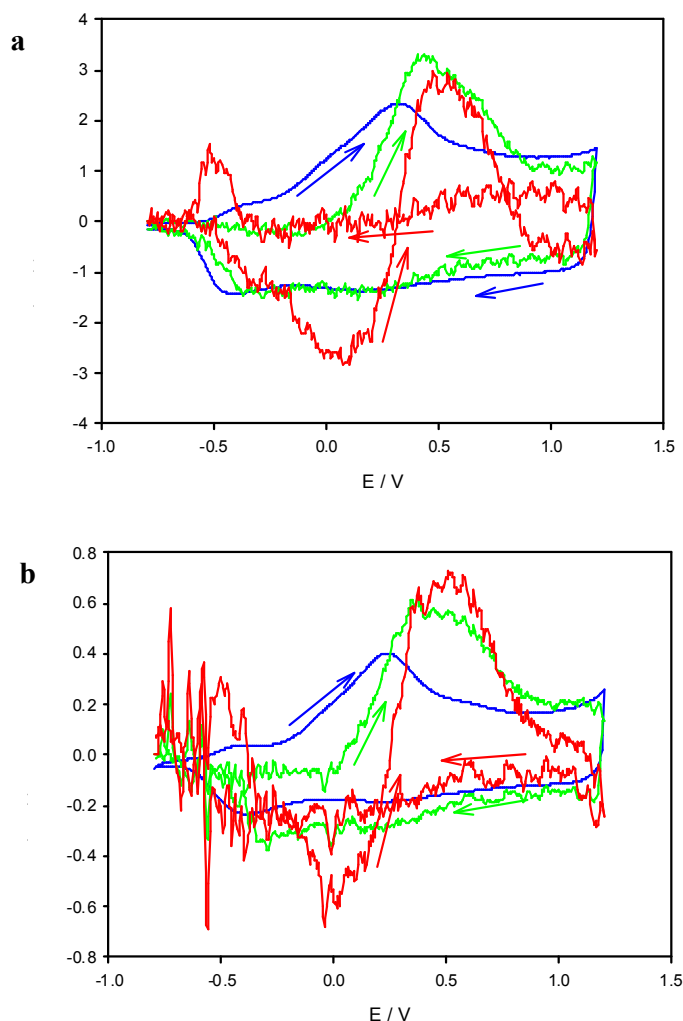


Figure 5.17. Fluxes of mobile species as functions of potential (E) for the experiment of figure 5.14 (CH_3CN solvent) for (a) $v = 250 \text{ mV s}^{-1}$; (b) $v = 50 \text{ mV s}^{-1}$. j_A trace (—) represents coupled electron/anion flux. j_T trace (—) represents combined fluxes of anion and solvent. Solvent flux (j_S) trace (—) calculated by subtracting anion flux (calculated using Faraday's law) from differential mass, see equation (5.6).

The solvent flux for dichloromethane shows a monotonic trace, for which solvent is constantly lost (expulsion), during the doping half cycle. In contrast solvent flux for acetonitrile, during the oxidation half cycle, shows an initial large expulsion followed by ingress of the solvent. The reduction half cycle for the films in both of the solvents are also different, acetonitrile shows a small expulsion of solvent before a final ingress of solvent into the film, but dichloromethane has continuous solvent entry. The solvent flux for the acetonitrile recorded here are analogous to those recorded for the p-doping of the PEDOT film in LiClO_4 in acetonitrile (section 5.5.1)

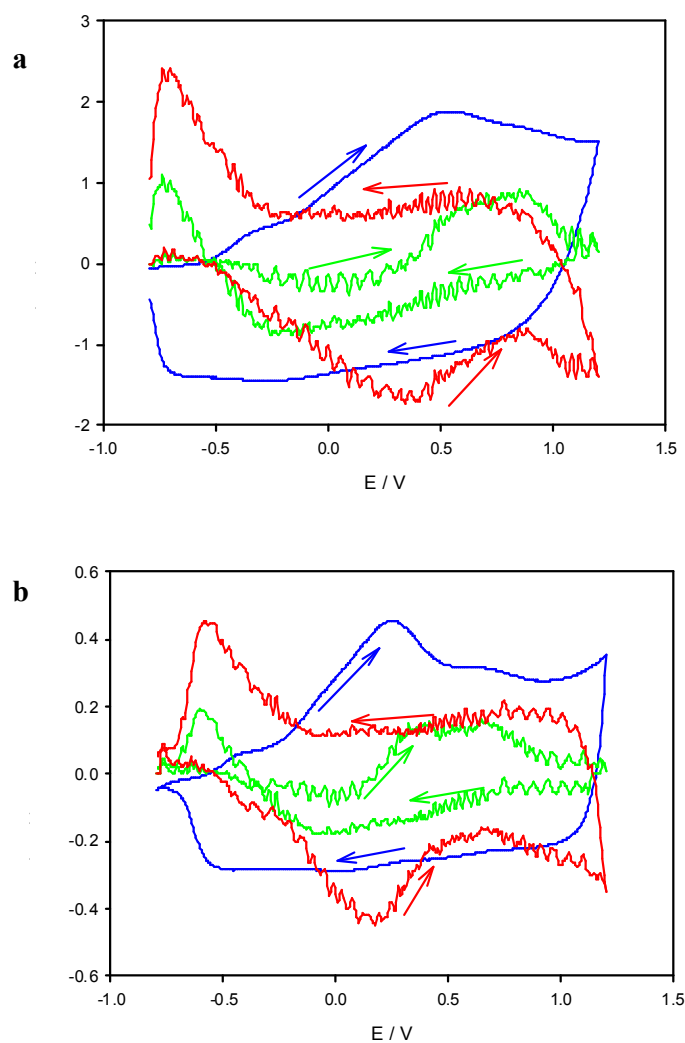


Figure 5.18. Fluxes of mobile species as function of potential (E) for the experiment of figure 5.15 (CH_2Cl_2 solvent) for (a) $v = 250 \text{ mV s}^{-1}$; (b) $v = 50 \text{ mV s}^{-1}$. j_A trace (—) represents coupled electron/anion flux. j_T trace (—) represents combined fluxes of anion and solvent. Solvent flux (j_S) trace (—) calculated by subtracting anion flux (calculated using Faraday's law) from differential mass, see equation (5.6).

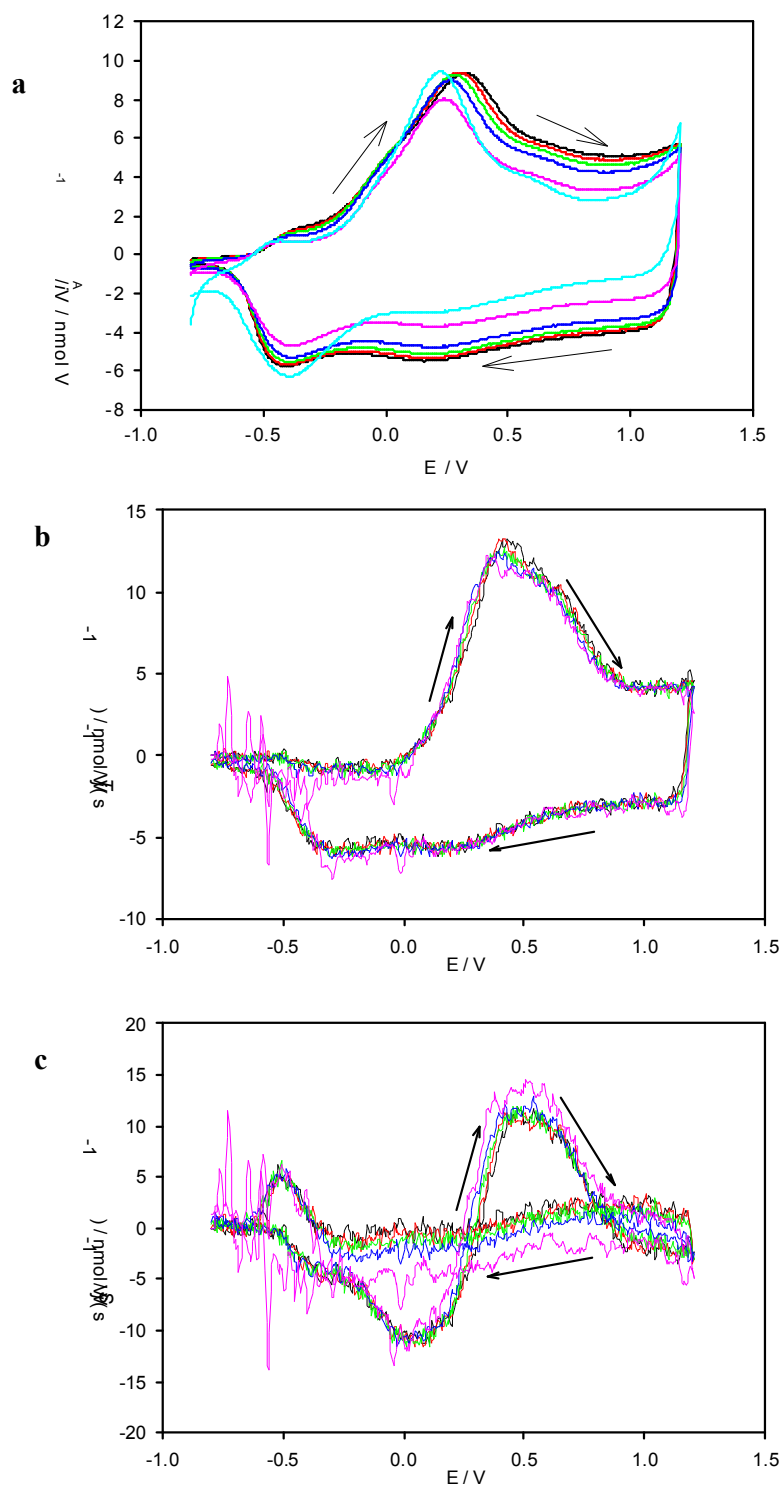


Figure 5.19. Normalized fluxes as functions of applied potential, E for the experiment of figure 5.14 ($\text{TEABF}_4/\text{CH}_3\text{CN}$). Panel a: j_A/v , representing coupled electron/anion transfer; panel b: j_T/v , representing all mobile species (anions and solvent); panel c: j_S/v , representing solvent transfer. Scan rate, $v / \text{mV s}^{-1} = 20$: —; 50: —; 100: —; 150: —; 200: —; 250: —. . . Arrows show the direction of the scan.

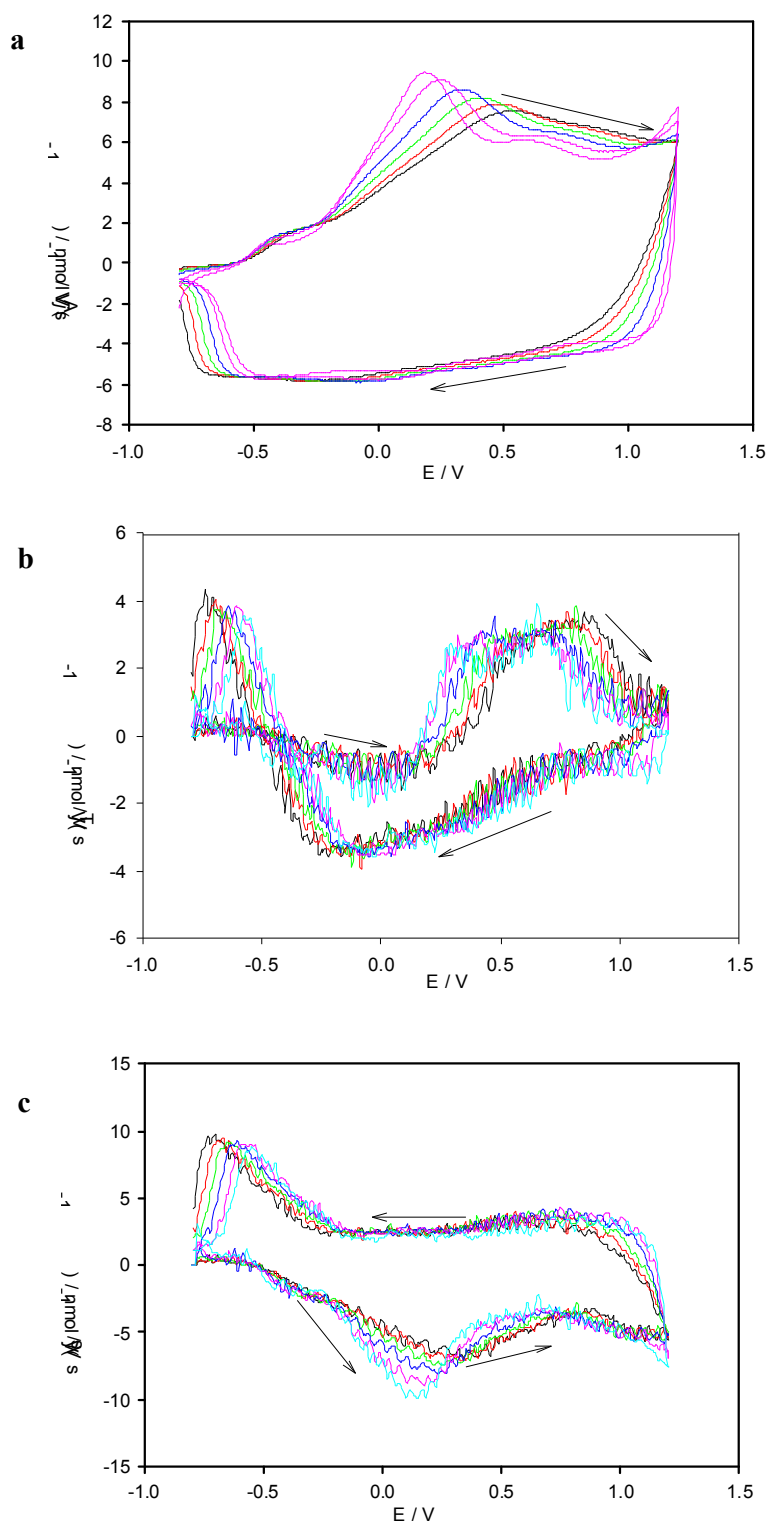


Figure 5.20. Normalized fluxes as functions of applied potential, E for the experiment of figure 5.15 ($\text{TEABF}_4/\text{CH}_2\text{Cl}_2$). Panel a: j_A/v , representing coupled electron/anion transfer; panel b: j_T/v , representing all mobile species (anions and solvent); panel c: j_S/v , representing solvent transfer. Scan rate, $v / \text{mV s}^{-1} = 20$: —; 50: —; 100: —; 150: —; 200: —; 250: —. Arrows show the direction of the scan.

As outlined in section 5.5.1 the main aim is to outline the kinetic and diffusional processes that underlie the above responses. To do this we first need to take into account the scan rate used for each experiment. As suggested previously, “diffusionless” systems, should have a response pattern in which the total population change is independent of timescale and the flux should be linear with scan rate and independent of scan direction. In order to interpret these data, we need to take account of the differing timescales of the experiments; normalizing the fluxes with respect to voltage scan rate does this. The previous case (section 5.5.1) for PEDOT in $\text{LiClO}_4 / \text{CH}_3\text{CN}$ illustrated that both the current and total mass fluxes normalised as functions of potential. The solvent flux also normalised extremely well (except for the lowest scan rate); this is not surprising as the solvent flux is the outcome of equation 5.6, which takes the flux data of the anion from the flux data of the total mass, both of which normalise by the same timescale function. Thus the first test carried out here will be the normalization of j_T and j_S with v for films exposed to acetonitrile and dichloromethane. The results are given in figures 5.19 and 5.20, respectively.

The results obtained for the normalisation with respect to potential for PEDOT in $\text{TEABF}_4/\text{CH}_3\text{CN}$ and $\text{TEABF}_4/\text{CH}_2\text{Cl}_2$, are more complicated than those obtained for PEDOT in $\text{LiClO}_4/\text{CH}_3\text{CN}$. For $\text{TEABF}_4/\text{CH}_3\text{CN}$ the normalisation for ion flux generally works well, although there is an issue with background current for the slower scans. The total mass flux, j_T , responses normalisation is excellent throughout the redox cycle, there is a slight issue with noise levels at slower scan rates. The total mass j_T change is monotonic during each half cycle, showing a constant increase during oxidation and decreasing during reduction. The solvent flux, j_S , also normalises well but unlike the total and anion, which show monotonic traces for both half cycles, the shape is more complex, solvent loss (egress) occurs followed by some solvent ingress during the oxidation cycle. The reduction half cycle is monotonic, solvent continually enters the film throughout and at the end of the cycle a sudden pulse of solvent entry occurs.

For CH_2Cl_2 , normalisation works well for the first half of the oxidation cycle of the $j_A - E$ plot and very well for the majority of the reduction cycle. The first half of the anodic and cathodic branch of the $j_T - E$ plot and most of the reduction and oxidation parts of the

j_S -E plot all normalise well. The dispersion in the j_S -E plot during the first part of oxidation mirrors that in the j_A - E plot.

5.5.3.3 Flux normalization with respect to timescale and film charge state

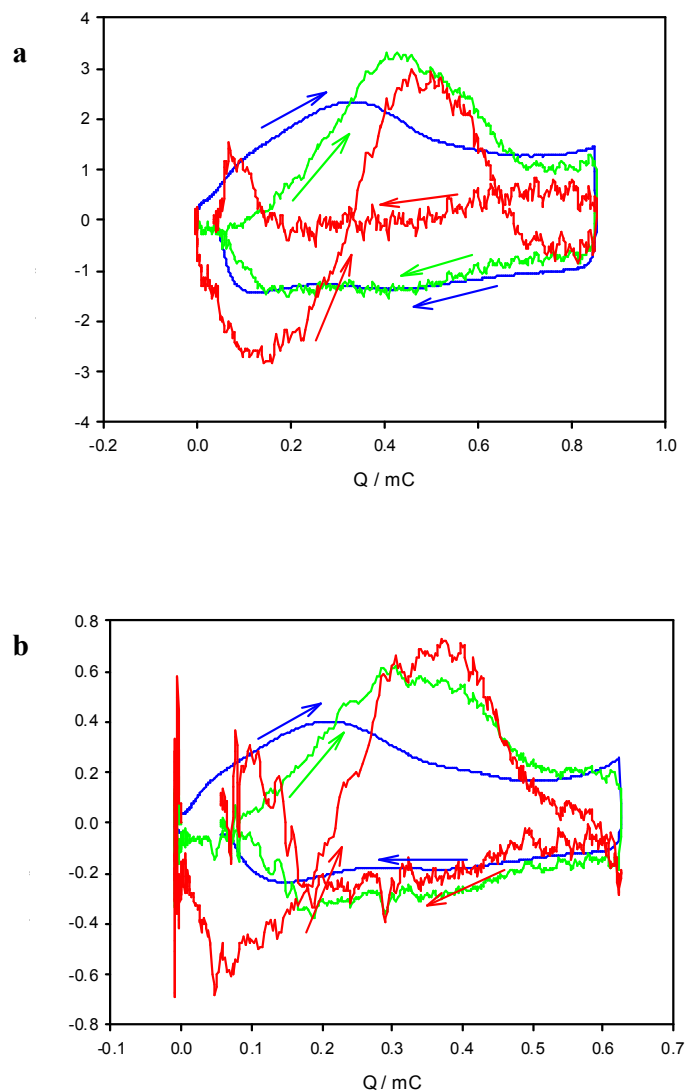


Figure 5.21 Fluxes of mobile species as functions of charge (Q) for the experiment of figure 5.14 (TEABF₄/CH₃CN). (a) 250 mV s⁻¹; (b) 50 mV s⁻¹. Trace (—) represents coupled electron/anion flux j_A , trace (—) represents total flux j_T and solvent flux (j_S) is represented by trace (—).

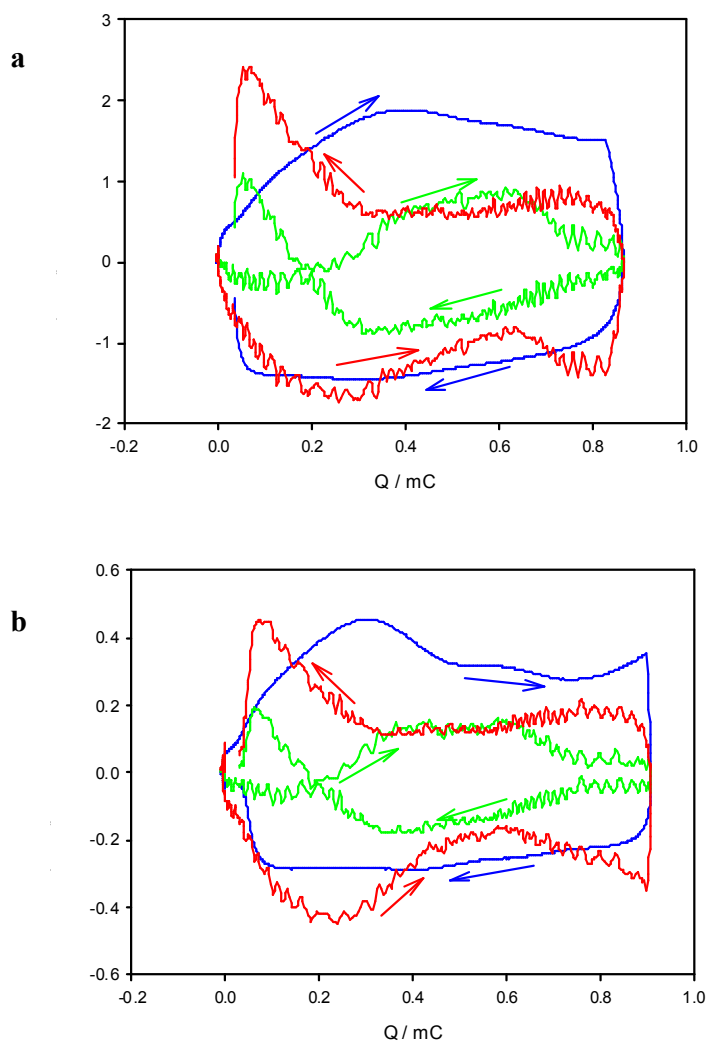


Figure 5.22 Fluxes of mobile species as functions of charge (Q) for the experiment of figure 5.15 (TEABF₄/CH₂Cl₂). (a) 250 mV s⁻¹; (b) 50 mV s⁻¹. Trace (—) represents coupled electron/anion flux j_A , trace (—) represents total flux j_T and solvent flux (j_S) is represented by trace (—).

Plotting the fluxes as a function of film charge state helps to distinguish the more chemical aspects of kinetics and diffusion from the complicated one of ohmic potential drop. Figures 5.21 and 5.22 shows the plots for fluxes vs. charge for films exposed to acetonitrile and dichloromethane, respectively. Both sets of graphs are very similar to their corresponding flux vs. potential plots; the similarities are a direct consequence of their relatively featureless i vs E plots.

In section 5.5.3.2 normalization of j_T and j_S with v was plotted. However, plotting the fluxes against normalised film charge state Q^* (defining normalized charge as $Q^* = Q/Q_T$, where Q_T is the charge for total redox conversion) gives more mechanistic insights. Figure 5.23 and 5.24 show the corresponding flux vs. Q^* for the two different solvents. Once again due to the problems associated with background currents (especially for the slowest scan rate), the flux data is plotted as a function of normalised charge, for which zero corresponds to the fully reduced film and unity to the fully oxidized film, thus avoiding over-interpretation of minor peak shifts.

In section 5.5.1 the observed behaviour for PEDOT in $\text{LiClO}_4 / \text{CH}_3\text{CN}$ shows that the solvent, total and anion fluxes all normalise with respect to scan rate when plotted against either potential or normalised charge. The pattern of behaviour of PEDOT when the dopant is BF_4^- , is more complicated, in the way that normalisation is only successful for some of the Q^* ranges. The significance of the superimposition of the normalisation data is that it confirms that the same processes are taking place and they are not diffusionally or kinetically limited. Figures 5.23 and 5.24 illustrate that for the majority of the oxidation/reduction half cycles the process of normalisation works well

The normalisation process, for electron/anion fluxes, for the redox switching of PEDOT in CH_3CN and CH_2Cl_2 are given in figures 5.23 (a) and 5.24 (a) respectively. During the oxidation half cycle the success of the normalisation procedure differs between the two solvents. With the exception of the slow scan rate, the normalisation works well for only the first half of CH_3CN and the latter half of CH_2Cl_2 of p-doping. In these normalization compliant regions, coupled electron/anion transfer cannot be rate limiting.

Normalised $j_A - Q^*$ plot for the reduction half of the cycle work extremely well when the film is exposed to CH_2Cl_2 . For the case of CH_3CN the normalization generally works to an acceptable degree, except for the slowest scan rate, for the reduction half cycle. Background current correction becomes more of an issue at the slower scan rates, because the background is a larger fraction of the measured signal.

For both solvents there are noticeable closure failures: not all the injected charge is recovered. Closure failure of this kind can be attributed to either trapping phenomena or background currents. If the closure failures were caused by trapping, then there would be a difference in the signature timescales for the different scan rates: slower scan rates would give less trapping, i.e. more time for charge recovery. As there is no difference in the signature timescales then trapping phenomena can be ruled out, thus leaving the observed closure failure as a result of background currents (on the order of $1 \mu\text{A}$ in CH_3CN and considerably less for CH_2Cl_2).

The total mass flux, j_T , responses for both solvents normalize well throughout the redox cycle. There appears to be no problem associated with background: the noise levels at the lower scan rates are high, but do not appear problematic. The j_T - Q^* normalisation works well for the first half of the anodic branch and all of the cathodic branch where the film is exposed to CH_2Cl_2 . The anodic branch shows a monotonic mass change whereas the cathodic trace shows a mass loss followed by a sudden mass gain in the last part of the un-doping process.

When the film is cycled using CH_3CN as the solvent, a monotonic mass change during both the oxidation and reduction half cycles is observed. There is a continuous increase of mass during the oxidation, which is followed by a decrease during the reduction half cycle. The shape of the j_T - Q^* plot is to a certain degree similar to that of the ion flux (figure 5.23 a). This suggests that the mass response is dominated by ion transfer. However, closer inspection shows that the anodic peak has shifted to slightly higher normalised charges.

The total flux (j_T) vs. potential (figures 5.19 and 5.20 b) and total flux vs. normalised charge (figures 5.23 and 5.24 b), normalize extremely well with respect to scan rate. If viewed on their own, one may conclude that all mobile species transfers individually are in equilibrium. However, one has to view these results together with those obtained for the ion flux (figure 5.24 and 5.24 a). This conclusion is then valid for the regions in which both of the fluxes (total mass and solvent) show no dispersion.

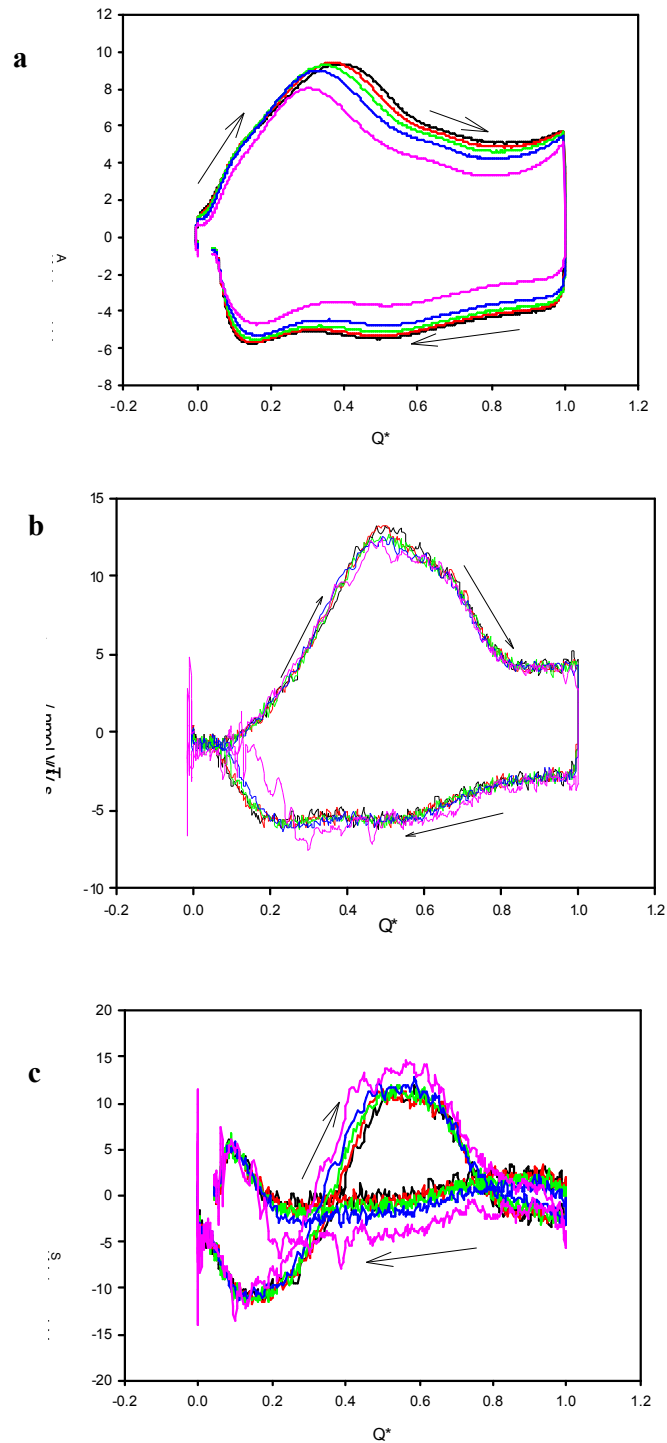


Figure 5.23 Normalized fluxes as functions of normalised charge (Q^*) for the experiment of figure 5.14 ($\text{TEABF}_4/\text{CH}_3\text{CN}$). Panel a: j_A/v , representing coupled electron/anion transfer; panel b: j_T/v , representing all mobile species (anions and solvent); panel c: j_S/v , representing solvent transfer. Scan rate, $v / \text{mV s}^{-1} = 20$: —; 50: —; 100: —; 150: —; 200: —; 250: —.

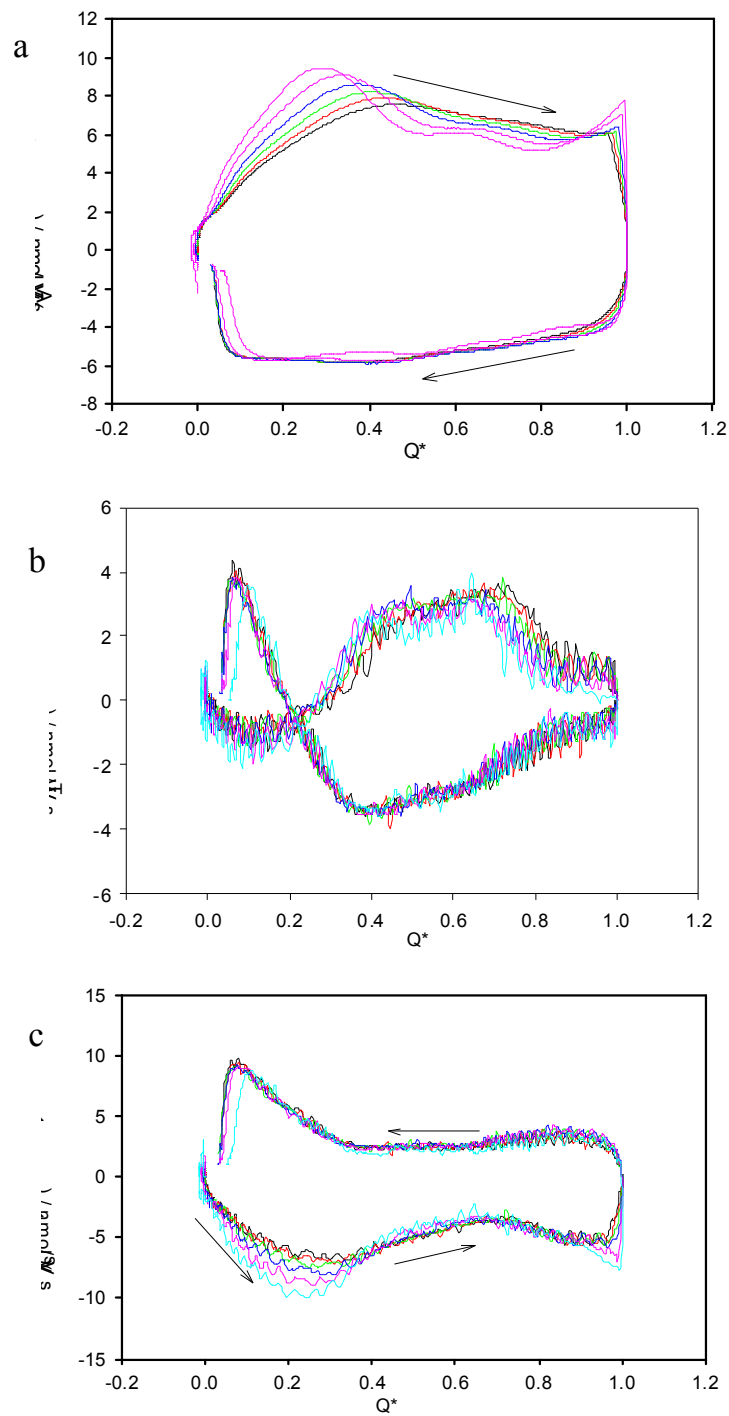


Figure 5.24 Normalized fluxes as functions of normalised charge (Q^*) for the experiment of figure 5.15 ($\text{TEABF}_4 / \text{CH}_2\text{Cl}_2$). Panel a: j_A/v , representing coupled electron/anion transfer; panel b: j_T/v , representing total flux (anions and solvent); panel c: j_S/v , representing solvent transfer. Scan rate, $v / \text{mV s}^{-1} = 20$: —; 50: —; 100: —; 150: —; 200: —; 250: —.

In those regions where total mass flux shows no dispersion, but ion flux does, it is a simple algebraic outcome of equation (5.6) that solvent flux will show dispersion. This dispersion is clear in the first part of the anodic branch of the j_s - Q^* plot for CH_2Cl_2 and to a certain degree for CH_3CN . As the fluxes are in the opposite direction (ion flux show an increase while the solvent flux shows a decrease), a qualitative suggestion for this is that solvent leaves to make way for the anion. The most obvious feature for both solvents in the cathodic branch is the sudden pulse of solvent into the film at the end of the half cycle. In general the processes occurring in both solvents are broadly analogous, but the different solvent characteristics influence both the rates of the processes and their sensitivity to the EQCM as a detector.

An interesting feature of the solvent flux for CH_2Cl_2 (figure 5.24 c) is the abruptness with which the solvent pulse ceases during the reduction half cycle. This sudden stop implies that solvent fills to a maximum capacity of the film and then stops. This sharp cut off is consistent with either zero order or high order kinetics. It is unlikely to be zero order as this would involve a constant rate until the cut off, which we do not see, so zero order may be eliminated.

The normalisation procedure for p-doping works for the first 30% and last 60% for CH_3CN and CH_2Cl_2 respectively. For the regions where the mass flux plot does not show any dispersion but both the solvent and electron/anion transfers do, we suggest that the electron/anion and solvent movement is coupled but kinetically slow. The solvent and electron/anion transfers are in opposite directions: this leads to the conclusion that the departure of solvent is necessary for the entry of anion.

The significance of the flux normalisation used is that, when the results superimpose for the different timescales, the same processes are taking place and they are neither kinetically or diffusionally limited. For the solvents used above (figures 5.23 and 5.24) this appears to be the case for the majority of the p-doping cycle, suggesting that the solvent and ion movements are in equilibrium with the film charge state. However, as there is hysteresis according to the scan direction then they are not in true equilibrium with the applied potential. This suggests that there must be some other chemical process(es) occurring. This means that the redox transformation in the cathodic and the anodic half cycles contain chemically distinguishable species with different redox

potentials. Both solvation changes and polymer reconfiguration would result in a change in redox energetics²⁶. We know that we have solvent changes and believe that there is also polymer reconfiguration. As the mass result indicates solvent transfer and any change in film volume will require polymer reconfiguration, both of these are definitely involved.

In the regions where normalisation works for both the anion and total mass flux, the mechanistic path involves these three elementary steps on timescales that are shorter than the experimental timescale. Thus, they cannot be separated, so the order of the three steps is undistinguishable. It is also impossible to confirm whether or not the solvent transfer and polymer reconfiguration are coupled.

5.5.3.4 Mechanistic possibilities

Section 5.5.1.5 illustrated the use of a 3D cube scheme²⁶ to represent a mechanistic pathway, for which descriptions are given in terms of chemical species (the corners) and electrochemical processes the edges involved in their interconversion. For both of the solvents studied here, a simple 1x1x1 cube scheme is appropriate, as shown in figure 5.9. As described in section 5.5.1.5, O and R symbolise the oxidised and reduced forms of the polymer. Subscript s (or absence thereof) indicates the solvation state and the superscript letters a and b represent the two limiting polymer configuration states²⁶ (the labels are arbitrary). The starting state of the polymer represented here is given by R_s^a , the product at the end of the oxidation half cycle is O^b , and there are 6 (3x2x1) possible mechanistic pathways connecting them in each switching direction²⁶.

5.5.3.4.1 PEDOT film cycled using acetonitrile as the solvent

Illustrated in figure 5.25 is the cube scheme showing the species and mechanistic pathway for the redox switching of TEABF₄ in CH₃CN. During the early stages of the oxidation process (see figures 5.19 and 5.23) all the processes normalise with respect to scan rate, so the overall process can be visualised using a 3D diagonal (figure 5.25 a).



As the scan is moved further along the oxidation cycle the anion and solvent fluxes both fail to normalize with scan rate. Thus solvent transfer is faster than the electron/anion transfer, so an initial desolvation is seen:



This is then followed by the coupled electron/anion transfer, which on the experimental timescale cannot be decoupled from polymer reconfiguration (figure 5.25 b):



In the reduction half cycle the solvent flux is initially low (figures 5.19 and 5.23), indicating that solvent transfer is slow. Again it is not possible to tell if charge transfer or the polymer reconfiguration comes first, so these are represented by the 2D diagonal across the cube face (figure 5.25 c):



This is then followed by the slow ingress of solvent:



The slow solvent transfer observed during the reduction half cycle is indicated by the low solvent flux. This is a complete contrast to what is observed in the oxidation half cycle. At the end of the reduction half cycle there is a pulse of solvent ingress, this indicates that the barrier to solvation is now small thus allowing a sudden influx of solvent. This is illustrated by the 3D diagonal in figure 5.25 d.



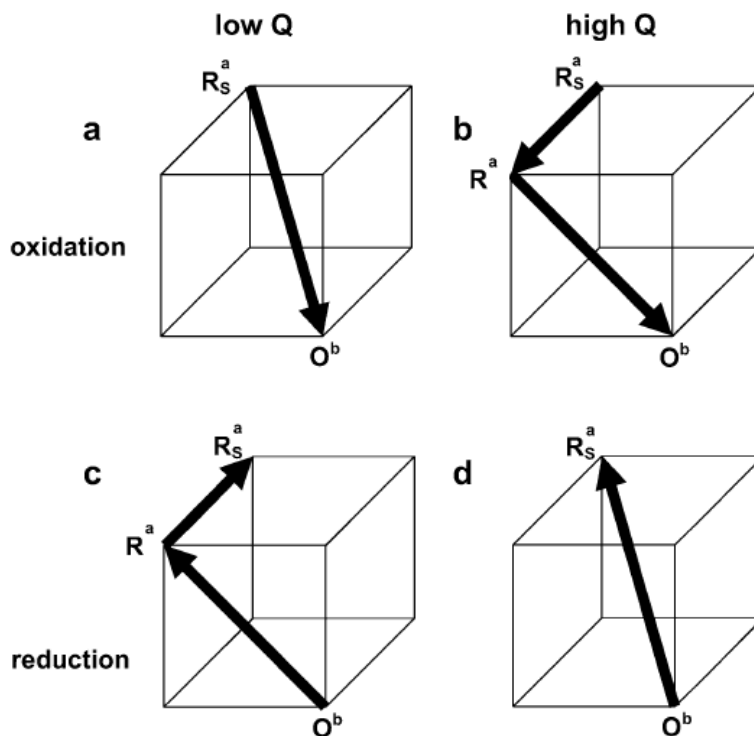


Figure 5.25. Cube scheme showing species and mechanistic pathways for PEDOT in TEABF₄/CH₃CN. Panel a: Oxidation, first stage ($Q^* < 0.3$), of the doping process, solvent and anion transfer occur together; panel b: Oxidation, second stage ($Q^* > 0.3$) of the doping process, solvent makes way for anion; panel c: reduction, first stage ($Q^* > 0.25$) of un-doping process; panel d: reduction second stage ($Q^* < 0.25$) of the un-doping process, sudden ingress of solvent. See reactions 5.9 – 5.14.

5.5.3.4.2 PEDOT film cycled using dichloromethane as the solvent

During the early stages of oxidation of PEDOT cycled in TEABF₄/CH₂Cl₂ solution, there is a coupled electron/anion and solvent transfer. This corresponds to the diagonal transfer across the horizontal plane of the cube (figure 5.26 a)



This is followed by the polymer reconfiguration:



As more charge is injected, the timescale dispersion for the mobile species transfer disappears. Thus a degree of normalisation occurs, so species transfer is represented as a 3D diagonal across through the cube (figure 5.26 b).



As with the response of PEDOT in acetonitrile, in the reverse direction initially the solvent flux is low, indicating that solvent transfer is slow. It is not possible to say if the reconfiguration precedes or follows the charge transfer step, so these are represented by the 2D diagonal across the cube face (figure 5.26 c):



This slow solvation step is then followed by followed by:



At the end of the reduction half cycle there is a pulse of solvent ingress. This indicates that the barrier to solvation is now small thus allowing a sudden influx of solvent. This is illustrated by the 3D diagonal in figure 5.26 d.



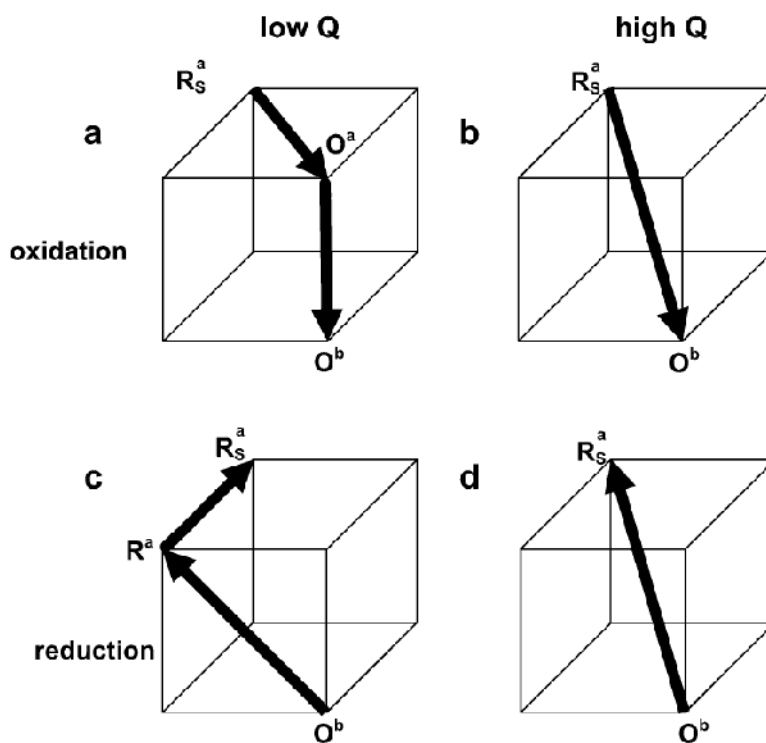


Figure 5.26 Cube scheme showing species and mechanistic pathways for PEDOT redox switching in $\text{TEABF}_4/\text{CH}_2\text{Cl}_2$. Nomenclature as in main text. Panel *a*: first stage ($Q^* < 0.35$) of doping process; panel *b*: second stage ($Q^* > 0.50$) of doping process; panel *c*: first stage ($Q^* > 0.15$) of un-doping process; panel *d*: second stage ($Q^* < 0.10$) of un-doping process. Only species involved are shown; see reactions (5.15)-(5.20).

5.6 Conclusions

There has been a wide range of studies for which the EQCM has been used with cyclic voltammetry to investigate electroactive polymer films. Thus there is a substantial repository of data representing both stoichiometric and mechanistic information. However, the majority of this data places emphasis on the complete redox cycle, i.e. averaging the response obtained at each end. During this chapter it is shown that considering the mass response for the redox process provides both mechanistic and stoichiometric information for partial film conversion. The use of time differentials lead to information on both mass (total mass, includes both solvent and ion mass transfer) and charge transfers. The use of the electroneutrality condition and Faraday's law enables the subtraction of the two fluxes to yield the solvent flux.

The EQCM coupled with cyclic voltammetry has enabled the exploration of dynamics of permselective films. Modern instrumentation has enabled the calculation of solvent flux with a precision down to 50 pmol s^{-1} and a time resolution of about 0.01 s . This means that it is possible to test for normalisation of the ion and solvent fluxes, offering an extension of mechanistic interpretative experiments.

Application of this approach to PEDOT films exposed to $\text{LiClO}_4/\text{CH}_3\text{CN}$, $\text{TEABF}_4/\text{CH}_3\text{CN}$ and $\text{TEABF}_4/\text{CH}_2\text{Cl}_2$ has led to exploration of the p-doping/un-doping mechanism under permselective conditions. For the case of $\text{LiClO}_4/\text{CH}_3\text{CN}$ both the solvent and anion fluxes normalise, whether viewed as a function of normalised charge or potential. The observed results, show that even though the normalisation process works well for the doping and un-doping half cycles, they proceed through different mechanistic paths. This suggests that polymer reconfiguration is a participant within the process. The scheme of cubes representation gives a visual mechanism for which there are three elementary steps; coupled electron/anion transfer, solvent transfer and polymer reconfiguration. However, on the experimental timescale used the resolution of the solvent transfer and polymer reconfiguration is not possible. Thus the scheme of cubes is reduced to a square.

For the case of the PEDOT film cycled in $\text{TEABF}_4/\text{CH}_2\text{Cl}_2$ the process is a little more complicated than the analogous film cycled in $\text{TEABF}_4/\text{CH}_3\text{CN}$. The normalised fluxes for PEDOT cycled in both $\text{TEABF}_4/\text{CH}_3\text{CN}$ and $\text{TEABF}_4/\text{CH}_2\text{Cl}_2$ are chemically but not thermodynamically reversible. At partial redox conversion during both the doping and un-doping half cycles there is a mechanistic switch, for which is observed for both solvents. However the specific mechanisms are different for the two solvents. The mechanistic differences between the two solvents are characterised by the different patterns of deviation shown in the experimentally measured electron/anion and solvent fluxes from the predicted values on the basis of scan rate normalization. The comparison of the ion and solvent fluxes illustrates that the ingress and egress of solvent rates are a key fact in determining the mechanism. There are changes between kinetically limiting and rapid solvent transfer for both scan directions, which is dependent on the solvent identity.

References

- (1) *Handbook of Conducting Polymers*, 2nd ed.; Marcel Dekker, New York, 1998.
- (2) Chandrasekhar, P. *Conducting Polymers, Fundamentals and Applications. A practical Approach*; Kluwer Academic Publishers, Boston, 1999.
- (3) Demanze, F.; Cornil, J.; Garnier, F.; Horowitz, G.; Valat, P.; Yassar, A.; Lazzaroni, R.; Bredas, J. L. *J. Phys. Chem. B* **1997**, *101*, 4553-4558.
- (4) Dkhissi, A.; Beljonne, D.; Lazzaroni, R.; Louwet, F.; Groenendaal, L.; Bredas, J. L. *Inter. J. Quantum Chem.* **2003**, *91*, 517-523.
- (5) Harrison, M. G.; Fichou, D.; Garnier, F.; Yassar, A. *Optical Mater.* **1998**, *9*, 53-58.
- (6) Rodriguez, M.; Romero, I.; Sens, C.; Llobet, A.; Deronzier, A. *Electrochim. Acta* **2003**, *48*, 1047-1054.
- (7) Deronzier, A.; Moutet, J. C. *Coord. Chem. Rev.* **1996**, *147*, 339-371.
- (8) Kong, Y. T.; Boopathi, M.; Shim, Y. B. *Biosensors & Bioelectronics* **2003**, *19*, 227-232.
- (9) Roncali, J. *Chem. Rev.* **1992**, *92*, 711-738.
- (10) Blanchard, F.; Carre, B.; Bonhomme, F.; Biensan, P.; Pages, H.; Lemordant, D. *J. Electroanal. Chem.* **2004**, *569*, 203-210.
- (11) Bund, A.; Neudeck, S. *J. Phys. Chem. B* **2004**, *108*, 17845-17850.
- (12) Carlberg, C.; Chen, X. W.; Ingnas, O. *Solid State Ionics* **1996**, *85*, 73-78.
- (13) Niu, L.; Kvarnstrom, C.; Ivaska, A. *J. Electroanal. Chem.* **2004**, *569*, 151-160.
- (14) Pei, Q. B.; Zuccarello, G.; Ahlskog, M.; Ingnas, O. *Polymer* **1994**, *35*, 1347-1351.
- (15) Pigani, L.; Heras, A.; Colina, A.; Seeber, R.; Lopez-Palacios, J. *Electrochem. Comm.* **2004**, *6*, 1192-1198.
- (16) Plieth, W.; Bund, A.; Rammelt, U.; Neudeck, S.; Duc, L. M. *Electrochim. Acta* **2006**, *51*, 2366-2372.
- (17) Roncali, J.; Blanchard, P.; Frere, P. *J. Mater. Chem.* **2005**, *15*, 1589-1610.
- (18) Hughes, G.; Bryce, M. R. *J. Mater. Chem.* **2005**, *15*, 94-107.
- (19) Cutler, C. A.; Bouguettaya, M.; Kang, T. S.; Reynolds, J. R. *Macromolecules* **2005**, *38*, 3068-3074.
- (20) Groenendaal, L.; Zotti, G.; Aubert, P. H.; Waybright, S. M.; Reynolds, J. R. *Adv. Mater.* **2003**, *15*, 855-879.
- (21) Mortimer, R. J. *Electrochim. Acta* **1999**, *44*, 2971-2981.
- (22) Careem, M. A.; Vidanapathirana, K. P.; Skaarup, S.; West, K. *Solid State Ionics* **2004**, *175*, 725-728.
- (23) Smela, E. *Adv. Mater.* **2003**, *15*, 481-494.
- (24) Dietrich, M.; Heinze, J.; Heywang, G.; Jonas, F. *J. Electroanal. Chem.* **1994**, *369*, 87-92.
- (25) Hillman, A. R. "The electrochemical quartz crystal microbalance", in *Encyclopaedia of Electrochemistry*; Wiley, New York, 2003.
- (26) Hillman, A. R.; Bruckenstein, S. *J. Chem. Soc.-Faraday Trans.* **1993**, *89*, 339-348.
- (27) Arnau, A.; Jimenez, Y.; Fernandez, R.; Torres, R.; Otero, M.; Calvo, E. J. *J. Electrochem. Soc.* **2006**, *153*, C455-C466.
- (28) Hillman, A. R.; Efimov, I.; Ryder, K. S. *J. Am. Chem. Soc.* **2005**, *127*, 16611-16620.
- (29) Randriamahazaka, H.; Plesse, C.; Teyssie, D.; Chevrot, C. *Electrochim. Acta* **2005**, *50*, 1515-1522.
- (30) Bruckenstein, S.; Shay, M. *Electrochim. Acta* **1985**, *30*, 1295-1300.

- (31) Sauerbrey, G. *Z. Phys.* **1959**, *155*, 206.
- (32) Henderson, M. J.; Hillman, A. R.; Vieil, E. *Electrochimica Acta* **2000**, *45*, 3885-3894.

CHAPTER 6

N-DOPING OF PEDOT

6.1 Introduction

There are two methods of doping conducting polymers, both involving oxidation-reduction processes. One method, chemical doping, involves exposing the polymer to an oxidising agent such as iodine, or less commonly, a reducing agent such as an alkali metal. The second method of doping a conducting polymer, and the method used here, is electrochemical doping. The electrochemical doping of a conducting polymer is carried out in an electrochemical cell in which the polymer-coated working electrode is suspended in an electrolyte solution along with a counter electrode and a reference electrode. A potential difference is created between the working and reference electrodes, which causes electronic charge, along with the counter ion, to enter or leave the polymer in either an n-doping (reduction) or p-doping (oxidation) process.

There are many studies illustrating the p-doping process for many different conducting polymers, however relatively few examples of n-doping. The reason n-doping is not so common is because the earth's atmosphere is rich in oxygen, leading to an oxidising environment. A polymer that has been n-doped will react immediately with the oxygen within the atmosphere, un-doping (oxidising) it back to its neutral form. Therefore n-doping has to be carried out in oxygen free environment, which is more challenging for both fundamental studies and practical applications.

Polyheterocycles possess a unique combination of optical, electrochemical and electronic properties. Thus over the last two decades^{1, 2}, a lot of attention has been given to polymers based on thiophene and pyrrole. PEDOT (from the thiophene family) has attracted a huge interest³⁻¹⁰. The presence of the ether groups on the conjugated ring leads to a highly conjugated linear molecule¹¹. The ether groups not only eliminate problems associated with cross-linking and regioisomerism, but also stop attack at the 3- and 4-position, thereby preventing polymer degradation and increasing its stability. The ether groups on the conjugated ring also provide a means to manipulate electronic properties and decrease the band gap. These characteristics have

led to investigation into PEDOT being used as the active material in electrochromic displays¹²⁻¹⁴, artificial muscles and actuators^{15, 16} and electroluminescence¹⁷.

The p-doping of PEDOT has been well studied^{3-7, 9, 11, 18} and has been discussed in chapter 5. Here we look at PEDOT's ability to be both n- and p-doped, which may be accredited to its unique electronic band structure. Inganas⁴ was the first person to report the electrochemical reduction (n-doping) of PEDOT. Since then other studies have shown that the combination of both p- and n-doping has made PEDOT a prime candidate for supercapacitors¹⁹⁻²¹ and rechargeable batteries^{2, 22, 23}.

In chapter 5 it was demonstrated how the EQCM charge and mass data in differential form can lead to kinetic and mechanistic features, also allowing the exploration of solvent and ion transfer at partial redox conversion. In chapter 5, attention was solely placed on the p-doping of the undoped (neutral) PEDOT. The primary focus of this chapter will be the analysis of the n-doping of the neutral polymer, using the EQCM as a gravimetric probe of dopant (cation) and solvent transfer. Extension to the n-doping experiments will involve consecutive p- and n-doping of the polymer film. Previous observations of the n-doping half cycle have focused mainly on the overall changes: here the response at partial conversion will be analysed.

6.2 Aims and objectives

There has been a wide range of studies for which the EQCM has been used to investigate the electroactive films such as PEDOT. Chapter 5 demonstrated how the use of charge and mass responses obtained from the EQCM during the redox process provides both mechanistic and stoichiometric information for the partial film conversion. In common with many other studies, chapter 5 was restricted to the analysis of the p-doping region of PEDOT films. Here the aim is to compliment these studies in the following respects:

- Explore the effects of partial film redox conversion for the n-doping region of PEDOT
- Consider the fluxes (time differentials of populations) of both dopant and solvent for the n-doping region

- Explore the effect of experimental timescale on these fluxes
- Explore the effects of consecutive p- and n-doping redox conversions for three different electrolytes
- Explore the trapping phenomena
- Consider the fluxes of both dopant and solvent for the consecutive p- and n-doping of PEDOT and the effect of experimental timescale on these fluxes.

Here we aim not only to give specific insights for PEDOT, but also pave the way for the interpretational methodology developed to be used on EQCM data obtained for other electroactive films.

6.3 Procedure

The electrochemical preparation of PEDOT films has been described in sections 3.6.3 and 5.3. Here PEDOT films with similar thickness to those in chapter 5, have been prepared for characterisation using EQCM.

To ensure the film was acoustically thin (rigid) and avoid obtaining results that correspond to viscoelastic responses of thicker films^{3, 4, 24, 25}, the crystal admittance was recorded both before and after deposition using an Agilent E5061 network analyzer.

Following deposition, films were rinsed with CH₃CN and transferred to monomer-free electrolyte solution for voltammetric characterization. Before the voltammetric characterisation of the films, a preconditioning procedure was carried out. This involved cycling the film 3 – 4 times (until the response was reproducible) in monomer-free electrolyte. This ensured that there was complete exchange of electrolyte from that of the deposition solution to that of the solution being used for characterisation. For each film the coulometric assay of surface coverage of the polymer (Γ / mol cm⁻²) was determined using the voltammetric responses of the p-doping region (at slow scan rate). The generally accepted value for the dopant level, in terms of monomer units for the p-doping is $n = 0.30$ ^{1, 2}; here the comparison the charge associated with the film deposition (Q_{dep}) and the p-doping ($Q_{\text{p-dop}}$) gave $n = 0.29$, which is very close to the accepted value.

Cyclic voltammetric experiments were performed on PEDOT films (different films of similar thickness were used) cycled in tetraethylammonium tetrafluoroborate (TEABF₄, Aldrich), tetrapropylammonium tetrafluoroborate (TPABF₄, Aldrich), or tetraethylammonium tosylate (TEATos, Aldrich) in acetonitrile (Aldrich 99.8 % stored over 4 Å molecular sieves). The solvent containing the electrolyte was de-oxygenated by purging with dry nitrogen before the start of each film analysis; during the measurements the nitrogen stream was directed across the surface of the solution in order to maintain the inert atmosphere.

The EQCM instrumentation, has been previously described²⁶; it consisted of a conventional three-electrode cell (nominally sealed from the laboratory atmosphere) with an Ag wire pseudo reference electrode and a Pt counter electrode. The working electrode (piezoelectric and electrochemically active areas 0.21 and 0.23 cm², respectively) was one of the Au electrodes of a 10 MHz AT-cut polished quartz crystal (ICM, Oklahoma City, OK): this electrode was exposed to the solution and the other electrode was exposed to air. The potential was supplied by a PGSTAT 20 Autolab, which was controlled by GPESW 4.2 computer software. All measurements were made at room temperature, 20 (±2) °C. Reliability of the results and film stability were confirmed by the repetition of the measurement at the first scan rate at the end of a set of measurements at different scan rates.

6.4 Data analysis

The data analysis used here was practically the same as that applied to the PEDOT p-doping in chapter 4^{27, 28}. There are two assumptions that are made during the data analysis. The first is that the films are acoustically thick (rigid): this was confirmed by the results obtained using the network analyser and interpreted using the Sauerbrey equation²⁹(equation 5.1). The second assumption is that the films are permselective. This means that the total mass change ($\Delta m_T/g$) recorded by the EQCM has contributions from the solvent and counterion transfer, but no co-ion participation. Section 5.5.3 demonstrated that, at the low concentrations used here, the measurements are independent of electrolyte concentration. Therefore the films are permselective.

However this situation is compromised when the film is subjected to sequential p- and n-doping. This is addressed with the benefit of the experimental data (see below). The measured current responses for film-coated electrodes were corrected for background currents observed at bare electrodes in the corresponding electrolyte. A five point moving average smoothing process was carried out on flux data.

The data analysis here involves three main steps: (i) the measured current is associated with the ion flux (electron flux); (ii) this is then converted to ion mass flux, using Faraday's law and the ion molar mass; (iii) the solvent flux is then obtained by subtracting this ion mass flux from the total mass flux (time differential of the mass). The EQCM frequency data obtained was interpreted gravimetrically using the Sauerbrey equation²⁹. Total mass flux was then obtained by differentiation (with respect to time) of the gravimetric result. The total mass change ($\Delta m_T / g$) at any stage of the redox process is made up of contributions from both the solvent (Δm_S) and ion (Δm_I) transfer. Here we focus on dynamics so only time differentials of the mass contributions will be considered. These are related by:

$$m'_T = m'_I + m'_S \quad (6.1)$$

where the prime indicates a time derivative and the subscript letter indicates the species, I = A (anion, during p-doping) *or* C (cation, during n-doping). We want the stoichiometry of the processes so it is helpful to express each of the species in terms of their fluxes $j / \text{mol s}^{-1}$. As outlined in chapter 5, ion flux is given by;

$$j_I = \frac{m'_I}{M_I} = \frac{i}{z_I F} \quad (6.2)$$

where M ($/ \text{g mol}^{-1}$) is the molar mass of the subscripted species and, in the case of the ions, z_I is its charge.

Total mass flux is:

$$j_T = \frac{m'_T}{M_I} \quad (6.3)$$

Equation 6.2 illustrates that there is no single molar mass that will normalise m'_T , as there are at least two contributing species. Defining total mass flux as in equation 6.3 allows immediate determination of solvent transfer. If no solvent transfer occurs then $j_T = j_I$, thus any difference between j_T and j_I indicates the extent of solvent transfer which may be defined by;

$$j_S = \frac{m'_S}{M_S} \quad (6.4)$$

Solvent flux is then obtained by combining equations (6.1) and (6.2):

$$j_S = \left(m'_T - \frac{i}{z_I F} \right) / M_S \quad (6.5)$$

6.5 Results

6.5.1 Overview of n-doping process

Figures 6.1 and 6.2 show the EQCM responses (panel a: i-E responses; and panel b: Δm -E responses) for the n-doping of two representative PEDOT films exposed to 0.1 mol dm⁻³ TEABF₄/CH₃CN and TPABF₄/CH₃CN, respectively. Both electrolytes give current responses (panel a) that are similar to previous reports illustrating n-doping of PEDOT^{7, 30, 31} and other polythiophene derivatives^{4, 32, 33}. The reduction half cycle for both electrolytes shows a small shoulder at $E \approx -1.75$ V and $E \approx -1.65$ V for TEABF₄ and TPABF₄ respectively. The un-doping of the polymer occurs at around $E \approx -1.90$ V and $E \approx -1.70$ V for the two electrolytes, signified by the presence of a single peak during the oxidation cycle. The mass responses (figures 6.1 and 6.2, panels b) illustrate that there is a significant mass increase during the reduction half cycle, which would imply that there is movement of mobile species into the film. However, there is a small mass loss during the first part of the reduction half cycle, which suggests that there is probably transfer of two species in opposite directions. During the oxidation half cycle there is a mass change that is monotonic and shows a decrease in mass from the film.

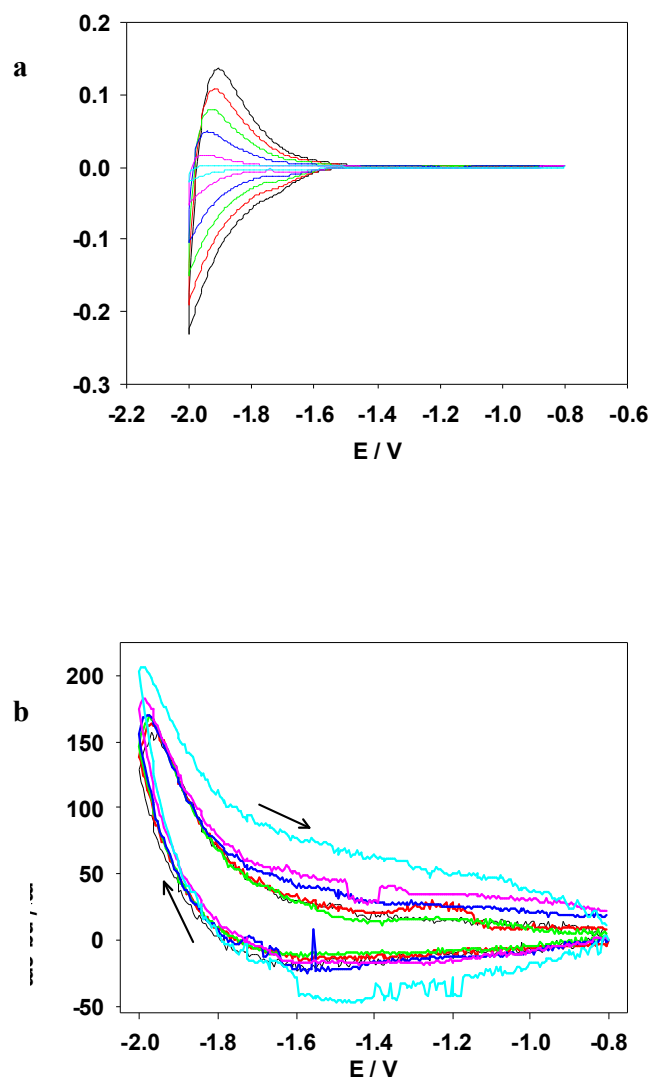


Figure 6.1 Experimental EQCM data for a cyclic voltammetric experiment involving n-doping of a representative PEDOT film ($\Gamma = 198 \text{ nmol cm}^{-2}$) exposed to 0.1 mol dm^{-3} TEABF₄ / CH₃CN. Scan rate, $v / \text{mV s}^{-1} = 20$: —; 50: —; 100: —; 150: —; 200: —; 250: —. Panel a: i vs E ; panel b: Δm vs E . Film mass changes calculated using Sauerbrey equation (5.1).

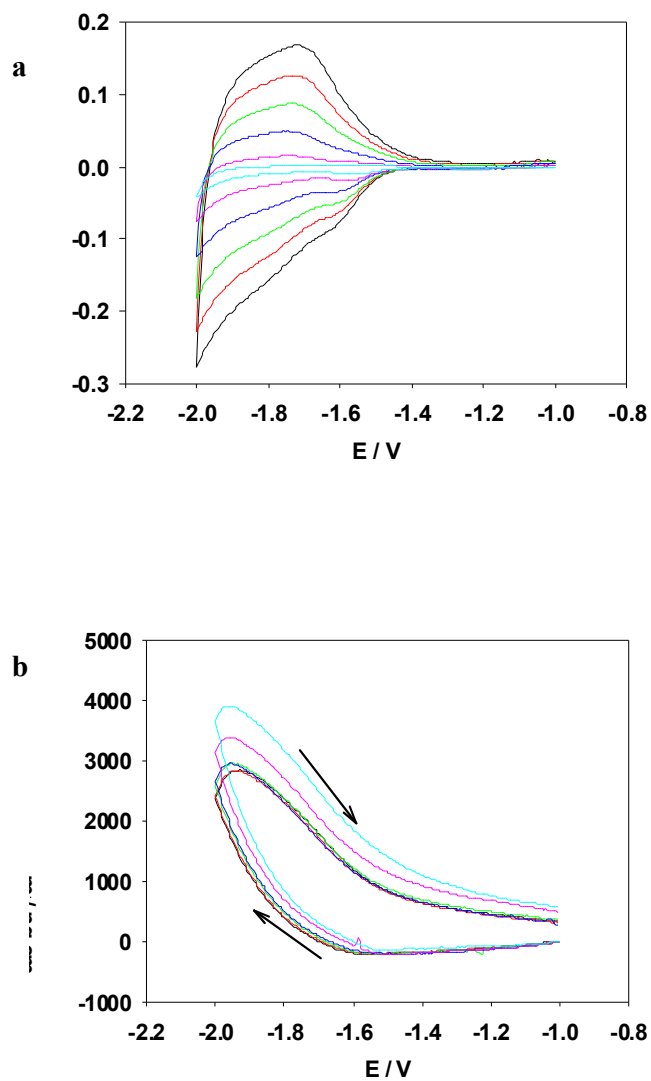


Figure 6.2 Experimental EQCM data for a cyclic voltammetric experiment involving n-doping of a representative PEDOT film ($\Gamma = 213 \text{ nmol cm}^{-2}$) exposed to 0.1 mol dm^{-3} TPABF₄ / CH₃CN. Scan rate, $\nu / \text{mV s}^{-1} = 20$: —; 50: —; 100: —; 150: —; 200: —; 250: —. Panel a: i vs E ; panel b: Δm vs E . Film mass changes calculated using Sauerbrey equation (5.1).

6.5.2 Mobile species fluxes during n-doping

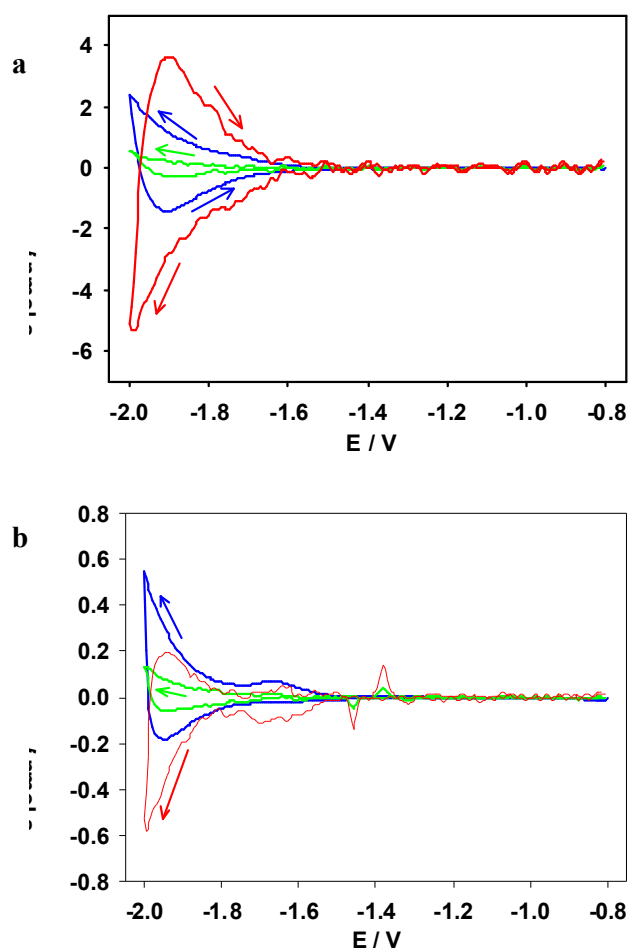


Figure 6.3 Fluxes, calculated using eqs. (3), (5) and (6), as functions of potential (E). Data from Figure 6.1 (exposed to TEABF_4). Panel a: $v = 250 \text{ mV s}^{-1}$; panel b: $v = 50 \text{ mV s}^{-1}$. j_I — blue —; j_T — green —; j_s — red —.

The individual solvent, total and ion fluxes were calculated from the data obtained in figures 6.1 and 6.2 using equations (6.1) - (6.5). The resulting j (flux)- E plots for two different scan rates are given in figures 6.3 and 6.4 for $\text{TEABF}_4/\text{CH}_3\text{CN}$ and $\text{TPABF}_4/\text{CH}_3\text{CN}$, respectively. The qualitative result for TEABF_4 is that the total mass change is much smaller than one would anticipate for a simple electroneutrality-based coupled electron/cation transfer process. The probable cause of such a small mass change is the large amount of solvent transfer. The fluxes in Figures 6.3 and 6.4 are expressed in molar rather than mass terms. It is worth noting that one cation is the

gravimetric equivalent to around three solvent molecules. Also, unlike p-doping, the ion (cation) flux in the n-doping process is in the opposite direction to the electron flux

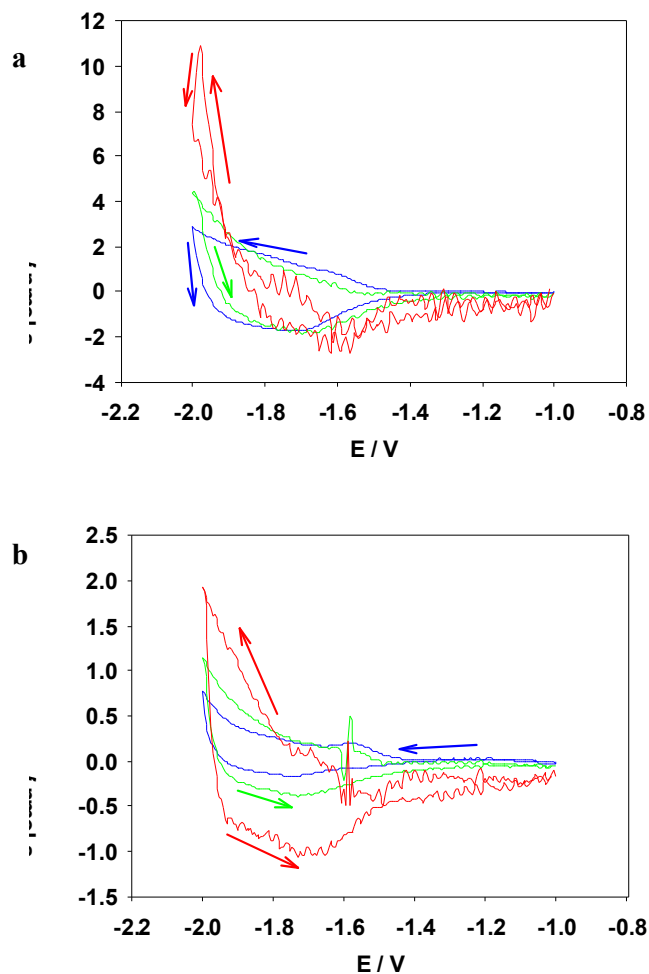


Figure 6.4 Fluxes, calculated using eqs. (3), (5) and (6), as functions of potential (E). Data from Figure 6.1 (exposed to TPABF_4). Panel a: $v = 250 \text{ mV s}^{-1}$; panel b: $v = 50 \text{ mV s}^{-1}$. j_I — blue —; j_T — green —; j_s — red —.

This compensatory motion may be explored further by comparing the results of TEA^+ (figure 6.3) with those obtained for the larger cation TPA^+ (figure 6.4). The comparison shows that the overall magnitudes of the ion fluxes for the two films are similar (as expected for two films of nominally similar electroactive site surface coverage). However the patterns of solvent transfer are very different. The comparison of the total mass fluxes clearly shows a difference for the two cations. There is a much smaller ion flux for TEA^+ than that of TPA^+ . When the solvent fluxes are calculated for the two

cases it is noticeable that TEA^+ has a compensatory motion situation (i.e. the solvent and cation transfers are in opposite directions). In contrast, the solvent and TPA^+ transfers, with a small exception in the early stages of n-doping, are primarily in the *same* direction. It is presumed that this is a consequence of different solvation energetics, although this cannot be predicted from electrochemical data alone.

As previously suggested in chapter 5, for surface immobilised species that do not have any kinetic or diffusional complications, the response pattern should show that the total population change is independent of timescale and the flux is linear with scan rate and independent of scan direction. The standard test for this is a current response that normalises with respect to voltage scan rate. Here this concept is extended to the j_T and j_S data. Normalisation of the flux data may be carried out by simply dividing the flux data by its corresponding scan rate. The outcomes of this procedure for each of the fluxes as a function of potential are shown in figures 6.5 and 6.6 for TEABF_4 and TPABF_4 , respectively.

Figure 6.6 shows the normalisation for a PEDOT film cycled in TPABF_4 . The general pattern here is that the ion, solvent and total mass fluxes, with the exception of those at very slow scan rates, normalise extremely well with respect to potential scan rate. This illustrates that there is no question of timescale dependent dispersion. It is also noticeable from figure 6.6 (panels a and c) that the solvent and ion move in the same direction, which is in complete contrast to that observed for TEABF_4 (figure 6.5).

Figure 6.5 shows the normalisation results for a PEDOT film cycled in TEABF_4 (figure 6.3). Here the solvent and ion fluxes normalise well with respect to potential scan rate, demonstrating complete redox conversion on the timescale of the experiment. The total mass flux also normalises very well, although it is noticeably small and noisy. This is because the movement of ions and solvent in the opposite directions results in a very small measured total mass signal. Thus it appears that the film volume does not change very much because the two species of similar density exchange places. The very slow scan rate appears to be an exception to this behaviour. However, slow scan rates are vulnerable to background currents so no further interpretation of this is made.

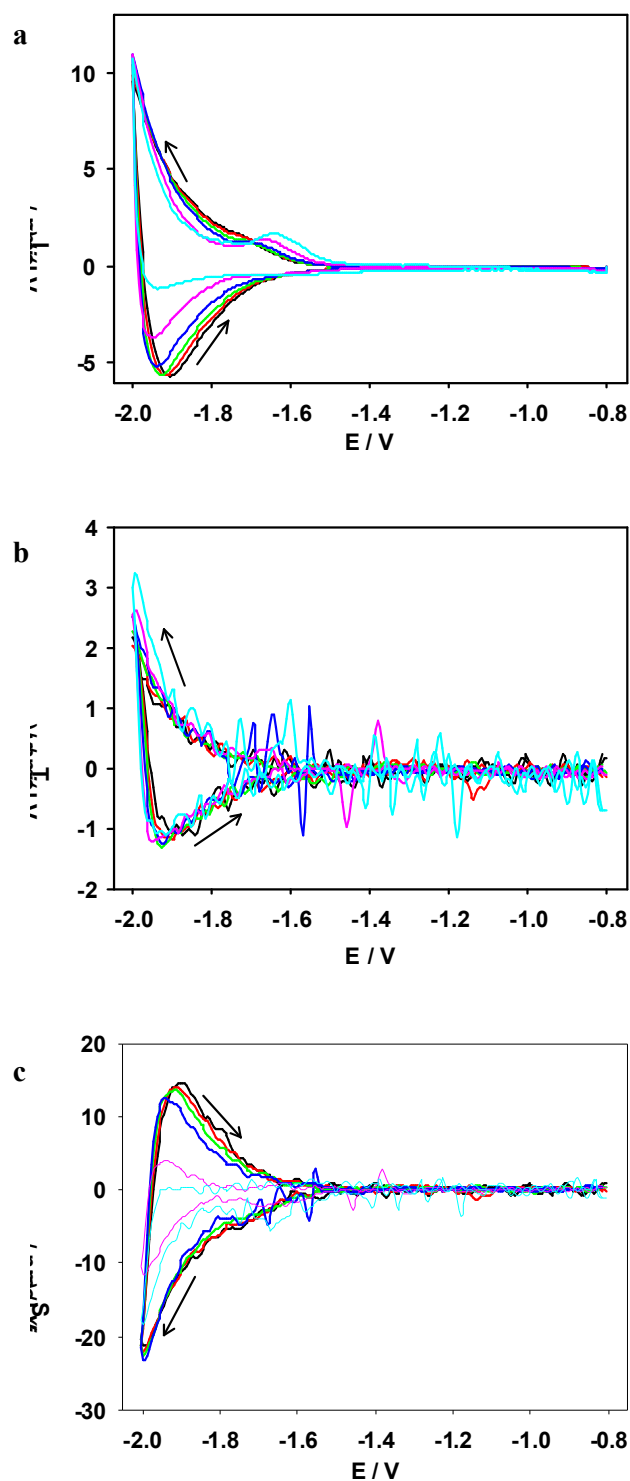


Figure 6.5 Normalized fluxes (j/v) as functions of applied potential, for the experiment of Figure 6.1. Panels (a) j_I ; (b) j_T ; (c) j_S . Scan rate, $v / \text{mV s}^{-1} = 20$: —; 50: —; 100: —; 150: —; 200: —; 250: —.

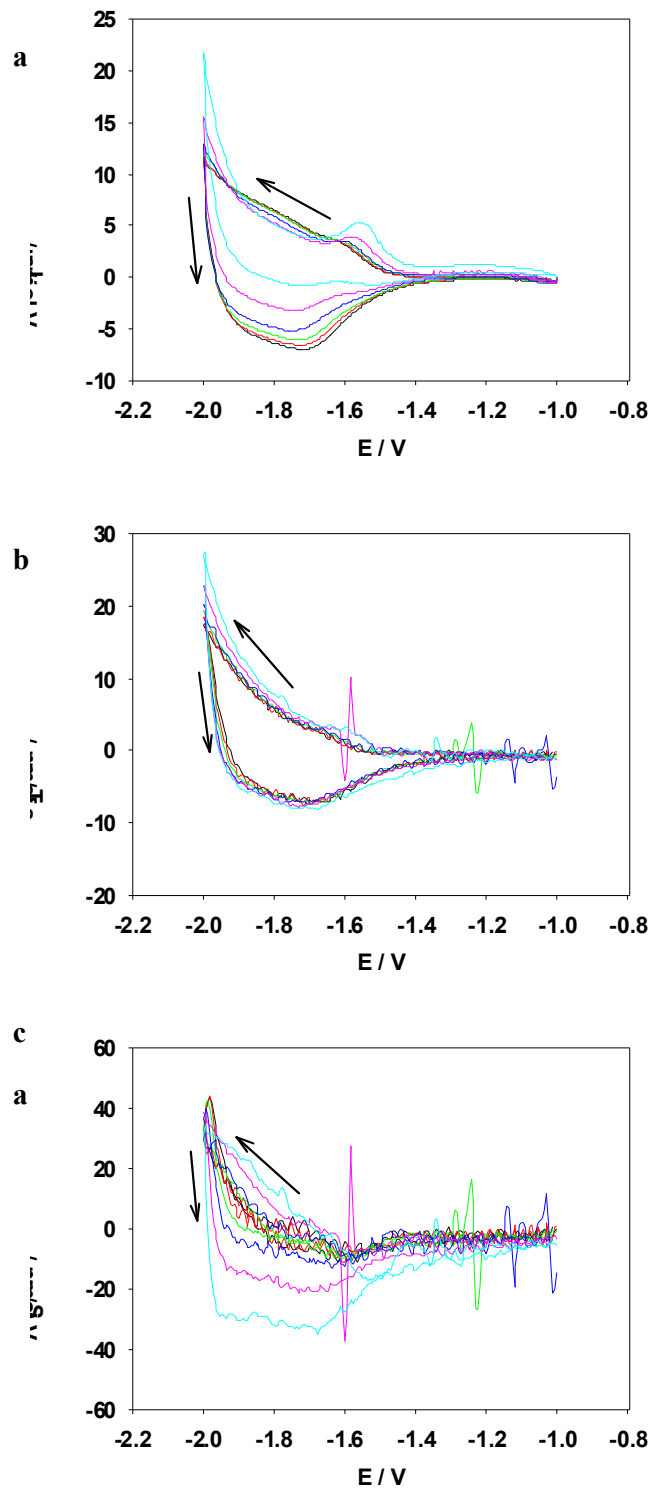


Figure 6.6 Normalized fluxes (j/v) as functions of applied potential, for the experiment of Figure 6.2. Panels (a) j_I ; (b) j_T ; (c) j_S . Scan rate, $v / \text{mV s}^{-1} = 20$: —; 50: —; 100: —; 150: —; 200: —; 250: —.

Kinetic effects or diffusional limitations would result in smaller normalized fluxes at higher scan rates. Here, although the solvent transfer is different for the two electrolytes (movement in different directions) both flux data do normalise with respect to scan rate. This indicates that, within a half-cycle (either doping or un-doping), there are no kinetic effects or diffusional limitations. However, there is significant hysteresis between the two scan direction responses, which signifies that there are polymer-based processes involved.

6.5.3 Effect of consecutive p- and n-doping

Figures 6.7 and 6.8 show the EQCM responses for three different PEDOT films (of similar thickness) each exposed to different electrolytes. The films were cycled from an initial un-doped state and then taken through the p-doping/un-doping and n-doping/un-doping regimes to the un-doped state. The data shown for each film/electrolyte are given as functions of potential scan rate. Figure 6.7 (panel a; i vs E) shows sequential n- and p-doping for a film exposed to TEABF₄. Comparison of this result with those in chapter 5 (figure 5.14) for p-doping and figure 6.1 (this chapter), shows that all the main features of the individual n- and p-doping are as one might expect. However it is also obvious that there are also two additional features, one during the early stages of the p-doping process (at $E \approx -0.5$ V) and another during the n-doping process (at $E \approx -1.8$ V).

This behaviour has been reported on a number of occasions for a number of thiophene – based polymers^{7, 20, 30, 34}, including PEDOT. The main consensus of opinion is that these features are attributed to the release of the trapped dopant ion from within the polymer matrix. However, this has not been proved directly; the data here permit this for the first time.

The release of the trapped dopant ion may be explained as follows. During the first half of the cycle (p-doping) the polymer film is oxidised and, to balance the charge, one anion enters the film matrix per electron removed. The reduction of the p-doped film

generated in the first half cycle undergoes reduction, but this is not complete. The film now contains isolated islands of conducting material with its associated dopant anion within an insulating matrix of un-doped polymer. The thermodynamic drive is present for them to be reduced but there is no facile kinetic pathway for electron exchange with the underlying electrode. As the potential is scanned to more negative regions n-doping of the polymer starts. As the conducting path opens up, the electron exchange between the trapped p-doped polymer and the underlying electrode is now possible. Thus a sharp peak appears associated with the release of the trapped charge. During the following n-doping cycle an analogous process occurs, this time with the trapping of n-doped material and counter cations. The film is cycled once again through the p-doping region and at the onset of film oxidation there is a rapid cation ejection.

Here we try to give an indication of the extent of ion trapping during the both the n-doping and p-doping cycles. As suggested above, separating the partial currents associated with the normal doping and the un-trapping phenomenon is not possible as the un-trapping phenomenon is fundamentally coupled to the normal doping process, since the normal doping process facilitates the un-trapping process.

Although the charges of the un-trapping process and the normal doping process cannot be separated, some insight may be gained into the relative magnitude of the un-trapping charge by comparing the i-E curves of a film cycled first in the n-doping region and then in the p-doping, to the response of the film cycled sequentially through the n- and p-doping regions. Figure 6.9 directly compares the current responses for a film p- and n-doping individually and then sequentially. Simple subtraction (which is probably an oversimplification, but gives a reasonable approximation) of the charge for each of the separate cycles, leads to an estimation of the percentage charge associated with the release of the trapped ion. Table 6.1 gives the charges associated with the n- and p-doping along with the charge for the release of the trapped ion. Using the first four scan rates ($250 - 100 \text{ mV s}^{-1}$) we estimate the charge associated with the release of the anion at the start of the n-doping cycle to be $5.3(\pm 0.3)\%$ of the total injected p-doping charge. This un-trapping charge for the anion is independent of potential scan rate over the range $100 - 250 \text{ mV s}^{-1}$. Data at lower scan rates are not so reliable due to the background current contributions.

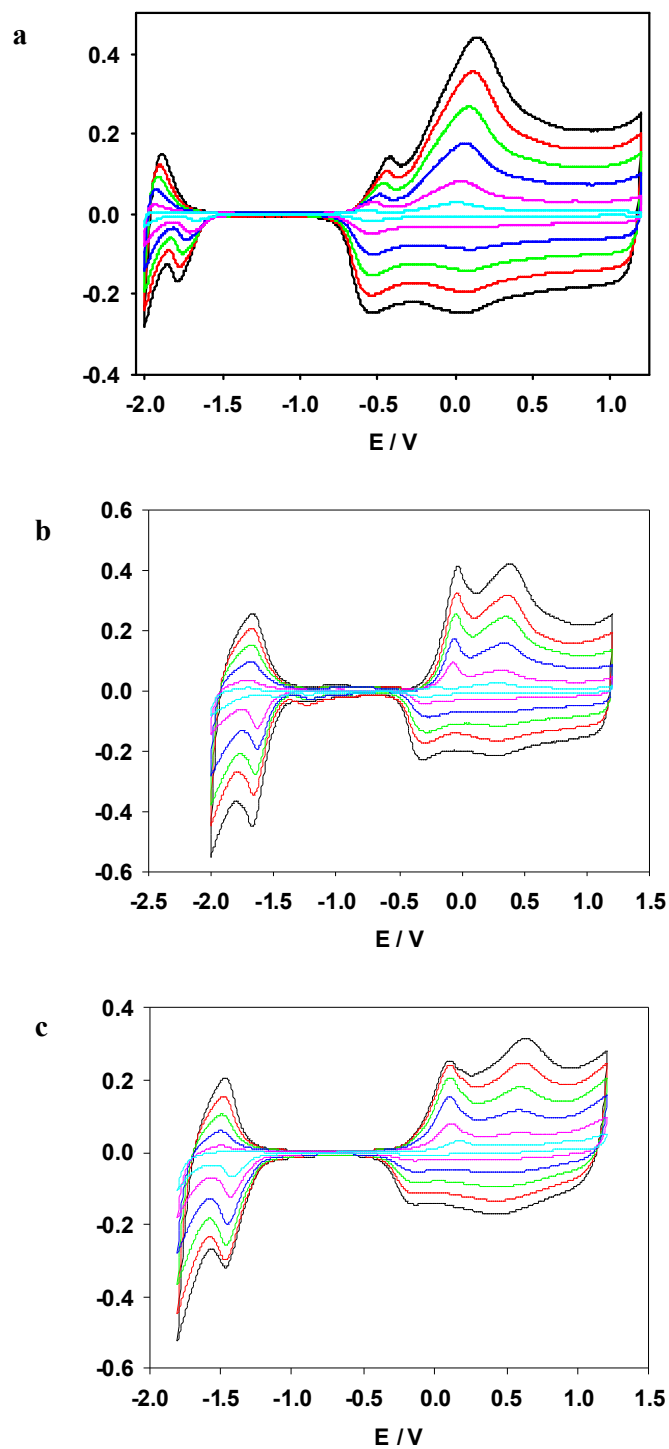


Figure 6.7. Experimental EQCM (i vs E) data for a cyclic voltammetric experiment involving n- and p-doping for PEDOT films exposed to 0.1 mol dm^{-3} (a) $\text{TEABF}_4 / \text{CH}_3\text{CN}$; (b) $\text{TPABF}_4 / \text{CH}_3\text{CN}$; (c) $\text{TEAToS} / \text{CH}_3\text{CN}$. Scan rate, $v / \text{mV s}^{-1} = 20$: —; 50: —; 100: —; 150: —; 200: —; 250: —.

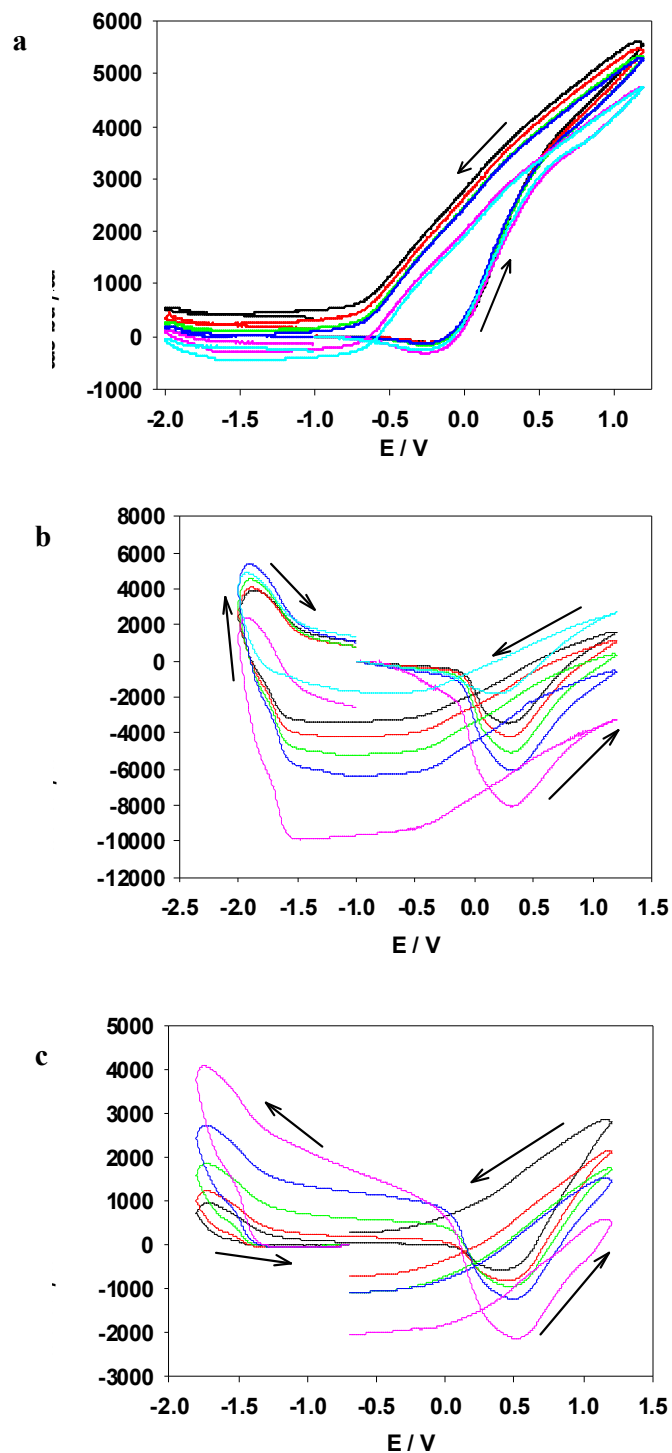


Figure 6.8 Experimental EQCM (Δm vs E) data for a cyclic voltammetric experiment involving n- and p-doping for PEDOT films exposed to 0.1 mol dm^{-3} (a) TEABF₄ / CH₃CN; (b) TPABF₄ / CH₃CN; (c) TEAToS / CH₃CN. Scan rate, $v / \text{mV s}^{-1} = 20$: —; 50: —; 100: —; 150: —; 200: —; 250: —.

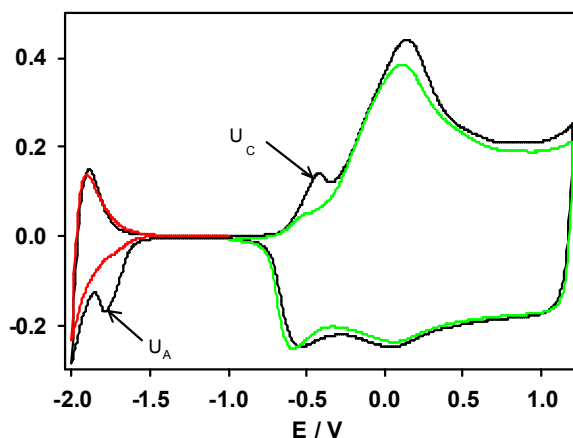


Figure 6.9 Cyclic voltammetric experiment on a representative PEDOT film exposed to 0.1 mol dm^{-3} TEABF₄ / CH₃CN. Response of film cycled through; — n and p doping regions: —; p doping region: —; n doping region.

In the mirror image process, the percentage charge associated with the release of the trapped cation at the start of the p-doping is calculated to be $43 (\pm 4)\%$ of the total injected charge (once again this value is averaged taken over the higher scan rates as the data at lower scan rates are subject to background contributions).

The doping level may be calculated using:

$$n = \frac{Q_{cv} / Q_{dep}}{\left(1 - \left(Q_{cv} / Q_{dep}\right)\right)} \quad (6.6)$$

where n is the doping level, Q_{cv} is the charge during film cycling and Q_{dep} is the charge during deposition. The calculated doping level for n-doping is $n_n \approx 0.033$ and the calculated doping level for p-doping is $n_p \approx 0.29$ for the case of TEABF₄. Thus the doping level for n-doping is smaller than for p-doping by around an order of magnitude. We speculate that this results in lesser opportunity for charge to be drained from the film during the undoping process, thus giving rise to a greater chance of charge trapping. Figure 6.10 shows the percentage trapping for both n- and p- doping versus scan rate.

Scan rate mV s^{-1}	Un-trapping charge for cation (U_c) / mC	n doping charge (N) / mC	Percentage charge trapped (U_c/N) %	Un-trapping charge for anion (U_a) / mC	p doping charge (P) / mC	Percentage charge trapped (U_a/P) %
250	0.0492	0.124	39.7	0.0760	1.536	4.9
200	0.0515	0.124	41.5	0.0773	1.522	5.1
150	0.0548	0.121	45.2	0.0826	1.500	5.5
100	0.0580	0.120	48.4	0.0862	1.482	5.8
50	0.0931	0.112	82.6	0.1401	1.204	11.6
20	0.0691	0.115	60.4	0.1002	0.853	11.7

Table 6.1 Calculation of percentage trapping with respect to scan rate

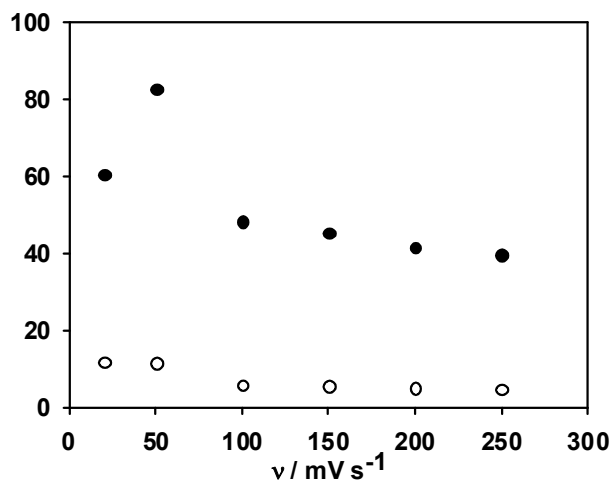


Figure 6.10. Relative trapping (with respect to total doping charges) of p-doping (o; associated with trapped anion) and n-doping (•; associated with trapped cation) charges as functions of potential scan rate for a PEDOT film ($\Gamma = 213 \text{ nmol cm}^{-2}$) exposed to $0.1 \text{ mol dm}^{-3} \text{ TEABF}_4 / \text{CH}_3\text{CN}$.

Figure 6.8 illustrates the mass traces for PEDOT films subjected to three different electrolytes. These mass traces correspond to the $i - E$ plots in figure (6.7). It is clear from the current traces that the trapping phenomenon occurs for all three electrolytes.

However the trapping phenomenon is not altogether obvious when looking at the mass traces of any of the electrolytes, as a consequence of the trapping feature sizes compared to those for the primary doping processes. The fluxes were calculated using equations (6.1) - (6.5) for the data obtained (for the three electrolytes) in figures 6.7 and 6.8 and are shown for two different scan rates in figures 6.11, 6.12 and 6.13 for TEABF₄, TPABF₄ and TEAToS respectively.

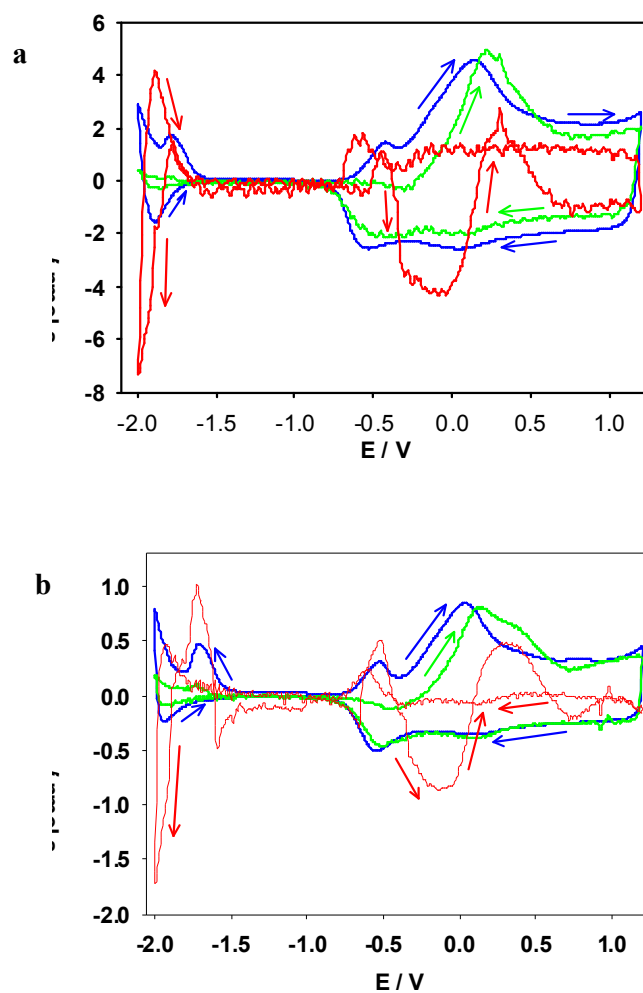


Figure 6.11 Flux representation as a function of potential, for data of Figures 6.7 and 6.8 panels a (TEABF₄). Panel a: $v = 250 \text{ mV s}^{-1}$; panel b: $v = 50 \text{ mV s}^{-1}$. j_I : —; j_T : —; j_s : —.

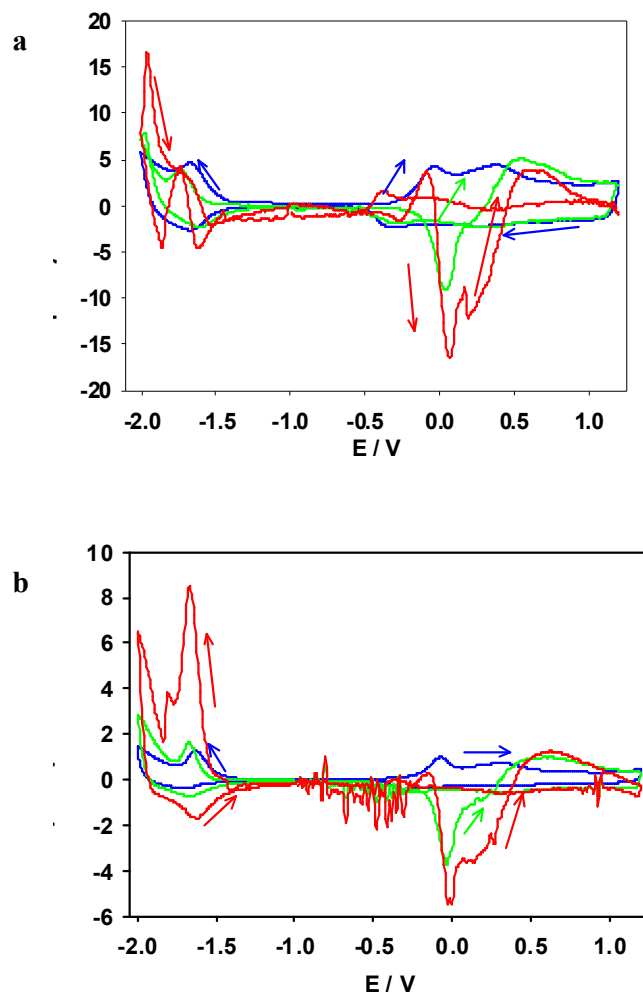


Figure 6.12 Flux representation as a function of potential, for data of Figures 6.7 and 6.8 panels b (TPABF₄ CH₃CN $\Gamma = 213 \text{ nmol cm}^{-2}$). Panel a: $v = 250 \text{ mV s}^{-1}$; panel b: $v = 50 \text{ mV s}^{-1}$. j_I : —; j_T : —; j_S : —.

The application of the flux methodology (equations (6.1) – (6.5)) to the data for the combined p- and n-doping experiments has to include two additional alterations. Firstly, as there are two different doping regimes, it is necessary to change the identity of the dopant ion (i.e. the associated mass and charge values). This change occurs as one moves from the p- to the n-doping regime, which occurs at a potential of $E = -1.0 \text{ V}$; at this potential all the fluxes are insignificant (figures 6.11-6.13).

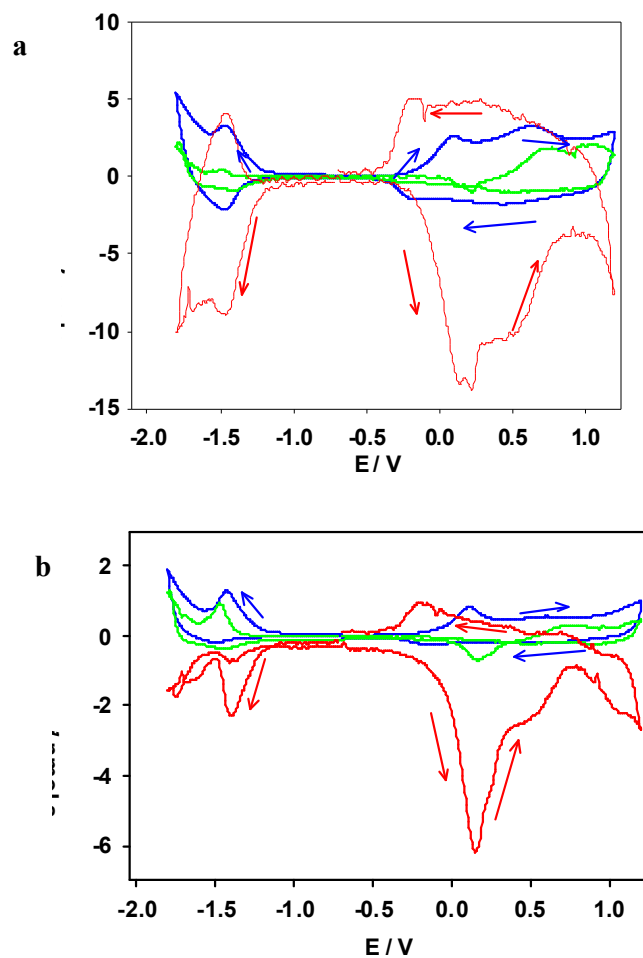


Figure 6.13 Flux representation as a function of potential, for data of Figures 6.7 and 6.8 panels c (TEATos / CH_3CN ; $\Gamma = 208 \text{ nmol cm}^{-2}$). Panel a: $v = 250 \text{ mV s}^{-1}$; panel b: $v = 50 \text{ mV s}^{-1}$. j_I : —; j_T : —; j_S : —.

The second alteration centres on the un-trapping processes. The un-trapping peaks show the movement of the opposite ion to that of the dopant ion involved in the doping process under consideration, i.e. the peak at ca. 0.5 V (figure 6.11) is for cation ejection during p-doping and the peak at -1.7 V is for anion ejection during the n-doping process. In theory, this suggests failure of the permselectivity assumption, because the film contains both the anion and cation. It is therefore necessary to separate the overall response into the two components associated with the un-trapping and doping processes. Calculating the difference between the current responses for the single doping and consecutive doping experiments enables the separation of these two components. The fluxes were then calculated using equations (6.1)-(6.5) and correcting

the data for both the identity change of the dopant ion and the un-trapping process. The whole process generates components for both ion and solvent fluxes. The solvent flux is the algebraic sum of the total mass and ion contributions. It is expected that the solvent flux is predominantly in the opposite direction to that of the ion, i.e. solvent needs to move out of the film in order to make room for the ion.

Figure 6.11 shows the flux data (at two different scan rates) for a film exposed to TEABF₄. During the oxidation (p-doping) the solvent flux is non-monotonic. There is first ingress of solvent (solvent entry during the un-trapping of the cation), which is followed by solvent loss and then finally a small amount of solvent entry. The reduction of the polymer back to neutral form (p-doping) shows solvent continually enters the film throughout the process; with a pulse of solvent entering at the end of the un-doping regime. The solvent flux during n-doping also shows an initial solvent ingress (for the loss of trapped BF₄⁻), followed by solvent egress associated with the entry of TEA⁺. Solvent entry then occurs as the film is oxidised back to its neutral form.

Figure 6.14 shows the normalisation (with respect to scan rate), of the flux data (from figures 6.7 and 6.8, panels a) for the film exposed to TEABF₄. The process works well for both the solvent and total fluxes (figure 6.14, panels b and c), during both the n- and p-doping regions. The process also works to a degree for the electron/ion flux data except at low scan rate, for which there is an issue associated with the background currents (see above). However, comparison of the responses for doping and undoping (of both p- and n-doped polymer) shows that they are not mirror images. This suggests different mechanistic pathways, as previously discussed in chapter 5, for p-doping of a PEDOT film.

The flux patterns for p-doping are basically the same for a PEDOT film exposed to TPABF₄ (figure 6.12) as for a film exposed to TEABF₄. Both results show that during p-doping the anion and solvent move in *opposite* directions. However, for the n-doping region, the solvent and cation are moving in the *same* direction for the film exposed to TPABF₄ but the *opposite* direction when a film is exposed to TEABF₄. The fluxes for the experiment data shown in figure 6.7 and 6.8 (panels b) were also normalised with

respect to scan rate. These processes work well with the exception of the data at slower scan rates (figure 6.15).

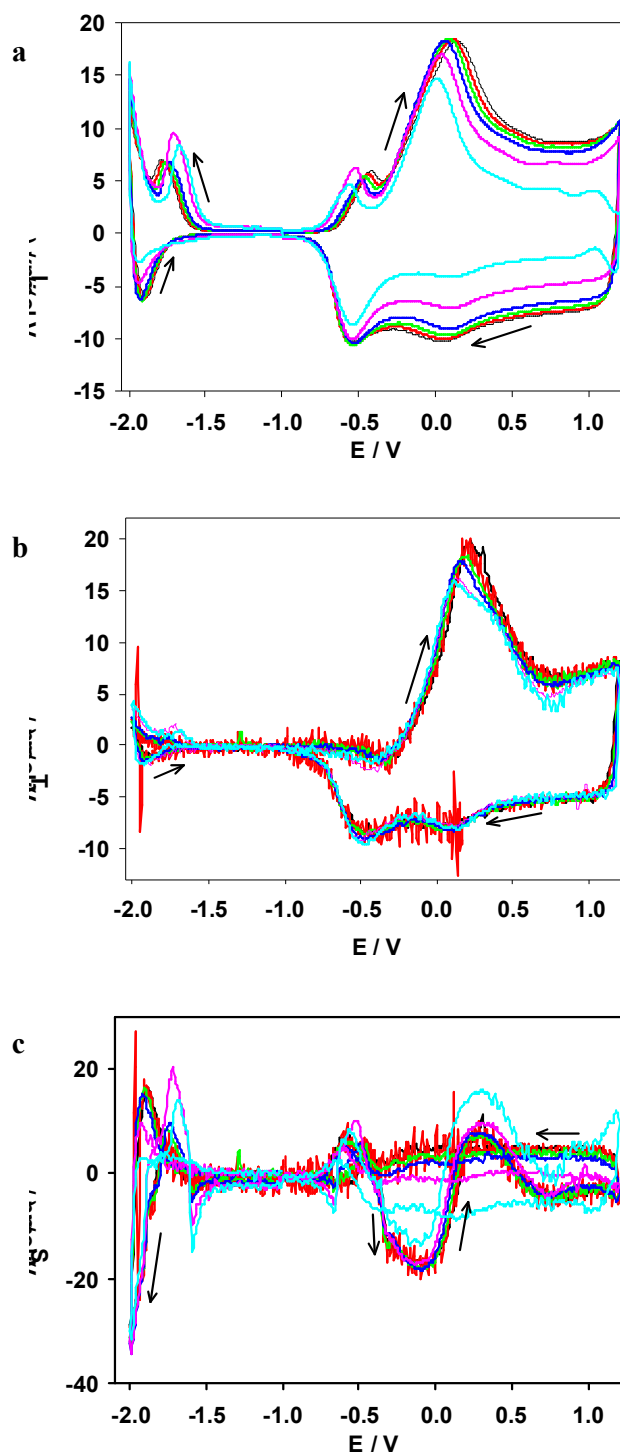


Figure 6.14 Normalized fluxes as functions of applied potential for the data of Figures 6.7 and 6.8, panels a (TEABF₄). Panel a: j_I ; panel b: j_T ; panel c: j_S . Scan rate, $v / \text{mV s}^{-1}$ = 20: —; 50: —; 100: —; 150: —; 200: —; 250: —.

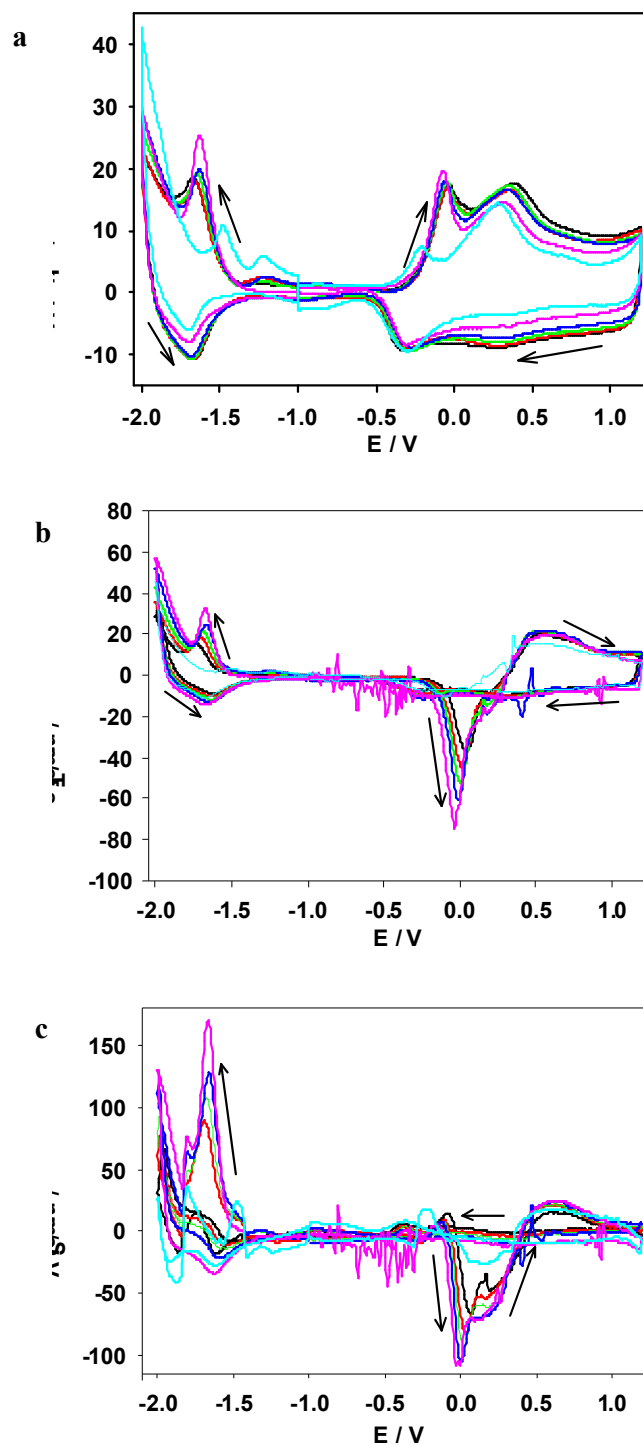


Figure 6.15 Normalized fluxes as functions of applied potential for the data of Figures 6.7 and 6.8, panels b (TPABF₄). Panel a: j_I ; panel b: j_T ; panel c: j_S . Scan rate, $v / \text{mV s}^{-1}$ = 50: —; 100: —; 150: —; 200: —; 250: —.

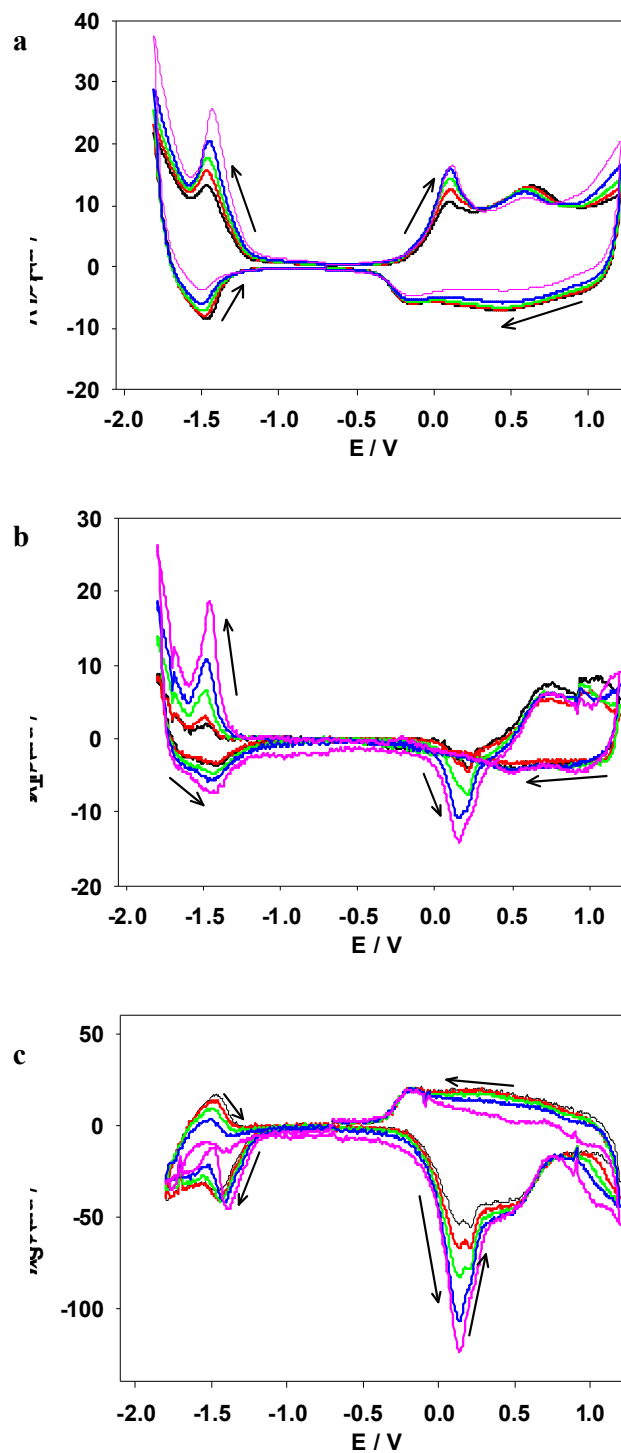


Figure 6.16 Normalized fluxes as functions of applied potential for the data of Figures 6.7 and 6.8, panels c (TEAToS). Panel a: j_I ; panel b: j_T ; panel c: j_S . Scan rate, $v / \text{mV s}^{-1}$ = 50: —; 100: —; 150: —; 200: —; 250: —.

The process of separating out the total mass response into its components (solvent and ion flux) was also applied to the combined p- and n-doping processes for a PEDOT film exposed to TEAToS/CH₃CN (data from figures 6.7 and 6.8, panels c). The results show similar complicated non-monotonic solvent fluxes, associated with the ion transfers, for which there are doping/un-doping and untrapping components. As with the other two films exposed to the other electrolytes, the normalisation of the flux data works well (figure 6.16).

6.6 Conclusions

For the n-doping experiments (no entry into the p-doping region) it was found that there is significant solvent transfer, but the direction varies with the cation identity. When the experimental flux data are subjected to the normalisation procedure (division of the flux data with the scan rate) we find that both the ion and solvent fluxes normalise at all potentials and in both scan directions. The fact that the data normalise with respect to scan rate signifies that there are no kinetic or diffusional limitations under the conditions used here. There is hysteresis between the scan directions, signifying that there is participation of another process, which is ascribed to be polymer reconfiguration.

During this chapter PEDOT films were subjected to n-doping and sequential p- and n-doping. Comparison of the results for separate p- and n-doping with those of the films cycled sequentially through both the p- and n-doping regime shows all the main features of the n- and p-doping that one might expect. However, it is also obvious that there are two additional features (evident from both current and mass data) for the trapping of charge within the film. During p-doping, anions become trapped within the polymer matrix. These anions are subsequently untrapped at the onset of n-doping (a peak seen at $\approx -1.5\text{V}$, corresponding to ca. 5% of the total injected charge). For cations trapped during n-doping and then untrapped at the onset of p-doping, the value is ca. 40%. It would appear that the relative extent of trapping for the cation is far more than that of the anion, but if one looks at the fact that the level of p-doping exceeds that of n-doping by a factor of ca. 10, this reveals that the *absolute* amount of trapped charge is very similar in the two cases.

The experiments in which the film is sequentially p- and n-doped generate complex non-monotonic solvent fluxes as a function of potential. However, flux data within both regions normalise with respect to scan rate.

References

- (1) *Handbook of Conducting Polymers*, 2nd ed.; Marcel Dekker, New York, 1998.
- (2) Chandrasekhar, P. *Conducting Polymers, Fundamentals and Applications. A practical Approach*; Kluwer Academic Publishers, Boston, 1999.
- (3) Carlberg, C.; Chen, X. W.; Ingnas, O. *Solid State Ionics* **1996**, *85*, 73-78.
- (4) Pei, Q. B.; Zuccarello, G.; Ahlskog, M.; Ingnas, O. *Polymer* **1994**, *35*, 1347-1351.
- (5) Blanchard, F.; Carre, B.; Bonhomme, F.; Biensan, P.; Pages, H.; Lemordant, D. *J. Electroanal. Chem.* **2004**, *569*, 203-210.
- (6) Bund, A.; Neudeck, S. *J. Phys. Chem. B* **2004**, *108*, 17845-17850.
- (7) Niu, L.; Kvarnstrom, C.; Ivaska, A. *J. Electroanal. Chem.* **2004**, *569*, 151-160.
- (8) Pigani, L.; Heras, A.; Colina, A.; Seeber, R.; Lopez-Palacios, J. *Electrochemistry Communications* **2004**, *6*, 1192-1198.
- (9) Plieth, W.; Bund, A.; Rammelt, U.; Neudeck, S.; Duc, L. M. *Electrochim. Acta* **2006**, *51*, 2366-2372.
- (10) Roncali, J.; Blanchard, P.; Frere, P. *Journal Of Materials Chemistry* **2005**, *15*, 1589-1610.
- (11) Roncali, J. *Chem. Rev.* **1992**, *92*, 711-738.
- (12) Cutler, C. A.; Bouguettaya, M.; Kang, T. S.; Reynolds, J. R. *Macromolecules* **2005**, *38*, 3068-3074.
- (13) Groenendaal, L.; Zotti, G.; Aubert, P. H.; Waybright, S. M.; Reynolds, J. R. *Advanced Materials* **2003**, *15*, 855-879.
- (14) Mortimer, R. J. *Electrochim. Acta* **1999**, *44*, 2971-2981.
- (15) Careem, M. A.; Vidanapathirana, K. P.; Skaarup, S.; West, K. *Solid State Ionics* **2004**, *175*, 725-728.
- (16) Smela, E. *Advanced Materials* **2003**, *15*, 481-494.
- (17) Hughes, G.; Bryce, M. R. *Journal Of Materials Chemistry* **2005**, *15*, 94-107.
- (18) Pigani, L.; Heras, A.; Colina, A.; Seeber, R.; Lopez-Palacios, J. *Electrochem. Commun.* **2004**, *6*, 1192-1198.
- (19) Fusalba, F.; El Mehdi, N.; Breau, L.; Belanger, D. *Chem. Mater.* **1999**, *11*, 2743-2753.
- (20) Loveday, D. C.; Hmyene, M.; Ferraris, J. P. *Synth. Metals* **1997**, *84*, 245-246.
- (21) Rudge, A.; Raistrick, I.; Gottesfeld, S.; Ferraris, J. P. *Electrochim. Acta* **1994**, *39*, 273-287.
- (22) MacDiarmid, A. G.; Kaner, R. B. *Handbook of Conducting Polymers*, 2nd ed.; Marcel Dekker, New York, 1998.
- (23) Nishio, K.; Fujimoto, M.; Yoshinaga, N.; Furukawa, N.; Ando, O.; Ono, H.; Suzuki, T. *J. Power Sources* **1991**, *34*, 153-160.
- (24) Arnau, A.; Jimenez, Y.; Fernandez, R.; Torres, R.; Otero, M.; Calvo, E. J. *J. Electrochem. Soc.* **2006**, *153*, C455-C466.
- (25) Hillman, A. R.; Efimov, I.; Ryder, K. S. *J. Am. Chem. Soc.* **2005**, *127*, 16611-16620.
- (26) Bruckenstein, S.; Shay, M. *Electrochim. Acta* **1985**, *30*, 1295-1300.
- (27) Hillman, A. R.; Bruckenstein, S.; Daisley, S. J. *Electrochem. Commun.* **2007**, *9*, 1316-1322.
- (28) Hillman, A. R.; Bruckenstein, S.; Daisley, S. J. *Phys. Chem. Chem. Phys.* **2007**, *9*, 2379-2388.
- (29) Sauerbrey, G. *Z. Phys.* **1959**, *155*, 206-222.
- (30) Ahonen, H. J.; Lukkari, J.; Kankare, J. *Macromolecules* **2000**, *33*, 6787-6793.

- (31) Kvarnstrom, C.; Neugebauer, H.; Ivaska, A.; Sariciftci, N. S. *J. Molecular Structure* **2000**, *521*, 271-277.
- (32) Fu, Y. P.; Cheng, H. T.; Elsenbaumer, R. L. *Chem. Mater.* **1997**, *9*, 1720-1724.
- (33) Huang, H.; Pickup, P. G. *Chem. Mater.* **1998**, *10*, 2212-2216.
- (34) Seshadri, V.; Wu, L.; Sotzing, G. A. *Langmuir* **2003**, *19*, 9479-9485.

CHAPTER 7

CONCLUSIONS AND FUTURE WORK

7.1 Conclusions

The quartz crystal microbalance has been used both on its own and coupled with electrochemical techniques throughout this thesis to study thin metal and electroactive polymer films. Under the conditions used, the quartz crystal microbalance is an ultra-sensitive mass sensor. Two types of quartz surface finish were used during this thesis, differing in the level of surface finish: these are described as etched and polished. The surface feature sizes of the two types were investigated using scanning electron microscopy, atomic force microscopy and acoustic wave fluid entrainment measurements. The surface feature size of the etched crystals were found to be ca. 200 nm using AFM and SEM and ca. 140nm by fluid entrainment measurements. Fluid entrainment measurements showed the polished quartz to have surface features of ca. 20nm. Neither SEM nor AFM could confirm the feature size of the polished crystals, but this was below the accessible resolution. Surface feature size analysis confirmed that etched quartz had surface features that were too large for the metal templating techniques based on polystyrene spheres.

Wetting is an important phenomenon in a number of electrochemical devices. It is well documented that de-wetting occurs at rough surfaces. Nanoporous metallic films were prepared to investigate wetting of surface features. Nanoporous films were prepared using colloidal template techniques, which involved the preparation by sedimentation of polystyrene spheres into hexagonal close-packed arrays. The required metal was then electrochemically deposited into the interstices of the template. Removal of the templates by dissolution using toluene left the required nanoporous metallic films.

Formation of a well-ordered template is dependant on the rate of solvent evaporation and sedimentation times. A diverse range of sedimentation and

solvent evaporation times showed the optimum preparation conditions to be a long settling period (between 2 - 5 days for 1000 nm spheres, 4 - 8 days for 750 nm spheres, 7 - 10 days for 500 nm spheres and 10 - 21 days for 200 nm sphere diameter templates) followed by a three - five day solvent evaporation period. It is thought, although not proven here, that both the temperature and humidity of the cell during template preparation affects the formation of the templates. AFM confirmed the structure of the templates.

Copper nanoporous films were prepared by simple galvanostatic deposition through polystyrene latex microsphere templates. The optimum current density for deposition of smooth copper films was found to be 4.52 mA cm^{-2} . It was calculated that copper nanoporous films with a thickness that corresponds to half the diameter of the template spheres would require a deposition time (at the optimum current density) of 16.9 and 6.8 s for 500 and 200 nm diameter spheres, respectively. The actual deposition time to achieve this was recorded to be 55 and 30 seconds for templates using spheres of 500 and 200 nm. It is thought that this inefficiency may be caused either by partial wetting, ohmic loss or deposition of loose (mechanically detachable or gravimetrically undetectable) copper on the external surface. Subsequent dissolution of the templates left copper films that mirror the morphology of the polystyrene arrays. Confirmation of the film's pore size was carried out by SEM, AFM and fluid entrainment measurements.

The copper films were then used to investigate the wetting of the nanoporous surface. For the most highly ordered deposits the QCM frequency shifts for films in air and in water indicate partial (ca. 41%) fluid filling of the hemispherical voids left by the dissolved polystyrene templates. Previous theoretical calculations carried out¹ suggest that for contact angles of $90^\circ - 120^\circ$ the surface is in the transition from being fully wet to completely de-wetted. The sharpness of the transition depends on surface feature size. The contact angle value (water on copper surfaces are between $96^\circ - 115^\circ$ ^{2, 3}) and QCM observations place the results obtained here within this region.

Platinum nanoporous films were prepared through polystyrene latex sphere templates; separate experiments used spheres with 500 nm, 750 nm and 1000 nm

diameters. The platinum deposits were smoother than those obtained for analogous experiments using copper. Wetting of the resulting platinum films indicated partial fluid filling of around 37, 24 and 10 % for nanoporous films prepared using 500, 750 and 1000 nm sphere diameter templates, respectively. This suggests that, as the pore size increases, the percentage filling decreases.

There has been a wide range of studies for which the EQCM has been used with cyclic voltammetry to investigate electroactive polymer films. However the majority of studies have placed the emphasis on the complete redox cycle, i.e. the average response obtained between fully reduced and fully oxidised films. During this thesis it is shown that consideration of the mass response for partial film conversion provides both mechanistic and stoichiometric information on the redox process.

The use of time differentials of film populations leads to information on both mass (total mass, includes both solvent and ion mass transfer) and charge transfers. The use of the electroneutrality condition and Faraday's law enables the subtraction of the ion flux from the total mass flux to yield the solvent flux. The EQCM coupled with cyclic voltammetry has enabled the exploration of dynamics of permselective films. Modern instrumentation has enabled the calculation of solvent flux with a precision down to 50 pmol s^{-1} and a time resolution of about 0.01 s. This means that it is possible to test for normalisation with respect to scan rate (the timescale parameter) of the ion and solvent fluxes, offering an extension of mechanistic experiments. Application of this approach to PEDOT films exposed to various electrolytes and solvents has lead to exploration of both the p- and n-doping regimes under permselective conditions.

For the case of PEDOT films exposed to $\text{LiClO}_4/\text{CH}_3\text{CN}$, both the solvent and anion fluxes normalise with respect to scan rate, whether viewed as a function of normalised charge or potential. The results show that even though the normalisation process works well for the doping and un-doping half cycles, each process has a different mechanistic path. As the mechanistic paths for the doping and un-doping half cycles are different this suggests that polymer reconfiguration is a participant within the process. The scheme of cubes representation gives a visual mechanism for which there are three

elementary steps: coupled electron/anion transfer, solvent transfer and polymer reconfiguration. However, on the experimental timescale used, the resolution of the solvent transfer and polymer reconfiguration is not possible. Thus the 3D scheme of cubes is reduced to a 2D representation, a square.

Comparison of data for a PEDOT film cycled in two different solvents shows distinct differences. The case of a PEDOT film cycled in TEABF₄/CH₂Cl₂ is a little more complicated than when the film is film cycled in TEABF₄/CH₃CN. The normalised fluxes for PEDOT cycled in both TEABF₄/CH₃CN and TEABF₄/CH₂Cl₂ are chemically, but not thermodynamically, reversible. Both sets of data show that at partial redox conversion during both the doping and un-doping half cycles a mechanistic switch occurs. However, the specific mechanisms are different for the two solvents. The mechanistic differences between the two solvents are characterised by the different patterns of deviation of the experimentally measured electron/anion and solvent fluxes from the predicted values on the basis of scan rate normalization. The comparison of the ion and solvent fluxes illustrates that the solvent ingress and egress rates are key factors in determining the mechanism. There are changes between kinetically limiting and rapid solvent transfer for both scan directions, which is dependent on the solvent identity.

For PEDOT films cycled only in either TEABF₄/CH₃CN or TPABF₄/CH₃CN it was found that there is significant solvent transfer, but the direction varies with the cation identity. The total mass fluxes for the two electrolytes are also different. For the film cycled in TEABF₄/CH₃CN, the total mass flux is much smaller than one would expect. The probable cause of such a small mass change is the large amount of solvent transfer. When the experimental flux data are subjected to the normalisation procedure (division of the flux data by the scan rate), we find for both electrolytes that the ion and solvent fluxes all normalise with respect to scan rate. This is the case in both scan directions. As the fluxes normalise across all potentials, this suggests that the films have no kinetic or diffusional limitations. There is hysteresis between the scan directions for the data of both films (cycled in the two electrolytes). This signifies that there is participation of another process, which we ascribed to be polymer reconfiguration.

A PEDOT film was subjected to separate p- and n-doping, then cycled sequentially through p- and n-doping regimes. Comparison of the results for separate p- and n-doping with those of the films cycled sequentially through both the p- and n-doping regime shows all the main features of the n- and p-doping are as one might expect. However, there are two additional features (evident from the current response) for the trapping of charge within the film. During p-doping, anions become trapped within the polymer matrix. These anions are subsequently untrapped at the onset of n-doping and give rise to an extra current peak at -1.5 V. The trapped charge corresponds to ca. 5% of the total injected charge. A similar process occurs during n-doping. Cations become trapped within the polymer matrix and are ejected at the onset of p-doping. The trapped charge is ca. 40% of the total injected charge. It would appear that the relative extent of trapping for the cation is far more than that of the anion, but if one looks at the fact that the level of p-doping exceeds that of n-doping by a factor of ca. 10, this reveals that the *absolute* amount of trapped charge is very similar in the two cases. The experiments in which the film is sequentially p- and n-doped generate complex non-monotonic solvent fluxes as functions of potential. However, flux data within both regions normalise with respect to scan rate.

7.2 Future work

This thesis has demonstrated that it is possible to prepare both platinum and copper nanoporous films by deposition through a polystyrene latex microsphere template. However, it is clear from both sets of results that a more detailed study is required in order to optimise the preparation of these nanoporous films. It is believed that the large range of settling period for the template preparation may be a result of a constant change in both humidity and temperature. Thus, a starting point for future study could be an investigation to find the effects of both temperature and humidity on the preparation of the polystyrene template.

It is well known that interfacial wetting of a solid surface is dominated by both its chemical properties and the surface geometric microstructure. Once the optimisation of the template formation has been carried out, this naturally leads to the preparation of different metallic nanoporous film possibilities. In turn this leads to useful information on the wettability of these films, not only in water but also other solvents.

Nanoporous films offer increased surface area in comparison to traditional (flat) films; therefore an interesting idea is to link the work on metal templating and conducting polymer deposition and produce nanoporous conducting polymer films. Nanoporous conducting polymer films may offer more interesting electrochemical and chemical properties due to the increase in surface area and fact that the resulting films are opalescent.

Here it was demonstrated that flux data can lead to information on mechanistic processes. There have been extensive studies based on PEDOT and other conducting polymer films giving a vast amount of data. There are volumes of $\Delta m-Q$ data detailed in the literature; this data could be re-appraised, using the data analysis developed here, into ion and solvent flux data. This could lead to the comparison of mechanistic routes for a variety of conducting polymers.

Reference

- (1) Theisen, L. A.; Martin, S. J.; Hillman, A. R. *Anal. Chem.* **2004**, *76*, 796-804.

Publications and contributions to conference presentations

Publications

“Kinetics and mechanism of the electrochemical p-doping of PEDOT” A. R. Hillman; S. J. Daisley; S. Bruckenstein. *Electrochem. Comm.*, **9** (2007) 6 1316-1322

“Solvent effects on the electrochemical p-doping of PEDOT” A. R. Hillman; S. J. Daisley; S. Bruckenstein. *Phys. Chem. Chem. Phys.*, **9** (2007) 2379-2388

“Ion and solvent transfers and trapping phenomena during n-doping of PEDOT films” A. R. Hillman; S. J. Daisley; S. Bruckenstein. *Electrochem. Acta*, **53** (2008) 3763–3771

Conference presentations

207th Meeting of Electrochemical Society, Quebec City, Canada (May 15-20, 2005)
“Characterization of nanoporous metallic films of controlled architecture” A. Robert Hillman, Samantha J. Daisley

57th Annual Meeting of International Society of Electrochemistry, (31 August to 5 September 2006) *“Interfacial wetting at nano-scale contoured surfaces”* A. Robert Hillman, Samantha J. Daisley

Midlands Electrochemistry Group Meeting, The university of Warwick (April 2005)
“Interfacial wetting at nano-scale contoured surfaces” A. Robert Hillman, Samantha J. Daisley

Midlands Electrochemistry Group Meeting, The university of Leicester (April 2006)
“Characterization of nanoporous metallic films of controlled architecture” A. Robert Hillman, Samantha J. Daisley

International conference on Electrified Interface (24-29 June 2007) *“EQCM studies of dopant and solvation dynamics in p- and n-doping of PEDOT films”* A. Robert Hillman, Samantha J. Daisley